UNIVERSITÀ DI SIENA

Dipartimento di Biotecnologie, Chimica e Farmacia

Corso di dottorato in Scienze Chimiche e Farmaceutiche

XXXIII ciclo

Settore scientifico disciplinare: CHIM/03

Functionalization of Black Phosphorus with Inorganic Reagents

Tutor:

Dr. Maurizio Peruzzini

Dr.ssa Maria Caporali

Prof. Stefano Mangani

Dottorando:

Matteo Vanni

MATTEO VANNI
15.02.2021
14:26:08 UTC

Matteo Vanni

Coordinatore:

Maurizio Taddei

Anno Accademico 2020/2021

ABSTRACT

PhD candidate: Matteo Vanni
Tutor: Dr. Maurizio Peruzzini, Dr.ssa Maria Caporali, Prof. Stefano Mangani
Dissertation: Functionalization of Black Phosphorus with Inorganic Reagents

---

Since its first reported exfoliation in 2014, the interest in black phosphorus has grown dramatically. The direct band gap, the high carrier mobility and the large specific surface area of BP open up great opportunities in different topical sectors of physics and chemistry including catalysis. As each phosphorus atom in BP has an sp^3 hybridization and is bearing a lone-pair, an effective approach to surface modification could encompass the coordination of transition metal fragments. In this thesis, the functionalization of exfoliated black phosphorus (2D BP) with different palladium precursors is presented. In particular, a new nanohybrid was obtained growing Pd NPs *in situ* on 2D BP. The new material, named Pd/BP, was characterized by means of different spectroscopic techniques and electron microscopy measurements. The existence of Pd–P bonds of 2.26(3) Å between peripheral Pd atoms of the nanoparticles and BP flakes was revealed via EXAFS measurements, highlighting the ability of 2D BP to act as an effective ligand toward the surface of metal NPs. The nanohybrid Pd/BP was used successfully as heterogeneous catalyst in the liquid phase hydrogenation of chloronitrobenzene to chloroaniline, resulting extremely selective in the process. Remarkably, comparative studies carried out with Pd NPs supported on carbon as reference material, revealed that the use of BP as support is crucial to reach higher selectivity.

Following a distinct approach, the functionalization of 2D BP was accomplished by addition of the organometallic precursor $[Pd(C_3H_5)Cl]_2$ to 2D BP. In-depth solid state characterization carried out by means of powder XRD and solid state ^{31}P CP-MAS NMR allowed to unravel the nature of the new material. HAADF-STEM microscopy performed at atomic level was exploited to probe the morphology of the flakes, revealing the existence of a uniform distribution of the metal within 2D BP, with no formation of metal aggregates, such as Pd NPs. EXAFS measurements, together with DFT simulations, revealed the existence of unprecedented interlayer Pd–Pd dimers, bridging two BP layers. Consistently with morphological and structural analysis, testing the material (named Pd_2/BP) in the benchmark hydrogenation of C=C and C≡C bonds, the metal sites resulted inaccessible to organic substrates. Conversely, preliminary studies on the application of Pd_2/BP in the hydrogen evolution reaction (HER) from acidic medium, pointed out a strong enhancement in electrocatalytic activity compared to pristine 2D BP.

Alla mia famiglia

e a Benedetta

Index

Chapter I

Introduction

Chapter II

Pd/BP nanohybrid: unravelling the nature of Pd–P interaction and application in selective hydrogenation

Chapter III

Interlayer functionalization of black phosphorus with Pd–Pd dimers

Chapter I

Introduction

1.1 The 15th Element

1.1.1 Overview

Phosphorus (symbol P) is a chemical element of the nitrogen group, with atomic number 15. Its name comes from ancient greek φόςφορος (light bearer), because of the faint glow emitted when the white allotrope is exposed to oxygen. Though not present on Earth as a free element, phosphorus is found inside minerals, such as phosphate rocks (containing the tetrahedral anion PO_4^{3-}) and in living beings. An adult human body contains an average of 0.7 Kg of phosphorus, mainly located in teeth and bones in the form of apatite. At a molecular level, phosphorus plays a crucial role in the architecture and in the metabolism of cells. Cytoplasmic membranes consist of a bilayer structure of phospholipids, whose orientation is imparted by the polarity of the phosphorus-containing heads. Phosphate groups are key components of both DNA and RNA frameworks, and noticeably, all forms of life base their intracellular energy transport on the molecular vector ATP (adenosine triphosphate). Notably, it was by urine, a biological source, that phosphorus was isolated for the first time in 1669 by Henning Brand, a German alchemist. Besides its crucial biological role, phosphorus is also extensively used in industry to prepare a plethora of compounds, including fertilizers, pesticides, plasticisers and flame retardants. In its elemental state, at ambient conditions, phosphorus can take different allotropic forms, among these, the only molecular compound is white phosphorus, made of discrete P_4 molecules. The others, namely red, violet and black phosphorus, are all polymeric solids with different structures. The next section will be dedicated to a survey of the distinct phosphorus allotropes, indulging a little bit on their fascinating story and structure determination

1.1.2 White phosphorus

White phosphorus (WP) is the most common and reactive form of the element and for this reason the most interesting from the industrial point of view. In pure form, it looks like a white and waxy solid, with a melting point of 44.1 °C and boiling point of 280 °C. WP reacts immediately with oxygen forming P_4O_{10}, a reaction highly exothermic that leads to self-ignition. For this reason, WP is usually stored under a layer of water and is carefully handled always under inert atmosphere. Beside the risk related to flammability, this substance is also extremely toxic, causing severe liver damage if ingested or adsorbed

through the skin. When first isolated by H. Brand after a tedious and somewhat serendipitous process, phosphorus was obtained concentrating large quantities of urine to a paste, heating this residue at high temperature inside a retort and collecting the evolved vapours in water. What most likely happened during such process was the reduction of phosphate salts by organic compounds present in the mixture, yielding gaseous phosphorus that condensed as the white allotrope. White phosphorus is composed of tetrahedral P_4 molecules of suggestive beauty, where the phosphorus atoms occupy the vertices of the simplest platonic solid, as shown in Figure 1a. The presence of tetratomic molecules in the gas phase was guessed by early vapour density measurements, but their geometry was determined only in 1935 by L.R. Maxwell *et al.* [1] through electron diffraction studies of heated vapours. Today it is known that P_4 is stable in the gas phase until 800 °C, when dissociation takes place with formation of P_2 diatomic molecules. Atomic distribution studies carried out in 1938 by S. Gingrich *et al.* [2] demonstrated the existence of P_4 molecules also in the liquid state. Solid white phosphorus may exist in three different modifications, named α-, β- and γ-P_4. The solid phase obtained by condensation of the vapours is α-P_4. Early crystallographic investigations carried out on this phase suffered from the slow conversion to the red allotrope under light illumination or from the high degree of thermal disorder [3,4], which prevents any structure solution. The crystal lattice is likely body-centred cubic, with a complex structure featuring 58(1) molecules in the unit cell. If α-P_4 is cooled down at ambient pressure, at −77.6 °C a reversible transition to β-P_4 takes place. An alternative approach to obtain β-P_4 is to crystallize it from concentrated solutions of α-P_4 in CS_2 below -77.6 °C. The β phase may be stabilized at room temperature under a pressure of 10 Kbar. Single crystal determinations carried out on β-P_4 by A. Simon *et al.* [5] revealed a triclinic lattice (P-1) with 3 molecules in the asymmetric unit. The refined structure is shown Figure 1.

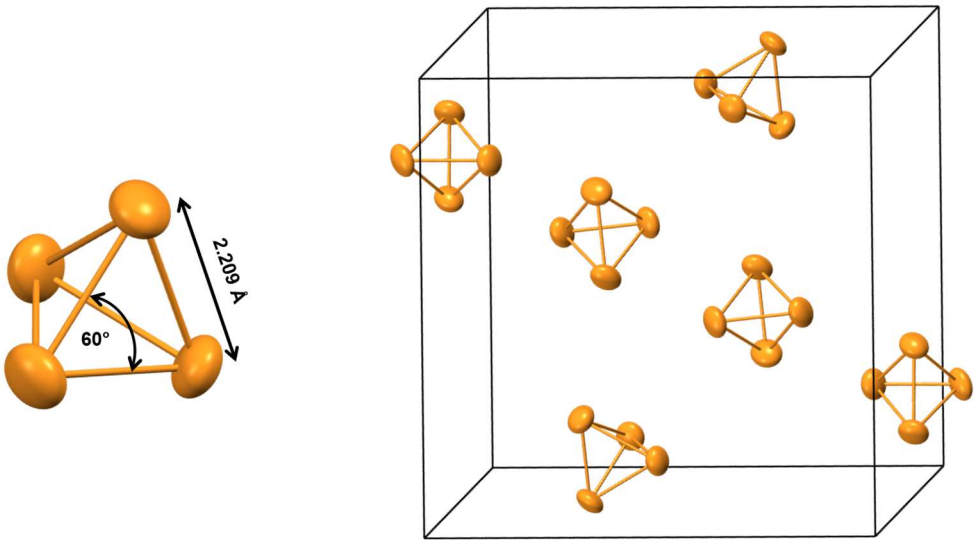

Figure 1. Molecular structure of P_4 (left) and unit cell of β-P_4 (right), generated from data by A. Simon [5]. Thermal ellipsoids are drawn at 50% probability.

Finally, yet another low-temperature modification of white phosphorus was discovered in 1974 and named γ-P_4 [6]. This form is monoclinic, with only two P_4 molecules inside the unit cell mirroring each other. γ-P_4 can be prepared quenching α-P_4 to – 165°C and keeping it at this temperature to enable the α → γ transition. The tetrahedral geometry of P_4, lacking a central atom as in the case of tetrahedral carbon, is quite rare in chemistry. Other examples are As_4, related mixed pnictogen compounds A_nB_{4-n} (n= 1-3), as well as C_4H_4 (tetrahedrane) and B_4Cl_4 and some polyatomic anions belonging to the bewilding family of Zintl ions [7]. In a simple valence bond description, each P atom is sp^3 hybridized. However, as the P−P−P angles measure ~ 60°, there is a strong distortion from the ideal value of 109.5°, making the P_4 tetrahedron extremely strained and reactive. That is why WP is the industrially most relevant allotrope of the element, with an annual production of about 910,000 tons. Today, WP is still produced by reduction of phosphates, although of inorganic origin (phosphorites). Phosphates ores, rich in fluorapatite, are mixed with silica and reduced with carbon at temperatures greater than 1100 °C in an arc-furnace, through a highly energy-consuming process. Silica is added in the form of gravel to lower the melting point in the slug. The overall reaction is the following:

$$2\ Ca_5F(PO_4)_3 + 9\ SiO_2 + 15\ C \rightarrow 9\ CaSiO_3 + CaF_2 + 15\ CO_{(g)} + 3\ P_{2\ (g)}$$

On cooling down P_2 gas dimerizes yielding P_4. The off gas, mainly containing P_4 and CO, is sent to a condensation tower were WP is recovered under water. About 85% of P_4 produced is burned to P_2O_5 and hydrated to make high purity phosphoric acid. The remaining 25% is mainly employed in the production of phosphorus-containing molecules that require the element as a reactant, such as PCl_3, $POCl_2$, P_2S_5, NaH_2PO_2 and to a less extent red phosphorus.

1.1.3 Red Phosphorus, violet phosphorus and related modifications

Among the elements, the ease of phosphorus to form chains is matched only by that of carbon. Moving from discrete P_4 tetrahedra to larger P_x motifs and extended structures, this feature gives rise to a tremendous structural variability. Since the discovery of white phosphorus, early investigators noticed that upon exposure to sun light the solid acquired a yellow colour. Sometimes, even a reddish coating formed on its surface. However, chemists of the time considered the red residue just a lower product of oxidation. It was only in 1850 that the existence of a red form as a distinct modification of elemental phosphorus was established by A. von Schrötter [8], who also managed to prepare red phosphorus (RP) heating the white allotrope at 280°C in inert gas. Unlike WP, RP is both thermodynamically and kinetically more stable at room temperature and does not react with oxygen if exposed to air. Indeed, ignition takes place only at 300°C. It is insoluble in most solvents due to its polymeric nature and contrary to the white allotrope, it is non-toxic. Thanks to this feature, the first application of RP after its discovery was in the manufacture of matches, replacing toxic WP used previously. Today, RP is principally used as flame retardant in plastic materials and in the production of some phosphorus containing materials such as semiconductors, pyrotechniques, fertilizers and pesticides. The actual

production is usually based on a batch process, in which white phosphorus is heated slightly above its boiling point for one-two days. During this time red phosphorus accumulates in the slurry, which gets more and more viscous over time. When solidification takes place (at about 70% of yield), conversion to the red allotrope is completed heating at higher temperatures. The material prepared heating the white allotrope is amorphous, but if specific thermal treatments are applied, different modifications of the red allotrope are accessible, with different degree of crystallinity but all reddish in colour. This variability created much confusion among early investigators. This is also the reason why WP was historically chosen as reference state for the element in thermodynamic calculations, despite being the less stable allotrope. In 1947, based on thermal analysis and XRD powder patterns, W.L. Roth assessed the existence of five distinct polymorphs of red phosphorus, of which two had crystalline character [9]. One of these crystalline modifications had been known since 1865, when it was prepared by J.W. Hittorf [10], and today is called violet phosphorus (VP) or Hittorf's phosphorus. Hittorf's synthetic method consisted in sealing amorphous red phosphorus inside an ampoule and heating at 550°C, growing violet phosphorus crystals by sublimation on the colder end of the ampoule. Violet phosphorus may also be prepared by recrystallization from solutions in molten lead or bismuth. The structure of this modification, shown in Figure 2, was solved in 1966 by Thurn and Krebs from single crystal data, resulting monoclinic and characterized by a complex architecture [11].

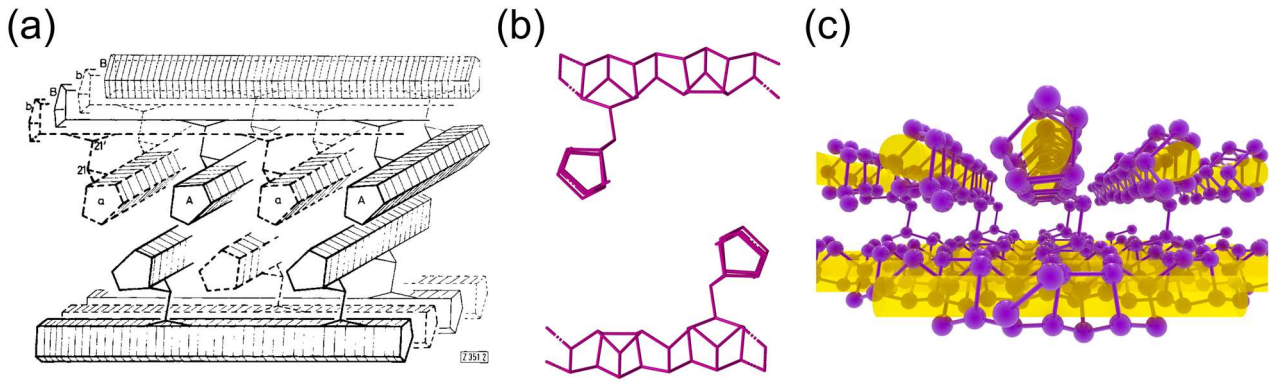

Figure 2. a) and (b) Structural models of Hittorf's phosphorus reported by Thurn and Krebs [11].c) Ball and stick representation of VP structure with added yellow tubes to highlight the orientation of tubular channels inside the structure. Reproduced from reference [12].

The building blocks are tubular units with pentagonal cross section, that are arranged in layers. Double-layer structures are formed by vertical covalent linking of perpendicular tubular strings. Independent tubular units inside each layer, as well as distinct double-layer motifs, are held together by weak van der Waals interactions. The space group of the structure, originally assigned to P2/c by Thurn and Krebs, was recently corrected to P2/n (no.13) during a single crystal structural redetermination carried out by J. Zhang and coworkers [13]. Remarkably, the second crystalline modification of RP suggested by Roth back in 1947 was identified and fully characterized in 2005 by M. Ruck and coworkers [14]. Because

of its morphology, it was named fibrous phosphorus. This modification often crystallizes with the violet one. The structure is closely related to that of VP and the two have exactly the same density. They differ in the alignment of the linked phosphorus channels, which instead of being perpendicular run parallel to each other (see Figure 3a-b).

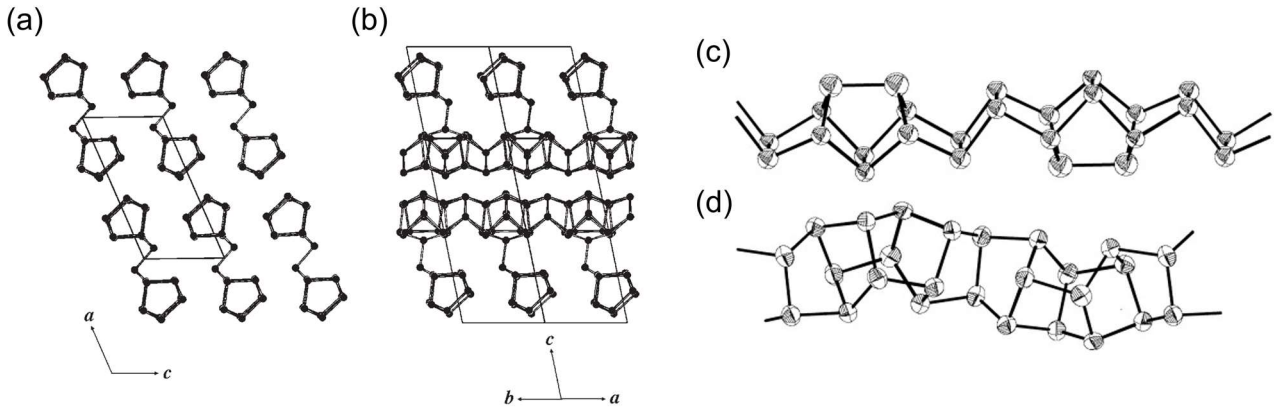

Figure 3. a) Arrangement of the double tubes along the fiber axis in fibrous phosphorus. b) Stacking of the layers in Hittorf's phosphorus. Reproduced from reference [14]. c) Structure of $^{1}_{\infty}[P_{12}]$ phosphorus strands present in $(CuI)_8P_{12}$ and (d) $(CuI)_3P_{12}$. Reproduced from reference [15].

It should now be remarked that the discover of fibrous phosphorus by Ruck was anticipated by theoretical studies, carried out by Böcker and Häser, addressing the systematic investigations of plausible bonding pattern in phosphorus chains [15,16]. The structure of fibrous phosphorus, still unknown at the time of these investigations, was predicted to be a stable modification of the element, energetically equivalent to the violet allotrope. This report highlighted also how distinct structures, built out of similar units, closely related to the violet and fibrous ones, could display a comparable thermodynamic stability. Some examples of these architectures may be found in $(CuI)_8P_{12}$ or $(CuI)_3P_{12}$ [15], whose structures contain independent phosphorus chains, see Figure 3b-d. In 2004 A. Pfitzner [18] managed to isolate these units through a Cu-extraction method by cyanide complexation, washing crystal of the copper halide adduct with cyanide solutions. The isolated material consisted in phosphorus nanorods with amorphous structure (likely caused by a difficult packaging of the phosphorus strands), in fact a new amorphous modification of the element. These findings, from theoretical investigations to experimental characterizations, helped to unravel the nature of common (amorphous) RP, which is probably made up of the same building units of violet and fibrous phosphorus, but lacking an ordered structure. This conclusion is further strengthened by recent research on phosphorus nanostructures. Starting from ab initio calculations on the stability of ring-shaped chains (named r-P) [19,20], in 2017 J. Zhang and coworkers [21] succeeded growing ring-type structures inside multi-walled carbon nanotubes (MWCNTs) nanoreactors. Sealing red phosphorus and carbon nanotubes inside an evacuated ampoule, then heating at 500°C, phosphorus fragments slowly diffused inside the nanotubes and polymerized in ring shapes (see Figure 4f-g).

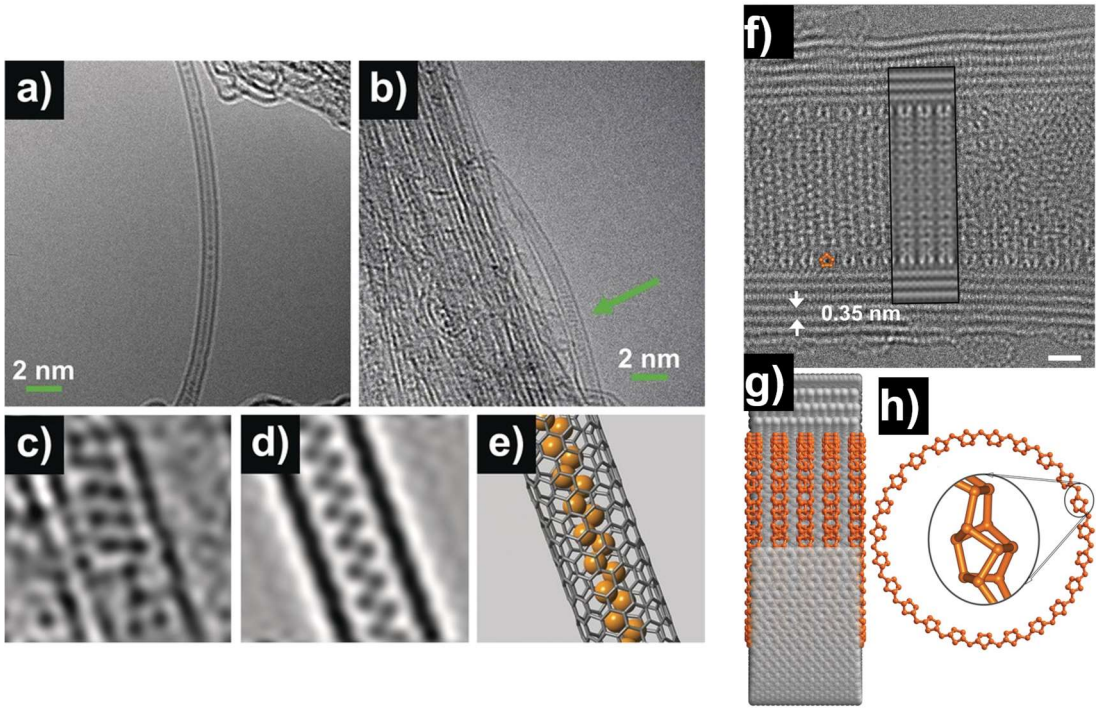

Figure 4. Polymerization of P_4 molecules inside MWCNTs. a) and (b) HRTEM images of MWCNTs containing polymeric phosphorus structures. c) Noise-filtered HRTEM image of the region highlighted in (b). d) Simulated HRTEM image and (e) the corresponding atomic structure of a single *zigzag* P-chain inside MWCNT. Reproduced from reference. [22] f) HRTEM image of r-P grown inside a MWCNT (named r-P@MWCNT). Rectangular inset: simulation of the r-P@MWCNT based on the structural model in (g). Scale bar = 1 nm. h) Side view of r-P. Reproduced from reference [21]

The cylindrical walls of the MWCNT acted as a template during the polymerization in rings and provided a stabilization to the growing structure. Similarly, M. Hart *et al.* [22,23] used single wall carbon nanotubes (SWCNTs), much thinner in diameter than MWCNs, to encapsulate P_4 molecules, up to about 10 $\%_{wt}$. When lined up inside the nanotube, P_4 tetrahedra polymerized forming different 1D structures. Of these, the zig-zag ladder (see Figure 4d-e) is a structural motif that is present also in Hittorf's and fibrous phosphorus architectures. Thus, these 1D structures could represent a snapshot of the very first stage in the transition from WP to RP. These last examples show how exciting this area of structural inorganic chemistry still is. Despite being started more than a century ago, new recent discoveries have been made that help to clarify old missing points.

1.1.4 Black phosphorus

Back in 1914 physicist and Nobel prize winner P. Bridgman, in an attempt to induce a transition from WP to RP under the influence of hydrostatic pressure, obtained unexpectedly a dark solid material. He recognized it as a new allotropic modification of the element and called this substance black phosphorus (BP) [24], being thermodynamically more stable than WP and RP and with higher density (2.691 g/cm^3). The new material looked crystalline and with fracture similar to that of graphite, however a structural characterization was not carried out. The preparation of BP from white phosphorus under Bridgman's

conditions was not an easy task, requiring 1.2 GPa of pressure at 200°C, taking approximately 30 minutes. Later in 1935 R. Hultgren et al. [2], working on samples prepared by Bridgman himself, were able to determine the structure of BP from powder patterns, with the aid of radial distribution functions. As it turned out, BP is orthorhombic with space group Cmce (no. 64), and has a layered structure reminiscent of graphite, where each monolayer (named *phosphorene*) is made of P_6 rings. However, in graphite the C_6 motif is planar, making the *graphene* monolayer flat meanwhile BP is formed by P_6 unit with a chair conformation, like a cyclohexane molecule. This makes the *phosphorene* layer puckered, with an alternation of ridges and valleys, enabling the distinction of two non-equivalent coplanar directions, an armchair direction (AC) and a zigzag direction (ZG) (see Figure 5b-c). Different perspectives of the structure of BP are reported in Figure 5. This structural divergence between *phosphorene* and *graphene* is easy to explain taking into account the different hybridization of the two elements, namely sp^3 for phosphorus in BP and sp^2 for carbon in graphite.

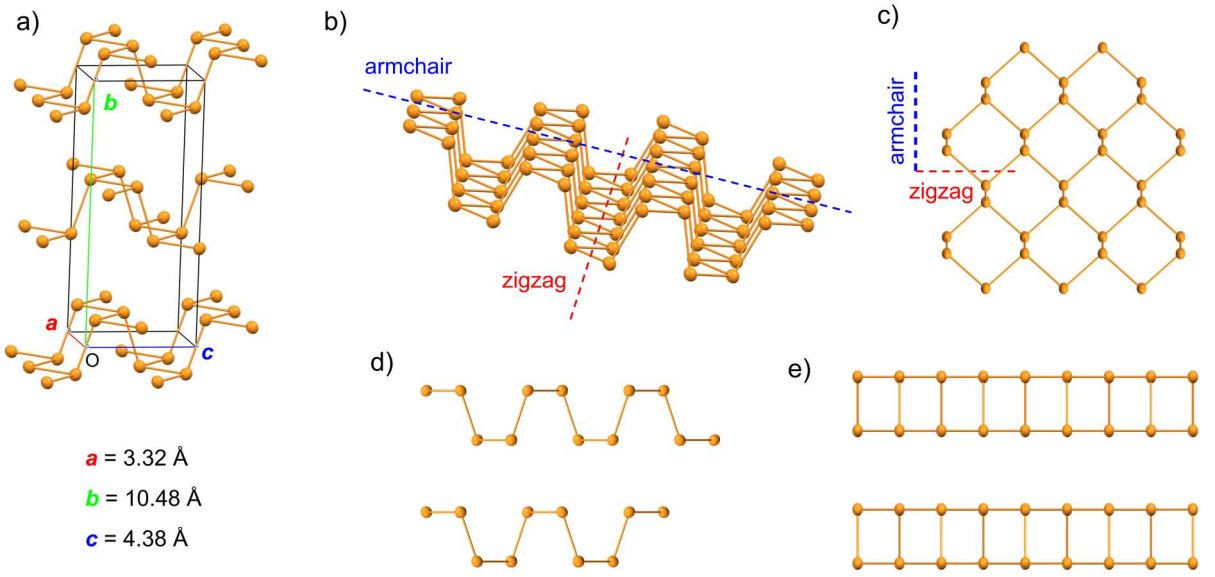

Figure 5. a) Detail of the BP structure with highlighted unit cell. b) Prospective view of a BP monolayer featuring the puckered arrangement of the phosphorus atoms and highlighting the two non-equivalent zigzag (red line) and armchair (blue line) directions. Different views of the structure along the *b* axis (c), the *a* axis (d) and the *c* axis (e) are also shown. Ellipsoids are drawn at 80% probability.

After the early studies by Bridgman, the first low pressure synthesis of BP was reported in 1955 [25] [26] and starting from equal amounts of WP and mercury, which were sealed inside an evacuated glass ampoule and heated at increasing temperatures from 280 to 380 °C, over a week. However, this method was strongly affected by the purification steps required to eliminate mercury impurities from BP. Improvements were made growing crystals of BP from WP solutions in molten bismuth, which provided needle-shaped crystals, easier to purify from Bi with nitric acid washings. This method allowed A. Brown and S. Rundqvist to obtain a sample of BP suitable for single crystal characterization [27]. Structure refinement by single crystal established that the model of Hultgren and coworkers was

substantially correct. Recrystallization from bismuth remained the method of choice for many decades, though it did not overcome the need of an easy, non-toxic and effective preparative route. This was fulfilled in 2007 by T. Nilges and coworkers [28], who reported a chemical vapour transport (CVT) route to grow large BP crystals from RP inside a sealed ampoule, heating the red allotrope for several days at 600°C in presence of AuSn alloy and SnI_4 as mineralizing agent. Later, using a programmed temperature with heating and cooling ramps, it was possible to reduce the reaction time at 33 h [29]. Beside the possibility of growing crystals more than 1 cm in diameter, the great value of this method was the remarkable quality and purity of the crystals obtained. Though traces of reagents and by-products were found on the surface of the BP crystals, they could be conveniently removed by mechanical separation without any further chemical purification step. The reacting mixture is complex, as many simultaneous equilibria are present at 600°C involving gaseous P_4, molten Sn, SnI_2, I_2, in addition to binary and ternary systems such as Sn_4P_3 and Au_3SnP_7. The latter was indicated as the potential site for an epitactic growth of BP, based on structural similarities. A remarkable improvement of the synthesis, which still represents the state-of-the-art, came in 2014 [30]. This last optimization allowed to reject the use of expensive Au, saving costs and drastically reducing the number of byproducts. Following this procedure, only Sn and SnI_4 are needed beside RP to prepare BP. The reagent mixture is sealed in a quartz ampoule, which is heated at ~ 650 °C inside an oven, building up a temperature gradient of 45-50 °C along the ampoule. The bulk regents are located at the hotter end of the ampoule and products form by vapour transport at the colder one (see Figure 6).

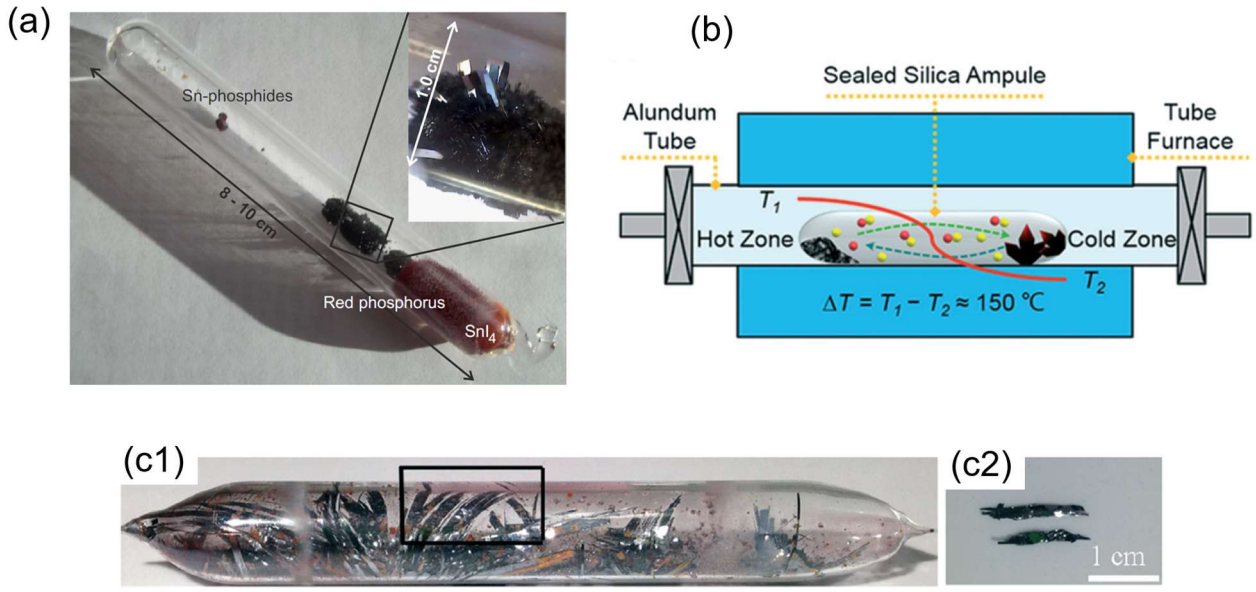

Figure 6. Synthesis of bulk BP crystals from RP according to the CVT method reported by T. Nilges, based on the Sn/I couple. a) Representative silica glass ampoule after the synthesis of BP. SnI_4 (orange) and red phosphorus (red) from the gas phase are condensed at the right hand side of the ampoule. BP is formed in large bunches. Excessive Sn reacted to form Sn_xP_y species, which are present in small round spheres. Reproduced from reference [30]. b) Experimental setup of the CVT reaction, according to reference [31]. c1) Quartz ampoule as it looked at the end of the reaction, featuring large BP crystals (c2). Reproduced from reference [32]

Some debate still exists around the actual mechanism of BP growth. To gain insights on the role of the Sn/SnI_4 additives, M. Zhao *et al.* [32] investigated 32 different metal-halide systems (e.g. Sn/I_2, $Sn/SnCl_2$, Pb/I_2, In/BiI_3, to name a few). A superior conversion from RP to BP was reached only when a Sn/I couple was employed, regardless of the specific formulation of the metal (e.g. Sn or Sn_4P_3) and of the iodide used (e.g. I_2, SnI_4 or PI_3), suggesting that all these species decomposed under the reaction conditions to form common active intermediates. Z. Zhang *et al.* [31] highlighted in particular the role played by the violet phosphorus modification during the growth of BP. According to their study, VP would form first, and then BP would start to nucleate on top of VP crystals, which slowly convert to the black modification. Leaving aside these mechanistic issues, the synthetic protocol based on the Sn/I couple has been pivotal in boosting BP research over the last six years, providing scientists an easy access to high-quality crystals, suitable for electronic and chemical applications.

The interest in new 2D phosphorus phases has prompted theoretical investigations beyond phosphorene. In 2014 Z. Zhu and D. Tomanek [33] proposed a new stable phase named blue phosphorus (BlueP). The structure of BlueP shows the same honeycomb motif of BP, but instead of being puckered its layers are buckled, featuring a zig-zag profile when viewed along the edge, resembling silicene [34] and bismuthene [35] (see Figure 7a,b). Remarkably, this phase was predicted to be almost as stable as BP and to possess a tunable band gap (from 2 eV in the monolayer to ~ 1.2 eV in the bulk). Soon after, blue P was successfully synthesized on Au(111) substrate by molecular beam epitaxy (see Figure 7) [36].

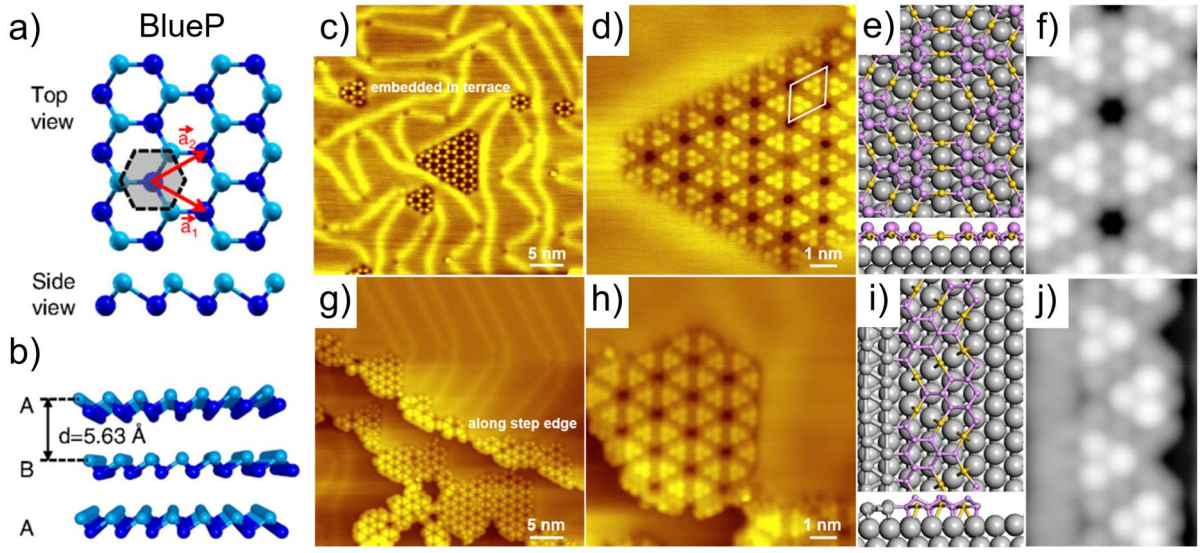

Figure 7. a) Top and (b) side views of BlueP structure. BlueP−Au alloy grown on Au(111): (c) Large-scale and (d) close-up STM images; (d) atomic model, and (e) simulated STM image of the BlueP−Au alloy embedded in the Au(111) terrace. (f) Large-scale and (g) close-up STM images, (h) atomic model, and (i) simulated STM image of the BlueP−Au alloy grown along the step edge. Violet, yellow, and gray spheres correspond to P atoms and Au atoms on/in the substrate, respectively. Reproduced from reference [37].

As recent studies have pointed out [38], the actual nature of BlueP/Au(111) is better described as a surface alloy, in which small BlueP islands are linked by bridging Au atoms, with a non-innocent role

play by the Au surface. W. Chen and coworkers [37] devised a silicon intercalation procedure to dealloy BlueP from the BlueP−Au binary lattice and to make the properties of pristine BlueP accessible. By this method, reaggregation of small BlueP fragments into nanometric domains took place. Though at present the existence of BlueP is limited to this scale, hopefully in future new preparative methods will make possible to deal with larger amount of this elusive 2D phase.

1.2 Black phosphorus: physical properties, exfoliation and characterization

1.2.1 Physical properties

Starting from its first reported exfoliation in 2014, in the last few years the research volume on BP has grown tremendously, embracing truly diverse fields, from high performance optoelectronics to batteries, catalysts, sensors and nanomedicine. Undoubtedly, the early interest aroused by BP was largely due to its potential application in nanoelectronics, thanks to its unique physical properties. Both theoretical and experimental studies showed that BP possess a thickness-dependent direct bandgap ranging from ~ 0.3 of the bulk material to ~ 2.0 eV in the monolayer (*phosphorene*), indicating that BP holds a wide light absorption from ultraviolet to visible light, and even near-infrared light (NIR), giving BP great potential for optoelectronic and other photomediated applications. In Figure 8a the band structure calculated by DFT for layer of increasing thickness is reported, while in Figure 8b angle resolved photoemission spectroscopy (ARPES) measurements are shown. The technique, which is basically a more sophisticated variant of common photoelectron spectroscopy, allows to reconstruct the valence band of a solid. The bandgap as a function of thickness, calculated using the GW method in the G_0W_0 approximation or the Bethe-Salpeter equation (BSE), is shown in Figure 8c and compared with the experimental value measured in 1L−BP. As evident from the graph, minor discrepancies may exist due to inherent assumptions in calculations.

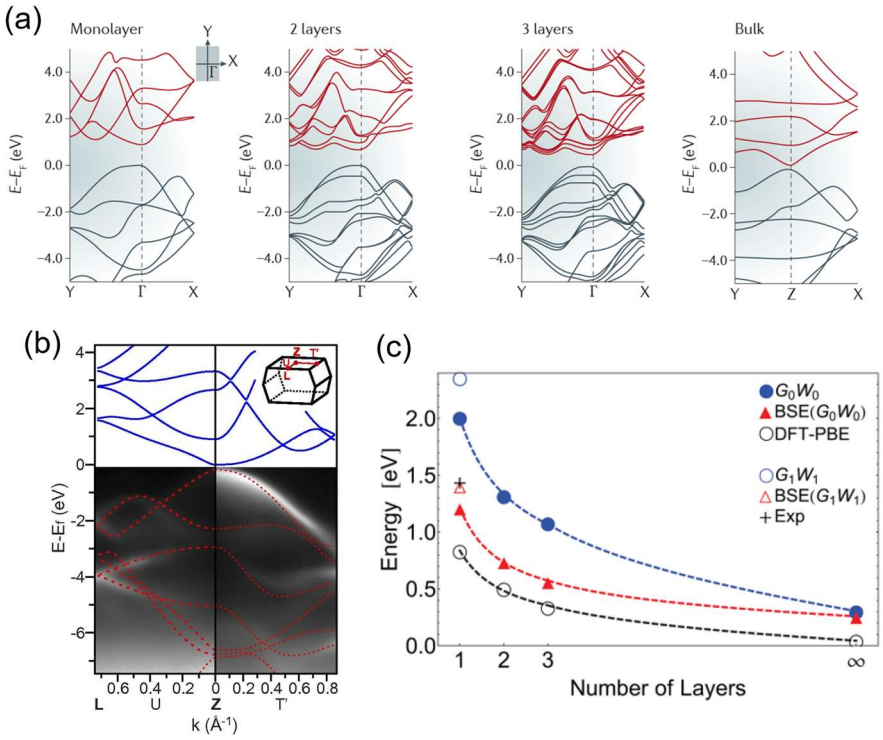

Figure 8. Band structures obtained by DFT calculations for 1L-, 2L-, 3L-BP and bulk BP. Γ = (0,0) denotes the centre of the 2D Brillouin zone. A gradual increase in band gap is observed moving from *phosphorene* to bulk BP. Reproduced from reference [39]. b) Band structure of bulk black phosphorus mapped out by ARPES measurements. A bandgap is clearly observed. Superimposed on top are calculated bands of the bulk crystal. Blue solid and red dashed lines denote empty and filled bands, respectively. Reproduced from reference [40]. c) Band gap as a function of the number of layers, calculated by various methods and compared with the experimental value (denoted + Exp). Reproduced from reference [41].

The existence of a direct bandgap for any number of layers sets phosphorene apart from common TMDs such as MoS_2 and WS_2, which display an indirect-to-direct bandgap transition upon going from bulk to monolayer. From the point of view of optoelectronic applications, this property represents an advantage, as it allows the use of few-layer BP in electronic devices instead of true *phosphorene*, much more challenging to isolate. As 2D BP is highly anisotropic it displays dichroism [42], which means that light rays with different polarization are absorbed at different rates. Dichroism is especially marked for frequencies close to that corresponding to the bandgap, as only light with a component of the polarization along the armchair direction is absorbed. However, the characteristic of BP that drew most attention after its first exfoliation was the high carrier mobility. The latter is inversely proportional to the carrier mass, which reflects the inertia opposed to motion under a perturbation. As for optical properties, the two-fold rotational symmetry of the lattice (point group D_{2h}) induces anisotropy in electrical behaviour along the zigzag and the armchair direction. The effective masses of holes and electrons in armchair direction are 0.15 m_0 and 0.17 m_0, respectively; meanwhile the effective mass of holes is 6.35 m_0 and that of electrons is 1.12 m_0 along the zigzag direction. Thus, charge transport displays a larger inertia (one order of magnitude) along the zigzag than along the armchair direction, which is way more effective to conduct electricity. Measured mobility along the armchair direction reached 1000 $cm^2\ V^{-1}\ s^{-1}$ at room temperature for a thickness of 10 nm [40]. Although first principle

calculations predict for phonon-limited carrier mobilities a value in the range 10000-14000 $cm^2 V^{-1} s^{-1}$, experimental determinations are limited by charge impurity scattering at low temperatures and electron–phonon scattering at high temperatures. This leaves much space for improvement and to better exploit the potential of the material. For instance, in a ~ 4 nm-thick (6–8 layers) BP flake sandwiched between h-BN layers, a hole mobility as high as 5200 $cm^2 V^{-1} s^{-1}$ along the armchair direction was reported at room temperature [43]. The carrier mobility of BP places it midway between graphene (~ 10000 $cm^2 V^{-1} s^{-1}$) and TMDCs (~ 300 $cm^2 V^{-1} s^{-1}$). Remarkably, theoretical studies predicted that in-plane strains in monolayer BP could modify its electronic band structure, resulting in a dramatic anisotropic change in carrier mobilities. Apart from the alterable bandgap and ultrahigh charge mobility, BP has interesting mechanical and thermal properties. It is characterized by an anisotropic Young's modulus, about one order of magnitude smaller than other 2D layered materials (~ 58 and ~ 27 GPa in zigzag and armchair directions respectively) that infers good mechanical flexibility [44]. Furthermore, BP is the first natural material (*i.e.* not man-made through microscopic engineering) to possess a negative Poisson ratio, a property characteristic of materials defined *auxetic*. [45,46]. When a solid is stretched in one direction by ΔL it usually tends to contract in the other two directions perpendicular to the one of stretching, as depicted in Figure 9. Similarly, when a material experiences a compressive force along an axis, it usually expands laterally. This common behaviour is associated to a positive Poisson ratio.

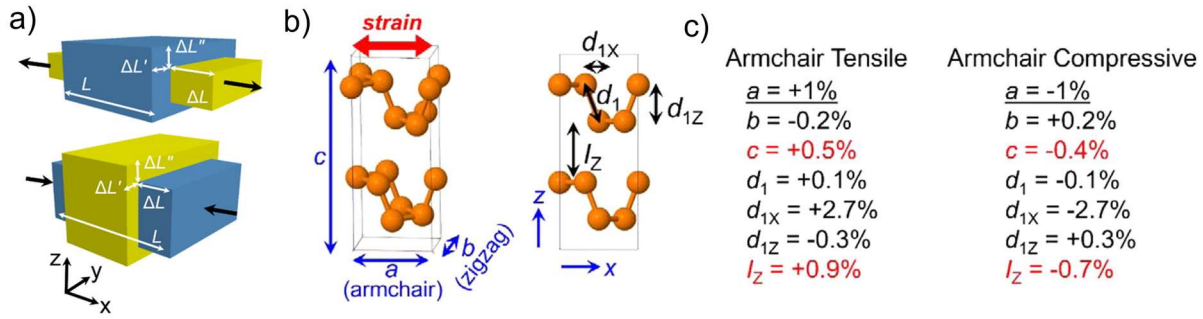

Figure 9. Schematic view of the positive Poisson's effect. A cube with sides of length L of an anisotropic linearly elastic material subject to both tensile and compressive strains along x axis. The blue box is unstrained. The yellow box is stretched (compressed) in the x direction by ΔL, and contacted (expanded) in the y and z directions by ΔL′ and ΔL″, respectively. b) Bulk structure of BP with highlighted lattice parameters: lattice constants (a, b, c), cross-plane bond (d_1), its x and z projections (d_{1x} and d_{1z}), and the interlayer distance (I_z). c) Variation of the other lattice parameters of BP upon tensile or compressive stress along a. Reproduced from reference [46].

A negative value of this property means that, somewhat counterintuitively, if stretched along a direction, the solid expands in the perpendicular one. In case of BP, both theoretical calculations and experiments showed the presence of in-plane anisotropic Poisson's ratio and negative out-of-plane Poisson's ratio, that means once the lattice is stretched along the armchair or zigzag directions, the interlayer distance (orthogonal to the direction of applied stress) increases. Conversely, if a compressive stress is applied, the interlayer distance gets shorter. In Figure 9bc, lattice variations induced applying strain along the armchair direction are summarized. This intriguing property depends entirely on the puckered anisotropic structure of BP, together with its hinge-like bonding configuration [47]. Noteworthy, the

negative Poisson's ratio typically can enhance toughness, shear resistance and sound absorption, all these properties are extremely helpful for applications in tissue engineering, fasteners, tougher composites, aerospace and defence. Thermal properties of BP also show in-plane anisotropic behaviour [48]. Thermal conductivity is higher along the zigzag direction by a factor 2 to 1.5 with increasing number of layers (see Figure 10). For instance, thermal conductivity values measured in a flake ~ 20 nm-thick resulted 34 $Wm^{-1}K^{-1}$ and 18 $Wm^{-1}K^{-1}$ along the zigzag and armchair directions respectively (see Figure 10a). These magnitudes are below the values reported for other 2D materials (graphene, TMDCs, h-BN).

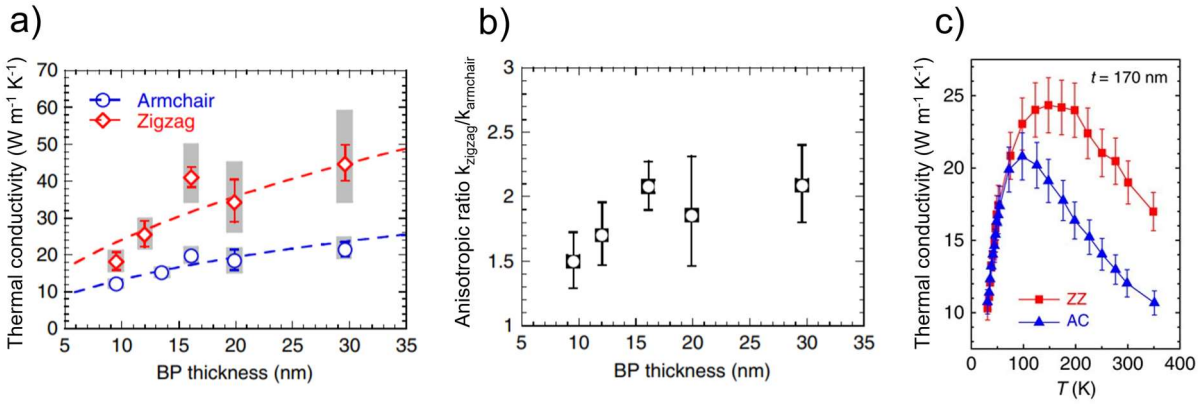

Figure 10. a) Armchair and zigzag in-plane thermal conductivities of multiple BP films measured via micro-Raman technique. The grey error bars account for the uncertainty of substrate thermal conductivity, whereas the blue/red error bars do not. b) The anisotropic thermal conductivity ratio at different BP thicknesses. c) Thermal conductivity vs temperature plot of BP nanoribbons along the *zigzag* (ZZ) and armchair (AC) directions, respectively. Flake thickness t = 170 nm. Reproduced from reference [48].

Lee *et al.* [49] studied the effect of temperature on the thermal conductance in BP nanoribbons, finding a peak-shaped dependence, as shown in Figure 10c. Interestingly, the high carrier mobility and the low thermal conductivity of BP make it possess excellent thermoelectric properties (TE) [50]. These are characterized by the dimensionless figure of merit ZT[1], whose value in BP is the highest among 2D materials. Thus, because of its excellent thermoelectric characteristics, another potential application of BP is in TE devices, whose function is the solid-state interconversion of thermal to electric energy.

1.2.2 Exfoliation of BP: routes to 2D BP and BPQDs

BP nanosheets (2D BP). As with other 2D materials, two distinct approaches may be used, at least in principle, to prepare few-layers BP, namely a bottom-up and a top-down method. To date, top-down methods as mechanical exfoliation, liquid-phase-exfoliation and plasma etching have found widespread application with BP. On the other hand, the bottom-up approach gave phosphorene with small size and

[1] ZT=S 2sT/*k*, where S, s, T, and *k* are Seebeck coefficient (thermopower), electrical conductivity, absolute temperature, and thermal conductivity, respectively. The thermal conductivity ($k=k_e+k_{ph}$) consists of the contributions from the electrons (k_e) and phonons (k_{ph}).

non-uniformity, being challenging the control of the growth process of BP, thus researchers are currently exploring bottom-up procedures to synthesize large scale and high quality 2D BP. For instance most 2D materials have been successfully grown by chemical vapour deposition (CVD) techniques [51], including graphene [52] and TMDCs [53], similar synthetic protocols were unsuccessful with 2D BP. J.B. Smith *et al.* [54] used a two-step method to prepare large (> 100 μm^2) BP films on a SiO_2/Si substrate. The authors used CVD to deposit thin films of red phosphorus onto the silicon support, which was then pressurized with argon at 27 bar inside an autoclave and heated at 900°C in presence of the couple Sn/SnI_2 to promote the conversion from red to black phosphorus (see Figure 11a-d,).

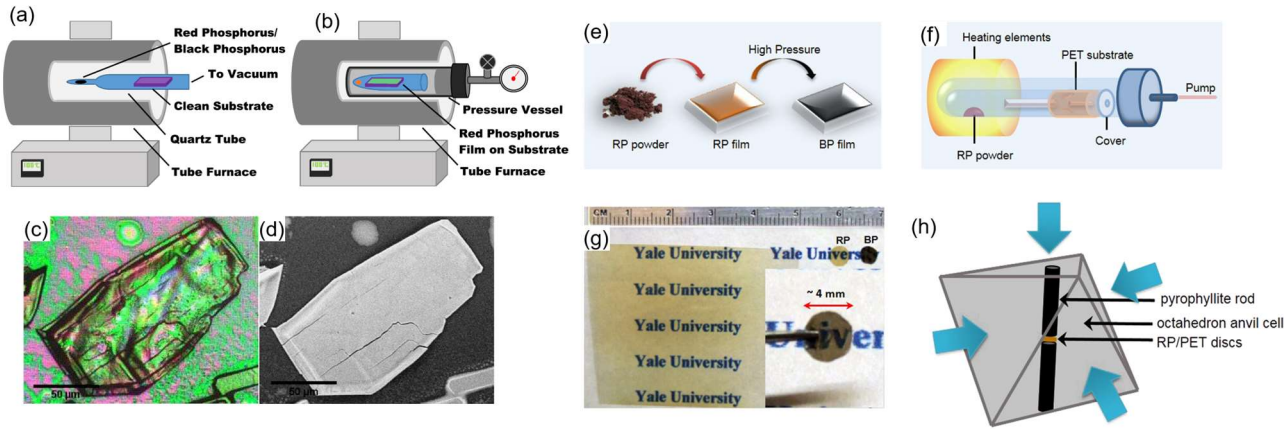

Figure 11. a-d) BP films preparation described in reference [54]. a) Schematic representation of amorphous red phosphorus thin film growth from CVD of bulk red phosphorus or bulk BP. b) Growth of BP film on substrate from amorphous red phosphorus thin film inside a pressure vessel reactor. c) A bright field image and (d) a SEM image of a 600 nm thick BP sample. The scale bar is 50 µm. e)-h) BP films preparation described in reference [55]. e) General synthetic strategy f) Schematic apparatus for the deposition of RP film. g) Image of a thin RP film on PET substrate (left), RP/PET disc for pressurization (middle) and BP/PET disc after pressurization. The inset shows the transparency of the BP/PET film. h) Schematic representation of the high-pressure anvil cell for conversion. The arrows indicate the directions along which the pressure is applied in conversion process.

Though effective producing large BP films (the term 'flakes' seems inappropriate, considering their size) sparse above the silicon support, this method had scarce control of their thickness, which reached 600 nm in largest films. X. Li *et al.* [55] developed a related method to grow black phosphorus films on top of a flexible polyester (PET) substrate, using high-pressures to carry out the conversion from red phosphorus (see Figure 11e-h). After deposition of red phosphorus coating by CVD, a circular disc of ~ 4 mm in diameter was cut from the support and mounted inside a multi-anvil cell. The pressure was then slowly increased to 10 GPa and held for several hours to allow the transformation. BP films with the outstanding dimension of 4 mm could be obtained by this method. Furthermore, compared to the thermal conversion, using anvil cells allows to keep the thickness around 40 nm. However, these examples are the only ones in literature and some concerns remain on the degree of crystallinity achieved, as pointed out by the low measured mobility of 0.5 $cm^2V^{-1}s^{-1}$, lower by four order of magnitudes than typical values obtained with mechanically exfoliated flakes. This point is of crucial

relevance for electronic applications (see Section 1.2.1). Similar considerations suggested the introduction of the expression 'electronic-grade BP' with reference to a form of BP characterized by a high degree of crystallinity and purity, with optimal performance in BP-based FETs. Historically, top-down methods were used first. Indeed, when 2D BP was prepared for the first time independently by Y. Zhang [56] and P.P. Ye [40] groups back in 2014, the exfoliation of BP crystals was carried out mechanically, using a classical adhesive-tape method (also termed micromechanical cleavage). This technique is well established in the field of nanoscience, being developed in 2004, when A. Geim and K. Novoselov used it to prepare graphene from graphite [57]. In a typical procedure, the crystal of a 2D material is attached to a piece of adhesive tape, supposed to have with the material an adhesion stronger than that existing between adjacent layers. Another tape is also attached to the crystal, at the opposite face, and then it is peeled off. The weak interlayers interactions are easily broken, and flakes of the material remain stacked on the tape, to be later transferred on a support (e.g. SiO_2/Si). In Figure 12a, a representative example of micromechanical cleavage of bulk BP is shown. Repeating the procedure on the detached flakes, thinner and thinner structures are successively obtained, even composed of few monolayers (FL-BP). In Figure 12b, the AFM image of a mechanically cleaved flake reported by Peide Ye's group, demonstrating the possibility to reach even single monolayers (1L-BP, or phosphorene), is reported.

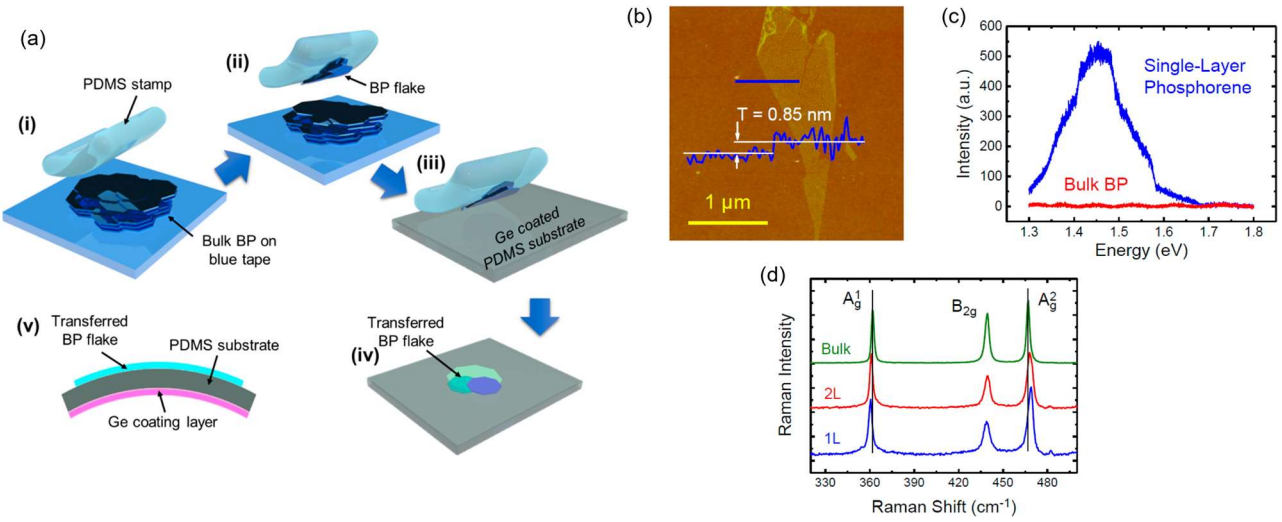

Figure 12. a) Representative mechanical exfoliation of a BP flake. In this example, a PDMS tape is used to peel off the material. After delamination, the material can be transferred to the target substrate, Ge-coated PDMS in this case. Reproduced from reference [58]. b)-d) Material characterizations of single-layer and few-layer phosphorene. b) AFM image of a single-layer phosphorene flake with the measured thickness of ~ 0.85 nm. Reproduced from reference [56]. c) Photoluminescence spectra for single-layer phosphorene and bulk black phosphorus samples on a 300 nm SiO_2/Si substrate, showing a pronounced PL signal around 1.45 eV. To prevent the single-layer phosphorene reacting with the environment, it is covered by PMMA layer during experiments. d) Raman spectra of single-layer and bilayer phosphorene and bulk black phosphorus films. Reproduced from reference [40].

Mechanical exfoliation allows the isolation of flakes having larger lateral dimensions compared to other top-down methods (*i.e.* solvent assisted and electrochemical exfoliation, see below). It also keeps the

crystallinity of the material perfectly unaltered and allows to obtain very thin flakes suited for electronic applications. However, a major limitation of this approach is the intrinsic poor yield, with no possible scaling. Thus, if a massive amount of material is needed, distinct approaches must be used, the most common being liquid phase exfoliation (LPE). As for micromechanical cleavage, LPE had been widely applied to other materials such as graphite [59], g-C_3N_4 [60], TMDCs [61] or h-BN [62]. The method consists in dipping a bulk crystal inside a suitable solvent and then using ultrasounds to achieve the exfoliation. Sonication generates cavitation bubbles inside the solvent. The latter collapse generating shock waves, which propagate and disrupt the BP structures, peeling the layers apart with formation of 2D BP flakes. In practice, ultrasounds may be generated using a sonication tip immersed inside the solvent. Alternatively, the chosen solvent and BP microcrystals are sealed inside a glass ampoule which is then immersed in a refrigerated ultrasonic bath. As 2D BP is sensitive to oxidation, the solvent is first degassed aiming to exclude oxygen during exfoliation. The role of solvent is not just that of a mere propagating medium for shock waves, actually its molecules should interact effectively with the surface of BP and provide stabilization to the layers, enabling their separation. Of course, in addition to the choice of solvent different factors are crucial to control the quality and the dimensions of 2D BP flakes, including sonication power (typically 20-50 KHz), time (some hours, usually more than 10) and temperature (around 20°C). In 2014, J.R. Brent *et al.* [63] were the first to carry out the LPE of BP. They used N-methyl-2-pyrrolidone (NMP) as solvent and obtained flakes that ranged from larger ones 200 x 200 nm with thickness 5 nm (11 layers) to smaller 20 x 20 nm and made of just 2-3 layers. The LPE process, beyond the separation of flakes, exerts the fragmentation as well, thus different flakes are produced, whose size and thickness are spread over a large interval of magnitude. An effective exfoliation protocol should produce homogeneous flakes, namely characterized by a sharp size distribution. Typically, increasing the sonication time helps reaching thinner flakes on one side, but causes breaks on the other, with a reduction in flakes average dimensions. M.C. Hersam *et al.* [64] studied the exfoliation of BP in different organic solvents, using a sealed-tip sonication apparatus (see Figure 13).

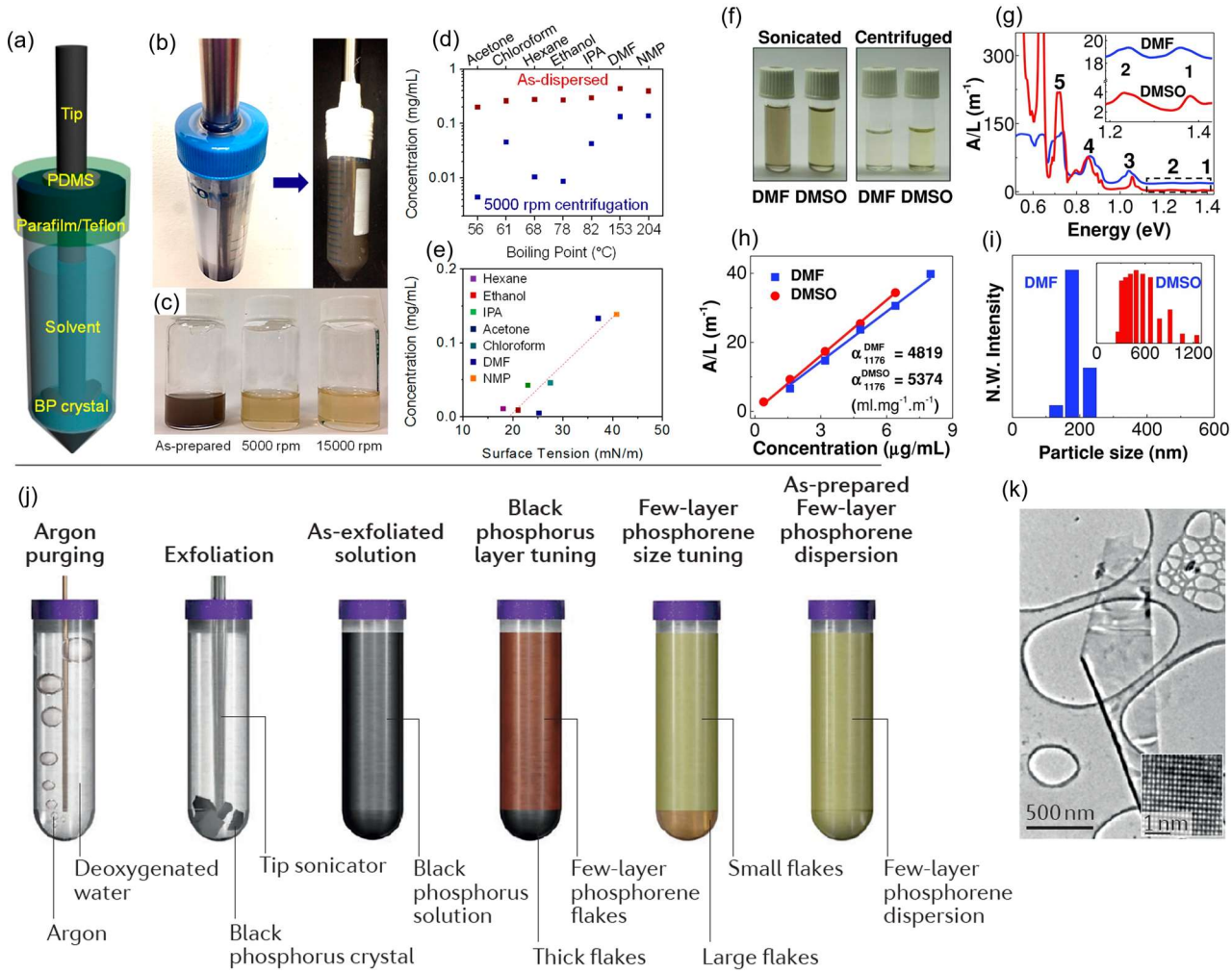

Figure 13. a) Schematic and (b) photograph of the custom-tip ultrasonication setup that minimized exposure to ambient air during processing described in reference [64]. c) 2D BP suspension in NMP obtained after ultrasonication (left), 5000 rpm centrifugation and 15000 rpm centrifugation (right). BP concentration after 5000 rpm centrifugation evaluated by UV/VIS absorption spectroscopy for various solvents as a function of boiling point (d) and surface tension (e). The red markers in (d) represents the value before centrifugation (immediately after ultrasonication). f) Photograph of 2D BP dispersions in DMSO and DMF solvents after sonication (left) and after centrifugation and supernatant collection (right). Reproduced from reference [65]. g) Optical absorption spectra obtained from dispersions in DMSO and DMF and (h) Absorbance normalized to the characteristic length of the cell at different concentrations (λ = 1176 nm). The extinction coefficient α extracted was used to evaluate the concentration of the subsequent solutions. i) DLS histogram for DMSO and DMF solution showing the flake lateral size distribution. j) Schematic of the preparation method for FL-BP aqueous dispersions described in reference [66]. Water with 2% (wt/vol) SDS was deoxygenated with Ar purging. The BP crystal was exfoliated in a sealed container using tip ultrasonication and then centrifuged to remove unexfoliated BP crystals and to isolate the FL-BP suspension. k) TEM image of a FL-BP flake obtained by this method.

Afterwards, centrifugation was carried out to separate the heavier fraction of the exfoliated material, the concentration of thin flakes left in solution was evaluated via UV-Vis absorbance measurements. This concentration indeed may be considered a figure of merit of the ability to sustain the peeling of BP into few-layer flakes, and it turned out that polar aprotic solvents with a high dielectric constant are the best suited for LPE (see Figure 13e,h). As revealed by microscopy (Figure 13k), spectroscopic (XPS, Raman) and electron diffraction studies, 2D BP flakes prepared by LPE in organic solvents are pure, structurally

intact and morphologically comparable to mechanically exfoliated ones. Furthermore, FETs built with solvent exfoliated flakes showed current on/off ratios and mobilities up to ~104 and ~ 50 $cm^2\ V^{-1}\ s^{-1}$ respectively, lower but still comparable to mechanically exfoliated flakes [64]. Further studies showed that DMSO is also extremely effective for LPE, with similar performance to DMF in terms of exfoliating ability (evaluated by the concentration of the final suspension) and flake size distribution (see Figure 13j). M. Serrano-Ruiz *et al.* [67] carried out a detailed investigation on the use of DMSO in BP LPE, studying the effect of added water on the morphology of the exfoliated material. Surprisingly, it turned out that water is a non-innocent player during the exfoliation of BP in DMSO. Remarkably, while common DMSO always contains some traces of water, being very hygroscopic, using rigorously anhydrous DMSO leaded to decomposition of BP under sonication, despite all manipulations were carried out under nitrogen. When small amounts of deoxygenated water were added, 2D BP flakes were successfully obtained, whose homogeneity and dimensions were function of the specific P/H_2O molar ratio. The best results came using $1.5 < P/H_2O < 14$, which yielded brown suspensions. After centrifugation (6000 rpm x 1h) a heavier fraction was isolated, composed of thicker flakes (30-100 nm), while FL-BP flakes with average size 500 x 800 nm^2 and thickness 5-20 nm remained in suspension. M.C. Hersam and coworkers have demonstrated that BP can be successfully exfoliated in water if stabilizing surfactant (sodium dodecylsuplhate) are present [66]. By this method, homogeneous suspensions of thin flakes with mean lateral size 150 nm and thickness 5 ± 4 nm were obtained. However, despite being electronically and optically active, these flakes likely bear traces of surfactant impurities, which may prevent subsequent chemical applications of the material. An advantage of LPE compared to mechanical exfoliation is that, in addition to peeling bulk BP into 2D BP flakes, the solvent may provide a barrier toward oxidation, provided that its molecules have a strong affinity with the surface of BP and get adsorbed creating a protective film. D. Hanlon *et al.* [68] found out that using N-cyclohexyl-2-pyrrolidone (CHP), BP crystal could be exfoliated even under ambient conditions without particular precaution (*i.e.* solvent deoxygenation, maintenance of inert atmosphere), as revealed by statistical Raman measurements. Indeed, A^1_g/A^2_g intensity ratios were sampled in 120 flakes, and always the ratio turned out > 0.6, strongly suggesting the absence of layer oxidation. Other useful solvents for both LPE and stabilization of exfoliated 2D BP are ionic liquids (ILs, see Figure 14). [69-72]. The latter are organic salts typically formed by an alkyl-imidazolium cation and a non-coordinating anion (BF_4^-, PF_6^-, ClO_4^-, TfO^- are the most common). Due to packaging difficulties in the solid state, these compounds are liquid at room temperature. ILs possess several interesting properties, such as high dielectric constant and viscosity, non-toxicity and easy recyclability compared to common organic solvents, thus representing a greener alternative.

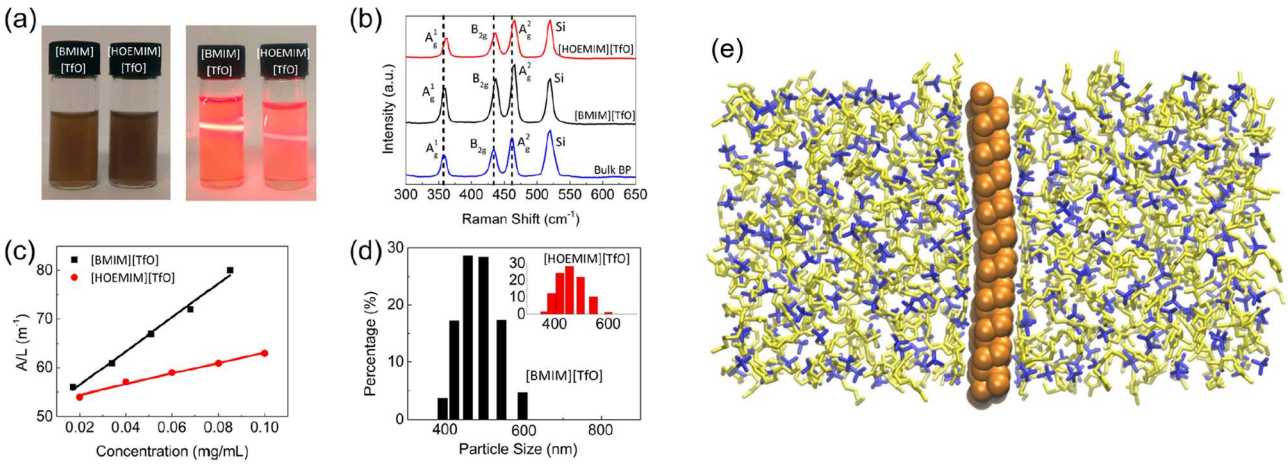

Figure 14. a-d) Optical characterization of IL-exfoliated BP nanosheets reported in reference [71]. a) Photograph of the 2D BP dispersions in [BMIM][TfO] and [HOEMIM][TfO] (left) and the Tyndall effect of diluted dispersions (right). b) Raman spectra of bulk BP and IL-exfoliated BP nanosheets in [BMIM][TfO] and [HOEMIM][TfO]. c) Plots of absorbance normalized to the length of the cell at different concentrations of BP for λ = 1188 nm in [BMIM][TfO] and [HOEMIM][TfO]. d) Size distribution histograms of IL-exfoliated BP nanoflakes in [BMIM][TfO] and [HOEMIM][TfO]. e) Molecular representation of phosphorene in [HMIM][BF_4]. Reproduced from reference [72].

Despite a π-p interaction between the electron-poor aromatic ring of imidazolium cations and BP lone pairs would be expected, recent theoretical calculations carried out by V.V. Chaban and coworkers [70] highlighted that the major contribution in this interaction comes from dispersion forces between BP and the lateral hydrophobic chains of the alkyl imidazolium cation. Polar imidazole rings instead form an electrostatically stabilized protective layer, limiting surface oxidation (see also Section 1.3.2). This effective interaction and the high viscosity of the solvent made possible to prepare stable 2D BP/ILs suspensions having concentration as high as ~ 1 mg/mL [71]. Although the yield and efficiency of LPE process have been largely improved in comparison to the mechanical exfoliation, alternative liquid-phase assisted methods have been proposed such as microwave [73] and solvothermal assisted methods [74]. Electrochemical exfoliation in particular has received some attention, since this method was previously employed successfully with graphene, giving high quality nanosheets by a simple, fast and environmental-friendly procedure, based on the use of water instead of organic solvents. In this process, bulk BP crystals are used as anodic material in a two-electrode cell with aqueous electrolyte. A constant potential difference is applied between the cathode and a counter electrode. As oxygen evolution starts to occur at the anode, electric current curses the BP crystals leading to layers detachment. M.B. Erande *et al.* [75] reported the preparation of 2D BP by this method using Pt wire as counter-electrode, working with 0.5 M aqueous Na_2SO_4 as electrolyte and an applied potential of 7 V. As shown in Figure 15e,f,g BP flakes obtained by this method displayed remarkable big lateral dimensions (0.5-30 μm), combined with a small thickness (3-15 layers).

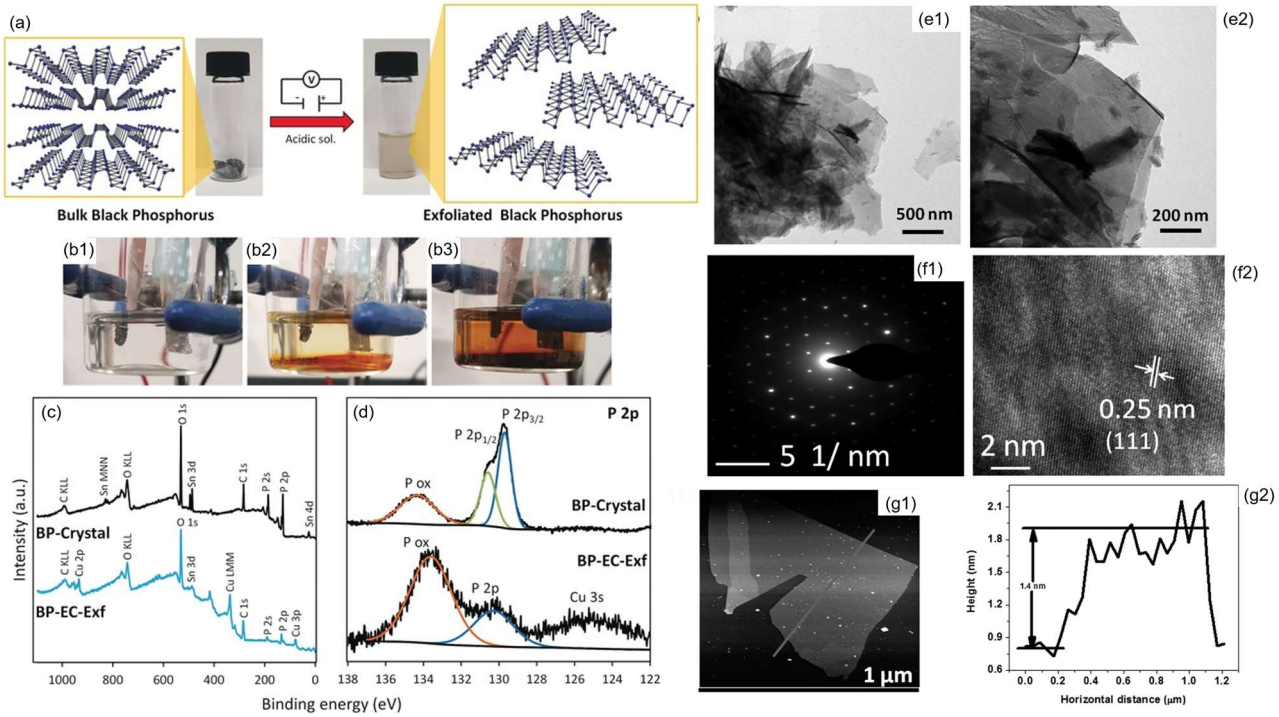

Figure 15. Electrochemical exfoliation procedure reported in reference [76]. a) Bulk BP is exfoliated in an acidic aqueous solution by the application of a DC voltage. The starting BP crystals (left) and the exfoliated material dispersion in DMF (right) are shown. b1) The electrochemical setup with the BP-flake anode and Pt-foil cathode, in acidic solution (H_2SO_4 0.5 M), separated by a fixed distance of 2 cm at no potential applied, (b2) after 20 min applying a voltage of +3 V, and (b3) after 2 h of applied voltage. c) Survey XPS spectrum of bulk and electrochemically exfoliated BP (BP-EC-Exf) and (d) Corresponding core level P2p XPS spectra. Cu was an impurity due to the sample holder. e)-g) Characterization of electrochemically exfoliated 2D BP described in reference [75]. e1, e2) TEM images of 2D-BP nanosheets and. f1) SAED pattern and (f2) HRTEM image of 2D BP highlighting the morphological integrity and the crystallinity of the material. g1) AFM imaging of a thin flake and (g2) corresponding height profile.

Similarly, M. Pumera and coworkers [76] reported the synthesis of 2D BP working in 0.5 M H_2SO_4 under a voltage of 3 V applied between the working electrode (BP) and Pt wire (see Figure 15a,b). As highlighted by XPS data, 2D BP flakes prepared by anodic exfoliation are partially oxidized, due to the intrinsic nature of the process (see Figure 15d). Nonetheless, M.B. Erande and coworkers assembled FETs using electrochemically exfoliated flakes and measured a field effect mobility and current ON/OFF ratio of 7.3 $cm^2V^{-1}s^{-1}$ and ~ 10^4 respectively, thus comparable to values obtained using different exfoliation protocols. A related electrochemical method was reported by the same group of M. Pumera [77] based on the concepts of bipolar electrochemistry. When immersed in the strong electric field generated by two parallel electrodes, BP crystal gets polarized at their opposite extremities and a potential difference builds up across each crystal, inducing fragmentation into smaller flakes. In practice, using two Pt foils as electrodes and a voltage as high as 10 V, BP microcrystals could be exfoliated into BP nanoparticles, with hydrodynamic radius ~ 70 nm. To overcome the problem of BP oxidation during the process of anodic exfoliation (due to the formation of oxidizing species as O_2), M. Lu and X. Xie have demonstrated that bulk BP can be efficiently exfoliated under a cathodic potential in an aqueous solution of hexadecyltrimethylammonium chloride [78]. The cation of the surfactant acts as intercalating

agent and applying the suitable voltage, BP can be peeled off in 30 minutes, once the temperature is raised to 50°C (meanwhile at RT the process did not take place). Whilst LPE requires many hours, this route is much faster and has the advantage of not using organic solvents and being easier to scale-up.

BP quantum dots (BPQDs). Quantum dots are semiconducting nanoparticles that possess unique optical and electronic properties, due to quantum confinement effects. Compared to BP nanosheets, BPQDs are 0D-nanostructures. Thus, despite being composed of stacked monolayers, their shape lacks the bidimensionality of 2D BP and their lateral-size-to-thickness ratio approaches 1, with absolute dimensions typically in the range 3−10 nm [79]. Though most research efforts focused on 2D BP, many studies on BPQDs have also been reported, mainly addressed to exploit their optical properties for biomedical applications such as fluorescence imaging, photoacoustic imaging and photothermal cancer therapy. BPQDs are usually prepared using LPE methods, both via tip and bath sonication or a combination of the two. The preferential formation of 0D-structure (BPQDs) compared to 2D nanosheets is dictated solely by the specific conditions under which LPE is carried out. For instance, Z. Sun et al. [80] synthetized BPQDs with ultrasound probe sonication followed by ice-bath sonication of bulk BP powder in NMP, producing high quality BPQDs with lateral dimension 2.6 ± 1.8 nm and average thickness 1.5 ± 0.6 nm (see Figure 16). H. Zhang *et al.* [81] reported the synthesis of BPQDs with lateral dimensions 4.9 ± 1.6 nm and thickness 1.9 ± 0.9 nm by ice-bath sonication in NMP (200 W x 3 h) followed by centrifugation to eliminate heavier particles. Other procedures using different solvents from NMP were reported, including N-vinyl-pyrrolidone, isopropyl alcohol, and DMF [79]. In addition to sonochemical exfoliation, some procedures based on solvothermal methods have been reported to prepare BPQDs.

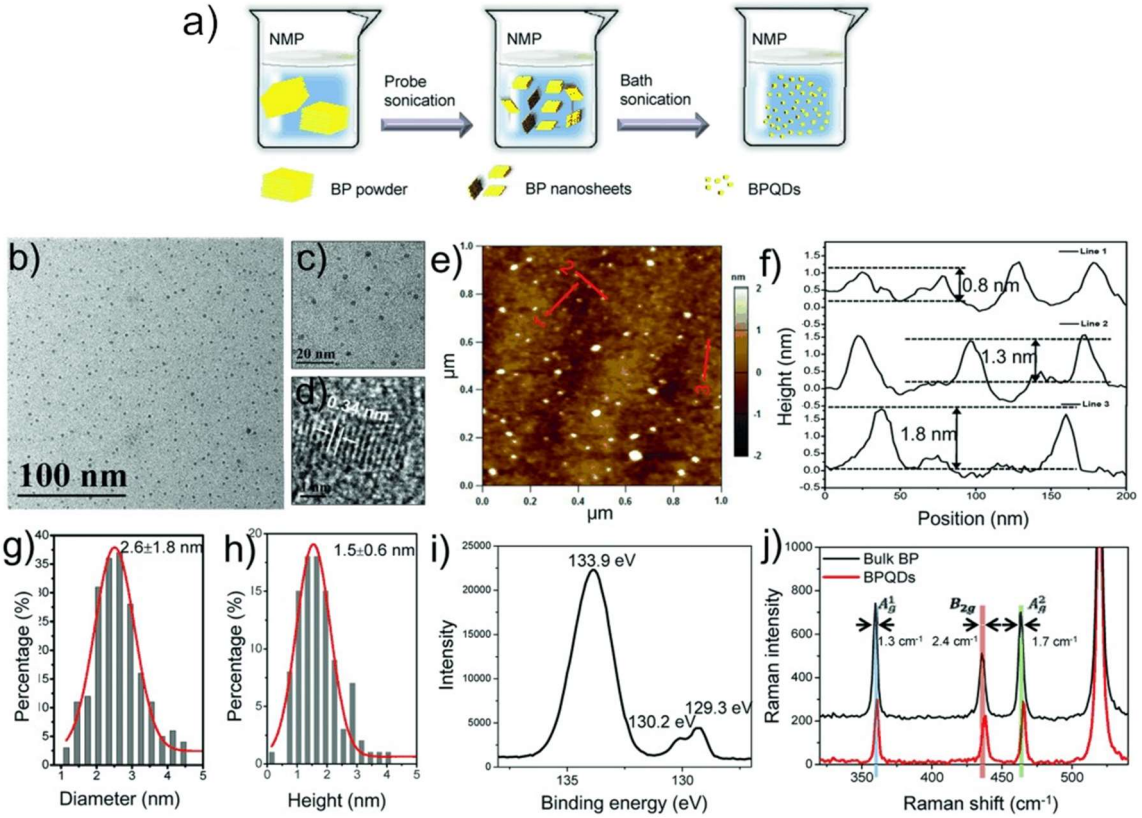

Figure 16. Synthesis and characterization of BPQDs from reference [80] a) Procedure of BPQDs synthesis by LPE. b) and (c) TEM imaging of BPQDs. d) HRTEM detail of a BPQD. The scale bar is 1 nm. e) AFM image and (f) height profiles measured along the red lines in (e). g) Statistical analysis of the lateral sizes and (h) thickness of 100 BPQDs as determined by TEM and AFM, respectively. i) XPS spectrum, showing a significative P−O contribution. j) Raman spectra of bulk BP and BPQDs.

These preparations exploit the combined effect of high temperature, solvent stabilization and mechanical shear-stress exerted by a magnetic stirring bar to exfoliate bulk BP. Ultrasmall BPQDs with average dimension 1.76 ± 0.32 nm were synthesized by W. Gu *et al.* [82] stirring BP powder in NMR at 140°C for 12 h, under N_2 atmosphere. Y. Xu *et al.* [83] followed a similar procedure but working with NaOH saturated solutions in NMP. After 6 h of vigorous stirring at 140°C, BPQDs with dimensions 2.1 ± 0.9 were isolated in suspension after centrifugation. Though NaOH saturated NMP has been used also in the LPE of BP [84], some doubts concern the stability of 2D BP toward high OH- concentrations in solution (see also Section 1.3.1). However, no XPS measurements were reported which would shed light on the presence of P−OH bonds.

1.2.3 Experimental characterization of exfoliated BP

Before moving towards the study of BP chemical reactivity, it's worth to spend some time describing how BP appears under the common experimental characterization techniques. The latter include spectroscopy, microscopy, and crystallography. Whilst these tools allow to establish the morphology and chemical purity of 2D BP, they make also possible to study surface and structure alteration following oxidation or chemical functionalization. Atomic-scale microscopy techniques (HRTEM, STEM, STM)

have been developed rapidly over the last ten years, allowing a clear visualization of local structural features and even atoms connectivity in materials (see Figure 17). Figure 17e shows an atomic scale image of the armchair direction along the edge of a BP nanosheet, obtained through aberration corrected STEM.

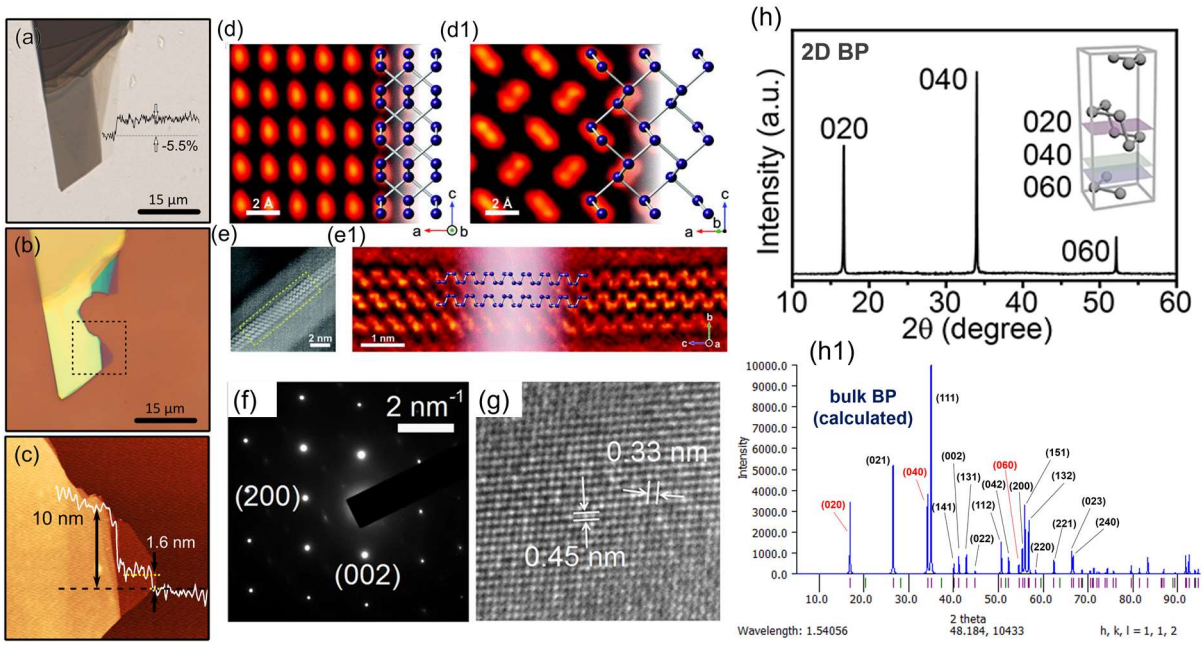

Figure 17. a) Transmission mode optical microscopy image of a few-layer black phosphorus flake exfoliated onto a PDMS substrate, featuring the reduction of about 5.5% in optical transmittance in the thinner part of the flake and (b) bright field optical microscopy image of the same flake after transferring it onto a SiO_2/Si substrate. c) AFM topography image and height profile of the region highlighted in (b). Reproduced from reference [85]. d) ADF-STEM image of a BP flake viewed along the *b* axis direction and (d1) upon 17° tilting of the *b* axis. (e) ADF-STEM viewed along the zigzag direction, showing multiple layers stacked together. e1) Magnified image of the region highlighted in (e) featuring the puckered motif of the layers. Reproduced from reference [86]. f) SAED pattern and (g) HRTEM image of a BP flake, indicating the presence of crystalline BP. Reproduced from reference [87]. h) Powder XRD spectrum of 2D BP featuring just three peaks corresponding to (0k0) reflections. Reproduced from reference [88]. For comparison purpose, the powder pattern calculated for bulk BP is shown in (h1). (0k0) reflections are highlighted in red.

High resolution TEM (HRTEM) is often used to study crystalline domains and to measure crystallographic distances, thus leading to phase characterization and identification at the nanometric scale. Scanning tunnelling microscopy (STM) as well allows to carry out atomic-level characterization of surfaces and even to study defective structures. Atomic force microscopy (AFM) is frequently employed to study the morphology of 2D BP flakes and to measure their thickness (see Figure 17c). This magnitude, together with the knowledge of the interlayer distance in BP of ~ 0.53 Å, allows to give an estimate of the layers number. When the material is a powder instead of bulk crystals, as it is the case of exfoliated BP, powder XRD measurement are usually carried out to assess the crystallinity and phase purity of the sample. The powder spectrum of a material has finger-print characteristic and provides a safe identification of a crystalline phase by simple comparison with a reference pattern. When BP is exfoliated and mounted in a sample holder for XRD measurements, its flakes are never randomly

oriented inside the sample, but tend to pile up. This behaviour, known as 'preferential orientation', is typical of exfoliated 2D materials and other specimens consisting in platelet or needle-shaped particles. If a random orientation is suppressed, the overall effect in the powder spectrum is an alteration of the peak relative intensities, as some reflections will be over-represented at the expense of others. This can even lead to the complete absence of some reflections in the spectrum. In case of 2D BP the effect is significant, giving XRD patterns dominated by (0k0) reflections, as shown in Figure 17h.

Raman spectroscopy is frequently used to characterize 2D BP samples. The reducible representation of atomic displacement parameters is $\Gamma = 2A_g \oplus B_{1g} \oplus B_{2g} \oplus 2B_{3g} \oplus A_u \oplus 2B_{1u} \oplus 2B_{2u} \oplus B_{3u}$. Of these vibration modes the only Raman active are the six with even parity (g), thus $2A_g \oplus B_{1g} \oplus B_{2g} \oplus 2B_{3g}$. Because of the preferential orientation effect described above, the flakes lay with the $\vec{b}$ axis orthogonal to the surface of the sample holder during the measurement. In the backscattering configuration of Raman experiments, the laser beam reaches the surface perpendicularly, thus parallel to $\vec{b}$. Under these conditions, because of the symmetry selection rule, the only visible modes are A^1_g, B_{2g}, A^2_g, which are observed at ~ 357.8, ~ 431.5, and ~ 459.2 cm^{-1}, respectively (see Figure 18a,b). The actual values may vary depending on the reference, in addition to other physical factors (flake thickness, oxidation, etc), as described below.

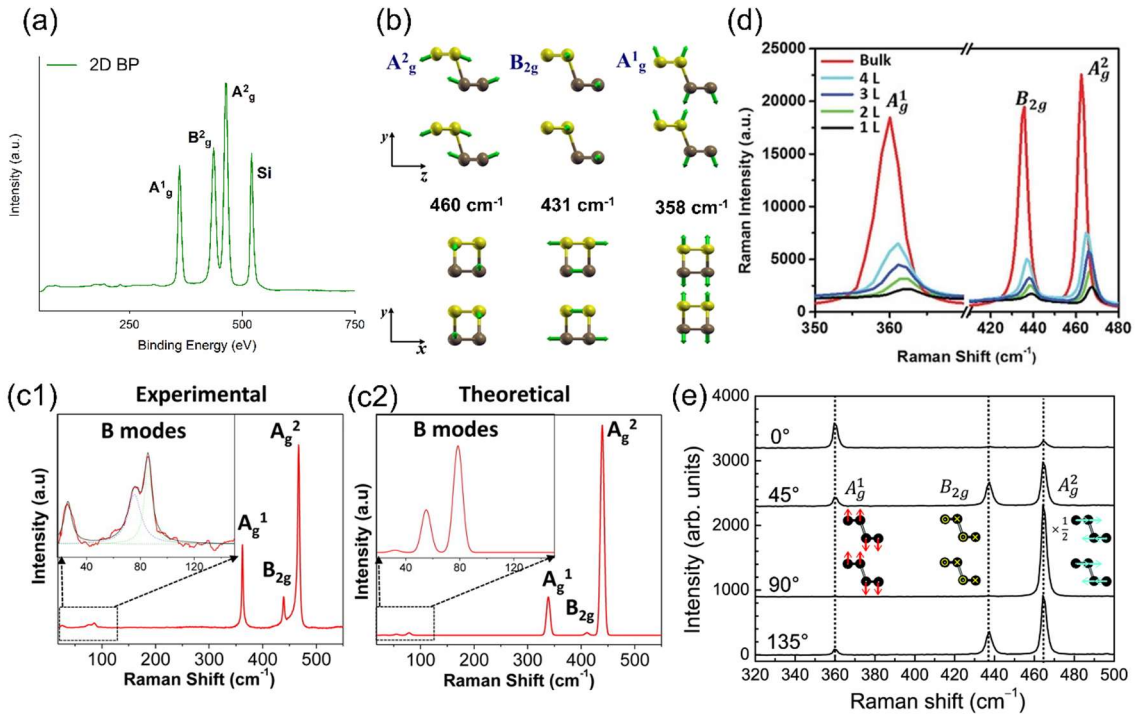

Figure 18. a) Representative average Raman spectrum measured out of 15 BP flakes. b) Atom displacements (green arrows) for the Raman-active modes. Axes indicate two view perspectives. Reproduced from reference [89]. c) Experimental Raman spectrum of 2D-BP. Inset: the zoom-in spectrum from 20 to 150 cm^{-1}, the dotted lineshapes show the three fitted Lorentzian B modes. c1) Calculated Raman spectrum of 6L-BP in the experimental backscattering geometry. Inset: the zoom-in spectrum in the same LF region as (c). Reproduced from [90]. d) Raman spectra of bulk BP and 2D BP with different numbers of layers. Reproduced from reference [84]. e) Polarized Raman spectra (parallel polarization) of BP measured with 441.6 nm excitation.

The angle between the incident polarization and the zigzag direction for each spectrum is indicated. Reproduced from reference [91].

These three Raman modes are the only predicted for bulk BP and phosphorene (1L-BP), and correspond to intra-layer vibrations. In detail, A^1_g stands for the out-of-plane phonon mode, while B_{2g} and A^2_g are the two in-plane modes. Taking into account FL-BP flakes containing *n* layers (*n*L-BP), low-frequency (LF) inter-layer modes are predicted in addition to the three high-frequency (HF) shifts just described. LF vibrations involve sliding of adjacent layers (shear-modes) or their separation (breathing-modes). With backscattering geometries, only breathing modes with B symmetry are visible, whose number is $n/2$ or $(n - 1)/2$ for even or odd values of *n*, respectively (see Figure 18c). However, LF vibrations are seldom observed, as their intensities are much weaker compared to the three HF modes, and because Raman signals < 100 cm^{-1} are usually cut off by the notch filters used to reject the excitation light. Thus, in the rest of this manuscript, any reference to BP Raman peaks will refer to the three HF vibrations A^1_g, B_{2g}, A^2_g. Experimental results by Z. Guo *et al.* [84] highlighted a progressive red-shift upon increase in the number of layers (see Figure 18d). The A^2_g modes turned out to be the most sensitive, with a red-shift (*i.e.* downshift) of -2.6 cm^{-1} going from 1L-BP to 4L-BP. These differences are larger than the experimental uncertainty, which for most Raman spectrometers is ~ 0.5 cm^{-1}. The existence of a layer-dependence in Raman peak should always be taken into account dealing with flakes prepared via LPE. In this situation, in order to compare distinct samples (*e.g.* before and after chemical functionalization), Raman spectra should be acquired first on a statistical ensemble of flakes and then averaged to get one representative spectrum of each sample. Then, only the two averaged spectra should be compared. As most Raman measurements are performed on flakes supported on SiO_2/Si, the characteristic peak of Si at ~ 520 cm^{-1} is frequently used as internal standard to normalize the other peaks. An additional feature of Raman spectroscopy is that it is polarization sensitive. As it was highlighted in distinct theoretical and experimental studies, the intensity of the three Raman peaks is a function of polarization angle and flake orientation (see Figure 18e). Exploiting this characteristic, a procedure to determine the crystallographic orientation of a flake *via* Raman measurements has been devised [92]. Another useful application of Raman spectroscopy is to monitor the progress of surface oxidation in BP flakes during environmental-stability tests. Indeed, as better described in Section 1.3.1, Raman intensities drops over time upon oxidative damage, providing a straightforward method to follow the kinetics of the process. Furthermore, some reports highlight Raman frequency shifts following surface functionalization. Though surface modification could definitely led to this effect, care should always be taken comparing spectra of distinct samples, as explained above. Infrared spectroscopy (IR), both in transmittance and attenuated total reflectance (ATR) mode, is less frequently used with BP samples, being limited by the high absorption coefficient of BP in the NIR-IR region, and by the absence of characteristic spectral features in pristine BP. IR measurements has been used to highlight the presence of oxidation products

such as P=O, P–O–P and P–OH, or other moieties introduced *via* chemical functionalization (see Figure 19a).

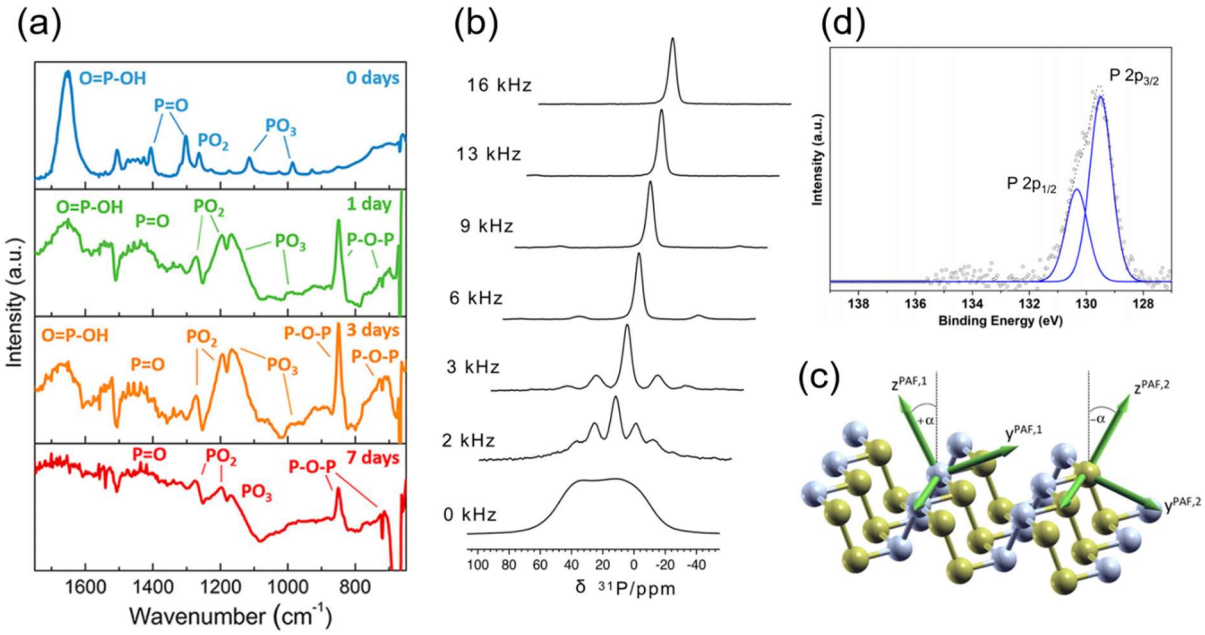

Figure 19. a) ATR-FTIR spectra recorded on 2D BP exposed to air over 1 week, displaying the spectral features of P−O species formed upon oxidation. Reproduced from reference [93]. b) ^{31}P NMR spectra of BP recorded under static (0 kHz) and MAS (from bottom to top at frequencies of 2, 3, 6, 9, 13, and 16 kHz) conditions. c) Structure of the single layer of BP, with magnetically non-equivalent phosphorus nuclei coloured in gray and yellow. The chemical shift principal axes frames ($x^{PAF,i}$, $y^{PAF,i}$, $z^{PAF,i}$) are also indicated. Reproduced from reference [94]. d) Core level P2p XPS spectrum of pristine BP, showing no trace of oxidation.

X-ray photoelectron spectroscopy (XPS) is a tool of paramount importance in materials chemistry. XPS allows to measure the elemental composition of a surface at the parts per thousand range, to identify distinct chemical environments of a same element and to gain subtle information on its chemical state (*i.e.* electron richness and oxidation state). Core level XPS spectra of 2D BP display an asymmetric peak at ~ 129.9 eV, resulting from the overlapping spin-orbit doublet $P2p_{3/2}$ and $P2p_{1/2}$ (see Figure 19d). Frequently, a second broad peak around 134-135 eV is observed in the P2p XPS spectrum. This peak corresponds to surface oxidized species (P=O, P−O). Even when reactions involving 2D BP are carried out under inert atmosphere, minor manipulations outside a controlled atmosphere (e.g. to perform centrifugation cycles or to load a sample before measurement) easily result in minor oxidation, which can be detected by XPS. As will be shown in Section 1.4, when some phosphorus atoms in BP get involved in strong P–X interactions with an heteroatom (X = C, N, metal), they give rise to a peak in the range ~ 132-133.0 eV. Thus, pristine BP atoms are easily distinguished by those originating either from surface oxides or from hetero-coordinated phosphorus. ^{31}P MAS NMR spectroscopy provides a complementary method to study distinct chemical environments. A theoretical and experimental characterization of the spin coupling interactions in BP and FL-BP has been reported recently by F. Martini *et al.* [94]. Intriguingly, solid state NMR measurements could be carried out on FL-BP

suspensions, in these conditions only 5 mg of sample were needed (meanwhile solid state NMR requires traditionally high amount of sample *i.e.* 40-50 mg) and showed that both the nanosheets dimensions and the choice of solvent have a negligible effect on the ^{31}P spectrum, which is characterized by a signal with isotropic chemical shift $\delta_{iso} = 18.5 \pm 0.5$ (see Figure 19b). Despite being of potential utility in BP chemistry, to date this technique has received limited application compared to other spectroscopies.

1.3 Environmental stability of 2D BP

1.3.1 BP degradation

The high stability of P−O and P=O bonds drives the thermodynamics of phosphorus oxidation to the side of products. In case of P_4, which is the least stable and the most reactive allotrope, oxidation occurs immediately upon air exposure, with formation of a characteristic white smoke made of P_4O_{10} particles. The other allotropes, in fact, are kinetically inert in their bulk form and can be manipulated without particular care under air. However, when BP is exfoliated, the change in thick-dependent physicochemical properties and the strong increase of surface area enhances the chemical reactivity, making 2D BP susceptible to oxidation. Though this is common to other van der Waals materials, ambient degradation is comparatively more serious with 2D BP. This in turn causes a rapid drop in performance of 2D BP-based FETs and a progressive loss in activity of 2D BP-derived catalysts. Thus, much effort has been devoted to understanding the mechanism of 2D BP oxidation and to devise effective solutions to prevent it. Oxidative degradation under air exposure is manifested by the formation of blobs on the surface of the flakes. Blobs occurs as bumps under an AFM height-profile characterization, with increasing height over exposure time, reaching several tenths of nanometres after few days (see Figure 20).

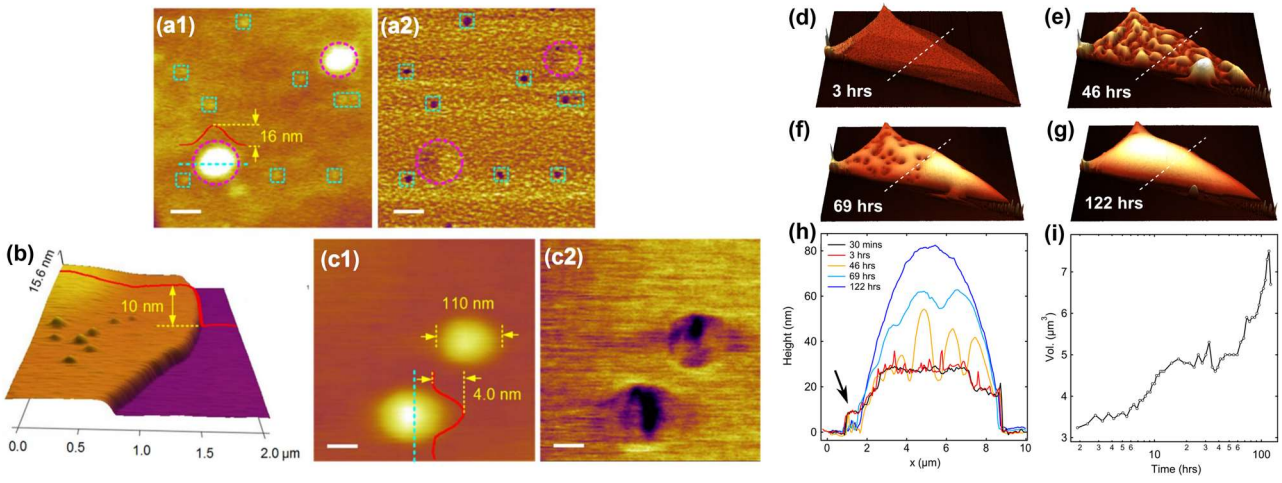

Figure 20. AFM study of degradation in 2D BP mechanically exfoliated flakes. a1) AFM height image and (a2) the corresponding friction image of the bump structure on the BP flake surface exposed for 2 h (scale bar: 1 µm). The larger bump structure of about 1.5 µm wide and 16 nm in height were mainly induced during the mechanical exfoliation process, which does not show the lower friction as the micro-bump caused by oxidized phosphorus. b) 3D morphology of a BP flake of 10 nm

thick exposed in air for 2 h. c1) height image and (c2) friction image (scale bar: 50 nm) of the micro-bumps shown in (b). Reproduced from reference [95] d)-g) Selected AFM scans of a BP flake in air taken at (d) 3 hours, (e) 46 hours, (f) 69 hours, and (g) 122 hours after exfoliation. Dotted white lines indicate the position of the line profiles shown in (h). h) Line profiles taken across the BP flake from the scans in (d–g) as well as a line profile for the AFM scan taken directly after exfoliation. i) Total volume of the flake and water droplets as a function of measurement period. Reproduced from reference [96]

Elemental mapping of partially oxidized flakes revealed a higher concentration of oxygen in the regions corresponding to the bumps. With time the blobs get larger and merge into droplets, ultimately covering the entire flake. Thus, degradation of the flake occurs as a nucleation process, starting from randomly distributed regions which eventually grow and coalesce. Oxidation introduces P–O–P and P=O moieties (see below) into the phosphorus net, locally turning the surface more hydrophilic. This in turn promotes adsorption of water at oxygen-rich regions, forming the blobs. Water then slowly dismantles P_xO_y structures forming phosphorus oxoacids that pass in solution. When 2D BP oxidation takes place under water (as is the case with 2D BP dispersions in water), the degradation of flakes preferentially starts from the edges, with a progressive reduction of their lateral size. In any case, both surface- and edge-initiated degradation ultimately leads to the complete consumption of 2D BP over several days. The process is also influenced by layer thickness, with thinner flakes being more sensitive to oxidation [97]. M. Pumera and coworkers [98] carried out ^{31}P NMR studies to identify the molecular compounds released in water during degradation. H_3PO_4 and H_3PO_3 resulted the main components (about 90% of the products, arising from hydrolysis of surface P_4O_5 and P_4O_6 respectively), in addition to $H_4P_2O_6$ (2%) and H_3PO_2 (10%) (see Figure 21). The presence of H_3PO_2, containing phosphorus in oxidation state +I, was explained assuming that during hydrolysis, some remaining P–P bonds are directly attacked by water, though in a less extent than P–O–P bonds.

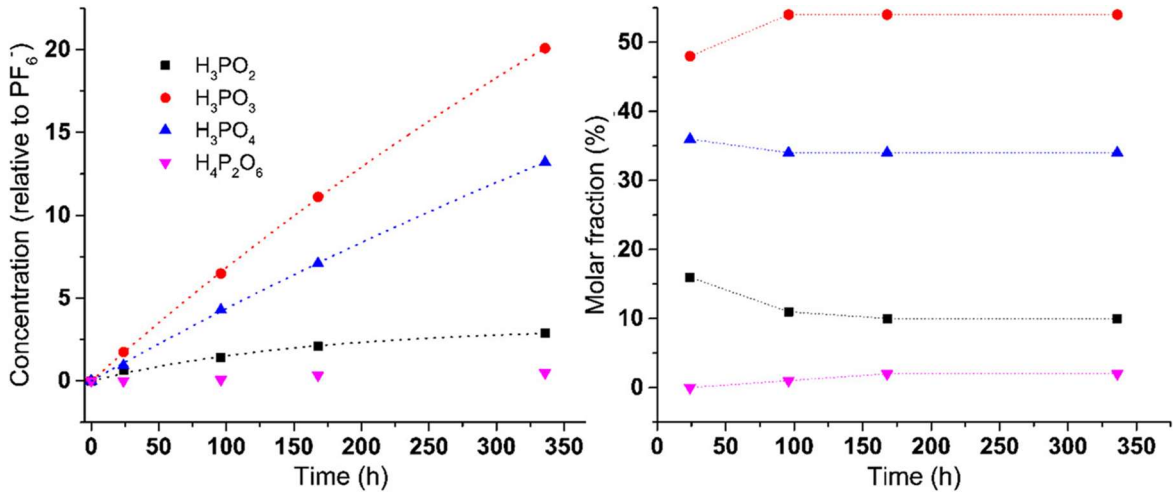

Figure 21. Kinetics of the BP oxidation in water in presence of oxygen. The relative concentrations of the respective acids (left) and the molar fractions of the acids (right) in the reaction mixture were determined by ^{31}P NMR spectroscopy. Reproduced from reference [98].

Notably, B. Xing and coworkers [99] have pointed out that in alkaline media 2D BP degradation takes place even in absence of oxygen. As explained, the nucleophile OH^- is strong enough to attack unoxidized phosphorus atoms causing a cleavage of the P−P network. In line with this mechanism, in alkaline medium H_3PO_2 becomes the main product.[2] High resolution XPS spectroscopy is a suitable tool to follow the progression of oxidation, as P_xO_y species appear as a broad band at 133-135 eV, well separated from the characteristic features of pristine BP at ~130 eV (P−P backbone). Both P(+III) and P(+V) species are detected by deconvolution of the P_xO_y band [95,100] , with the higher oxidation state +V becoming predominant over time (see Figure 22a).

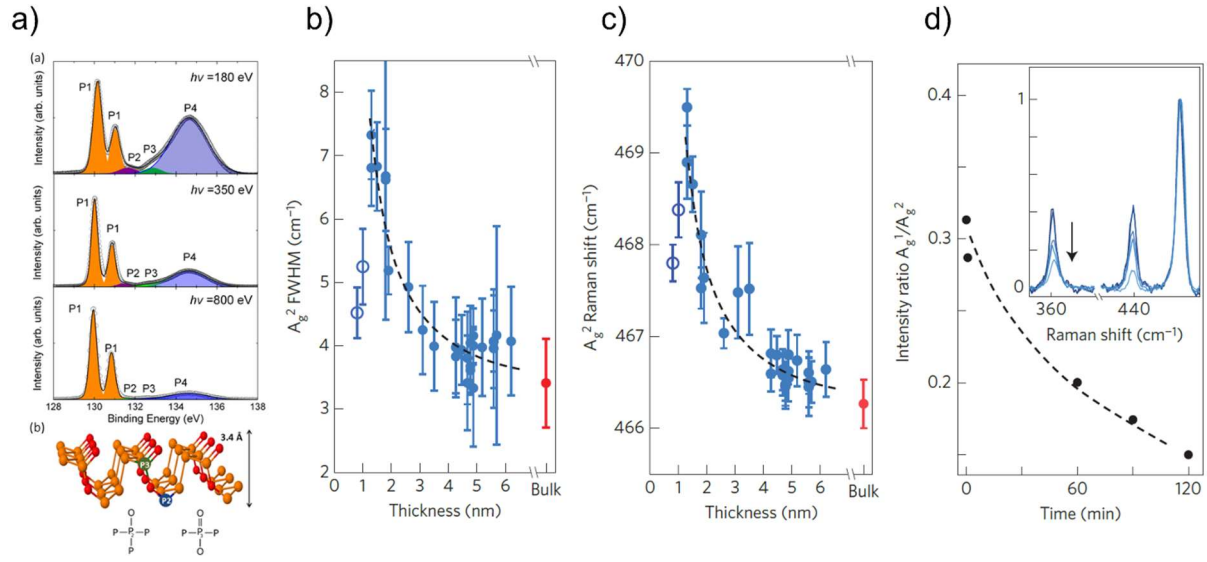

Figure 22. a) Core level P 2p XPS after two days of air exposure. Increasing the photon mean free path inside the material (*i.e.* using higher photon energies), the relative amount of oxide species decreases, highlighting that oxidation is confined to the surface. P1 corresponds to pristine P−P bonds; P2 and P3 correspond to the P−O and O−P=O species shown in the model below; P4 is attributed to P_4O_{10}. Reproduced from reference [101]. b) Evolution of Raman A^2_g mode full-width at half-maximum (FWHM) and (c) Raman shift as a function of layer thickness (λ = 532 nm). Open blue and solid red circles correspond to 1L- and bulk BP, respectively. d) Time evolution of the integrated peak ratio A^1_g/A^2_g from Raman spectra (inset) of 3L-BP during oxidation in ambient conditions under a bright lamp. Reproduced from reference [97].

Raman spectroscopy is another useful tool to monitor oxidation. Being a vibrational spectroscopy, alteration of the BP lattice under oxidative damage results in a progressive decrease of Raman intensities. The three Raman modes of 2D BP are not affected all to the same extent, thus relative intensities are altered during oxidation. In particular, the A^1_g/A^2_g intensity ratio drops exponentially with air exposure, resulting a useful indicator of flake degradation (see Figure 22b-d). Upon oxidation new Raman peaks appear in the range 800-900 cm^{-1} (phosphorus oxoacids) and 900-1100 cm^{-1} (phosphorus oxides P_xO_y). Some debate exists around the mutual role played by oxygen, water and light in the oxidation process. First principle calculations performed by different groups [102] showed that water has a scarce affinity for the surface of pristine BP, which basically is hydrophobic. Thus, H_2O molecules

[2] This reactivity parallels the alkaline hydrolysis of white phosphorus, though in the case of P_4 the overall reaction is a disproportion leading to PH_3 beside $H_2PO_2^-$.

are only slightly physisorbed at the surface and H−OH bond dissociation result energetically forbidden. Oxygen instead is easily chemisorbed with formation of an O_2-bridge, which dissociates in dangling P=O groups, a process favoured by ~ 4 eV per molecule (see Figure 23) [101-102].

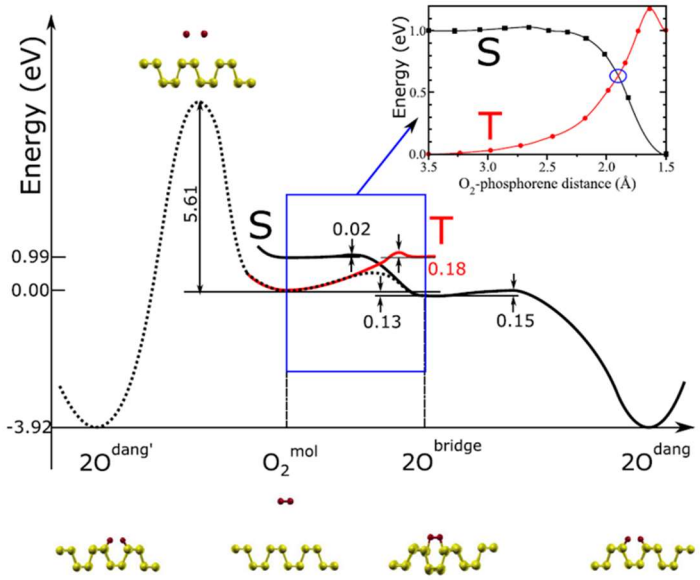

Figure 23. Schematic configuration-coordinate diagram for possible mechanism of phosphorene oxidation. The solid/dotted lines represent the potential energy surfaces (PESs) calculated with fixed/variable total magnetization. PESs calculated for singlet (S) and triplet (T) oxygen are shown in the inset as a function of phosphorene distance. Reproduced from reference [103].

Dangling oxygen atoms may then insert into P−P bonds forming oxo-bridged P−O−P moieties. The presence of both terminal and dangling oxygen atoms is consistent with XPS studies of oxidized BP cited above. Oxygen incorporation per se leaves the flake intact, only leading to surface passivation. However, once formed, P_xO_y triggers further reactivity with water, in a two-step mechanism. Not surprisingly, fresh 2D BP is stable in deaerated water suspensions (*i.e.* with constant N_2 bubbling or subjected to 'freeze and pump' cycles), undergoing degradation only when oxygen is also present (see Figure 24).

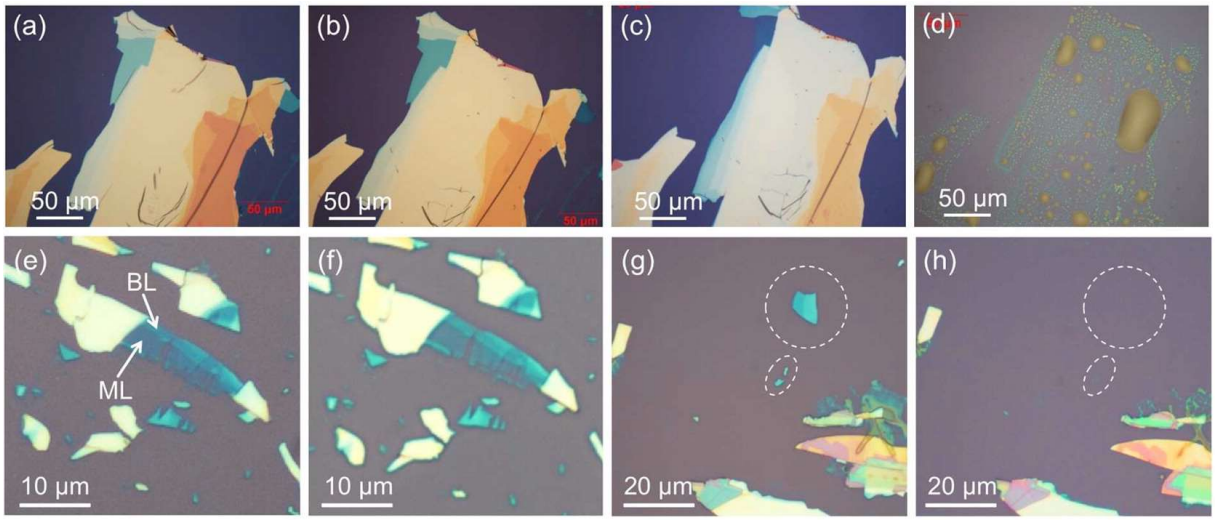

Figure 24. Morphology change of exfoliated BP flakes on SiO_2/Si after exposure to water, air, O_2-depleted and O_2-enriched (bubbling) water. a) Optical images of a freshly exfoliated BP flake. b) Same flake after being submerged in water for 1 week. c) Same flake after 2 weeks of exposure to water. d) Image after removal of the flake from water and exposure to air for 1 week, showing the complete dissolution of the flake and droplet-like residues within its footprint. Exposure to O_2-depleted (deaerated) water: e) Optical micrograph of freshly exfoliated BP flakes on SiO_2/Si. Based on their optical contrast, the deep blue segments are identified as 1L- and 2L-BP. f) Same sample region after immersion in oxygen-depleted water (N_2 bubbling) for 2 days. Exposure to O_2-enriched water: (g) freshly exfoliated BP flakes. h) Same sample region after immersion in oxygen-enriched water (O_2 bubbling) for 2 days, showing the complete disappearance of the flake. Reproduced from reference [102].

To check this model, Y. Huang *et al.* [102] devised a series of experiments using ^{18}O-labelled H_2O. Exposing fresh 2D BP to $H_2{}^{18}O$ and then analysing the flake via time-of-flight secondary ion mass spectrometry (TOF-SIMS), no ^{18}O was detected on the surface. Conversely, when partially oxidized fakes were used (*i.e.* previously air exposed), ^{18}O concentration maxima were observed in those regions of the flakes more damaged by pre-oxidation. These experiments proved that 2D BP is basically hydrophobic, becoming hydrophilic only after surface oxidation by O_2.[3] Experiments have pointed out that light also plays a crucial role in BP oxidation, boosting its degradation. R. Martel *et al.* [97] modelled the degradation kinetics of 2D BP under laser light irradiation and observed a linear growth with radiation energy. S. Walia and coworkers [87] studied the effect of UV-Vis light on 2D BP and identified the higher energy component represented by UV and blue light as the main responsible of photo-oxidation, suggesting exclusion of UV radiation from the working environment could highly extend the lifetime of pristine 2D BP. The role of light has been the focus of theoretical speculations as well. Ab initio calculations performed by A. Ziletti [103] showed that for O_2 chemisorption to occur, an energy barrier of ~ 0.54 eV must be overcome, which could be fulfilled by light induced excitation of O_2 (see Figure 23). It was also proposed by R. Martel *et al.* [97] the following three-step mechanism:

[3] It is worth to highlight the structural similarity between the products of P_4 oxidation, namely P_4O_6 and P_4O_{10}, and the oxidized surface of 2D BP containing dangling (P=O) and bridging (P−O−P) oxygen atoms (see Figure 22). Similarly, meanwhile P_4 is stable under water, its oxidation products containing polarized P−O bonds are easily hydrolysed.

first, BP is photoexcited; then, electron transfer from photoexcited-BP to O_2 occurs, generating the active oxidant O_2^- and holes-doped BP; finally, O_2^- reacts with BP forming surface PO_x species. The overall mechanism is depicted below:

$$P_n + h\nu \rightleftharpoons P_n^*$$

$$P_n^* + O_2 \rightleftharpoons P_n(h^+) + O_2^{\cdot-} \longrightarrow P_n(ox)$$

1.3.2 2D BP passivation

To keep the integrity of 2D BP under environmental working conditions, protection from moisture and oxygen is needed. This is a crucial issue for BP-based FETs, whose electric properties are severely affected by minimal surface alteration. In particular, BP degradation increases threshold voltage and diminishes on/off ratios and carrier mobility of devices. A common approach to face this problem is to passivate the surface of BP with environment-resistant materials, fabricating a physical barrier above the P–P lattice. The ideal passivation should isolate the surface keeping the electric properties of 2D BP unaltered. Using atomic layer deposition (ALD), flakes of 2D BP have been coated with layers of metal oxides, such as Al_2O_3 [105], SiO_2 [106] or HfO_2 [107]. For instance, thin film of Al_2O_3 were deposited on 2D BP either in a two-step procedure, from initial deposition of Al film (2-3 nm thick) followed by oxidative treatment at 120°C [108], or using trimethylaluminium (TMA) and water as mixed precursors for ALD [105,109,110] (see Figure 25).

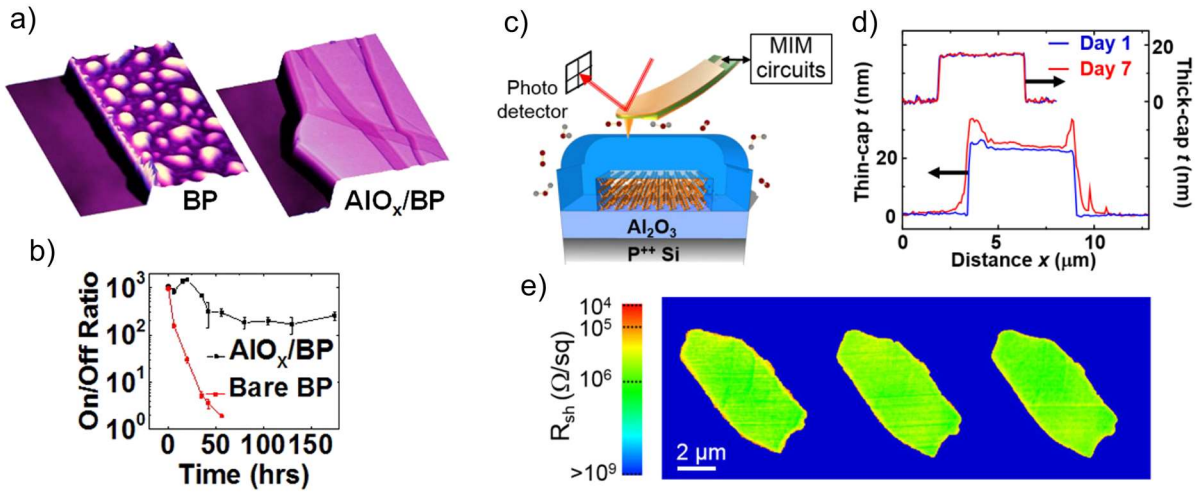

Figure 25. a) AFM 3D plots of one aged pristine BP flake (left), showing signs of degradation, and a corresponding flake capped with a protective film of AlO_x. b) Stable and higher on/off ratio of AlO_x/BP compared to pristine BP, maintained over 150 hours. Reproduced from reference [109]. c) Schematic representation of BP flakes on Al_2O_3/Si substrate with a thick (25 nm) Al_2O_3 capping layer. The AFM-based microwave impedance microscopy (MIM) setup is also illustrated. Adapted from reference [108]. d) AFM height profile of a thin- (bottom) and thick-capped (top) BP layer measured after one and two days of

air exposure. A thicker Al_2O_3 layer is more effective. e) Sheet resistance maps approximated by the MIM-Real data of a 16 nm-thick flake capped by thick Al_2O_3. The images were acquired daily over one week. No discernible change was detected, highlighting the effectiveness of AlO_x passivation. Reproduced from reference [108].

To date this method is one of the most effective, as passivated 2D BP remains stable for weeks or even months under ambient conditions. Other groups studied the encapsulation (coating) of BP flakes with different air stable 2D materials, building van der Waals heterostructures. This approach is rooted in well-established deterministic transfer methods [111]. Briefly, arbitrary 2D materials are exfoliated on distinct supports and their flakes are subsequently brought in contact using a micromanipulation station, which allows the high precision movement and alignment of the flakes. R. A. Doganov *et al.* [112] used a dry transfer method to encapsulate 2D BP with *h*-BN or graphene, highlighting by AFM and Raman measurements the superior environmental stability provided by encapsulation (see Figure 26). Remarkably, not only operational lifetime of the device was extended, but electron conduction was increased, thanks to exclusion of oxygen from the surface.

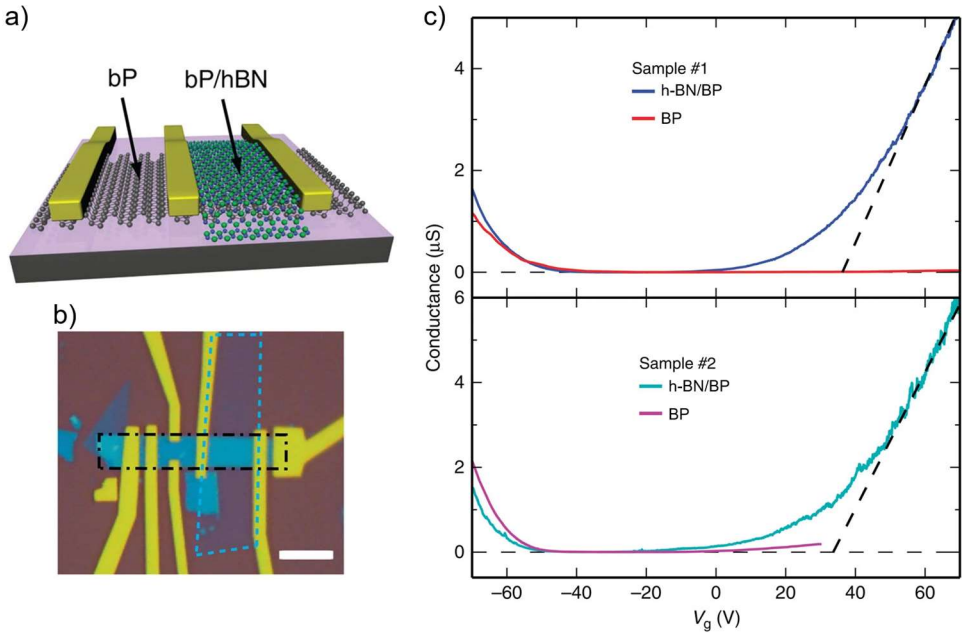

Figure 26. a) Schematic illustration of the h-BN/BP device. b) Optical image of a typical device with outlines of the BP flake (black dashed-dotted line) and the passivating hexagonal BN flake over imposed (blue dashed line). Scale bar 3 μm. c) Four-terminal conductance versus backgate voltage (V_g) of bare BP and h-BN/BP FETs at source–drain bias V_{sd}=50 mV and temperatrure T=300 K. Reproduced from reference [112].

A. Avsar *et al.* [113] improved the nanofabrication procedure using a capping layer of *h*-BN previously contacted with graphene strips. The 2D assembly featured hysteresis-free transport characteristics, with identical performance if operated under vacuum or exposed to air. Further improvements came from sandwiching BP between two *h*-BN layers [43]. Despite being effective to preserve the electrical performance of BP flakes, 2D encapsulation is limited by the sophisticated and expensive set-up needed.

Thus, efforts have been made to passivate 2D BP with polymeric coatings. V. Artel *et al.* [114] deposited above 2D BP a self-assembled monolayer of octadecyltrichlorosilane (OTS), simply dipping the Si-supported BP flake inside a hexane solution of OTS. This treatment extended the lifetime of the device to 28 days, without any significant alteration of the electric characteristics (see Figure 27). According to the authors, the presence of a small fraction of surface phosphorus oxide is crucial to anchor OTS at the surface via Si-O bonds (see Figure 27e,f).

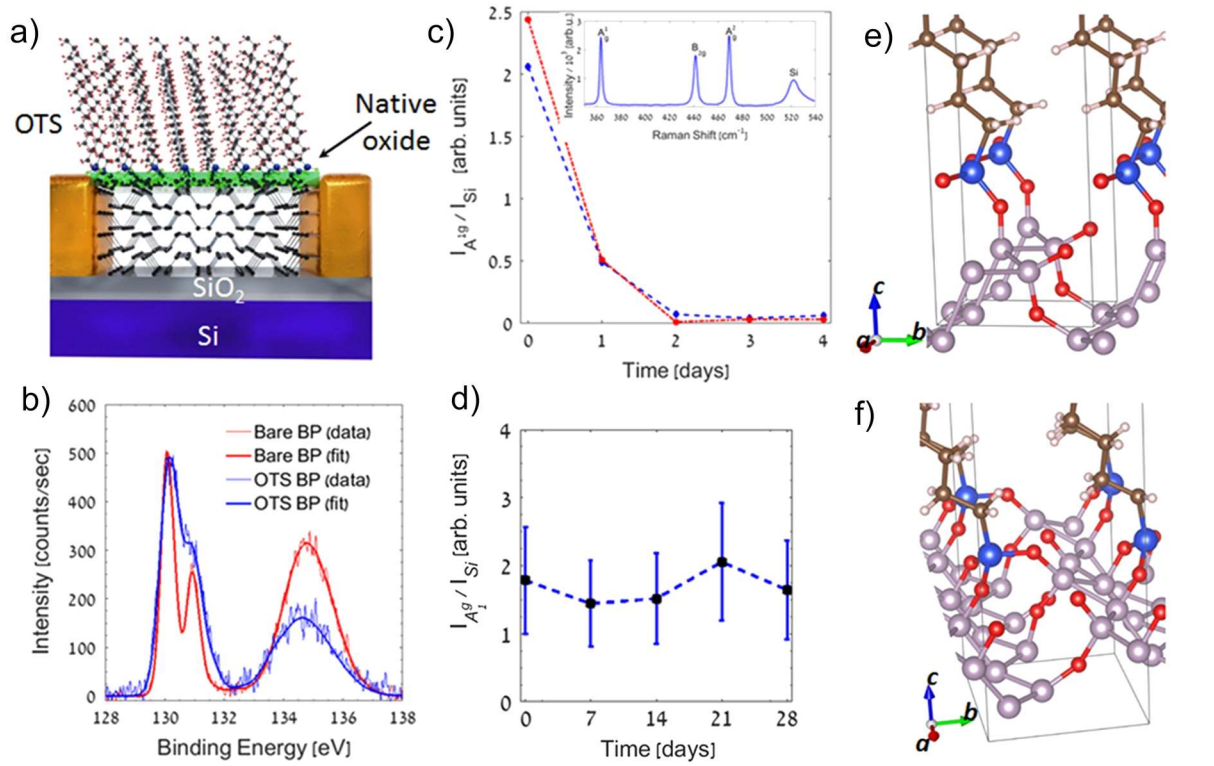

Figure 27. a) Schematic model of the OTS-passivated BP in a FET device, showing a thin native oxide layer mediating the bonding of BP to OTS. b) The Core level P2p XPS spectrum of bare (red) and OTS-coated (blue) BP. Normalized time-resolved Raman spectra showing height ratios between the A^1_g peak of BP and the Si substrate peak at 520 cm^{-1} of (c) uncoated and (d) OTS-coated BP samples. A full scanned spectrum is shown in the inset of (c). Colours correspond to different samples in (c). e-f) Molecular models of oxidized BP monolayer passivated by OTS where (e) the OTS molecules polymerize (via Si–O–Si bonds) along a ridge, and (f) the OTS molecules bind only to surface oxygens without any polymerization. For clarity, only the part of OTS closest to the BPO layer is shown. Colours code: P-gray, O-red, Si-blue, C-brown, H-white. Reproduced from reference [114].

Ionic liquids (ILs) were also investigated as passivating agents, resulting highly effective [70,113]. A major advantage of ILs is that carrying out LPE using them as solvent, exfoliation and surface protection are carried out at once. This coating not only isolates the surface of BP from the environment preventing oxidation, in the same way other organic and polymeric coatings do, it also acts as an active scavenger toward reactive oxygen species (*i.e.* $O_2^{\cdot-}$), thanks to the peculiar reactivity of imidazolium cations. Remarkably, FETs built with ILs-stabilized FL-BP preserved their electrical characteristics over 92 days. Compared to the growth of metal oxide layers or the realization of 2D heterostructures, organic

coatings have in their favour low-costs of realization and the possibility to scale-up the process, dealing with larger amounts of exfoliated material instead of single mechanically exfoliated flakes.

Surface functionalization, *i.e.* decoration of 2D BP surface with metal nanoparticles or molecular fragments covalently/non-covalently bonded to the surface, represents an alternative approach to protect BP from oxidation and at the same time to enrich its surface with additional functionalities, without actually forming coatings above the BP surface. For a description of these methods, the reader is referred to the next Section.

1.4 Chemical functionalization of 2D BP

1.4.1 Overview

Pristine 2D BP has undoubtedly unique properties that make possible its use for a wide variety of applications, ranging from optoelectronics and sensing to catalysis and nanomedicine. However, surface functionalization not only allows to overcome the limited stability of 2D BP or to widen its optical absorption, it also represents a powerful tool to tune its chemical reactivity and opens to entirely new applications. Many distinct approaches to surface functionalization have been devised, including decoration with metal nanoparticles, the use of conjugated organic molecules to form non-covalent adducts with the BP surface, and the covalent functionalization with molecular fragments. In Scheme 1 a possible rationalization of the several approaches reported so far is proposed. Surface passivation strategies, aimed to protect 2D BP from oxygen and moisture, have been already outlined in Section 1.3.2. In the following sections, a selection of relevant 2D BP functionalizations reported in literature will be presented, in order to settle the state of the art and show distinct approaches.

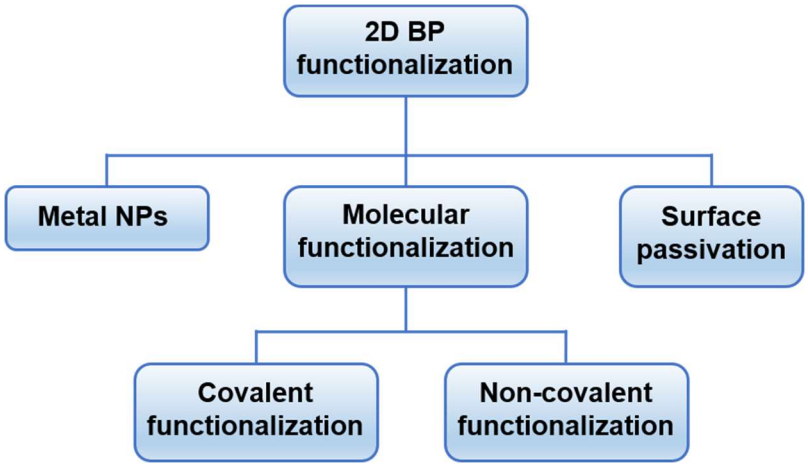

Scheme 1. Strategies for the functionalization of 2D BP.

1.4.2. Functionalization with metal nanoparticles

Recent studies have shown that, for some specific reactions, the intrinsic properties of 2D BP allow for its application in catalysis as a pristine material, without further modifications [114-117]. However, most of the times surface functionalization is crucial to broad the scope of BP in catalysis. In this respect, the coordinative abilities of BP render it particularly suitable to anchor metal nanoparticles (NPs). Usually, the physical and chemical properties of the modified material are not just a sum of those of the individual constituents. The mutual interaction between the metal NPs and the 2D BP surface imparts an entirely new reactivity to the heterostructure. This can depend on the energetics of the metal-phosphorus interface, or it can be the result of some ancillary role played by 2D BP orienting the selectivity toward a specific product during a catalytic cycle. Over the last six years, different M(0) NPs/BP nanohybrids (hereafter denoted M/BP) were described, including M = Co, Ni, Pd (to be described in Chapter II), Pt, Ag, Au. Two distinct synthetic methods may be distinguished:

1. Reduction of a metal salt precursor using 2D BP as a reducing agent
2. Reduction of the salt precursor using a reductant different from BP itself, to be performed in situ (metal salt, reducing agent and 2D BP are mixed together) or in two steps (M NPs are prepared first and then deposited on 2D BP).

Method 1 has been firstly reported to fabricate Au/BP heterostructures (see Section 1.4.2 below), lately it has been extended to Group 10 metals [118]. It seems that the presence of water in the reacting system is a prerequisite of this method. Indeed, water is likely involved in the redox reaction, as $P(OH)_x$ species are expected to be the oxidized products alongside the reduction product M(0) NPs. Simple salts of noble metals, lacking strongly stabilizing ligands and prone to reduction, may represent an additional thermodynamic requirement for reduction to take place. However, a strong limitation of using BP as sacrificial reducing agent is its subsequent consumption and degradation, which affects the integrity of the resulting flakes. The use of ancillary reducing agents (method 2), such as $NaBH_4$, H_2, HCHO or oleylamine, commonly employed in the synthesis of bare metal nanoparticles, helps to prevent degradation and is usually the method of choice to fabricate M/BP nanohybrids. Now, the preparation, characterization and catalytic application of some simple M/BP systems will be outlined briefly.

Co/BP. S. Feng *et al.* [119] devised a one-pot solvothermal procedure where a BP suspension in oleylamine, acting both as solvent and reducing agent, was heated with $Co(OAc)_2 \cdot 4H_2O$. XRD and HRTEM analysis of the recovered material confirmed the presence of nanometric *fcc* Co domains (≈ 21 nm) supported on 2D BP, thus assessing the formation of a Co/BP nanohybrid (see Figure 28a-f). P 2p and Co 2p core level XPS measurements revealed an electron migration from BP to Co, which was explained taking in account the higher Fermi level of BP compared to metallic Co.

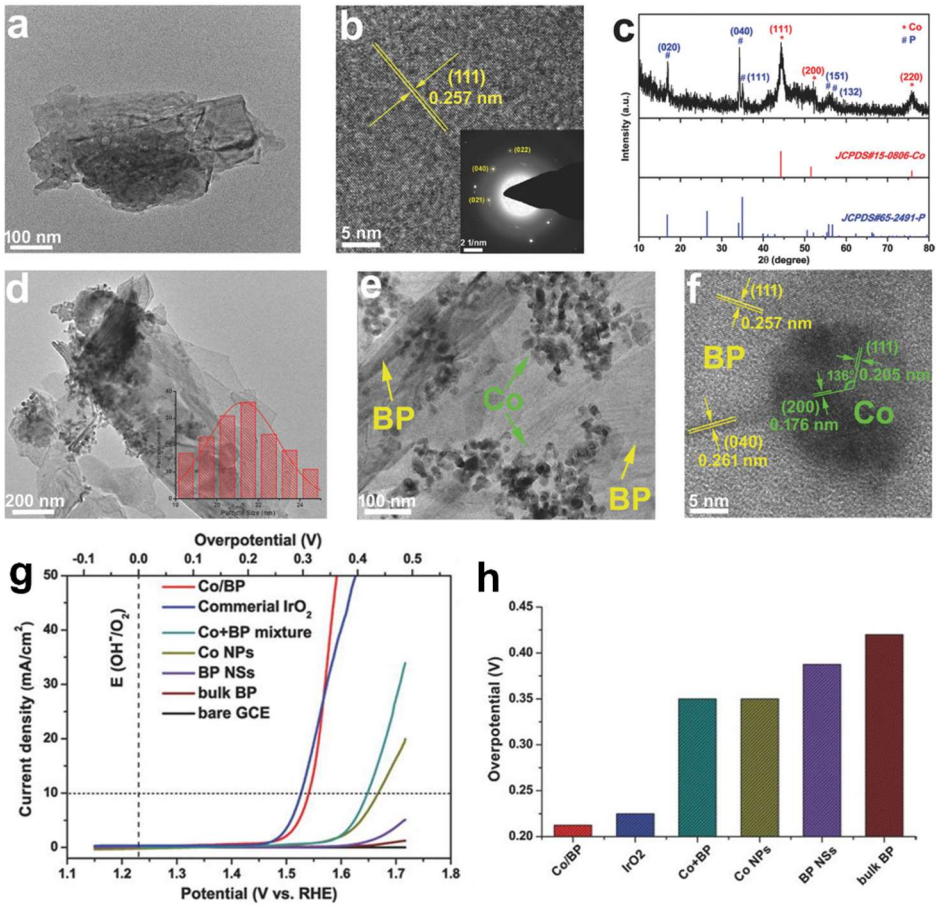

Figure 28. a) XRD patterns of the as-prepared Co/BP nanohybrids. b) TEM image of the exfoliated BP nanosheets with the size of hundreds of nanometers. c) HRTEM image of the BP nanosheets (the insets are the corresponding SAED patterns). d),e) TEM images of the Co/BP. f) HRTEM image of the Co/BP. g) LSV curves and h) onset overpotential of Co/BP, commercial IrO_2, the physical mixture of Co+BP, Co NPs, BP NSs, bulk BP. Reproduced from reference [119].

To evaluate the electrocatalytic activity of the new Co/BP nanohybrid, performances in the oxygen evolution reaction (OER) were evaluated by linear sweep voltammetry (LSV) using pristine BP, Co NPs and commercial IrO_2 for comparison. While both BP and Co NPs individually resulted poorly effective in OER, Co/BP performed exceptionally with the same onset potential of $\approx$ 210 mV as commercial IrO_2, and even outperforming it in activity above the overpotential of 310 mV (Figure 28h). Interestingly, a physical mixture of Co NPs and BP although able to catalyse the OER resulted much less active than the nanohybrid Co/BP, thus highlighting the key role played by the Co/BP interface and the importance of growing NPs in situ.

Ni/BP. One of the first example of BP decoration with M NPs involved the use of preformed Ni NPs, reported by M. Caporali *et al.* in 2017 [120]. Simply adding colloidal Ni NPs ($\approx$ 12 nm) to a suspension of 2D BP, the metal was successfully anchored to the surface of the flakes (see Figure 29 a,b). Exfoliated BP resulted able to stabilize Ni NPs even to a record molar ratio of P/Ni = 3. Environmental stability test showed that the Ni-functionalized material was much more stable than pristine BP, remaining morphologically unaltered after one week of air exposure.

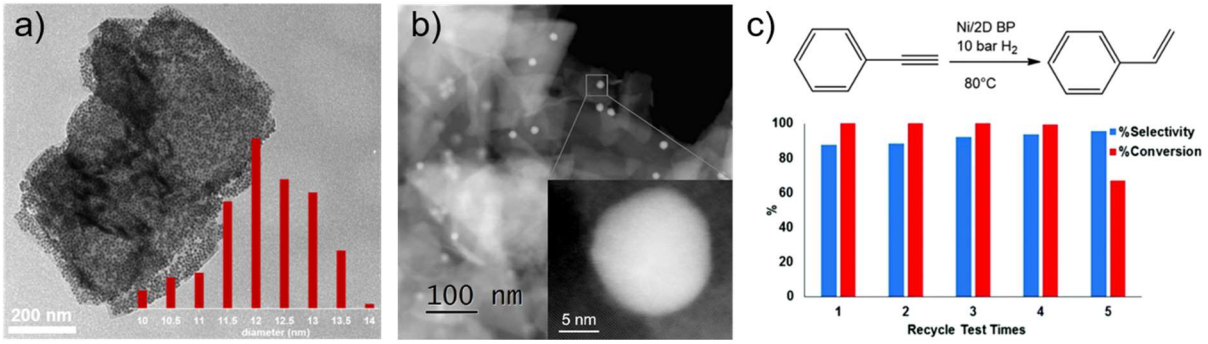

Figure 29. a) TEM and b) HRTEM image of Ni NPs supported on few-layer black phosphorus (Scale bar: 200 nm), P : Ni molar ratio 3 : 1, and size distribution of Ni NPs. c) Recycling tests. Reaction conditions: 10 bar H2, 80 °C, 2 hours, Ni NPs = 1.2 mol%, phenylacetylene = 0.3 mmol, 1.41 mg catalyst (15.2 wt% Ni). Reproduced from reference [120].

The ability of BP to stabilize Ni NPs on its surface was exploited using the nanohybrid as a catalyst for the selective hydrogenation of phenylacetylene (PA) to styrene, a process that is often affected by additional reduction of styrene to ethylbenzene. Ni/BP turned out to be very selective affording 92.8% of styrene at quantitative conversion, compared to 78.6% of bare Ni NPs (see Figure 29c). It is worth mentioning that M. Pumera and colleagues [118] recently have shown that the alternate route to Ni/BP following method 2, namely using BP as in situ reductant toward $NiCl_2$ in neutral or acidic solution, actually yielded Ni_2P NPs on BP instead of the expected Ni/BP.

Pt/BP. X.-F. Yu *et al.* [121] grew ultrasmall Pt NPs (≈ 1.1 nm) on BP using HCHO as reducing agent and the salt precursor K_2PtCl_4. The novel Pt/BP heterostructure showed greater stability under air exposure compared to pristine BP, keeping its morphology almost intact for at least 15 days of exposure. The Pt 4f XPS spectrum displayed a double contribution, corresponding to distinct Pt environments. One component, corresponding to metallic Pt, was attributed to the NP's core. The other is shifted at higher binding energy suggesting the formation of a surface Pt–P bond. As a confirmation, this higher energy component is absent in the XPS spectrum of Pt nanoparticles supported on P25 (TiO_2) or SiO_2 (see Figure 30a). As the O 1s spectrum of Pt/BP, besides the native P_xO_y peaks at 532.7 and 531.4 eV, displays a new smaller peak at 530.5 eV, this spectral feature was taken as an indication of some Pt-O bond (Figure 30b). By means of in situ XPS measurements performed while illuminating the heterostructure with green laser light, it was possible to show how photogenerated electrons promoted to the conduction band of BP were transferred to the Pt NPs, producing a slight shift in the Pt 4f levels toward lower energies. Such ability of the Pt centres to accumulate negative charge was exploited using the Pt/BP heterostructure to promote electron-assisted photochemical reactions.

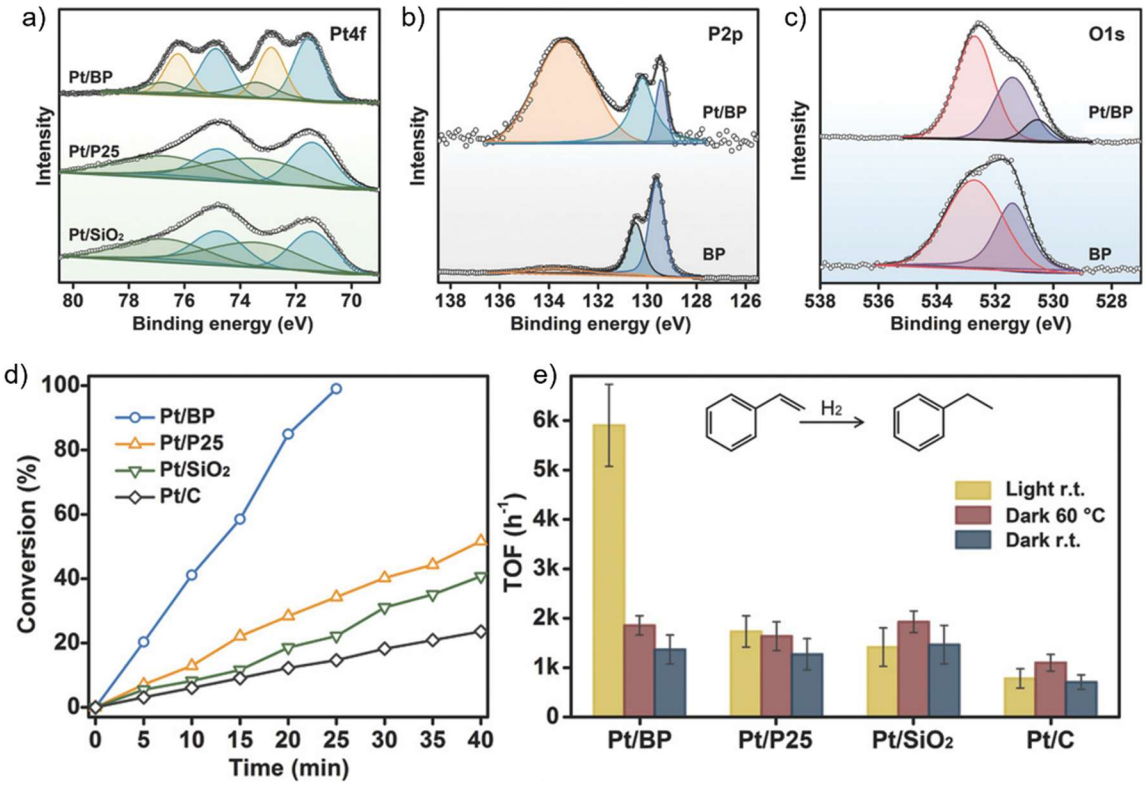

Figure 30. a) Pt 4f core level XPS spectra of Pt/BP, Pt/P25, and Pt/SiO_2. b) P 2p core level XPS spectra of the Pt/BP and BP NSs. c) O 1s core level XPS spectra of Pt/BP and BP NSs. d) Conversion/time plots under simulated solar light illuminations (styrene/Pt = 24.3). e) Catalytic performance of various Pt catalysts under different illumination and thermal conditions.

As a benchmark catalytic test, styrene was hydrogenated to ethylbenzene under solar light simulated irradiation and the performances of Pt/BP were compared with other Pt-based catalyst. Pt/BP showed excellent photocatalytic activity, much higher than commercial Pt/C or Pt NPs immobilized on SiO_2 or TiO_2. Moreover, carrying out the reaction in the dark, the measured TOF dropped to the value of the other catalysts, which were mainly unaffected by light irradiation conditions. Pt NPs immobilized on P25 (TiO_2), showed an increase in TOF of ≈ 36% under light irradiation, much lower than the increase of 400% exhibited by Pt/BP. Afterwards, S. Chen and co-workers [122] used thin-layered BP as a support for the deposition of noble metals NPs, Pt, Ag and Au. The precursors used were respectively $PtCl_4$, $AgNO_3$ and $HAuCl_4.4H_2O$, that once dissolved in water, were mixed with a suspension of 2D BP in NMP. By addition of $NaBH_4$, the reduction took place affording metal NPs with different size on the basis of the noble metal: Pt NPs (1.7 nm), Ag NPs (25 nm) and Au NPs(8.1 nm).

Ag/BP. Silver nanoparticles were grown on 2D BP nanosheets by reducing $AgNO_3$ with $NaBH_4$ in aqueous solution [123]. Two different metal loadings were used, 3 and 5 %wt, with average Ag NPs dimensions of 20 and 40 nm respectively. The interaction between silver and black phosphorus was studied by DFT calculation simplifying the system, as it was modelled with Ag adlayers stacked above a slub of black phosphorus. These calculations showed how the growth of Ag NPs on 2D BP is driven by the formation of new Ag–Ag interaction more than Ag–P bonds. Indeed, moving from 0.25

monolayers of Ag coverage to 2 monolayers, the adsorption energy decreases while the Ag–P bond distances increases, going from a scenario characterized by an ionic interaction to one better described as a covalent interaction between Ag and P. It was investigated the performance of the new Ag/2D BP nanohybrid in the photocatalytic degradation of rhodamine B (RhB) in water, a model reaction related to the study of environmental purification. The photoactivity of Ag/2D BP turned out to be layer dependent, increasing with decreasing 2D BP layer thickness. At higher Ag loadings, a parallel enhancement of RhB degradation was observed.

Au/BP. As demonstrated by different groups, BP nanosheets provide a robust platform for the in situ growth of gold NPs without the addition of an external reducing agent. Indeed, as shown in the Scheme below, the work function of BP is around 4.5 V, thus well above the reduction potential of $AuCl_4^-$ which is +1.002 V respect to E_{SHE}. Thus Au(0) NPs can spontaneously be formed via a redox reaction between BP and $AuCl_4^-$.

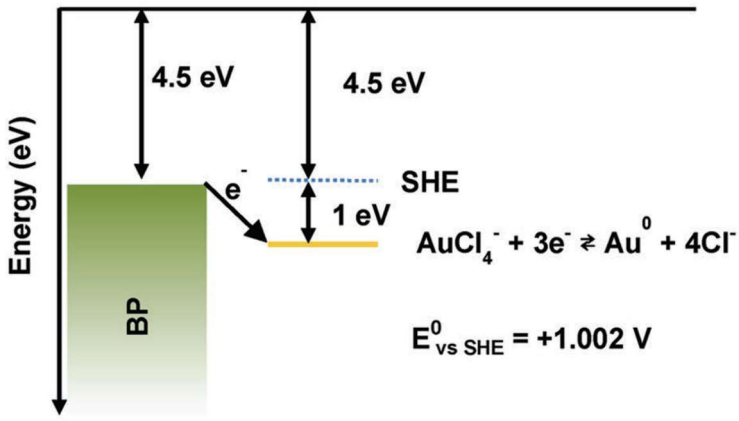

Scheme 2. Energy diagram representing the relative position of the Fermi level of BP and the reduction potential of $AuCl_4^-$.

X.-F. Yu *et al*. [124] were the first to report the application of 2D BP as an in situ reductant, fabricating Au/BP nanohybrids from BP and $HAuCl_4$. This study highlighted that an excess of $HAuCl_4$ in water completely consumed 2D BP after just 5 min stirring at RT, while using a balanced mixture of water and NMP slowed down the process leading to Au NPs supported on BP after 1 hour. Related protocols were devised by other authors [125-127] to prepare Au/BP systems with exact metal loading, simply injecting a controlled amount of $HAuCl_4$ solution in a 2D BP aqueous suspension. F. Wang *et al.* [126] in particular prepared Au/BP nanohybrids with controlled nanoparticles size and Au/P molar ratios and tested them as catalyst for the selective reduction of 4-nitrophenol (4-NP) to 4-aminophenol by $NaBH_4$. Aminophenol is an important building block in the pharmaceutical industry. The sample with a molar

fraction of Au equal to 10%, with average nanoparticles dimension ~ 5 nm, turned out to be the most effective in the process (see Figure 31a,b), outperforming bare Au NPs.

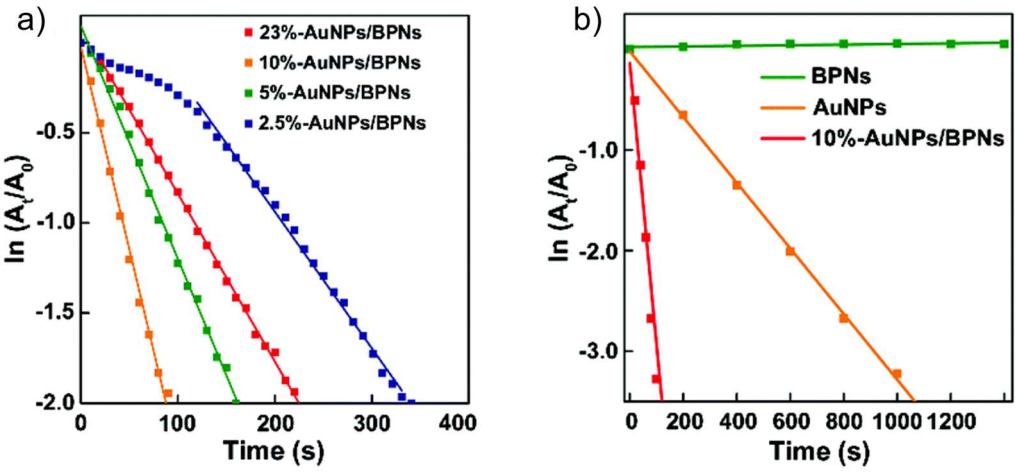

Figure 31. a) Various catalytic performances of different x%-AuNPs/BP nanohybrids as revealed by time-dependent absorbance changes of 4-NP (λ = 400 nm). (b) Comparative time-dependent absorbance changes of 4-NP upon introducing pristine 2D BP, bare Au NPs or 10%-AuNPs/BP nanohybrids into the 4-NP/$NaBH_4$ mixtures. A_t refers to the absorbance of 4-NP at the indicated time while A_0 refers to the original absorbance of 4-NP. Reproduced from reference [126]

Y.-N. Liu and coworkers instead used ultrasounds to assist the reduction of $HAuCl_4$ and grow Au NPs on the surface of the BP nanosheets [127].

1.4.3 Non-covalent functionalization of 2D BP

TCNQ-BP. In 2016 A. Hirsch and coworkers [128] described the use of 7,7,8,8-tetracyano-p-quinodimethane (TCNQ) and of a perylene bisimide (PDI) to form non-covalent adducts with 2D BP. The former is a wide studied building block for charge transfer compounds, behaving as an acceptor of electron density.

Chemical-assisted shear stress exfoliation was carried out under inert atmosphere simply mixing crushed BP powder with a solution of the organic modifier in THF or NMP and leaving the mixture under vigorous stirring 3-5 days. According to the authors, the mechanical shear stress caused by the stirring bar and the stabilization effect provided by the organic modifiers (TCNQ or DPI) progressively peeled down the bulk powder, yielding a suspension of functionalized 2D BP. The UV-VIS spectrum of TCNQ-BP suspension in THF, recorded under rigorously inert atmosphere, revealed the existence of a unique organic species similar to the dianionic $TCNQ^{2-}$, suggesting that in presence of BP a charge-transfer adduct between BP and TCQN forms, electronically close to $TCNQ^{2-}$. Scanning Raman microscopy measurements were carried out on the functionalized material, showing two well-defined ν_3 and ν_4

modes of TCQN at approximately 1580 and 1329 cm^{-1}, respectively (see Figure 32a). Mapping these two modes over the flake revealed a preferential passivation along the edges, as shown in Figure 32b.

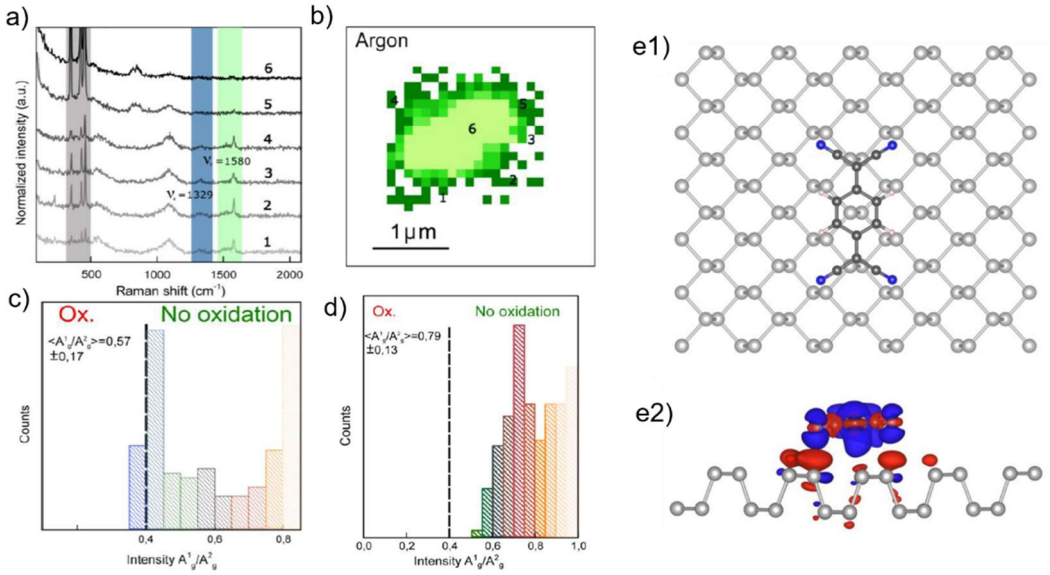

Figure 32. Raman characterization of TCNQ/BP and PDI/BP. a) Wide spectrum showing the ν_3 and ν_4 features of $TCNQ^{2-}$. b) Raman mapping of the ν_3 mode of the $TCNQ^{2-}$ showing the spatial distribution of the molecule. c) Histogram of the A^1_g/A^2_g intensity ratio mapped on TCNQ/BP immediately after the synthesis and d) on PDI/BP after 48 h of air exposure. e) DFT optimized structures of TCQN/1L-BP. Top (e1) and side (e2) views are shown. Side view also features the electron density difference between the adduct BP-TCQN and the isolated fragments (blue/red indicates higher/lower electron density, respectively). Reproduced from reference [129]

Furthermore, the mean $<A^1_g/A^2_g>$ intensity ratio (a measure of surface oxidation, see Section 1.3.1) measured immediately after functionalization was 0.57 (see Figure 32c), compared to the value of 0.79 measured for flakes functionalized with PDI after two days of air exposure, highlighting that PDI provides superior protection to the surface compared to TCNQ (see Figure 32d).

DFT calculations carried out on BP/TCNQ and BP/PDI revealed that a charge-transfer adduct was formed between BP and TCNQ, with 0.43|e| transferred from 1L-BP to the adsorbed TCNQ molecule (see Figure 32e). On the other hand, the interaction between BP and PDI is based on pure van der Waals interaction, keeping the neutrality of PDI and the BP surface.

Anthraquinone-BP. M. Pumera and coworkers [130] studied the non-covalent interaction between 2D BP and anthraquinone (AQ). The latter is a polycyclic aromatic compound often used for electrochemical labelling. 2D BP was prepared by shear stress exfoliation of bulk BP with a kitchen blender in aqueous solution of sodium cholate (a surfactant), working under air exposure. The un-exfoliated material was removed by centrifugation and large thin 2D BP flakes (roughly 400 x 20 nm) were obtained, although partially oxidized as revealed by P2p XPS. Functionalization with AQ was carried out mixing AQ and 2D BP in methanol and applying ultrasounds for 1 h. After washing the solid with ethanol, XPS analysis was performed. Core level C1s measurements highlighted a relatively

abundant C=O contribution, attributed to the carbonyl groups in AQ, confirming its successful immobilization on the BP surface. Flakes of BP/AQ were exposed to air and observed *via* AFM over 30 days to evaluate the effect of AQ over their air stability. Remarkably, only minor effects of degradation were detected, pointing out the protecting role of the organic layer.

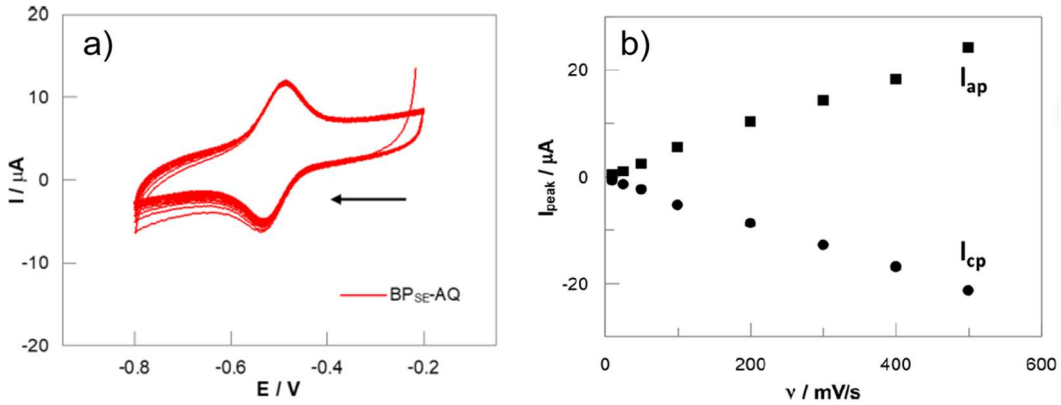

Figure 33. a) Cathodic scan 100 CVs of AQ/BP within the potential window in which AQ is active. b) Plots of anodic and cathodic peak currents as a function of scan rate. Reproduced from reference [130]

The strength of the interaction between 2D BP and AQ was highlighted through CV measurements, carried out in aqueous media using a three electrodes system. After a first forward scan in which BP oxidation takes place, attributed to naked areas of the flakes, only the peaks of the AQ redox process are left. The redox system remained extremely stable over 100 cycles, as shown in Figure 33a. Furthermore, the CV peaks of the redox couple looked symmetrical and the peak current showed a linear dependence on scan rate (Figure 33b). Such response is characteristic of a quasi-reversible redox system, in which both the oxidized and the reduced forms are strongly anchored to the electrode surface, thus pointing to a strong adhesion of both AQ and its reduced species AHQ to the BP surface.

Pyren-1-boronic acid-BP. S. Toffanin and coworkers [131] reported a detailed study of the non-covalent interaction between BP and boronic derivatives of pyrene. As trivalent boron is Lewis acidic, boronic compounds are supposed to have a good affinity for BP, being able to interact with phosphorus lone pairs. Furthermore, the extended planar conjugated system of pyrene may get involved in p-π interaction with the BP surface

Pyrene derivatives are also extensively studied fluorophores, with widespread applications in sensing and optoelectronic. Three distinct compounds were studied, namely pyrene (Py), pyren-1-boronic acid (PBA) and 4,4,5,5-Tetramethyl-2-pyren-1-yl-1,3,2-dioxaborolane (PBE), see Figure 34.

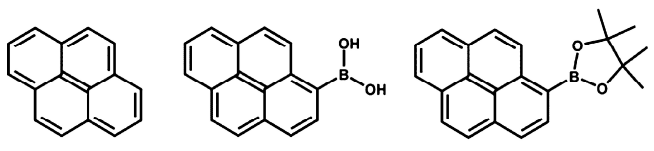

Py PBA PBE

Figure 34. Molecular structures of Py, PBA, PBE.

2D BP was prepared by LPE of BP powder under inert atmosphere in DMSO. The lighter material was isolated upon consecutive centrifugation cycles and was resuspended in anhydrous THF. The dye (Py, PBA or PBE) was then added and the mixture was sonicated to carry out the functionalization. Solid state DFT calculation were carried out to investigate the nature of the interaction with BP (see Figure 35). As expected, pyrene has a large affinity for the BP surface, characterized by an adsorption energy of – 2.2 eV. Although not covalently bonded, there is some degree of donation from the p lone pairs of BP to the π* orbitals of Py (π-p interaction). In PBA and PBE the presence of weak P···B interactions provides additional stabilization to the system, but the main contribution to the adsorption energy still comes from the pyrene backbone.

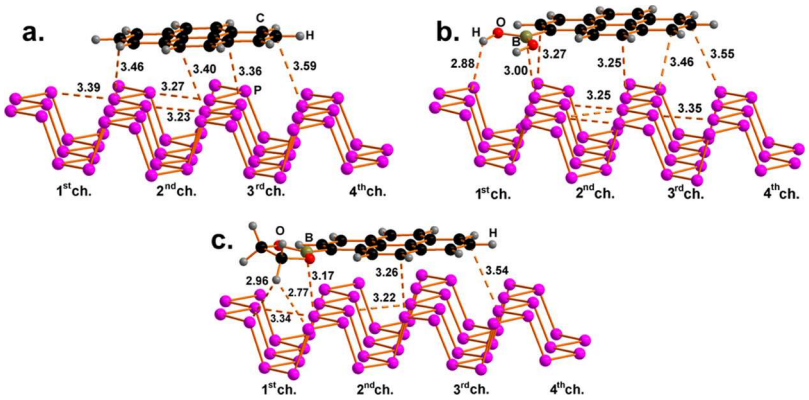

Figure 35. Optimized structure of the adducts of phosphorene with Py (a), PBA (b), and PBE (c). Reproduced from reference [131].

NMR MAS measurements were carried out on 2D-PBA/BP in THF-d_5 suspensions. The ^{31}P MAS spectrum featured the main peak of BP at an isotropic chemical shift of about 18.5 ppm without any evident modification or presence of additional peaks, consistent with a weak interaction. Time-resolved fluorescence measurements revealed a stabilizing effect of the excited state upon surface immobilization, following the same order of the calculated absorption energy, namely 2D-Py/BP < 2D-PBA/BP < 2D-PBE/BP.

1.4.4. Covalent functionalization of 2D BP

Functionalization via arylating reagents. In 2017 M.C. Hersam *et al.* [132] reported the use of aryl diazonium salts to functionalize 2D BP with aryl moieties through formation of covalent P−C bonds. Aryl diazonium salts, with general formula $ArN_2^+X^-$, are common arylating agents, already used successfully in the covalent grafting of graphene [134] and carbon nanotubes [135].They are easily

involved in single-electron-transfer (SET) reactions, accepting one electron with formation of a phenyl radical and release of N_2, the driving force for the reaction. The mechanism is illustrated in Figure 36a.

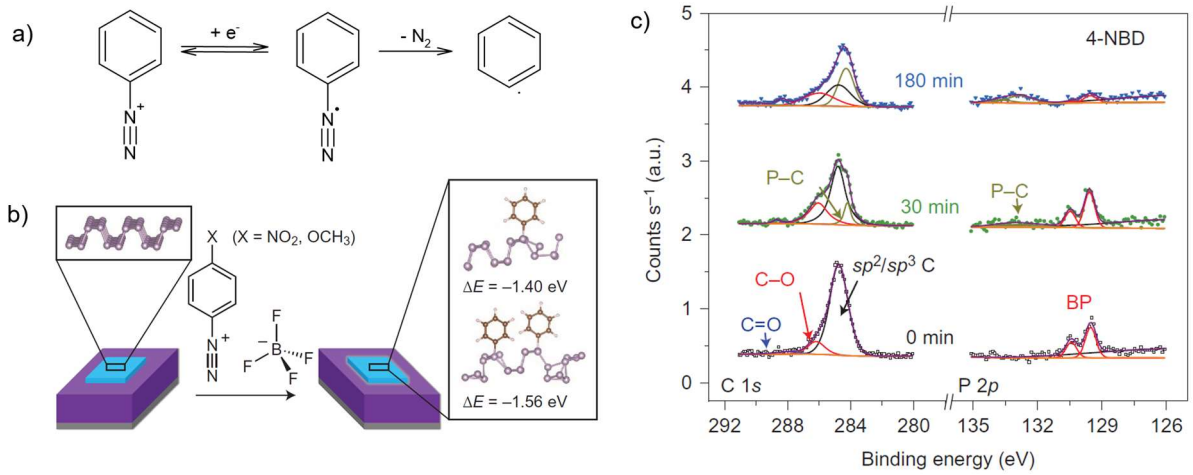

Figure 36. a) Formation of aryl radicals from diazonium cations upon single-electron-transfer and loss of N_2. b) Scheme of the reaction between diazonium slat and mechanically exfoliated BP (light blue). The left inset shows the pristine structure of BP and the right inset shows DFT-calculated structures of the thermodynamically favoured covalent bonding of aryl groups to BP. c) Deconvoluted C1s and P2p core-level XPS spectra of 4-NBD/BP. After 30 minutes, a peak attributed to P–C bonds appears at 284 eV in the C1s spectrum and increases after 3 h. In the P2p spectrum, a broad P–C feature at 133 eV is evident after 30 minutes and grows over 3 h. Reproduced from reference [132].

When mixed with 2D BP, electron transfer from phosphorus takes place, with formation of surface radical species which are then trapped by the phenyl radical. DFT calculations showed that grafting of aryl groups at the surface is energetically favoured. Functionalization was carried out with a flake mechanically exfoliated on SiO_2/Si (~ 10 nm in thickness), by simple dipping into a solution of 4-nitrobenzenediazonium tetrafluoroborate (4-NBD) in acetonitrile (see Figure 36b). An increase of ~ 1.3 nm in flake thickness, measured by AFM, pointed toward a successful covalent passivation of the layer. Correspondingly, high resolution P 2p XPS measurements detected a peak at ~ 133 eV assigned to P–C bonds (see Figure 36c). Remarkably, functionalized 2D BP displayed superior environmental stability compared to pristine BP, as only minor modifications were observed *via* AFM in 4-NBD/BP over 10 days. In a retrosynthetic perspective, diazonium chemistry provides a practical disconnection for P–C bonds and can be exploited to immobilize larger moieties on 2D BP flakes. Following this approach, Y. Zhao *et al.* [136] grafted to the surface of BP fluorescent dye Nile Blue 690 (NB), upon conversion of the amino group in $-N_2^+$. Other groups exploited the strategy based on aryldiazonium to grow polymeric chains covalently anchored to BP [137, 138]. G. Collins and coworkers [139] explored the use of related diaryliodonium salts (general formula $Ar_2I^+X^-$) as alternative reagents. Diaryliodonium salts are powerful tools in organic synthesis, able to arylate nucleophiles under mild conditions thanks to the excellent leaving group ability of the iodide. Remarkably, 2D BP arylation with iodonium salts provides a higher degree of surface functionalization compared to aryldiazonium chemistry and superior environmental stability.

Though diazonium chemistry has been considered the best-established protocol to covalently modify BP, recent studies by the group of A. Hirsch have seriously questioned this judgement [140]. According to their last investigations, not only would be aryl diazonium salts unreactive toward BP (as verified by Raman, TGA-MS and ^{31}P NMR MAS spectroscopy), even using the reductively activated intercalation compound KP_6 no straightforward arylation takes place, leading instead to disruptive amorphization of the BP lattice.

Functionalization with organic azides. In the Staudinger reaction an organic azide reacts with a phosphine with loss of N_2, leading to the formation of an iminophosphorane featuring P=N bonds. Y. Liu *et al.* [141] followed the same approach to functionalize 2D BP with 4-azidobenzoic acid (4-ABA), stirring a mixture of the two reagents in DMF at 140°C for 48h. FT-IR analysis of the recovered solid (4-ABA/BP) revealed a peak located at 1693 cm^{-1}, corresponding to a carbonyl stretching, and several signals between 1400-1600 cm^{-1} coming from the phenyl ring. The characteristic peak of the azido group $-N_3$ (1328 cm^{-1} in 4-ABA) instead was absent, suggesting a possible grafting of the nitrene intermediate after loss of N_2. Core level P2p XPS measurements highlighted a minor peak at 133.7 eV, attributed to P=N double bonds (see Figure 37a). Correspondingly, the N1s core level spectrum featured a unique peak at 401.5 eV (Figure 37b).

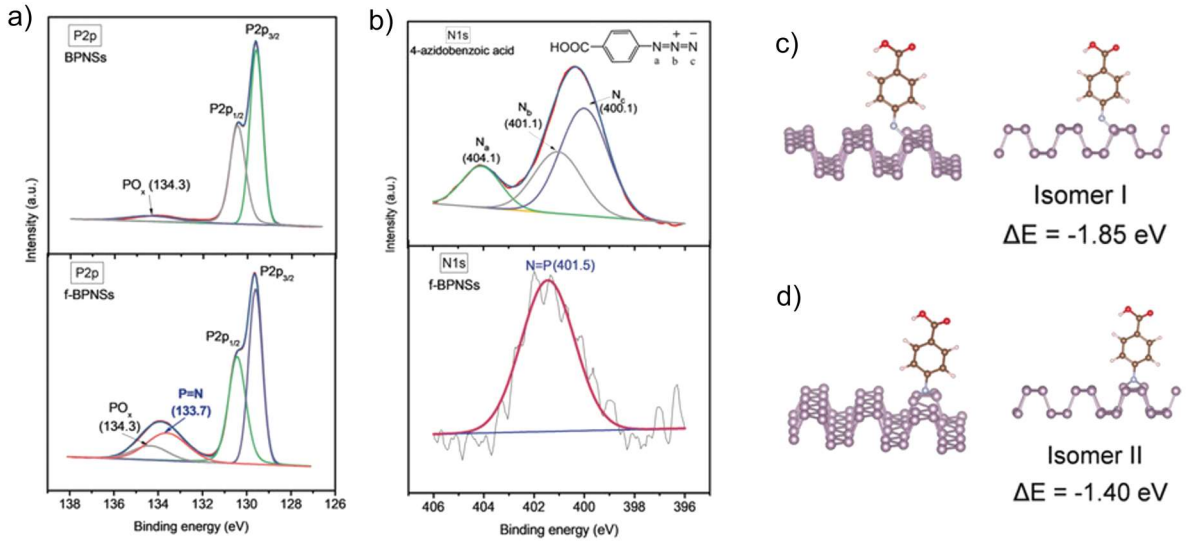

Figure 37. a) High-resolution P 2p XPS spectra of BPNSs and f-BPNSs. b) High-resolution N 1s XPS spectra of 4-ABA and f-BPNSs. DFT-calculated thermodynamically favoured two isomers and the corresponding formation energy per aryl group for (a) P=N and b) P−N covalent bonds. Reproduced from reference [141].

DFT calculation were carried on a model system and identified two candidate structures, one involving P=N bonds (isomer I), the other featuring a bridging P−N−P moiety (isomer II, see Figure 37c,d). The latter, less stable, was proposed as a potential intermediate toward the formation of isomer I.

Functionalization with organic electrophiles. In order to exploit the presence of lone pairs on the BP surface, as previously described to immobilize metal NPs on BP, M. Pumera and coworkers [142] studied its reactivity with electrophilic species such as (S)-bromomethyl ethanethioate (SBE) and tridecafluoroiodooctane (TFIO). These alkyl derivatives possess several heteroatoms (S, F) to facilitate their identification via elemental analysis. The reaction of 2D BP with SBE was carried out at reflux in $CHCl_3$. SEM-EDS elemental mapping of the flakes and their survey XPS spectrum revealed the presence of sulfur (see Figure 38a,b). The core level P2p XPS spectrum, beside the main BP doublet at ~ 130 eV and the PO_x band at 134-135 eV, featured an additional small peak at ~132.5 eV consistent with P−C bonds (see Figure 38c).

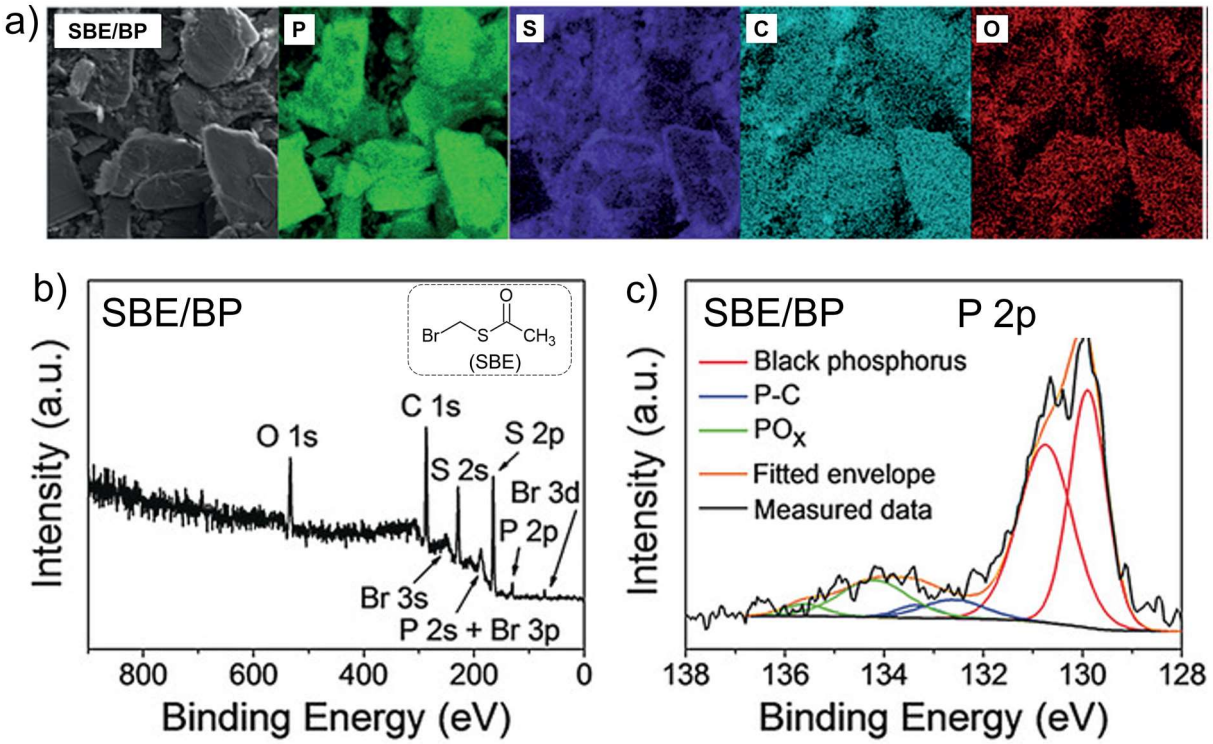

Figure 38. a) SEM-EDS mapping of the functionalized flakes. b) XPS survey spectrum and c) high-resolution P 2p spectrum of BP modified by (S)-bromomethyl ethanethiolate (molecular structure shown in the inset in b). Reproduced from reference [142].

DFT calculations were carried out on model 1L-BP and SBE, showing that direct chemisorption with P−C bond formation is energetically feasible and preferred to PO−C grafting. Similarly, upon reaction of 2D BP with the fluorinated electrophile TFIO, XPS analysis revealed the presence of fluorine and the absence of iodine in the material, suggesting the successful attachment of the fluoroalkyl unit to the phosphorus surface.

In order to enhance the reactivity of BP as a nucleophile, A. Hirsch and coworkers exploited its intercalation compounds (BPICs) [144,145]. The latter are obtained upon reduction of BP with alkali metals [145]. The advantage of this method is that the phosphorus network in BPICs is negatively

charged, increasing the reactivity toward electrophiles. The reaction between BPICs with M:P ratio 1:6 (namely KP_6 or NaP_6) and hexyl iodide was studied in situ via Raman spectroscopy (see Figure 39a).

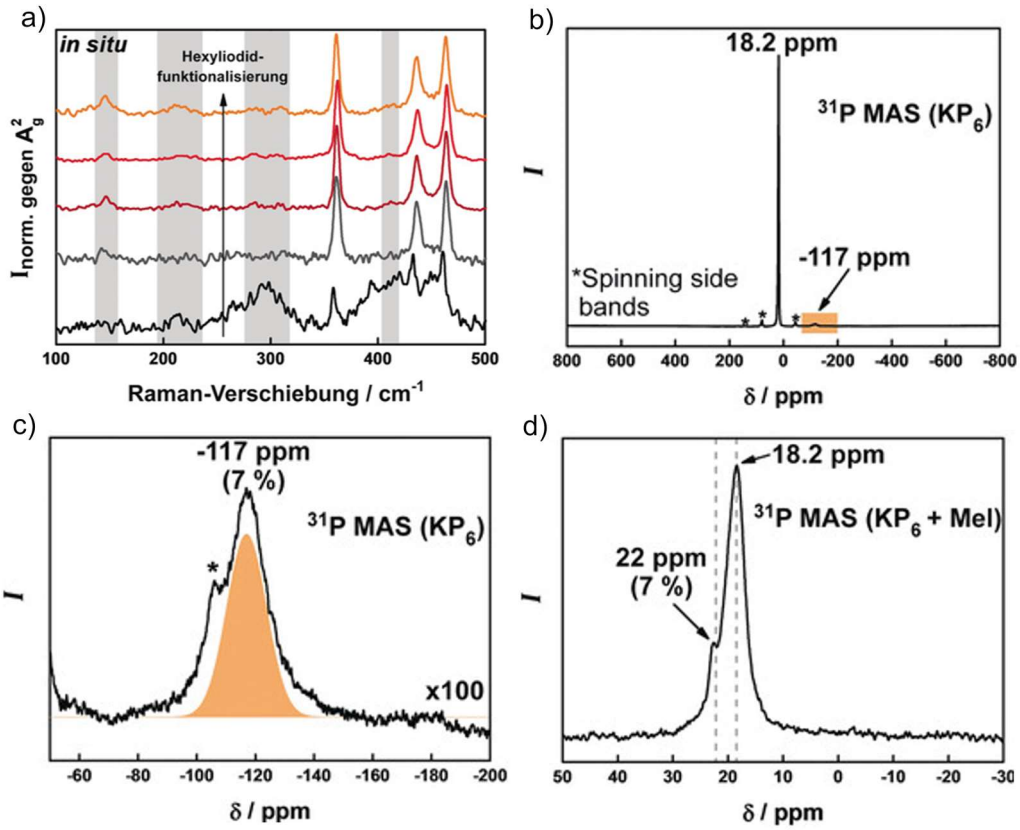

Figure 39. In situ Raman spectroscopy monitoring the reaction of hexyl iodide with KP_6 using an excitation wavelength of λ_{exc} = 633 nm. With increasing amounts of hexyl iodide distinct new Raman peaks arise at 145, 210, between 260 and 285, and at 410 cm^{-1}. b) ^{31}P MAS NMR spectra of KP_6 featuring the signal for pristine BP at 18.2 ppm as well as a signal at −117 ppm, which can be assigned to axially coordinated P atoms bearing a localized negative charge. c) Magnification of the deshielded peak d) ^{31}P MAS NMR spectrum of BP functionalized with methyl moieties showing the appearance of a new signal at 22 ppm arising from newly formed P−CH_3 bonds. Reproduced from reference [143].

Notably, new peaks appeared below 300 cm^{-1} and increased in intensity over time. Furthermore, the overall KP_6 Raman spectrum gradually converted to the typical BP spectrum with characteristic A^1_g, B^2_g and A^2_g BP modes. This observation is explained by the gradual quenching of negative charges by hexyl iodide and formation of KI and P−C_{alkyl} bonds, generating the new bands below 300 cm^{-1}. DFT calculation carried out on a model system were able to rationalize the observed Raman pattern. Core level P 2p XPS measurements revealed a peak located at ~132.7 eV, assigned to P−C covalent bonds. Solid state ^{31}P NMR measurements were also carried out on KP_6 before and after quenching with hexyl iodide. Notably, alongside the typical BP peak at 18.2 ppm, the spectrum of KP_6 featured a small signal at -117 ppm consistent with localized negatively-charged P atoms, corresponding to ~ 7 % of the total integrated area. Remarkably, after quenching with hexyl iodide this peak disappeared, being replace by a shoulder peak at ~ 22 ppm integrating for ~ 7 % of the total P atoms, in agreement with the expected chemical shift of a P−CH_3 bond (see Figure 39b,c,d).

Functionalization with fullerene. Mechanochemical BP exfoliation and functionalization approaches have also been reported so far [146,147,148]. In particular, X. Zhu *et al.* described the edge-functionalization of 2D BP with fullerene C_{60} balls [148]. Grinded BP powder and C_{60} were mixed inside a planetary ball-milling machine and milled under argon for 24 h. Ball milling provides both the shear stress for exfoliation and the energy to promote P–P bond cleavage and C_{60} activation. The dark product, named C_{60}-BP, was then Soxhlet extracted with CS_2 to eliminate unreacted fullerene. C_{60}-BP was made of thin flakes with lateral dimension ~ 1 μm and average thickness 2.5 ± 0.2 nm. Thermogravimetric analysis (TGA) of the material revealed a molar content of C_{60} equal to 1.9%. Remarkably, HRTEM imaging of C_{60}-BP flakes highlighted the presence of hollow nanosphere with diameter ~ 1 nm, corresponding to C_{60} balls, arranged along the flake edges (see Figure 40).

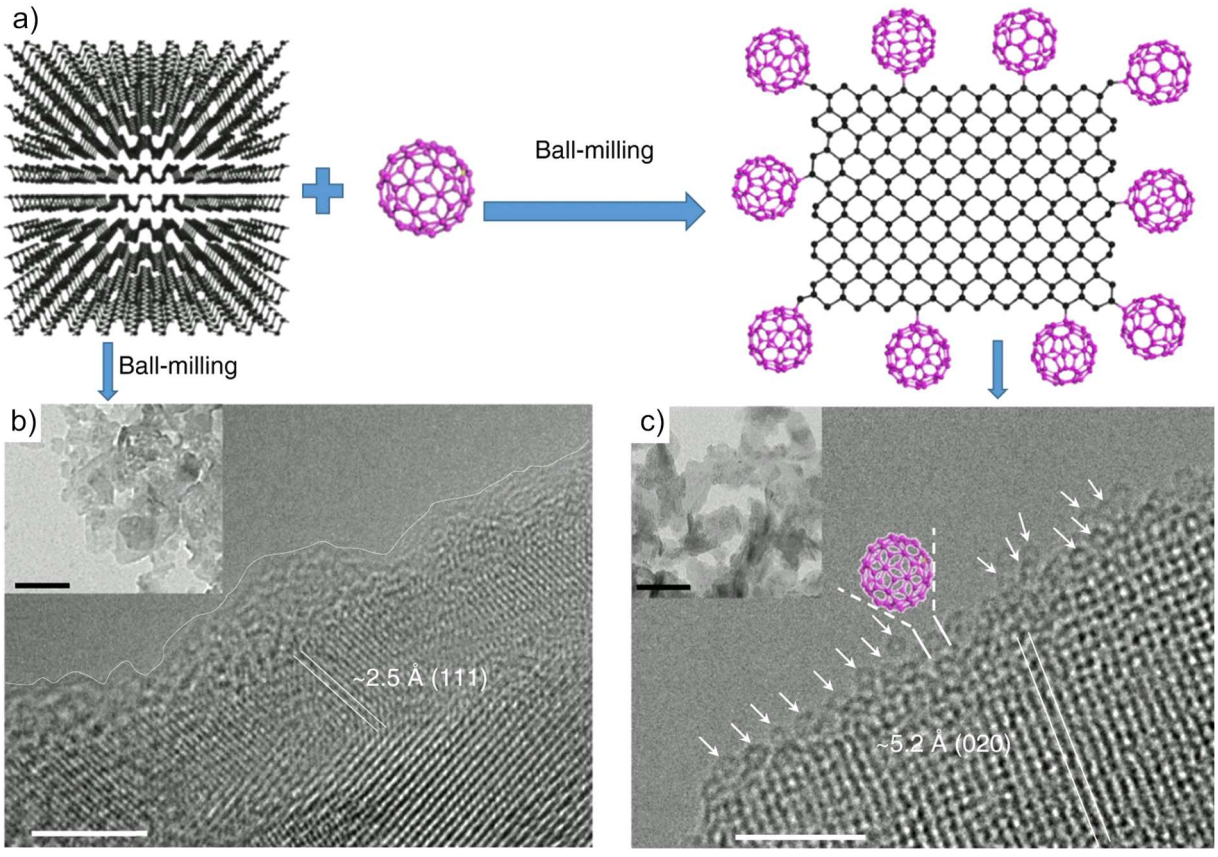

Figure 40. Microstructural characterizations. a) Scheme of the preparation process and structure of BP-C_{60} hybrid. b) HRTEM and low-magnification TEM (inset, scale bar: 100 nm) images of ball-milled BP (BP-BM). c) HRTEM, and low-magnification TEM (inset, scale bar: 100 nm) images of the BP-C_{60} hybrid. The arrows mark the C_{60} molecules. Reproduced from reference [148].

STEM-EDX elemental mapping confirmed a preferential edge-functionalization. To shed light on the nature of the interaction between C_{60} and phosphorus atoms, a spectroscopic characterization of the material was addressed using different techniques. FTIR measurements highlighted the presence of three

peaks at 707, 770 and 795 cm^{-1}, which were absent in 2D BP and physical mixture of BP and C_{60}, thus attributed to newly formed P−C bonds (see Figure 41a).

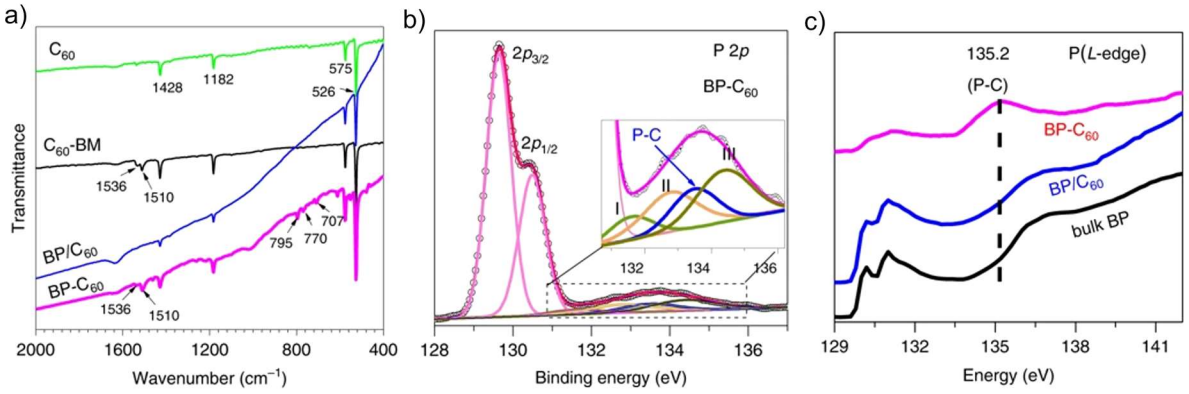

Figure 41. Spectroscopic characterizations. a) FTIR spectra of the pristine C_{60}, C_{60} balled milled (C_{60}-BM), a physical mixture (BP/C_{60}) and the BP-C_{60} hybrid. b) High-resolution P 2p XPS spectrum of the BP-C_{60} hybrid. Numbers I-III label the signals assigned to P-O-P (bridging bonding), O–P=O (dangling bonding), and P_2O_5, respectively. c) P *L*-edge XAS spectra of bulk BP, BP/C_{60} mixture and the C_{60}-BP nanohybrid. Reproduced from reference [148].

Correspondingly, P2p XPS measurements revealed a small peak at 133.5 eV consistent with P−C bonds (see Figure 41c). ^{13}C NMR MAS measurements showed typical signals of sp^2-C in the range 130-160 ppm, corresponding to C_{60}. Furthermore, an extra peak at δ = 75.75 ppm was detected, consistent with sp^3-C carbon, thus attributed to C–P. Further evidence toward the covalent functionalization with C_{60} bonds was provided by X-ray absorption spectroscopy (XAS) at the P L-edge. A comparison of the spectra acquired on bulk BP, physical mixtures (BP + C_{60}) and C_{60}-BP (see Figure 41b) revealed a unique spectral feature at ~135.2 eV in the functionalized material C_{60}-BP, in contrast to the other reference samples, pointing to a strong interaction between phosphorus and carbon. Environmental stability studies revealed that C_{60} acts as a sacrificial protective shield toward surface oxidation. Surface decoration with C_{60} results also in a photoinduced electron transfer from BP to C_{60}, as revealed by steady-state photoluminescence spectroscopy measurements, which enhance the photocatalytic activity of the material in the benchmark reaction of Rhodamine B degradation.

Functionalization with metal complexes. As in the case of functionalization with organic electrophiles (see Section 1.4.4), the presence of a lone pair on each phosphorus atom in BP suggests the possibility of developing a coordination chemistry of the black allotrope, much like has been done with P_4 [149]. However, this has received limited attention both experimentally and theoretically. The very few examples reported testify that major difficulties must be overcome moving from P_4 to BP. Theoretical calculations [150] have shown that, like P_4, BP is a much weaker Lewis base than phosphines. This is mainly attributed to the partial delocalization of the lone pairs of electrons on the phosphorus centers. Furthermore, the chair conformation of each P_6-unit in the skeleton of BP implies a tilting of the lone pairs at approximately 30° from the plane of the layer (see Fig. 42).

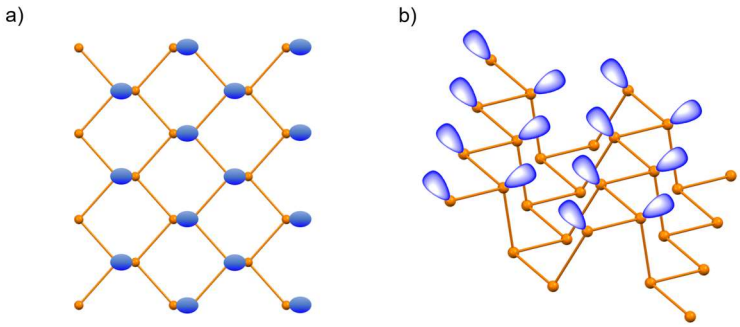

Figure 42. Top (a) and side (b) view of the phosphorene lone pairs. Image (b) clearly shows the tilting of the lone pairs with respect to the plane of the layer and the misalignment of two adjacent lone pairs due to P-P bond torsion of 60°.

Although η^1, η^2 and η^3-coordination modes were identified on the BP surface (see Fig. 43), lone pairs on distinct P-atoms are not perfectly convergent, preventing an optimal orbital overlap. This could be overcome at the cost of some local distortion of the BP surface, which however is difficult due to its rigid structure.

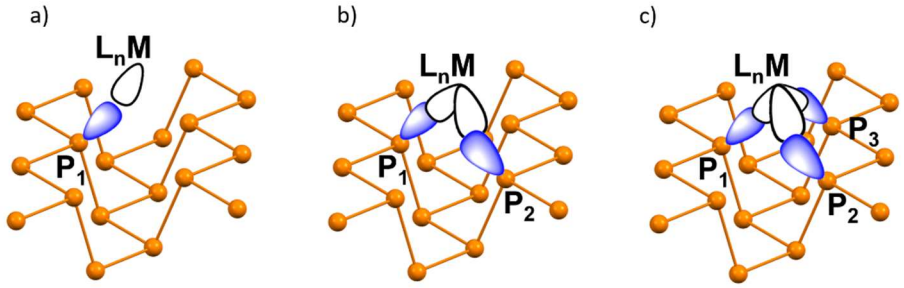

Figure 43. The three potential bonding modes of BP toward a metal fragment. (a) η^1 coordination with formation of single P-M bond (b) η^2 coordination and (c) η^3 coordination.

In 2016 Y. Zhao *et al.* [151] reported the functionalization of exfoliated BP with a transition metal fragment, namely TiL_4 (L = p-toluenesulfonate). Ultrasmall BP quantum dots (BPQDs) with a lateral size of 2.6 ± 1.8 nm and a thickness of 1.5 ± 0.6 nm were stirred with TiL_4 in NMP for 15 hours to obtain TiL_4/BP. XPS measurements performed on the material detected presence of titanium.

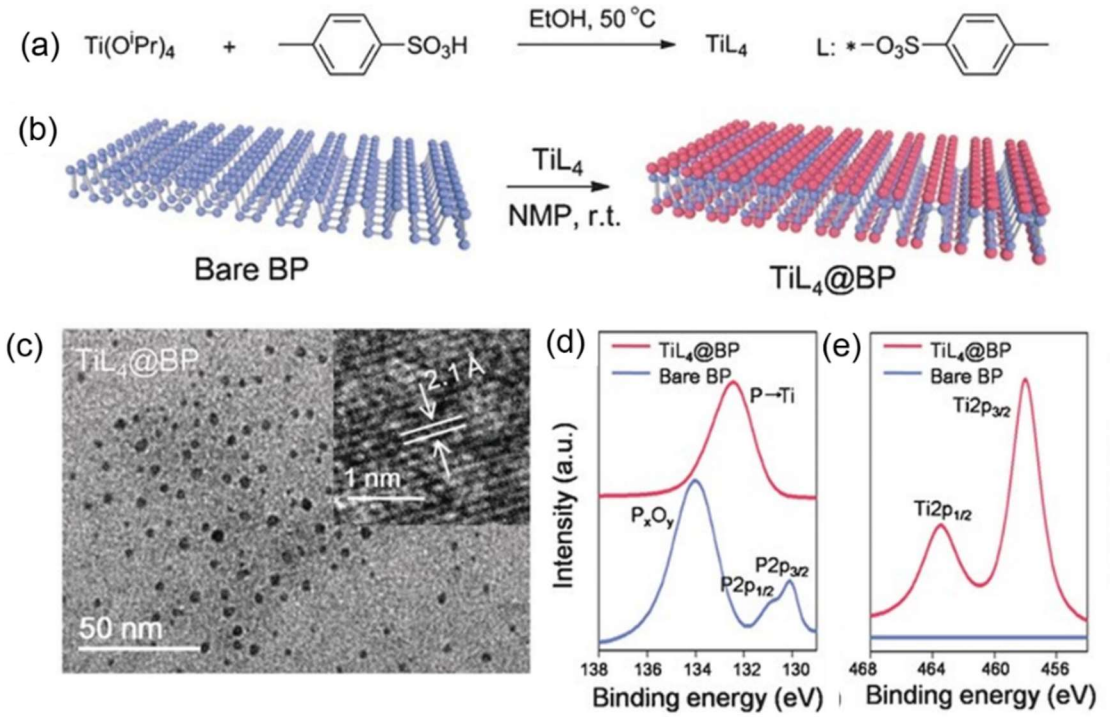

Figure 44. Fabrication and characterization of TiL_4-decorated BPQDs (denoted TiL_4@BP). a) Synthesis and structural formula of TiL_4; b) surface coordination of TiL_4 to BP; c) TEM image with inset HRTEM image of TiL_4@BP; d) P 2p and (e) Ti 2p XPS spectra of TiL_4@BP, acquired after 3 days of air exposure. Reproduced from reference [151].

Evidence of P–Ti bonding was attributed to the P 2p XPS signal at 132.4 eV. However, in the writer opinion, this interpretation is highly questionable, as no deconvolution of the P 2p signal was carried out. More astonishing, there is no presence of the peaks of pristine BP at ~ 130 ppm, which seems unrealistic as some unfunctionalized P atoms are always detected as main component in the P 2p XPS spectrum (see all the functionalizations previously described). No further studies were carried out to shed light on the structure of this adduct or strengthen the covalent depiction of the functionalization, and it seems likely that the interaction between BP and TiL_4 could just be of non-covalent nature. The functionalized material showed greater air stability compared to pristine BP and was used successfully as a contrast agent for in vivo photo-acoustic imaging of cancer. L. Wu *et al*. [152] attempted the metal functionalization of BP nanosheets using lanthanide complexes. Lanthanides have large atomic radii, which should allow for an easier interaction with the lone pairs of electrons of the phosphorus atoms. As in the case of TiL_4, a sulfonate anion was chosen as ancillary ligand, since it was thought suitable to enhance the electrophilicity of the metal, promoting the coordination to BP. Thus, different LnL_3 species (with L = trifluoromethanesulfonate and Ln = Gd, Y, La, Nd, Sm, Eu, Tb, Er) were tested. EDS analysis of the isolated LnL_3/BPQDs confirmed the successful functionalization of BPQDs (see Fig. 45).

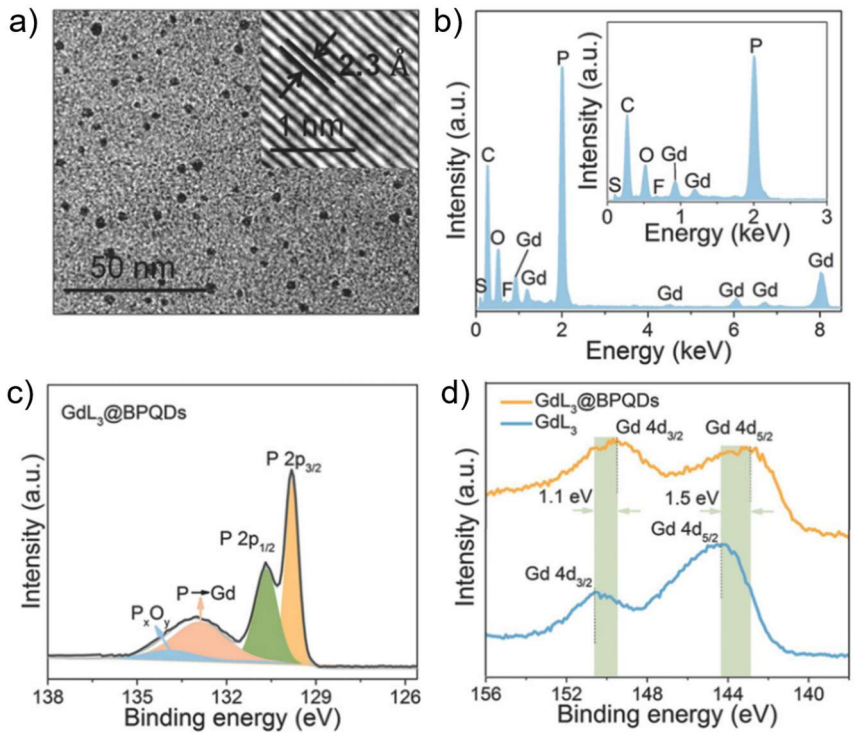

Figure 45. Characterization of GdL_3-coordinated BPQDs (named GdL_3@BPQDs). a) TEM image and HRTEM inset; b) EDS spectra; c) Gd 4d XPS spectra of GdL_3@BPQDs and free GdL_3; d) P 2p XPS spectrum of GdL_3@BPQDs. Reproduced from reference [152].

Although theoretical investigations were not carried out on the system, the authors propose that LnL_3 species will coordinate to three phosphorus atoms on the BP surface (η^3-BP), as shown in Fig. 46. This sounds reasonable taking into account the large atomic radius of lanthanide metals, which favours a larger hapticity of BP. XPS studies of GdL_3/BPQDs at the P 2p core level highlighted the presence of an electron-depleted phosphorus species at 132.9 eV, assigned to the P–Gd bonds (Fig. 45c). Furthermore, an appreciable red-shift is observed in the Gd 3d XPS spectrum compared to free GdL_3 (Fig. 45d), in accordance with donation of electron density from the σ orbitals of BP to Gd. As with the TiL_4 functionalization, LnL_3/BPQDs showed an enhanced stability toward air and water with respect to bare BPQDs.

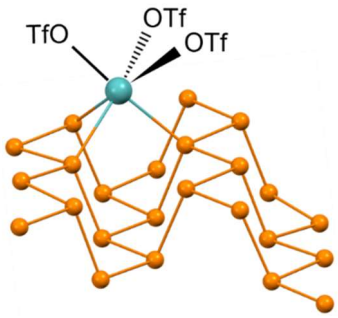

Fig. 46. Putative atomistic model of the adduct between BP and LnL_3 fragment, L = OTf = Trifluoromethanesulphonate.

1.5 List of abbreviations

Some abbreviations used in the thesis are listed below.

BP	Black phosphorus
BPQDs	Black phosphorus quantum dots
LPE	Liquid phase exfoliation
ICP-AES	Inductively coupled plasma – atomic emission spectroscopy
PXRD	Powder X-ray diffraction
TEM	Transmission electron microscopy
HRTEM	High-resolution electron microscopy
SEM	Scanning electron microscopy
EELS	Electron energy loss spectroscopy
HAADF STEM	High-angle annular dark-field scanning transmission electron microscopy
XPS	X-ray photoelectron spectroscopy
XAS	X-ray absorption spectroscopy
EXAFS	Extended X-ray absorption fine structure
CP-MAS NMR	Cross polarization – magic angle spinning NMR
DE-MAS NMR	Direct excitation – magic angle spinning NMR
DFT	Density functional theory
CNB	Chloronitrobenzene
DIM	$[Pd(C_3H_5)Cl]_2$

1.7 Chapter I References

[1] L.R. Maxwell, S.B. Hendricks, V.M. Mosley, Electron diffraction by gases, J. Chem. Phys. 3 (1935) 699–709. https://doi.org/10.1063/1.1749580.

[2] R. Hultgren, N.S. Gingrich, B.E. Warren, The atomic distribution in red and black phosphorus and the crystal structure of black phosphorus, J. Chem. Phys. 3 (1935) 351–355. https://doi.org/10.1063/1.1749671.

[3] G. Natta, L. Passerini, The crystal structure of white phosphorus, Nature. 125 (1930) 707–708.

[4] D.E.C. Corbridge, E.J. Lowe, Structure of white phosphorus: Single crystal X-Ray examination, Nature. 170 (1952) 629. https://doi.org/10.1038/170629a0.

[5] A. Simon, H. Borrmann, H. Craubner, Crystal Structure of Ordered White Phosphorus(β-P), Phosphorous Sulfur Relat. Elem. 30 (1987) 507–510. https://doi.org/10.1080/03086648708080631.

[6] H. Okudera, R.E. Dinnebier, A. Simon, The crystal structure of γ-P_4, a low temperature modification of white phosphorus, Zeitschrift Fur Krist. 220 (2005) 259–264. https://doi.org/10.1524/zkri.220.2.259.59137.

[7] C. Liu, Z.M. Sun, Recent advances in structural chemistry of Group 14 Zintl ions, Coord. Chem. Rev. 382 (2019) 32–56. https://doi.org/10.1016/j.ccr.2018.12.003.

[8] M. Kohn, The discovery of red phosphorus (1847) by Anton von Schrötter (1802-1875), J. Chem. Educ. 21 (1944) 522. https://doi.org/10.1021/ed021p522.

[9] A.J. Smith, W.L. Roth, T.W. DeWitt, Polymorphism of Red Phosphorus, J. Am. Chem. Soc. 69 (1947) 2881–2885. https://doi.org/10.1021/ja01203a072.

[10] W. Hittorf, Zur Kenntniss des Phosphors, Ann. Phys. Chem. (1865) 193–228.

[11] H. Thurn, H. Kerbs, Crystal Structure of Violet Phosphorus, Angew. Chemie Int. Ed. 5 (1966) 1047–1048. https://doi.org/10.1002/anie.196610473.

[12] G. Schusteritsch, M. Uhrin, C.J. Pickard, Single-Layered Hittorf's Phosphorus: A Wide-Bandgap High Mobility 2D Material, Nano Lett. 16 (2016) 2975–2980. https://doi.org/10.1021/acs.nanolett.5b05068.

[13] L. Zhang, H. Huang, B. Zhang, M. Gu, D. Zhao, X. Zhao, L. Li, J. Zhou, K. Wu, Y. Cheng, J. Zhang, Structure and Properties of Violet Phosphorus and Its Phosphorene Exfoliation, Angew. Chemie - Int. Ed. 132 (2020) 1090–1096. https://doi.org/10.1002/ange.201912761.

[14] M. Ruck, D. Hoppe, B. Wahl, P. Simon, Y. Wang, G. Seifert, Fibrous red phosphorus, Angew. Chemie - Int. Ed. 44 (2005) 7616–7619. https://doi.org/10.1002/anie.200503017.

[15] A. Pfitzner, E. Freudenthaler, $(CuI)_3P_{12}$: A Solid Containing a New Polymer of Phosphorus Predicted by Theory, Angew. Chemie - Int. Ed. 34 (1995) 1647–1649.

[16] S. Böcker, M. Häser, Covalent Structures of Phosphorus: A Comprehensive Theoretical Study, ZAAC - J. Inorg. Gen. Chem. 621 (1995) 258–286. https://doi.org/10.1002/zaac.19956210215.

[17] M. Häser, Structural Rules of Phosphorus, J. Am. Chem. Soc. 116 (1994) 6925–6926. https://doi.org/10.1021/ja00094a053.

[18] A. Pfitzner, M.F. Bräu, J. Zweck, G. Brunklaus, H. Eckert, Phosphorus nanorods - Two allotropic modifications of a long-known element, Angew. Chemie - Int. Ed. 43 (2004) 4228–4231. https://doi.org/10.1002/anie.200460244.

[19] D. Liu, J. Guan, J. Jiang, D. Tománek, Unusually Stable Helical Coil Allotrope of Phosphorus, Nano Lett. 16 (2016) 7865–7869. https://doi.org/10.1021/acs.nanolett.6b04128.

[20] A.J. Karttunen, M. Linnolahti, T.A. Pakkanen, Icosahedral and ring-shaped allotropes of phosphorus, Chem. - A Eur. J. 13 (2007) 5232–5237. https://doi.org/10.1002/chem.200601572.

[21] J. Zhang, D. Zhao, D. Xiao, C. Ma, H. Du, X. Li, L. Zhang, J. Huang, H. Huang, C.L. Jia, D. Tománek, C. Niu, Assembly of Ring-Shaped Phosphorus within Carbon Nanotube Nanoreactors, Angew. Chemie - Int. Ed. 56 (2017) 1850–1854. https://doi.org/10.1002/anie.201611740.

[22] M. Hart, E.R. White, J. Chen, C.M. McGilvery, C.J. Pickard, A. Michaelides, A. Sella, M.S.P. Shaffer, C.G. Salzmann, Encapsulation and Polymerization of White Phosphorus Inside Single-Wall Carbon Nanotubes, Angew. Chemie - Int. Ed. 56 (2017) 8144–8148. https://doi.org/10.1002/anie.201703585.

[23] M. Hart, J. Chen, A. Michaelides, A. Sella, M.S.P. Shaffer, C.G. Salzmann, One-Dimensional Pnictogen Allotropes inside Single-Wall Carbon Nanotubes, Inorg. Chem. 58 (2019) 15216–15224. https://doi.org/10.1021/acs.inorgchem.9b02190.

[24] P.W. Bridgman, Two new modifications of phosphorus, J. Am. Chem. Soc. 36 (1914) 1344–1363. https://doi.org/10.1021/ja02184a002.

[25] H. Krebs, H. Weitz, H. Worms, Z. Anorg. Allgem. Chem. 280 (1955) 119.

[26] H. Krebs, H. Majewski, Black Phosphorus, in : Inorganic Syntheses, 7, 60-62. https://doi.org/10.1002/9780470132388.ch16.

[27] A. Brown, S. Rundqvist, Refinement of the crystal structure of black phosphorus, Acta Crystallogr. 19 (1965) 684–685. https://doi.org/10.1107/s0365110x65004140.

[28] S. Lange, P. Schmidt, T. Nilges, Au_3SnP_7@Black Phosphorus: An easy access to black phosphorus, Inorg. Chem. 46 (2007) 4028–4035. https://doi.org/10.1021/ic062192q.

[29] T. Nilges, M. Kersting, T. Pfeifer, A fast low-pressure transport route to large black phosphorus single crystals, J. Solid State Chem. 181 (2008) 1707–1711. https://doi.org/10.1016/j.jssc.2008.03.008.

[30] M. Köpf, N. Eckstein, D. Pfister, C. Grotz, I. Krüger, M. Greiwe, T. Hansen, H. Kohlmann, T. Nilges, Access and in situ growth of phosphorene-precursor black phosphorus, J. Cryst. Growth. 405 (2014) 6–10. https://doi.org/10.1016/j.jcrysgro.2014.07.029.

[31] Z. Zhang, D.H. Xing, J. Li, Q. Yan, Hittorf's phosphorus: the missing link during transformation of red phosphorus to black phosphorus, CrystEngComm. 19 (2017) 905–909. https://doi.org/10.1039/c6ce02550a.

[32] M. Zhao, X. Niu, L. Guan, H. Qian, W. Wang, J. Sha, Y. Wang, Understanding the growth of black phosphorus crystals, CrystEngComm. 18 (2016) 7737–7744. https://doi.org/10.1039/c6ce01608a.

[33] Z. Zhu, D. Tománek, Semiconducting layered blue phosphorus: A computational study, Phys. Rev. Lett. 112 (2014) 176802. https://doi.org/10.1103/PhysRevLett.112.176802.

[34] L. Tao, E. Cinquanta, D. Chiappe, C. Grazianetti, M. Fanciulli, M. Dubey, A. Molle, D. Akinwande, Silicene field-effect transistors operating at room temperature, Nat. Nanotechnol. 10 (2015) 227–231. https://doi.org/10.1038/nnano.2014.325.

[35] F. Reis, G. Li, L. Dudy, M. Bauernfeind, S. Glass, W. Hanke, R. Thomale, Bismuthene on a SiC substrate :, Science. 357 (2017) 287–290.

[36] J.L. Zhang, S. Zhao, C. Han, Z. Wang, S. Zhong, S. Sun, R. Guo, X. Zhou, C.D. Gu, K. Di Yuan, Z. Li, W. Chen, Epitaxial Growth of Single Layer Blue Phosphorus: A New Phase of Two-Dimensional Phosphorus, Nano Lett. 16 (2016) 4903–4908. https://doi.org/10.1021/acs.nanolett.6b01459.

[37] J.L. Zhang, S. Zhao, S. Sun, H. Ding, J. Hu, Y. Li, Q. Xu, X. Yu, M. Telychko, J. Su, C. Gu, Y. Zheng, X. Lian, Z. Ma, R. Guo, J. Lu, Z. Sun, J. Zhu, Z. Li, W. Chen, Synthesis of

Monolayer Blue Phosphorus Enabled by Silicon Intercalation, ACS Nano 14 (2020) 3687-3695. https://doi.org/10.1021/acsnano.0c00822.

[38] S. Zhao, J.L. Zhang, W. Chen, Z. Li, Structure of Blue Phosphorus Grown on Au(111) Surface Revisited, J. Phys. Chem. C. 124 (2020) 2024–2029. https://doi.org/10.1021/acs.jpcc.9b10511.

[39] A. Carvalho, M. Wang, X. Zhu, A.S. Rodin, H. Su, A.H. Castro Neto, Phosphorene: From theory to applications, Nat. Rev. Mater. 1 (2016) 16061. https://doi.org/10.1038/natrevmats.2016.61.

[40] L. Li, Y. Yu, G.J. Ye, Q. Ge, X. Ou, H. Wu, D. Feng, X.H. Chen, Y. Zhang, Black phosphorus field-effect transistors, Nat. Nanotechnol. 9 (2014) 372–377. https://doi.org/10.1038/nnano.2014.35.

[41] V. Tran, R. Soklaski, Y. Liang, L. Yang, Layer-controlled band gap and anisotropic excitons in few-layer black phosphorus, Phys. Rev. B - Condens. Matter Mater. Phys. 89 (2014) 235319. https://doi.org/10.1103/PhysRevB.89.235319.

[42] J. Qiao, X. Kong, Z.X. Hu, F. Yang, W. Ji, High-mobility transport anisotropy and linear dichroism in few-layer black phosphorus, Nat. Commun. 5 (2014) 4475. https://doi.org/10.1038/ncomms5475.

[43] G. Long, D. Maryenko, J. Shen, S. Xu, J. Hou, Z. Wu, W.K. Wong, T. Han, J. Lin, Y. Cai, R. Lortz, N. Wang, Achieving Ultrahigh Carrier Mobility in Two-Dimensional Hole Gas of Black Phosphorus, Nano Lett. 16 (2016) 7768–7773. https://doi.org/10.1021/acs.nanolett.6b03951.

[44] Q. Wei, X. Peng, Superior mechanical flexibility of phosphorene and few-layer black phosphorus, Appl. Phys. Lett. 104 (2014) 251915. https://doi.org/10.1063/1.4885215.

[45] Y. Du, J. Maassen, W. Wu, Z. Luo, X. Xu, P.D. Ye, Auxetic Black Phosphorus: A 2D Material with Negative Poisson's Ratio, Nano Lett. 16 (2016) 6701–6708. https://doi.org/10.1021/acs.nanolett.6b03607.

[46] J.W. Jiang, H.S. Park, Negative poisson's ratio in single-layer black phosphorus, Nat. Commun. 5 (2014) 4727. https://doi.org/10.1038/ncomms5727.

[47] J.W. Jiang, An empirical description for the hinge-like mechanism in single-layer black phosphorus: The angle–angle cross interaction, Acta Mech. Solida Sin. 30 (2017) 227–233. https://doi.org/10.1016/j.camss.2017.04.002.

[48] Z. Luo, J. Maassen, Y. Deng, Y. Du, R.P. Garrelts, M.S. Lundstrom, P.D. Ye, X. Xu, Anisotropic in-plane thermal conductivity observed in few-layer black phosphorus, Nat. Commun. 6 (2015) 8572. https://doi.org/10.1038/ncomms9572.

[49] S. Lee, F. Yang, J. Suh, S. Yang, Y. Lee, G. Li, H.S. Choe, A. Suslu, Y. Chen, C. Ko, J. Park, K. Liu, J. Li, K. Hippalgaonkar, J.J. Urban, S. Tongay, J. Wu, Anisotropic in-plane thermal conductivity of black phosphorus nanoribbons at temperatures higher than 100 K, Nat. Commun. 6 (2015) 8573. https://doi.org/10.1038/ncomms9573.

[50] G. Qin, Q.B. Yan, Z. Qin, S.Y. Yue, H.J. Cui, Q.R. Zheng, G. Su, Hinge-like structure induced unusual properties of black phosphorus and new strategies to improve the thermoelectric performance, Sci. Rep. 4 (2014) 6946. https://doi.org/10.1038/srep06946.

[51] Z. Cai, B. Liu, X. Zou, H.M. Cheng, Chemical Vapor Deposition Growth and Applications of Two-Dimensional Materials and Their Heterostructures, Chem. Rev. 118 (2018) 6091–6133. https://doi.org/10.1021/acs.chemrev.7b00536.

[52] L. Lin, B. Deng, J. Sun, H. Peng, Z. Liu, Bridging the Gap between Reality and Ideal in Chemical Vapor Deposition Growth of Graphene, Chem. Rev. 118 (2018) 9281–9343. https://doi.org/10.1021/acs.chemrev.8b00325.

[53] Y. Zhang, Y. Yao, M.G. Sendeku, L. Yin, X. Zhan, F. Wang, Z. Wang, J. He, Recent Progress in CVD Growth of 2D Transition Metal Dichalcogenides and Related Heterostructures, Adv.

Mater. 31 (2019) 1901694. https://doi.org/10.1002/adma.201901694.

[54] J.B. Smith, D. Hagaman, H.F. Ji, Growth of 2D black phosphorus film from chemical vapor deposition, Nanotechnology. 27 (2016) 215602. https://doi.org/10.1088/0957-4484/27/21/215602.

[55] X. Li, B. Deng, X. Wang, S. Chen, M. Vaisman, S.I. Karato, G. Pan, M.L. Lee, J. Cha, H. Wang, F. Xia, Synthesis of thin-film black phosphorus on a flexible substrate, 2D Mater. 2 (2015) 31002. https://doi.org/10.1088/2053-1583/2/3/031002.

[56] H. Liu, A.T. Neal, Z. Zhu, Z. Luo, X. Xu, D. Tománek, P.D. Ye, Phosphorene: An unexplored 2D semiconductor with a high hole mobility, ACS Nano. 8 (2014) 4033–4041. https://doi.org/10.1021/nn501226z.

[57] I.V.G. and A.A.F. K. S. Novoselov, A. K. Geim, S. V. Morozov, D. Jiang, Y. Zhang, S. V. Dubonos, Electric Field Effect in Atomically Thin Carbon Films, 306 (2004) 666–669.

[58] S. Liang, M.N. Hasan, J.H. Seo, Direct observation of raman spectra in black phosphorus under uniaxial strain conditions, Nanomaterials. 9 (2019) 1–8. https://doi.org/10.3390/nano9040566.

[59] A. Ciesielski, P. Samorì, Graphene via sonication assisted liquid-phase exfoliation, Chem. Soc. Rev. 43 (2014) 381–398. https://doi.org/10.1039/c3cs60217f.

[60] S. Yang, Y. Gong, J. Zhang, L. Zhan, L. Ma, Z. Fang, R. Vajtai, X. Wang, P.M. Ajayan, Exfoliated graphitic carbon nitride nanosheets as efficient catalysts for hydrogen evolution under visible light, Adv. Mater. 25 (2013) 2452–2456. https://doi.org/10.1002/adma.201204453.

[61] K. Synnatschke, P.A. Cieslik, A. Harvey, A. Castellanos-Gomez, T. Tian, C.J. Shih, A. Chernikov, E.J.G. Santos, J.N. Coleman, C. Backes, Length- And Thickness-Dependent Optical Response of Liquid-Exfoliated Transition Metal Dichalcogenides, Chem. Mater. 31 (2019) 10049–10062. https://doi.org/10.1021/acs.chemmater.9b02905.

[62] H. Ye, T. Lu, C. Xu, B. Han, N. Meng, L. Xu, Liquid-Phase Exfoliation of Hexagonal Boron Nitride into Boron Nitride Nanosheets in Common Organic Solvents with Hyperbranched Polyethylene as Stabilizer, Macromol. Chem. Phys. 219 (2018) 1700482. https://doi.org/10.1002/macp.201700482.

[63] J.R. Brent, N. Savjani, E.A. Lewis, S.J. Haigh, D.J. Lewis, P. O'Brien, Production of few-layer phosphorene by liquid exfoliation of black phosphorus, Chem. Commun. 50 (2014) 13338–13341. https://doi.org/10.1039/c4cc05752j.

[64] J. Kang, J.D. Wood, S.A. Wells, J.H. Lee, X. Liu, K.S. Chen, M.C. Hersam, Solvent exfoliation of electronic-grade, two-dimensional black phosphorus, ACS Nano. 9 (2015) 3596–3604. https://doi.org/10.1021/acsnano.5b01143.

[65] P. Yasaei, B. Kumar, T. Foroozan, C. Wang, M. Asadi, D. Tuschel, J.E. Indacochea, R.F. Klie, A. Salehi-Khojin, High-Quality Black Phosphorus Atomic Layers by Liquid-Phase Exfoliation, Adv. Mater. 27 (2015) 1887–1892. https://doi.org/10.1002/adma.201405150.

[66] J. Kang, S.A. Wells, J.D. Wood, J.H. Lee, X. Liu, C.R. Ryder, J. Zhu, J.R. Guest, C.A. Husko, M.C. Hersam, Stable aqueous dispersions of optically and electronically active phosphorene, Proc. Natl. Acad. Sci. U. S. A. 113 (2016) 11688–11693. https://doi.org/10.1073/pnas.1602215113.

[67] M. Serrano-Ruiz, M. Caporali, A. Ienco, V. Piazza, S. Heun, M. Peruzzini, The Role of Water in the Preparation and Stabilization of High-Quality Phosphorene Flakes, Adv. Mater. Interfaces. 3 (2016) 1500441. https://doi.org/10.1002/admi.201500441.

[68] D. Hanlon, C. Backes, E. Doherty, C.S. Cucinotta, N.C. Berner, C. Boland, K. Lee, A. Harvey, P. Lynch, Z. Gholamvand, S. Zhang, K. Wang, G. Moynihan, A. Pokle, Q.M. Ramasse, N. McEvoy, W.J. Blau, J. Wang, G. Abellan, F. Hauke, A. Hirsch, S. Sanvito, D.D. O'Regan, G.S. Duesberg, V. Nicolosi, J.N. Coleman, Liquid exfoliation of solvent-stabilized few-layer

black phosphorus for applications beyond electronics, Nat. Commun. 6 (2015) 8563. https://doi.org/10.1038/ncomms9563.

[69] C.X. Hu, Q. Xiao, Y.Y. Ren, M. Zhao, G.H. Dun, H.R. Wu, X.Y. Li, Q.Q. Yang, B. Sun, Y. Peng, F. Yan, Q. Wang, H.L. Zhang, Polymer Ionic Liquid Stabilized Black Phosphorus for Environmental Robust Flexible Optoelectronics, Adv. Funct. Mater. 28 (2018) 1805311. https://doi.org/10.1002/adfm.201805311.

[70] V. V. Chaban, E.E. Fileti, O. V. Prezhdo, Imidazolium Ionic Liquid Mediates Black Phosphorus Exfoliation while Preventing Phosphorene Decomposition, ACS Nano. 11 (2017) 6459–6466. https://doi.org/10.1021/acsnano.7b03074.

[71] W. Zhao, Z. Xue, J. Wang, J. Jiang, X. Zhao, T. Mu, Large-Scale, Highly Efficient, and Green Liquid-Exfoliation of Black Phosphorus in Ionic Liquids, ACS Appl. Mater. Interfaces. 7 (2015) 27608–27612. https://doi.org/10.1021/acsami.5b10734.

[72] S. Walia, S. Balendhran, T. Ahmed, M. Singh, C. El-Badawi, M.D. Brennan, P. Weerathunge, M.N. Karim, F. Rahman, A. Rassell, J. Duckworth, R. Ramanathan, G.E. Collis, C.J. Lobo, M. Toth, J.C. Kotsakidis, B. Weber, M. Fuhrer, J.M. Dominguez-Vera, M.J.S. Spencer, I. Aharonovich, S. Sriram, M. Bhaskaran, V. Bansal, Ambient Protection of Few-Layer Black Phosphorus via Sequestration of Reactive Oxygen Species, Adv. Mater. 29 (2017) 1700152. https://doi.org/10.1002/adma.201700152.

[73] M. Bat-Erdene, M. Batmunkh, C.J. Shearer, S.A. Tawfik, M.J. Ford, L. Yu, A.J. Sibley, A.D. Slattery, J.S. Quinton, C.T. Gibson, J.G. Shapter, Efficient and fast synthesis of few-layer black phosphorus via microwave-assisted liquid-phase exfoliation, Small Methods. 1 (2017) 1700260. https://doi.org/10.1002/smtd.201700260.

[74] Z. Yan, X. He, L. She, J. Sun, R. Jiang, H. Xu, F. Shi, Z. Lei, Z.H. Liu, Solvothermal-assisted liquid-phase exfoliation of large size and high quality black phosphorus, J. Mater. 4 (2018) 129–134. https://doi.org/10.1016/j.jmat.2018.01.003.

[75] M.B. Erande, M.S. Pawar, D.J. Late, Humidity Sensing and Photodetection Behavior of Electrochemically Exfoliated Atomically Thin-Layered Black Phosphorus Nanosheets, ACS Appl. Mater. Interfaces. 8 (2016) 11548–11556. https://doi.org/10.1021/acsami.5b10247.

[76] A. Ambrosi, Z. Sofer, M. Pumera, Electrochemical Exfoliation of Layered Black Phosphorus into Phosphorene, Angew. Chemie - Int. Ed. 56 (2017) 10443–10445. https://doi.org/10.1002/anie.201705071.

[77] C.C. Mayorga-Martinez, N. Mohamad Latiff, A.Y.S. Eng, Z. Sofer, M. Pumera, Black Phosphorus Nanoparticle Labels for Immunoassays via Hydrogen Evolution Reaction Mediation, Anal. Chem. 88 (2016) 10074–10079. https://doi.org/10.1021/acs.analchem.6b02422.

[78] F. Luo, D. Wang, J. Zhang, X. Li, D. Liu, H. Li, M. Lu, X. Xie, L. Huang, W. Huang, Ultrafast Cathodic Exfoliation of Few-Layer Black Phosphorus in Aqueous Solution, ACS Appl. Nano Mater. 2 (2019) 3793–3801. https://doi.org/10.1021/acsanm.9b00667.

[79] R. Gui, H. Jin, Z. Wang, J. Li, Black phosphorus quantum dots: Synthesis, properties, functionalized modification and applications, Chem. Soc. Rev. 47 (2018) 6795–6823. https://doi.org/10.1039/c8cs00387d.

[80] Z. Sun, H. Xie, S. Tang, X.F. Yu, Z. Guo, J. Shao, H. Zhang, H. Huang, H. Wang, P.K. Chu, Ultrasmall Black Phosphorus Quantum Dots: Synthesis and Use as Photothermal Agents, Angew. Chemie - Int. Ed. 54 (2015) 11526–11530. https://doi.org/10.1002/anie.201506154.

[81] X. Zhang, H. Xie, Z. Liu, C. Tan, Z. Luo, H. Li, J. Lin, L. Sun, W. Chen, Z. Xu, L. Xie, W. Huang, H. Zhang, Black phosphorus quantum dots, Angew. Chemie - Int. Ed. 54 (2015) 3653–3657. https://doi.org/10.1002/anie.201409400.

[82] W. Gu, X. Pei, Y. Cheng, C. Zhang, J. Zhang, Y. Yan, C. Ding, Y. Xian, Black Phosphorus

Quantum Dots as the Ratiometric Fluorescence Probe for Trace Mercury Ion Detection Based on Inner Filter Effect, ACS Sensors. 2 (2017) 576–582. https://doi.org/10.1021/acssensors.7b00102.

[83] Y. Xu, Z. Wang, Z. Guo, H. Huang, Q. Xiao, H. Zhang, X.F. Yu, Solvothermal Synthesis and Ultrafast Photonics of Black Phosphorus Quantum Dots, Adv. Opt. Mater. 4 (2016) 1223–1229. https://doi.org/10.1002/adom.201600214.

[84] Z. Guo, H. Zhang, S. Lu, Z. Wang, S. Tang, J. Shao, Z. Sun, H. Xie, H. Wang, X.F. Yu, P.K. Chu, From Black Phosphorus to Phosphorene: Basic Solvent Exfoliation, Evolution of Raman Scattering, and Applications to Ultrafast Photonics, Adv. Funct. Mater. 25 (2015) 6996–7002. https://doi.org/10.1002/adfm.201502902.

[85] A. Castellanos-Gomez, L. Vicarelli, E. Prada, J.O. Island, K.L. Narasimha-Acharya, S.I. Blanter, D.J. Groenendijk, M. Buscema, G.A. Steele, J. V. Alvarez, H.W. Zandbergen, J.J. Palacios, H.S.J. Van Der Zant, Isolation and characterization of few-layer black phosphorus, 2D Mater. 1 (2014) 025001. https://doi.org/10.1088/2053-1583/1/2/025001.

[86] R.J. Wu, M. Topsakal, T. Low, M.C. Robbins, N. Haratipour, J.S. Jeong, R.M. Wentzcovitch, S.J. Koester, K.A. Mkhoyan, Atomic and electronic structure of exfoliated black phosphorus, J. Vac. Sci. Technol. A Vacuum, Surfaces, Film. 33 (2015) 060604. https://doi.org/10.1116/1.4926753.

[87] T. Ahmed, S. Balendhran, M.N. Karim, E.L.H. Mayes, M.R. Field, R. Ramanathan, M. Singh, V. Bansal, S. Sriram, M. Bhaskaran, S. Walia, Degradation of black phosphorus is contingent on UV–blue light exposure, Npj 2D Mater. Appl. 1 (2017) 1–7. https://doi.org/10.1038/s41699-017-0023-5.

[88] D. Wang, P. Yi, L. Wang, L. Zhang, H. Li, M. Lu, X. Xie, L. Huang, W. Huang, Revisiting the growth of black phosphorus in Sn-I assisted reactions, Front. Chem. 7 (2019) 21. https://doi.org/10.3389/fchem.2019.00021.

[89] H.B. Ribeiro, C.E.P. Villegas, D.A. Bahamon, D. Muraca, A.H. Castro Neto, E.A.T. De Souza, A.R. Rocha, M.A. Pimenta, C.J.S. De Matos, Edge phonons in black phosphorus, Nat. Commun. 7 (2016) 12191. https://doi.org/10.1038/ncomms12191.

[90] X. Ling, L. Liang, S. Huang, A.A. Puretzky, D.B. Geohegan, B.G. Sumpter, J. Kong, V. Meunier, M.S. Dresselhaus, Low-Frequency Interlayer Breathing Modes in Few-Layer Black Phosphorus, Nano Lett. 15 (2015) 4080–4088. https://doi.org/10.1021/acs.nanolett.5b01117.

[91] J. Kim, J.U. Lee, J. Lee, H.J. Park, Z. Lee, C. Lee, H. Cheong, Anomalous polarization dependence of Raman scattering and crystallographic orientation of black phosphorus, Nanoscale. 7 (2015) 18708–18715. https://doi.org/10.1039/c5nr04349b.

[92] J. Wu, N. Mao, L. Xie, H. Xu, J. Zhang, Identifying the crystalline orientation of black phosphorus using angle-resolved polarized Raman spectroscopy, Angew. Chemie - Int. Ed. 54 (2015) 2366–2369. https://doi.org/10.1002/anie.201410108.

[93] M. Van Druenen, F. Davitt, T. Collins, C. Glynn, C. O'Dwyer, J.D. Holmes, G. Collins, Evaluating the Surface Chemistry of Black Phosphorus during Ambient Degradation, Langmuir. 35 (2019) 2172–2178. https://doi.org/10.1021/acs.langmuir.8b04190.

[94] F. Martini, S. Borsacchi, G. Barcaro, M. Caporali, M. Vanni, M. Serrano-Ruiz, M. Geppi, M. Peruzzini, L. Calucci, Phosphorene and black phosphorus: The 31P NMR View, J. Phys. Chem. Lett. 10 (2019) 5122–5127. https://doi.org/10.1021/acs.jpclett.9b01788.

[95] S. Wu, F. He, G. Xie, Z. Bian, J. Luo, S. Wen, Black Phosphorus: Degradation Favors Lubrication, Nano Lett. 18 (2018) 5618–5627. https://doi.org/10.1021/acs.nanolett.8b02092.

[96] J.O. Island, G.A. Steele, H.S.J. Van Der Zant, A. Castellanos-Gomez, Environmental instability of few-layer black phosphorus, 2D Mater. 2 (2015) 011002. https://doi.org/10.1088/2053-1583/2/1/011002.

[97] A. Favron, E. Gaufrès, F. Fossard, A.L. Phaneuf-Laheureux, N.Y.W. Tang, P.L. Lévesque, A. Loiseau, R. Leonelli, S. Francoeur, R. Martel, Photooxidation and quantum confinement effects in exfoliated black phosphorus, Nat. Mater. 14 (2015) 826–832. https://doi.org/10.1038/nmat4299.

[98] J. Plutnar, Z. Sofer, M. Pumera, Products of degradation of black phosphorus in protic solvents, ACS Nano. 12 (2018) 8390–8396. https://doi.org/10.1021/acsnano.8b03740.

[99] S. Zhang, X. Zhang, L. Lei, X.F. Yu, J. Chen, C. Ma, F. Wu, Q. Zhao, B. Xing, pH-Dependent Degradation of Layered Black Phosphorus: Essential Role of Hydroxide Ions, Angew. Chemie - Int. Ed. 58 (2019) 467–471. https://doi.org/10.1002/anie.201809989.

[100] W. Luo, D.Y. Zemlyanov, C.A. Milligan, Y. Du, L. Yang, Y. Wu, P.D. Ye, Surface chemistry of black phosphorus under a controlled oxidative environment, Nanotechnology. 27 (2016) 4033-4041. https://doi.org/10.1088/0957-4484/27/43/434002.

[101] M.T. Edmonds, A. Tadich, A. Carvalho, A. Ziletti, K.M. O'Donnell, S.P. Koenig, D.F. Coker, B. Özyilmaz, A.H.C. Neto, M.S. Fuhrer, Creating a stable oxide at the surface of black phosphorus, ACS Appl. Mater. Interfaces. 7 (2015) 14557–14562. https://doi.org/10.1021/acsami.5b01297.

[102] Y. Huang, J. Qiao, K. He, S. Bliznakov, E. Sutter, X. Chen, D. Luo, F. Meng, D. Su, J. Decker, W. Ji, R.S. Ruoff, P. Sutter, Interaction of black phosphorus with oxygen and water, Chem. Mater. 28 (2016) 8330–8339. https://doi.org/10.1021/acs.chemmater.6b03592.

[103] A. Ziletti, A. Carvalho, D.K. Campbell, D.F. Coker, A.H. Castro Neto, Oxygen defects in phosphorene, Phys. Rev. Lett. 114 (2015) 26–29. https://doi.org/10.1103/PhysRevLett.114.046801.

[104] Q. Zhou, Q. Chen, Y. Tong, J. Wang, Light-Induced Ambient Degradation of Few-Layer Black Phosphorus: Mechanism and Protection, Angew. Chemie - Int. Ed. 55 (2016) 11437–11441. https://doi.org/10.1002/anie.201605168.

[105] H. Zhu, S. McDonnell, X. Qin, A. Azcatl, L. Cheng, R. Addou, J. Kim, P.D. Ye, R.M. Wallace, Al_2O_3 on Black Phosphorus by Atomic Layer Deposition: An in Situ Interface Study, ACS Appl. Mater. Interfaces. 7 (2015) 13038–13043. https://doi.org/10.1021/acsami.5b03192.

[106] B. Wan, B. Yang, Y. Wang, J. Zhang, Z. Zeng, Z. Liu, W. Wang, Enhanced stability of black phosphorus field-effect transistors with SiO_2 passivation, Nanotechnology. 26 (2015) 435702. https://doi.org/10.1088/0957-4484/26/43/435702.

[107] B. Xing, L. Guan, Y. Yu, X. Niu, X. Yan, S. Zhang, J. Yao, D. Wang, J. Sha, Y. Wang, HfO_2-passivated black phosphorus field effect transistor with long-termed stability and enhanced current on/off ratio, Nanotechnology. 30 (2019) 345208. https://doi.org/10.1088/1361-6528/ab1ffe.

[108] J.S. Kim, Y. Liu, W. Zhu, S. Kim, D. Wu, L. Tao, A. Dodabalapur, K. Lai, D. Akinwande, Toward air-stable multilayer phosphorene thin-films and transistors, Sci. Rep. 5 (2015) 8989. https://doi.org/10.1038/srep08989.

[109] J.D. Wood, S.A. Wells, D. Jariwala, K.S. Chen, E. Cho, V.K. Sangwan, X. Liu, L.J. Lauhon, T.J. Marks, M.C. Hersam, Effective passivation of exfoliated black phosphorus transistors against ambient degradation, Nano Lett. 14 (2014) 6964–6970. https://doi.org/10.1021/nl5032293.

[110] J. Na, Y.T. Lee, J.A. Lim, D.K. Hwang, G. Kim, W.K. Choi, Y. Song, I. Control, F. Convergence, S. Korea, E. Engineering, S. Korea, Few-Layer Black Phosphorus Field-E ff ect Transistors with, ACS Nano. (2014) 11753–11762.

[111] R. Frisenda, E. Navarro-Moratalla, P. Gant, D. Pérez De Lara, P. Jarillo-Herrero, R. V. Gorbachev, A. Castellanos-Gomez, Recent progress in the assembly of nanodevices and van der Waals heterostructures by deterministic placement of 2D materials, Chem. Soc. Rev. 47

(2018) 53–68. https://doi.org/10.1039/c7cs00556c.

[112] R.A. Doganov, E.C.T. O'Farrell, S.P. Koenig, Y. Yeo, A. Ziletti, A. Carvalho, D.K. Campbell, D.F. Coker, K. Watanabe, T. Taniguchi, A.H.C. Neto, B. Özyilmaz, Transport properties of pristine few-layer black phosphorus by van der Waals passivation in an inert atmosphere, Nat. Commun. 6 (2015) 6647. https://doi.org/10.1038/ncomms7647.

[113] A. Avsar, I.J. Vera-Marun, J.Y. Tan, K. Watanabe, T. Taniguchi, A.H. Castro Neto, B. Özyilmaz, Air-stable transport in graphene-contacted, fully encapsulated ultrathin black phosphorus-based field-effect transistors, ACS Nano. 9 (2015) 4138–4145. https://doi.org/10.1021/acsnano.5b00289.

[114] V. Artel, Q. Guo, H. Cohen, R. Gasper, A. Ramasubramaniam, F. Xia, D. Naveh, Protective molecular passivation of black phosphorus, Npj 2D Mater. Appl. 1 (2017) 6. https://doi.org/10.1038/s41699-017-0004-8.

[115] G. Abellán, S. Wild, V. Lloret, N. Scheuschner, R. Gillen, U. Mundloch, J. Maultzsch, M. Varela, F. Hauke, A. Hirsch, Fundamental Insights into the Degradation and Stabilization of Thin Layer Black Phosphorus, J. Am. Chem. Soc. 139 (2017) 10432–10440. https://doi.org/10.1021/jacs.7b04971.

[116] V. Lloret, M.Á. Rivero-crespo, J.A. Vidal-moya, S. Wild, A. Doménech-carbó, B.S.J. Heller, S. Shin, H. Steinrück, F. Maier, F. Hauke, M. Varela, A. Hirsch, A. Leyva-pérez, G. Abellán, Few Layer 2D Pnictogens Catalyze the Alkylation of Soft Nucleophiles With Esters, Nat. Commun. (2019) 509. http://dx.doi.org/10.1038/s41467-018-08063-3.

[117] M. Tejeda-Serrano, V. Lloret, B.G. Márkus, F. Simon, F. Hauke, A. Hirsch, A. Doménech-Carbó, G. Abellán, A. Leyva-Pérez, Few-layer Black Phosphorous Catalyzes Radical Additions to Alkenes Faster than Low-valence Metals, ChemCatChem. 12 (2020) 2226–2232. https://doi.org/10.1002/cctc.201902276.

[118] J. Plutnar, Z. Sofer, M. Pumera, Layered black phosphorus as a reducing agent-decoration with group 10 elements, RSC Adv. 10 (2020) 36452–36458. https://doi.org/10.1039/d0ra06884e.

[119] F. Shi, Z. Geng, K. Huang, Q. Liang, Y. Zhang, Y. Sun, J. Cao, S. Feng, Cobalt Nanoparticles / Black Phosphorus Nanosheets : An Efficient Catalyst for Electrochemical Oxygen Evolution, 1800575 (2018). https://doi.org/10.1002/advs.201800575.

[120] M. Caporali, M. Serrano-ruiz, F. Telesio, S. Heun, G. Nicotra, C. Spinella, M. Peruzzini, Decoration of exfoliated black phosphorus with nickel nanoparticles and its application in catalysis, Chem. Commun. 53 (2017) 10946–10949. https://doi.org/10.1039/c7cc05906j.

[121] L. Bai, X. Wang, S. Tang, Y. Kang, J. Wang, Y. Yu, Z. Zhou, C. Ma, X. Zhang, J. Jiang, P.K. Chu, X. Yu, Black Phosphorus / Platinum Heterostructure : A Highly Efficient Photocatalyst for Solar-Driven Chemical Reactions, 30 (2018) 1803641. https://doi.org/10.1002/adma.201803641.

[122] Y. Peng, B. Lu, N. Wang, J.E. Lu, C. Li, Y. Ping, S. Chen, Oxygen Reduction Reaction Catalyzed by Black-Phosphorus-Supported Metal Nanoparticles: Impacts of Interfacial Charge Transfer, ACS Appl. Mater. Interfaces. 11 (2019) 24707–24714. https://doi.org/10.1021/acsami.9b05471.

[123] W. Lei, T. Zhang, P. Liu, G. Liu, M. Liu, Bandgap- and Local Field-Dependent Photoactivity of Ag/Black Phosphorus Nanohybrids, 6 (2016) 8009-8020. https://doi.org/10.1021/acscatal.6b02520.

[124] H. Huang, Q. Xiao, J. Wang, X. Yu, H. Wang, H. Zhang, Black phosphorus : a two-dimensional reductant for in situ nanofabrication, Npj 2D Mater. Appl. (2017) 20. https://doi.org/10.1038/s41699-017-0022-6.

[125] S. Cho, H. Koh, H. Yoo, H. Jung, Tunable Chemical Sensing Performance of Black Phosphorus by Controlled Functionalization with Noble Metals, Chem. Mater., 17 (2017)

7197-7205. https://doi.org/10.1021/acs.chemmater.7b01353.

[126] Q. Wu, M. Liang, S. Zhang, X. Liu, F. Wang, Development of functional black phosphorus nanosheets with remarkable catalytic and antibacterial performance, Nanoscale. 10 (2018) 10428–10435. https://doi.org/10.1039/c8nr01715h.

[127] J. Ouyang, L. Deng, W. Chen, J. Sheng, Z. Liu, L. Wang, Y.N. Liu, Two dimensional semiconductors for ultrasound-mediated cancer therapy: The case of black phosphorus nanosheets, Chem. Commun. 54 (2018) 2874–2877. https://doi.org/10.1039/c8cc00392k.

[128] G. Abellán, P. Ares, S. Wild, E. Nuin, C. Neiss, D.R.-S. Miguel, P. Segovia, C. Gibaja, E.G. Michel, A. Görling, F. Hauke, J. Gómez-Herrero, A. Hirsch, F. Zamora, Noncovalent Functionalization and Charge Transfer in Antimonene, Angew. Chemie. 129 (2017) 14581–14586. https://doi.org/10.1002/ange.201702983.

[129] G. Abellán, V. Lloret, U. Mundloch, M. Marcia, C. Neiss, A. Görling, M. Varela, F. Hauke, A. Hirsch, Noncovalent Functionalization of Black Phosphorus, Angew. Chemie - Int. Ed. 55 (2016) 14557–14562. https://doi.org/10.1002/anie.201604784.

[130] R. Gusmão, Z. Sofer, M. Pumera, Functional Protection of Exfoliated Black Phosphorus by Noncovalent Modification with Anthraquinone, ACS Nano. 12 (2018) 5666–5673. https://doi.org/10.1021/acsnano.8b01474.

[131] M. Bolognesi, S. Moschetto, M. Trapani, F. Prescimone, C. Ferroni, G. Manca, A. Ienco, S. Borsacchi, M. Caporali, M. Muccini, M. Peruzzini, M. Serrano-Ruiz, L. Calucci, M.A. Castriciano, S. Toffanin, Noncovalent Functionalization of 2D Black Phosphorus with Fluorescent Boronic Derivatives of Pyrene for Probing and Modulating the Interaction with Molecular Oxygen, ACS Appl. Mater. Interfaces. 11 (2019) 22637–22647. https://doi.org/10.1021/acsami.9b04344.

[132] C.R. Ryder, J.D. Wood, S.A. Wells, Y. Yang, D. Jariwala, T.J. Marks, G.C. Schatz, M.C. Hersam, Covalent functionalization and passivation of exfoliated black phosphorus via aryl diazonium chemistry, Nat. Chem. 8 (2016) 597–602. https://doi.org/10.1038/nchem.2505.

[133] G.L.C. Paulus, Q.H. Wang, M.S. Strano, Covalent electron transfer chemistry of graphene with diazonium salts, Acc. Chem. Res. 46 (2013) 160–170. https://doi.org/10.1021/ar300119z.

[134] A. Sinitskii, A. Dimiev, D.A. Corley, A.A. Fursina, D. V. Kosynkin, J.M. Tour, Kinetics of diazonium functionalization of chemically converted graphene nanoribbons, ACS Nano. 4 (2010) 1949–1954. https://doi.org/10.1021/nn901899j.

[135] J.L. Bahr, J. Yang, D. V. Kosynkin, M.J. Bronikowski, R.E. Smalley, J.M. Tour, Functionalization of carbon nanotubes by electrochemical reduction of aryl diazonium salts: A bucky paper electrode, J. Am. Chem. Soc. 123 (2001) 6536–6542. https://doi.org/10.1021/ja010462s.

[136] Y. Zhao, L. Tong, Z. Li, N. Yang, H. Fu, L. Wu, H. Cui, W. Zhou, J. Wang, H. Wang, P.K. Chu, X.F. Yu, Stable and Multifunctional Dye-Modified Black Phosphorus Nanosheets for Near-Infrared Imaging-Guided Photothermal Therapy, Chem. Mater. 29 (2017) 7131–7139. https://doi.org/10.1021/acs.chemmater.7b01106.

[137] Y. Cao, X. Tian, J. Gu, B. Liu, B. Zhang, S. Song, F. Fan, Y. Chen, Covalent Functionalization of Black Phosphorus with Conjugated Polymer for Information Storage, Angew. Chemie - Int. Ed. 57 (2018) 4543–4548. https://doi.org/10.1002/anie.201712675.

[138] M. Gu, B. Zhang, B. Liu, Q. Che, Z. Zhao, Y. Chen, Solution-processable black phosphorus nanosheets covalently modified with polyacrylonitrile for nonvolatile resistive random access memory, J. Mater. Chem. C. 8 (2020) 1231–1238. https://doi.org/10.1039/c9tc06007c.

[139] M. Van Druenen, F. Davitt, T. Collins, C. Glynn, C. O'Dwyer, J.D. Holmes, G. Collins, Covalent Functionalization of Few-Layer Black Phosphorus Using Iodonium Salts and Comparison to Diazonium Modified Black Phosphorus, Chem. Mater. 30 (2018) 4667–4674.

https://doi.org/10.1021/acs.chemmater.8b01306.

[140] A.A. Mitrović, S. Wild, V. Lloret, M. Assebban, B. Márkus, F. Simon, F. Hauke, G. Abellán, A. Hirsch, Interface amorphization of two-dimensional black phosphorus upon treatment with diazonium salts, (2020). https://doi.org/10.1002/chem.202003584.

[141] Y. Liu, P. Gao, T. Zhang, X. Zhu, M. Zhang, M. Chen, P. Du, G.W. Wang, H. Ji, J. Yang, S. Yang, Azide Passivation of Black Phosphorus Nanosheets: Covalent Functionalization Affords Ambient Stability Enhancement, Angew. Chemie - Int. Ed. 58 (2019) 1479–1483. https://doi.org/10.1002/anie.201813218.

[142] Z. Sofer, J. Luxa, D. Bouša, D. Sedmidubský, P. Lazar, T. Hartman, H. Hardtdegen, M. Pumera, The Covalent Functionalization of Layered Black Phosphorus by Nucleophilic Reagents, Angew. Chemie - Int. Ed. 56 (2017) 9891–9896. https://doi.org/10.1002/anie.201705722.

[143] S. Wild, M. Fickert, A. Mitrovic, V. Lloret, C. Neiss, J.A. Vidal- Moya, M.Á. Rivero-Crespo, A. Leyva-Pérez, K. Werbach, H. Peterlik, M. Grabau, H. Wittkämper, C. Papp, H.P. Steinrück, T. Pichler, A. Görling, F. Hauke, G. Abellán, A. Hirsch, Lattice opening upon bulk reductive covalent functionalization of black phosphorus, ArXiv. (2019).

[144] S. Wild, X.T. Dinh, H. Maid, F. Hauke, G. Abellán, A. Hirsch, Quantifying the Covalent Functionalization of Black Phosphorus, Angew. Chemie - Int. Ed. 59 (2020) 20230–20234. https://doi.org/10.1002/anie.202008646.

[145] G. Abell, C. Neiss, V. Lloret, S. Wild, J.C. Chac, K. Werbach, F. Fedi, H. Shiozawa, A. Gçrling, H. Peterlik, T. Pichler, F. Hauke, A. Hirsch, Exploring the Formation of Black Phosphorus Intercalation Compounds with Alkali Metals Angewandte, 2 (2017) 15267–15273. https://doi.org/10.1002/anie.201707462.

[146] X. Zhu, T. Zhang, Z. Sun, H. Chen, J. Guan, X. Chen, H. Ji, P. Du, S. Yang, Black Phosphorus Revisited: A Missing Metal-Free Elemental Photocatalyst for Visible Light Hydrogen Evolution, Adv. Mater. 29 (2017) 1605776. https://doi.org/10.1002/adma.201605776.

[147] L. Shao, H. Sun, L. Miao, X. Chen, M. Han, J. Sun, S. Liu, L. Li, F. Cheng, J. Chen, Facile preparation of NH_2-functionalized black phosphorene for the electrocatalytic hydrogen evolution reaction, J. Mater. Chem. A. 6 (2018) 2494–2499. https://doi.org/10.1039/c7ta10884b.

[148] X. Zhu, T. Zhang, D. Jiang, H. Duan, Z. Sun, M. Zhang, H. Jin, R. Guan, Y. Liu, M. Chen, H. Ji, P. Du, W. Yan, S. Wei, Y. Lu, S. Yang, Stabilizing black phosphorus nanosheets via edge-selective bonding of sacrificial C_{60} molecules, Nat. Commun. 9 (2018) 4177. https://doi.org/10.1038/s41467-018-06437-1.

[149] C.M. Hoidn, D.J. Scott, R. Wolf, Transition Metal-Mediated Functionalization of White Phosphorus, Chem. – A Eur. J. 26 (2020). https://doi.org/10.1002/chem.202001854.

[150] A. Ienco, G. Manca, M. Peruzzini, C. Mealli, Modelling strategies for the covalent functionalization of 2D phosphorene, Dalt. Trans. 47 (2018) 17243–17256. https://doi.org/10.1039/C8DT03628D.

[151] Y. Zhao, H. Wang, H. Huang, Q. Xiao, Y. Xu, Z. Guo, H. Xie, J. Shao, Z. Sun, W. Han, X.F. Yu, P. Li, P.K. Chu, Surface Coordination of Black Phosphorus for Robust Air and Water Stability, Angew. Chemie - Int. Ed. 55 (2016) 5003–5007. https://doi.org/10.1002/anie.201512038.

[152] L. Wu, J. Wang, J. Lu, D. Liu, N. Yang, H. Huang, P.K. Chu, X.F. Yu, Lanthanide-Coordinated Black Phosphorus, Small. 14 (2018) 1801405. https://doi.org/10.1002/smll.201801405.

Chapter II

Pd/BP nanohybrid: unravelling the nature of Pd–P interaction and application in selective hydrogenation

2.1 Introduction

The variety of M(0)/BP systems described in Chapter 1 of this thesis demonstrate the efficiency of 2D BP as support to grow M(0) NPs, and the broad scope of the resulting nanohybrids in catalysis. However, the nature of the interaction between phosphorus atoms and metal nanostructures was scarcely addressed. Evidence of M–P interaction was provided by P 2p XPS measurements and DFT calculations were carried out on one Ag/BP system taking into account a simplified model (see Section 1.4.2). Nonetheless, a detailed experimental investigation of structural character has never been performed on M/BP. The sp^3 nature of phosphorus atoms in BP stimulates the comparison with molecular compounds like phosphines, which can behave as strong and effective ligands toward the surface of M NPs. The question arises to which extent this comparison is correct and whether 2D BP can itself play the role of an extended polydentate ligand toward metal NPs. As Pd NPs have never been grown on bare 2D BP, the only related systems being the ternary nanocomposites Pd-BP-TiO_2 and Pd-BP-rGO [1,2], a new Pd/BP nanohybrid was prepared with an *in situ* reduction process, using molecular H_2 as reducing agent and $Pd(NO_3)_2 \cdot 2H_2O$ as Pd(II) precursor. Then, to answer the above questions, an extensive characterization was carried out on Pd/BP to shed light on the interaction between phosphorus and metal. Furthermore, the new Pd/BP nanohybrid was then tested as heterogeneous catalyst in the selective batch hydrogenation of chloronitrobenzene to chloroaniline.

2.2 Materials synthesis and characterization

2.2.1 Preparation of 2D BP

Bulk BP crystals were prepared following the literature method reported by T. Nilges *et al.* [3] and described in Section 1.1.4, which allows to prepare BP via chemical vapour transport (CVT), starting from red phosphorus as P-source and Sn/SnI_4 as mineralizing agents. The synthetic procedure is depicted in Figure 47a.

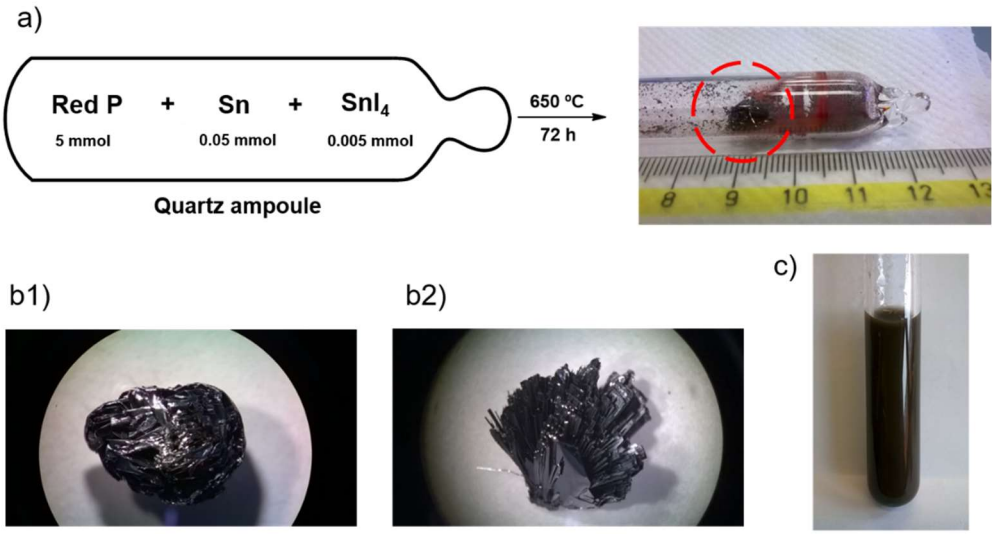

Figure 47. Synthesis and LPE of BP. a) CVT synthesis of BP. The black solid highlighted in the circle corresponds to BP; the red residue on the inner walls of the ampoule is unreacted red phosphorus. b1,2) BP crystalline aggregates obtained by the procedure in (a). c) Exfoliated BP suspended in DMSO (1 mg/mL) obtained after ultrasonication.

Liquid phase exfoliation (LPE) of BP was carried out in dry DMSO (H_2O < 30 ppm), working on a 5 mg batch scale, following a literature method with minor modifications (see also Section 1.2.2) [4]. BP crystals and deoxygenated DMSO (BP/DMSO = 1 mg/mL) were transferred inside a borosilicate glass tube (length = 300 mm, outer diameter = 15 mm; inner diameter = 11.3 mm), then a controlled amount of deoxygenated water was added (keeping the ratio 0.8 < P/H_2O < 1.2) and the ampoule was sealed under inert atmosphere. The ampoule was dipped inside an ultrasonic bath (37 kHz, 80% power) and sonicated over 6 days at 30°C. After this time, a dark brownish dispersion was obtained (see Figure 47c). As probed via AFM and TEM analysis, the resulting flakes have lateral dimensions within the range 300-900 nm and average thickness below 30 nm. Prior to functionalization, the exfoliated material was washed to eliminate DMSO. In detail, the suspension resulting from sonochemical exfoliation (5 mg/5 mL_{DMSO}) was centrifuged at 9500 rpm for 30 minutes to isolate 2D BP as a solid residue (the supernatant was discarded). The collected solid was resuspended in deaerated ethanol using ultrasounds (5 min), before being recovered after centrifugation. This washing cycle was repeated 3 times in total.

2.2.2 Preparation of Pd/BP

2D BP was suspended in degassed THF to have a suspension containing about 1.0 mg/mL. 1.5 mL of this suspension (1.5 mg of BP, 0.048 mmol) were transferred to a glass vial equipped with a stirring bar and put inside a Schlenk tube. Under stirring, 0.75 mL of degassed ethanol were added, followed by 1.3 mL of an aqueous solution of $Pd(NO_3)_2 \cdot 2H_2O$ (3.75 mM, 0.00487 mmol, molar ratio P : Pd = 10). The vial was transferred in an autoclave, pressurized with 5 bar of H_2 and kept on a stirring plate at room temperature for 1 hour. After this time, the autoclave was vented, the catalyst Pd/BP settled down at the bottom of the vial and the colourless supernatant was removed by syringe. 5 mL of degassed ethanol

was added and Pd/BP was resuspended by sonication and transferred to a centrifuge tube. After centrifugation at 9000 rpm for 30 minutes the supernatant was discarded, and the washing procedure was repeated two times. The solid material was then collected and dried under vacuum for the night. The actual composition of the nanohybrid was evaluated with an inductively coupled plasma atomic emission spectrometer (ICP-AES) measuring both Pd and P amount. The Pd relative content resulted 10.6%$_{mol}$. The yield of this preparation as determined from the final P content was 88%, due to minor material losses during the workup procedure.

2.3 Characterization and discussion

The morphology of the new 2D material was first studied by SEM which shows that Pd NPs are embedded in the BP nanosheets, see Figure 48. Inspection by TEM, high angle annular dark field scanning transmission electron microscopy (HAADF STEM) and energy dispersive X-ray spectroscopy (EDS) confirmed the formation of nearly spherical palladium nanoparticles homogeneously distributed on the BP nanosheets and with a relative narrow size distribution centred at 3.1 ± 0.8 nm. Atomic force microscopy (AFM) revealed the presence of both thin and thick flakes with lateral size within 300-900 nm and thickness of ~ 5 and 200 nm, respectively (Figure 48e,f). The latter are likely aggregates of several smaller flakes. The nanohybrid Pd/BP was characterized by powder X-ray diffraction (PXRD) which confirms the phase purity of the 2D material and shows strong preferential orientation along the (0k0) direction, with three most intense peaks at 2θ = 16.8°, 34.2° and 52.2° assigned respectively to the (020), (040) and (060) planes of orthorhombic black phosphorus, see Figure 49a. This is also characteristic of the pristine material suggesting that its crystalline structure is retained upon functionalization with Pd NPs. A very broad peak around 2θ = 39.5° assigned to the (111) planes of Pd confirms the presence of an *fcc* phase of the metal. The severe broadening of this signal is consistent with nanosized crystalline domains, and (possibly) with some partial amorphous character.

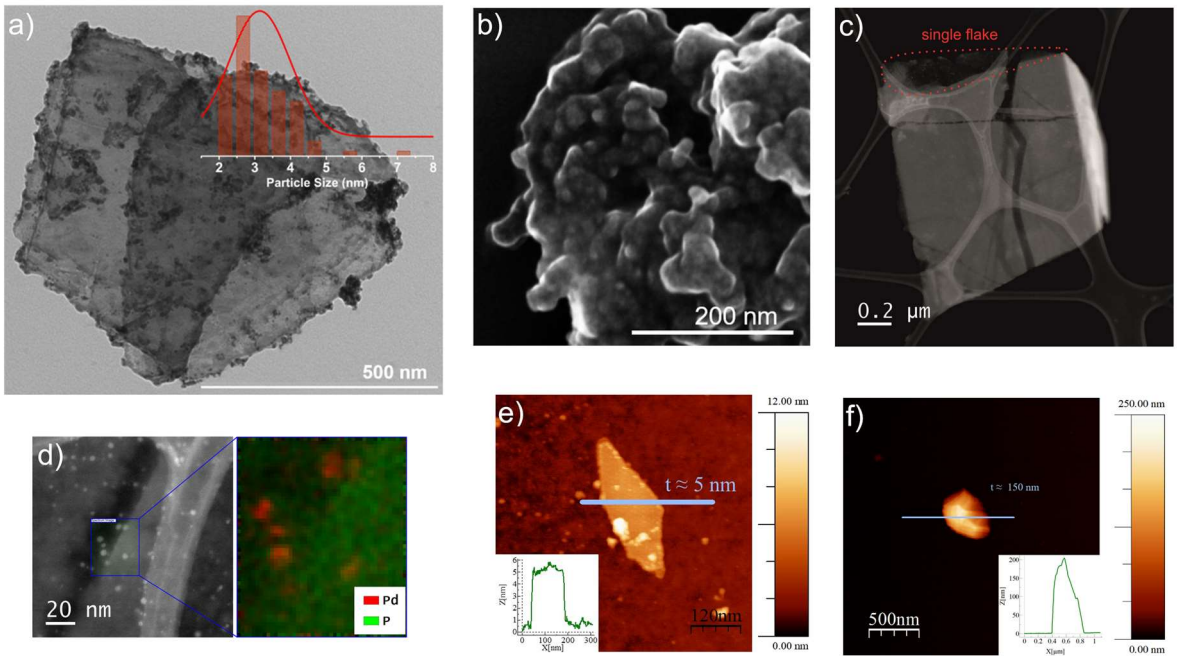

Figure 48. Electron microscopy and AFM characterization of Pd/BP. a) TEM image of Pd/BP and relative size distribution. Scale bar: 500 nm. b) SEM image of Pd/BP. c) HAADF STEM image of a Pd/BP flake on a lacey carbon grid. d) High resolution HAADF-STEM image of a flake portion showing the presence of small Pd NPs (b1) and EDS mapping of the area highlighted on the left (b2). Green regions correspond to P, red regions to Pd. The EDS elemental mapping was obtained integrating the signals from the Pd L-lines and the P K-lines. e) AFM images of Pd/BP flakes on Si/SiO_2. The blue line corresponds to the cross-sectional profile shown as an inset. Both thin (e1) and thicker (e2) objects were detected in the sample.

It is well established that the three Raman peaks of BP at 357.8, 431.5 and 459.2 cm^{-1}, corresponding to the Raman active phonon mode A^1_g, B_{2g} and A^2_g respectively, are thickness dependent and may undergo a frequency shift with varying flake thickness (see Section 1.2.3). Given the thickness polydispersity of BP prepared by sonochemical exfoliation, micro-Raman spectra were collected for a large set of flakes in order to take into account the broad range of thickness. As shown in Figure 49b, the Raman spectrum of Pd/BP displays the three peaks characteristic of the orthorombic phase of BP observed above by XRD, however no significant frequency shift was detected compared to pristine BP. A detailed statistic for the A^1_g, B^2_g and A^2_g Raman modes of pristine BP and Pd/BP is reported in Appendix A.

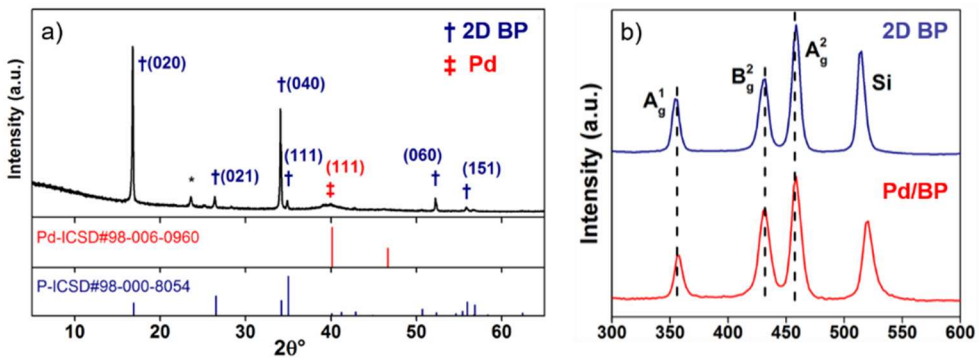

Figure 49. a) XRD spectrum of Pd/BP. b) Comparison of Raman spectra collected on the pristine BP (red) and Pd/BP (blue). Each spectrum has been obtained combining the data from 15 different flakes.

EELS (Electron Energy Loss Spectroscopy) is an important tool to gain information on the chemical shifts of core-level states, as well as on the fine structure of the unoccupied valence-band states, thus we performed a comparative EELS analysis between BP (simulated and measured) and Pd/BP measured by HAADF-STEM-SI, see Figure 50. An appreciable difference in the P L-edge is observed at around 137 eV for Pd/BP. This reveals a modification of the electronic structure of BP which can be interpreted as due to a strong interaction between P atoms of BP and Pd NPs.

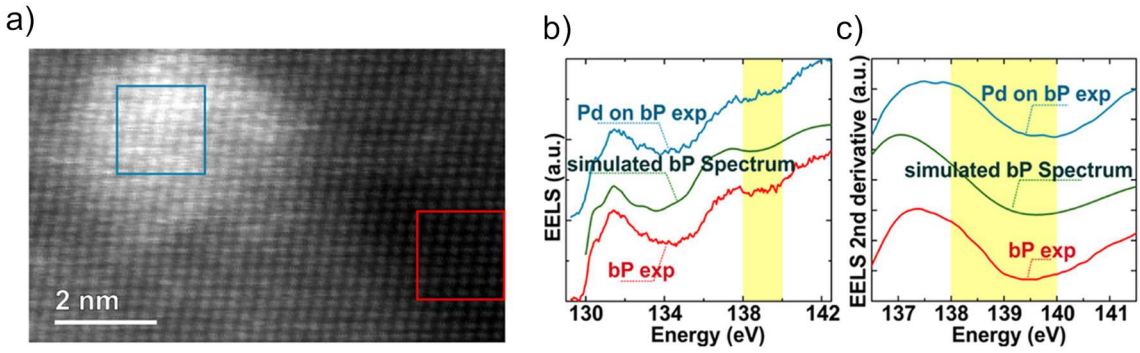

Figure 50. a) HAADF-STEM-SI of Pd/BP acquired along the [101] zone axis, at the P L edge. b) EELS spectra: red curve, experimental BP, obtained integrating the EELS-SI (spectrum imaging) along the red box in a); green curve: simulated BP; blue curve: experimental Pd/BP, obtained integrating the EELS-SI along the blue box in a). c) second derivative plots of the three EELS spectra within the region highlighted in b).

The chemical states of the Pd NPs were determined by the Pd 3d core-level XPS spectrum (Figure 51a), which is fitted by the use of two doublets due to spin-orbit couplings. The components at binding energy B.E. = 335.8 eV (Pd 3d5/2) and at B.E. = 341.0 eV (Pd 3d3/2) accounts for bulk metallic palladium. The smaller doublet at B.E. = 338.1 eV and B.E. = 343.5 eV is attributable to an electrodepleted palladium species, probably with an oxidation state +II. The presence of PdO can be ruled out being absent the peaks with corresponding B.E. values [5], thus the signal at higher binding energy can be explained as the result of a partial valence orbital overlap between surface Pd atoms and BP nanosheets. This is consistent with the presence of Pd–P bonds, as deduced from the EELS measurements. The presence of a layer of electron-depleted palladium atoms on the surface of Pd NPs, which strongly interact with P-atoms, has been already observed in the study of Pd NPs capped with the hydrosoluble phosphine ligand PTA (PTA = 1,3,5-triaza-7-phophaadamantane) [6], which indeed show a comparable XPS spectrum.

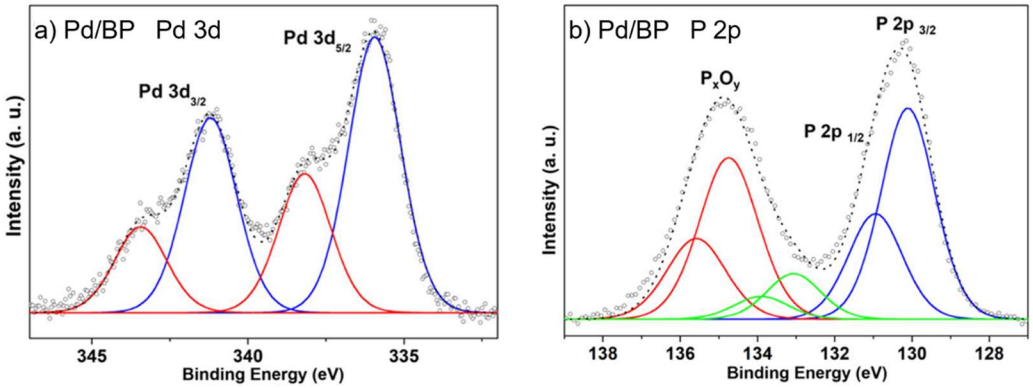

Figure 51. Pd 3d core-level XPS spectrum of Pd/BP, metallic and electron-depleted palladium doublets are depicted by blue and red lines, respectively. b) P 2p core-level XPS spectrum of Pd/BP.

The deconvolution of P 2p core level spectrum for pristine BP shows the characteristic doublet representing the P $2p_{3/2}$ and P $2p_{1/2}$ peaks located at 129.7 eV and 130.6 eV, typical of elemental phosphorus, see Figure 51b. Intriguingly, P 2p core level spectrum of Pd/BP results much more complex requiring the use of at least three components. Alongside the doublet attributable to elemental phosphorus (two peaks at B.E.= 130 eV and B.E. = 131 eV), components at higher B.E. values are present as well, see Figure 51b, that can be interpreted as due to phosphorus in different chemical environments. The doublet at intermediate B.E. values (green line fitting in Figure 51b) is likely due to P–Pd bonds. The large doublet characterized by the highest binding energy (red line fitting in figure 51b) accounts for the presence of phosphorus oxides species such as P–OH, P=O and P–O–P on the surface of BP sheets. Since peaks at lower BE values characteristic of P having a phosphide nature (128.6 eV) are absent, the presence of phosphides as Pd_xP_y species can be reasonably excluded. As explained in the introduction to this Chapter, the nature of the interaction between metal nanoparticles and BP has been so far approached only by theoretical calculations. To unravel the real nature of the Pd–P interaction, X-ray absorption spectroscopy (XAS) measurements were performed on Pd/BP taking the following compounds as standards: Pd NPs capped with the phosphine ligand PTA and labelled as Pd@PTA [6], PdP_2 NPs, Pd NPs supported on carbon (Pd/C) and Pd metal foil.

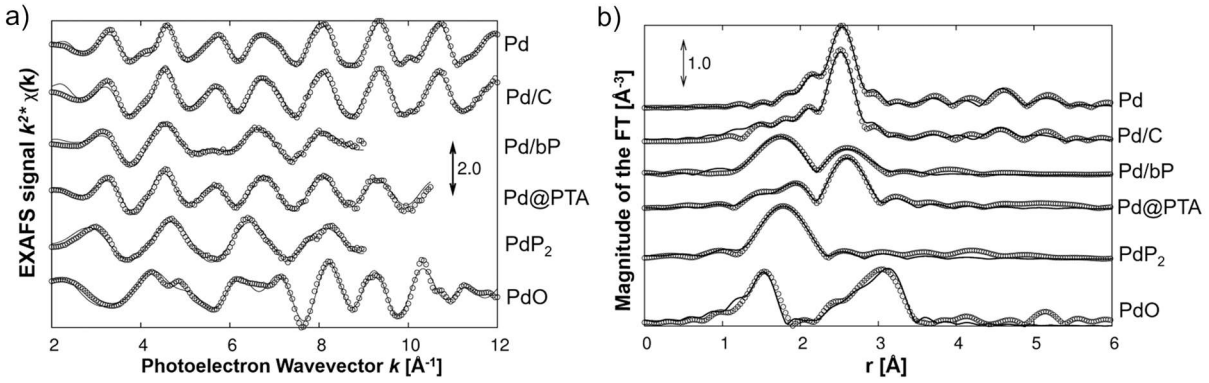

Figure 52. a) EXAFS data at the Pd-K edge; b) the corresponding Fourier transforms. Dots are experimental data while continuous lines are the calculated best-fit data.

In Fig. 52, the raw EXAFS spectra and the corresponding Fourier Transforms show clearly the presence of a peak just below 2 Å in the sample Pd/BP that can be attributed to Pd–P bonds having a very similar shape and almost the same R (Å) value as the peak present in PdP_2. A second peak just below 3 Å can be ascribed to Pd–Pd bonds, being present both in Pd metal foil, Pd/C and Pd@PTA. This means that Pd atoms are involved in two different bonds: Pd–Pd and Pd–P, the former arising from the bonds with inner metal atoms of the nanoparticle, the latter from an interaction between the surface Pd atoms and P atoms of BP. The precise value of bond lengths and relative coordination numbers can be obtained from the following Table 1:

Sample	**CN $_{Pd-Pd}$**	**R $_{Pd–Pd}$(Å)**	**$\sigma^2_{Pd–Pd}$ (Å^2)**	**CN $_{Pd-P}$**	**R $_{Pd–P}$(Å)**	**$\sigma^2_{Pd–P}$ (Å^2)**
Pd foil	12	2.74(1)	0.0059(4)	-	-	-
Pd/C	7(2)	2.73(1)	0.0065(5)	4(2)	1.94(3)	0.013(5)
Pd/BP	8(2)	2.77(3)	0.016(4)	1.7(6)	2.26(3)	0.0018(6)
Pd@PTA [6]	8(2)	2.73(2)	0.009(2)	0.7(2)	2.25(3)	0.004
PdP_2	-	-	-	3.8(6)	2.32(2)	0.004(2)
PdP_2 [7]	-	-	-	2 2	2.335 2.341	-
PdP_3 [8]	-	-	-	6	2.235	-
Pd foil [9]	12	2.7453	-	-	-	-

Table 1. EXAFS analysis. CN $_{Pd–Pd}$ = average coordination number of Pd atoms; $R_{Pd–Pd}$ (Å)= Pd–Pd distance; $\sigma^2_{Pd–Pd}$ (Å^2) Debye-Waller factor of the Pd–Pd bond; $CN_{Pd–P}$ = average Pd–P coordination number; $\sigma^2_{Pd–P}$ = Debye-Waller factor of the Pd–P bond; $R_{Pd–P}$ (Å) = Pd–P distance. Errors on the last digit are given in brackets.

To better highlight the extent of surface interaction between P and Pd, and to better grasp the meaning of the measured CNs, a rough calculation can be carried out as follows. From TEM analysis, the average diameter of Pd NPs is ~ 3 nm. If we consider *fcc*-cuboctahedral Pd NPs, this loosely corresponds to a central atom surrounded by 6 layers of Pd atoms, for a total of 923 atoms. Of these, 362 lay on the surface. H.-G. Fritsche and R.E. Benfield [10] derived formulae to compute the mean coordination number ($\overline{CN}$) in metal clusters having specific geometries, as a function of m (number of outer layers + 1). For cuboctahedral clusters the relation is:

$$\overline{CN} = \frac{12(m-1)(10m^2-14m+6)}{(2m-1)(5m^2-5m+3)}$$

In our specific case (m=7) it gives $\overline{CN}$ = 10.3, which is in fair agreement with $CN_{Pd\text{-}Pd}$ = 8(2) taking into account the error bar. In order to give an estimate of how large the interaction between surface Pd atoms and BP is, let's assume that every surface Pd atom is additionally bonded to three phosphorus atoms. Thus, the apparent Pd–P coordination number, weighed by the fraction of surface atoms, would be CN = 3·(362/923) = 1.2, likewise consistent with the experimental value $CN_{Pd\text{-}P}$ = 1.7(6) within the error bar. Despite being solely of qualitative nature, this simple analysis suggest that many surface Pd atoms are extensively involved in bonding with P atoms of the BP layers. This is also in agreement with the morphology observed by SEM and with the occasional stacking of the flakes highlighted by AFM analysis (see Figure 48).

In addition to coordination numbers, of particular interest is the short Pd–P distance $R_{Pd\text{–}P}$ = 2.26(3) Å measured in Pd/BP, suggesting that the latter is a very strong interaction. As a comparison, the phosphide PdP_2 has longer bonds, $R_{Pd\text{–}P}$ = 2.32(2) Å, as measured by us and according to literature, while PdP_3 has $R_{Pd\text{–}P}$ = 2.235 Å which is close to Pd/BP, although the presence of phosphide can be safely ruled out in our sample on the basis of the previously discussed XPS and XRD measurements. Remarkably, Pd@PTA exhibits $R_{Pd\text{–}P}$ = 2.25 Å, which is consistent with the coordination bond distance Pd–P of 2.203(3) Å measured via single-crystal X-ray diffraction analysis in the complex cation $[Pd(PTAH)_4]^{4+}$ [11], and it is almost the same value measured in Pd/BP. This reveals that the Pd–P interaction in Pd/BP can be seen as a coordination bond of covalent nature and closely resembles the one existing in Pd@PTA: the P atoms of the BP nanosheets surround Pd NPs acting similarly to the molecular phosphine ligand PTA towards Pd NPs.

To the best of the writer knowledge, this is the first experimental demonstration that BP nanosheets may act as a polydentate phosphorus ligand towards metal nanoparticles via strong coordination bonds of covalent nature.

2.4 Catalytic tests

The strong interaction observed in Pd/BP is expected to provide stabilization to Pd NPs, preventing their agglomeration, thus making Pd/BP a good candidate for catalytic applications. Intrigued by these results, it was decided to investigate the reduction of chloro-nitroarenes to the corresponding chloroanilines. as benchmark standards for assessing the catalytic performance of Pd/BP. Chloroanilines are high valuable intermediates for the manufacture of many agrochemicals, pharmaceuticals, polymers and dyes [12]. Since traditional methods employing stoichiometric reducing agents have drawbacks for both economic

and environmental issues [13,14], efforts have been devoted to replace them with protocols based on the use of hydrogen gas as reductant [14]. Moreover, many tested catalysts are severely affected by undesired dehalogenation due to the C–Cl hydrogenolysis, (see Scheme 1). Thus, finding a catalyst able to efficiently carry out the chemoselective reduction of nitroarenes remains still a challenge. The hydrogenation of *ortho*- and *meta*-chloronitrobenzene was thus chosen as benchmark reaction to test the nanohybrid Pd/BP, for the following reasons:

- other heterogeneous systems based on phosphorus and palladium were reported to be active promoting the selective conversion of chloronitrobenzene to chloroaniline. These include PdP_x NPs [15] and Pd NPs supported on P-activated carbon [16];
- the affinity of the 2D BP surface to gaseous NO_2 [17,18] and to aromatic systems (see Section 1.4.3) may anticipate a good affinity for nitrobenzene and related molecules.

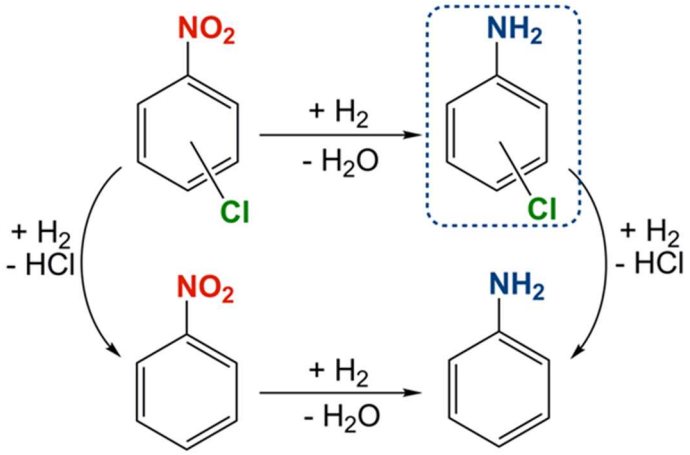

Scheme 1. The two possible pathways for the secondary reaction of C-Cl hydrogenolysis of chloronitrobenzene.

To evaluate the effect imparted by BP as support, a reference Pd-nanocatalyst was prepared for comparison, growing Pd NPs on carbon (ketjen black). To make the comparison meaningful, this reference system should be as close as possible to Pd/BP, except for the different NPs support. Thus, the same synthetic protocol of Pd/BP was applied to ketjen black (*i.e.* keeping unchanged solvent mixture, reaction time and temperature, H_2 pressure). By this method, Pd NPs with average dimension 2.4 ± 0.5 nm were grown on ketjen black (see Figure 53). As shown by ICP-AES analysis, the Pd loading in the recovered material (named Pd/C) amounted to 7.7 $\%_{at}$.

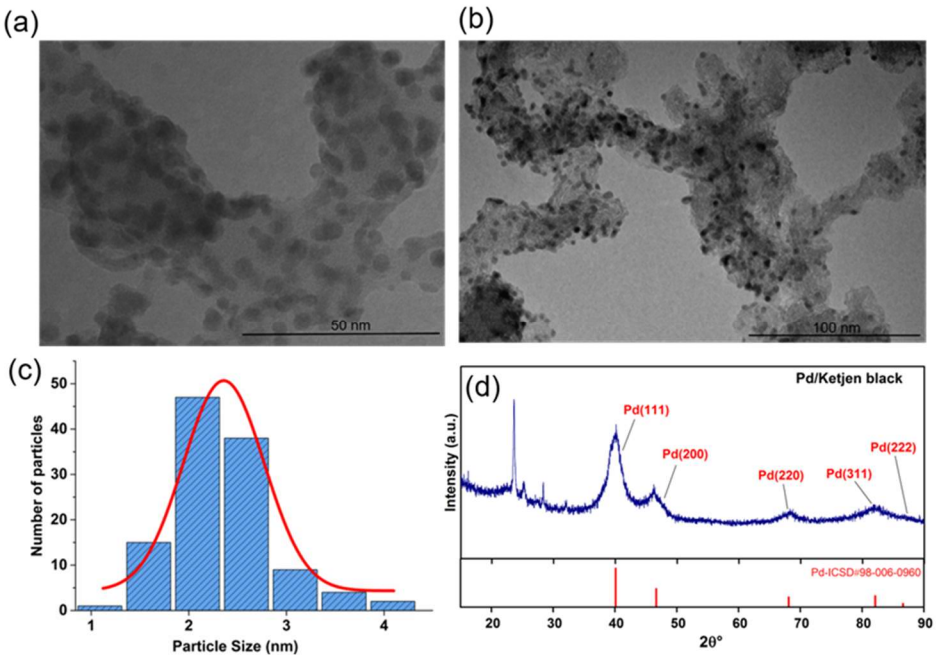

Figure 53. a-b) TEM image of the catalyst Pd/C and (c) relative size distribution of Pd NPs. d) XRD spectrum of Pd/C, featuring the presence of Pd(0) peaks overlapping with the broad signal of the amorphous support ketjen black.

Catalytic tests were performed in batch reactions. The solid catalyst (Pd/BP or Pd/C) was suspended in MeOH and added to the substrate inside a stainless steel autoclave, then the system was pressurized with 5 bar of H_2 and stirred at room temperature. After a given time the system was vented, the supernatant was isolated upon centrifugation at 9000 rpm x 30', and GC-MS analysis was carried out to evaluate conversion and selectivity. The following table summarizes reaction conditions and performances observed:

Catalyst	Substrate	Time (min)	S/C	Conversion %[a]	Selectivity %[a]	TOF (h^{-1})
Pd/BP	*m*-CNB	30	162	99.1	97.7	313
Pd/BP	*o*-CNB	40	162	99.5	97.3	235
Pd/C	*o*-CNB	30	191	99.9	78.1	298

Table 2. *o*-CNB = 1-chloro-2-nitrobenzene; *m*-CNB = 1-chloro-3-nitrobenzene. Reaction conditions: solvent: methanol, [substrates] = 0.242 M; room temperature; 5 bar H_2; magnetic stirring, 1200 rpm. S/C: substrate/catalyst ratio (mol/mol). a) Data from GC analysis and GC-MS; b) Turn over frequency.

Satisfyingly, Pd/BP showed a remarkable chemoselectivity in the reduction of both ortho- and meta-chloronitrobenzene, reaching 97.3% of selectivity toward the formation of chloroaniline at 99.5% conversion for the ortho isomer. Remarkably, switching from BP to C as catalytic support, the selectivity measured at 99.9% of conversion dropped to 78.1%, as shown in Table 2. This means that in the presence of Pd/C, the secondary reaction of C−Cl hydrogenolysis takes place simultaneously with $–NO_2$

reduction, while with Pd/BP, first $–NO_2$ is reduced to NH_2 and then C−Cl hydrogenolysis starts. In the case of hydrophobic charcoal, affinities to both chloronitrobenzene and chloroaniline are expected to be comparable and once chloroaniline is formed, presumably its desorption from the surface is slow, which ultimately leads to hydrogenolysis. On the other hand, the adsorption of gaseous NO_2 on the surface of BP is known to be a highly favoured process from energy point of view. As shown in Section 1.4.3, BP may be involved in non-covalent p→π interactions with aromatic systems, which are stronger the more electron-poor the aromatic ring. Thus, chloronitrobenzene is expected to be easily adsorbed on Pd/BP; however, once the nitro group is hydrogenated to amine, the latter product is desorbed easily from the surface, leaving the catalytic system and impeding the secondary reaction of C−Cl hydrogenolysis to take place.

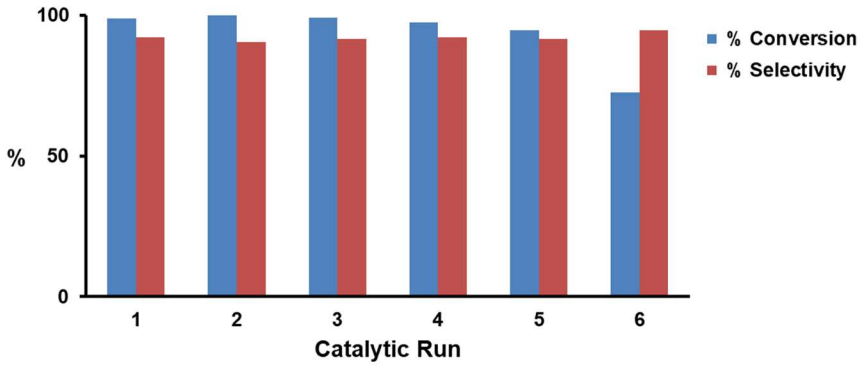

Figure 54. Catalyst reuse in the hydrogenation of 1-chloro-2-nitrobenzene.

To probe the stability of Pd/BP under reaction conditions, recycling tests were carried out. In detail, after one catalytic run Pd/BP was isolated by centrifugation, resuspended in methanol and added to fresh substrate for the next catalytic run. The selectivity toward the target chloroaniline was maintained unaltered after six consecutive runs and only a small decrease of the conversion was observed, possibly due to a progressive loss of material during the catalyst recovery step (see Figure 54). In order to rule out metal leaching from the Pd/BP catalyst, after one first catalytic run the reaction mixture was centrifuged, the solid catalyst was discharged, and the supernatant was added to fresh substrate for a second run. As expected, no conversion was observed by GC-MS after the second run, confirming that the catalytically active phase is Pd/BP, instead of some possible molecular Pd species formed *in situ* under the reaction conditions or colloidal Pd NPs detached from BP flakes and being left in suspension. TEM investigation on Pd/BP recovered after the catalytic runs, confirmed that the initial morphology of the material was preserved, being the average size of Pd NPs equal to 3.6 ± 0.9 nm, see Figure A1 in Appendix A. Thus, the presence of Pd–P bonds prevents BP degradation and provides an excellent structural stability to the catalyst.

2.5 Conclusions

In summary, a new Pd/BP nanohybrid was developed and for the first time, the intimate nature of the interaction between Pd NPs and BP nanosheets was elucidated by EXAFS. A very short Pd–P distance of 2.26(3) Å was disclosed, accounting for a coordinative bond of covalent nature between surface Pd atoms and P atoms of phosphorene. Moreover, the average Pd–P coordination number turned out to be 1.7 suggesting that BP acts as a sort of polydentate phosphine ligand towards Pd NPs, stabilizing them toward agglomeration and preventing leaching of the metal in solution. Pd NPs are thus embedded between BP flakes yielding a new 0D-2D heterostructure. The latter was also investigated with other surface techniques, such as XPS and EELS-STEM, all of them were consistent with the presence of a strong Pd–P interaction. Finally, the synergy between Pd NPs and BP was successfully exploited in the reduction of chloronitroarenes to the corresponding chloroanilines, showing a far superior chemoselectivity in comparison to other heterogeneous systems based on palladium. Furthermore, successful catalyst reuse was demonstrated, keeping the catalytic performance almost unaltered after six consecutive runs.

2.6 Appendix A:

A1 Synthesis and catalysis

A2 Materials Characterization

A.1 Synthesis and Catalysis

A1.1 General Methods and materials. All manipulations were performed under inert atmosphere using Schlenk techniques. Tetrahydrofuran (THF) was distilled from sodium/benzophenone and degassed prior to use. $Pd(NO_3)_2 \cdot 2H_2O$, 1-chloro-2-nitrobenzene and 1-chloro-3-nitrobenzene were used as received from Sigma Aldrich. Ketjen black EC 600JD (surface area = 1400 m^2/g) was purchased from Akzo Nobel and used as received. Black phosphorus (BP) was prepared as described in section 2.2.1. The nanohybrid Pd/BP with 0.5 % mol loading of Pd used for comparison in Raman characterization (see A.2.7) was prepared following exactly the same procedure of Pd/BP 10.6% mol (Section 2.2.2).

A1.2 Synthesis of Pd/C. Ketjen black (0.6 mg, 0.050 mmol) was dispersed in 1.5 mL of distilled and degassed THF by means of ultrasounds. To this black suspension, 1.3 mL of degassed ethanol were

added, followed by 1.3 mL of a 3.75 mM aqueous solution of $Pd(NO_3)_2 \cdot 2H_2O$ (0.00487 mmol, Pd : C = 1:10). The mixture was transferred inside a glass vial equipped with a magnetic stirring bar. The vial was put inside an autoclave, pressurized with 5 bar of H_2 and left stirring for 1 h. After this time the autoclave was vented, the mixture was transferred in a centrifuge tube, 5.0 mL of degassed ethanol were added and the solid catalyst was isolated upon centrifugation at 9000 rpm for 30 minutes. The washing procedure was repeated two times and the final solid was dried under vacuum for 10 hours. The actual Pd content was measured by ICP-AES and resulted equal to 7.7 % mol.

A1.3 Catalytic hydrogenation of nitroarenes and recycling tests. In a typical run, 1-chloro-2-nitrobenzene (114.2 mg, 0.725 mmol) was added to the solid catalyst Pd/BP 10% mol (1.3 mg BP, 0.042 mmol, 0.044 mmol Pd) in a screw capped centrifuge tube, 3 mL of degassed MeOH were added and the mixture was sonicated for 5 minutes to suspend the catalyst and dissolve the substrate. The suspension was then transferred to a glass vial placed inside an autoclave and equipped with a magnetic stirring bar. The autoclave was purged with hydrogen (3 times) and then pressurized up to 5 bar. The mixture was kept stirring for the required time, after which the gas was vented and the mixture was transferred in a centrifuge tube. 5 mL of degassed MeOH were added and the suspension was centrifuged at 9000 RPM for 30 minutes. The supernatant was analyzed by GC. To the solid residue containing the catalyst, the nitroarene and methanol were added, and a new catalytic run was launched.

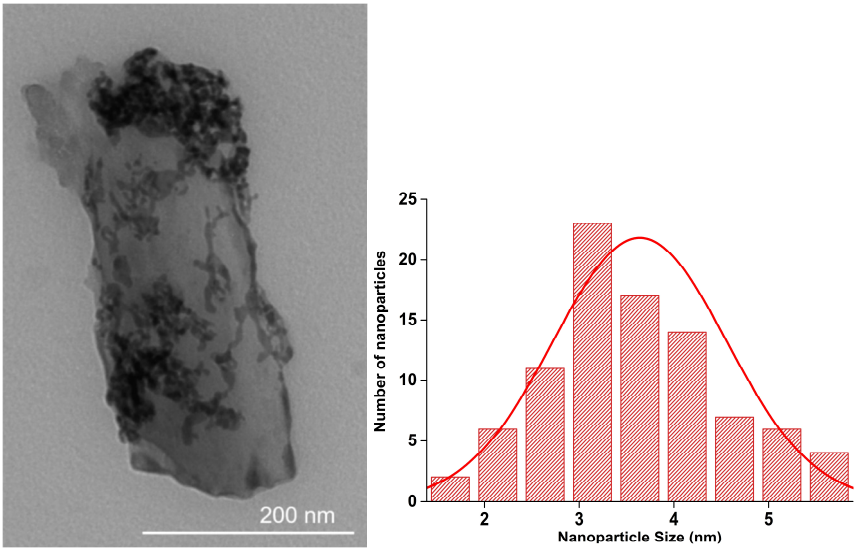

Figure A1. TEM image of Pd/BP after catalytic tests and relative size distribution of the Pd NPs.

A1.4 Test for the heterogeneous nature of the catalyst. A catalytic run was started under the standard reaction conditions described above. After 15 minutes the reaction was stopped, the autoclave was vented and the reaction mixture was transferred in a centrifuge tube. The solid material was isolated by centrifugation at 9000 RPM for 30 minutes. A small fraction of the supernatant (2 µL) was taken for

GC-MS analysis, Entry 1 in Table A1. The remaining was transferred into the autoclave, pressurized with 5 bar of H_2 and kept stirring for 40 minutes. After this time the autoclave was vented and GC-MS analysis was carried out. The supernatant gave no further conversion (Entry 2), confirming that the catalytic activity is due entirely to the solid phase. A further catalytic run was performed recycling the recovered solid catalyst under the same reaction conditions. Results comparable with fresh catalyst Pd/BP were obtained, see Entry 3.

Entry	Catalytic run	Time (min)	Conversion %	Selectivity %	TOF (h^{-1})
1	1st run	15	42.6	95.1	263
2	no solid phase	40	42.8	94.7	-
3	1st recycle	40	97.8	90.7	215

Table A. Tests of the heterogeneous nature of the catalytically active Pd species.

A2. Characterization techniques

A2.1 Transmission electron microscopy. TEM studies were carried out at Ce.ME-CNR (Florence) using a Philips instrument operating at an accelerating voltage of 100 kV. Few drops of Pd/BP and Pd/ketjen black in methanol were placed on the TEM copper/carbon grid, air dried, and measured.

A2.2 Scanning transmission electron microscopy. STEM measurements were performed at CNR-IMM (Catania, Italy). Atomic-resolution characterization was performed through a probe aberration-corrected JEOL ARM200CF, equipped with a Ceos hexapole-type Cs corrector, named CESCOR, and operated at a primary beam energy of 60 keV. The electron gun is a cold-field emission gun with an energy spread of 0.3 eV. The probe size was 1.0 Å at 60 kV. Micrographs were acquired in Z-contrast mode (High-Angle Annular Dark Field, HAADF).

A Centurio Energy Dispersive Spectrometer (EDS) equipped with a 100 mm^2 Silicon Drift Detector was used for the EDS acquisitions.

A GIF Quantum ER as Electron Energy Loss Spectrometer (EELS) was used for EELS measurements. Both low- and core-loss EELS spectra were acquired with the DualEELS capability through Gatan Digital Micrograph software, which allows the accurate energy calibration of EELS spectra, thanks to the simultaneous alignment of the zero-loss peak position for every single acquisition, which removes any artefact coming from energy shifts. The use of Fourier logarithmic deconvolution on a full spectrum obtained by splicing together low- and core-loss EELS allows removing thickness-related plural

scattering. All the STEM-EELS and STEM-EDS measurements were performed simultaneously by using the Gatan spectrum imaging (SI) tool.

A2.3 Gas Chromatography. GC analyses were performed on a Shimadzu GC-14A gas chromatograph (with polar column) equipped with flame ionization detector and a SPB-1 Supelco fused silica capillary column (30 m, 0.25 mm i.d., 0.25 μm film thickness).

A2.4 Inductively coupled plasma mass spectrometry. ICP-MS measurements were performed with an Agilent 7700 Series spectrometer. Samples followed a microwave-assisted digestion in Nitric acid for trace analysis. Then, different dilutions of each sample with water for trace analysis were prepared, in order to obtain concentrations in the sensitivity range of the instrument for the elements under investigation (namely Pd and P). Standards at different concentrations have also been prepared and measured contextually to sample measurements, in order to obtain a calibration curve for each element under investigation.

A2.5 Atomic Force Microscopy. AFM measurements were performed at NEST (Pisa, Italy) with a Bruker Dimension Icon Atomic Force Microscope, in pick force mode. Samples for AFM were prepared by drop cast of a suspension of Pd/BP in THF/MeOH (1:1) on a Si/SiO_2 substrate. The drop was left in contact with the substrate for one minute, then the sample was washed with ethanol and dried first under a stream of nitrogen and then in vacuum for five hours. Samples prepared with this method have almost no solvent traces, at least far from the edges, and quite small aggregates. During AFM, regions where no aggregates were visible in the optical microscope were approached, revealing both thin and thick structures, as shown in Figure 48. Thicker structures likely result from the stacking of thinner flakes. These structures have an average lateral dimension of 500 nm and a thickness of up to 200 nm.

A2.6 Powder X-ray Diffraction. PXRD data were collected with an X'Pert PRO diffractometer operating in a Bragg-Brentano parafocusing geometry with Cu-Kα radiation (λ = 1.5418) working at 40 kV and 30mA. Samples were prepared by slow dropcast of about 1 mg of material (Pd/BP or Pd/C) suspended in EtOH (1 mg/mL). A nitrogen flux was directed onto the sample during the dropcast to accelerate evaporation after the deposition of each drop. The process was continued until a layer of the material was uniformly distributed on the sample holder.

A2.7 Raman scattering. Raman measurements were carried out at CNR-IFAC (Florence) using a micro-Horiba Xplora system coupled to a 532 nm wavelength laser. The backscattered light was collected by a 100× microscope objective with 0.9 NA, which generates a ~1-μm large laser beam waist. Integration times of 10 s, laser power values in the 1-2 mW range and a grating of 1200 cm^{-1} were employed. The samples were prepared by dropcasting a suspension of BP and Pd/BP in tetrahydrofuran

on a Si/SiO_2 wafer. After one minute of exposure, the wafers were rinsed with ethanol and dried under a stream of nitrogen for 30 minutes. To study the influence of Pd NPs on the Raman shift of black phosphorus, Pd/BP was prepared with two different Pd loading, namely 0.5 % mol and 10% mol, using the same batch of pristine BP for both preparations. Raman spectra were collected from 15 different nanosheets in each sample of pristine BP, Pd/BP 0.5% mol and Pd/BP 10% mol. The average Raman shift of each active mode was calculated for the three samples and is displayed in Figure S5 with relative error bars. No relevant shift in the peak positions was observed for the two Pd/BP samples compared to pristine BP.

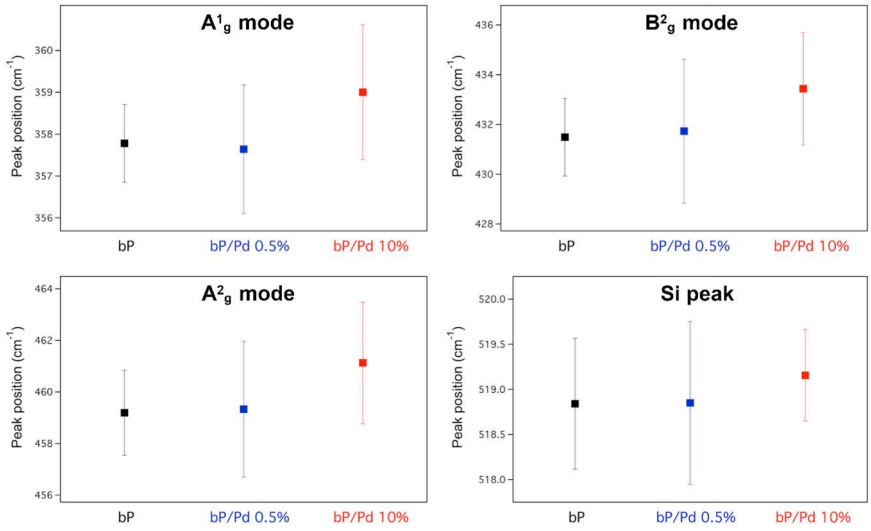

Figure A2. Comparison of Raman data of pristine BP with Pd/BP having two different loading of Pd.

A2.8 X-ray Photoelectron Spectroscopy (XPS). X-ray Photoelectron Spectroscopy (XPS) measurements were performed at the Chemistry Department, University of Florence (Italy) in an ultra-high vacuum (10^{-9} mbar) system equipped with a VSW HAC 5000 hemispherical electron energy analyser and a non-monochromatized Mg-Kα X-ray source (1253.6 eV). The source power used was 100 W (10 kV×10 mA) and the spectra were acquired in the constant-pass-energy mode at E_{pas} = 44 eV. The overall energy resolution was 1.2 eV as a full-width at half maximum (FWHM) for the Ag $3d_{5/2}$ line of a pure silver reference. The recorded spectra were fitted using XPS Peak 4.1 software employing Gauss-Lorentz curves after subtraction of a Shirley-type background. The powder sample was introduced in the UHV system via a loadlock under inert gas (N_2) flux, in order to minimize the exposure to air contaminants and kept in the introduction chamber for at least 12 hours before the measurements.

A2.9 X-ray Absorption Spectroscopy (XAS). To study in depth the nature of the interaction between the palladium atoms on the surface of the nanoparticles in contact with P atoms of BP sheets, X-ray Absorption Spectroscopy (XAS) experiments at the Pd-K edge (E_{edge}=24350 eV) have been carried out

at the LISA beamline at 'The European Synchrotron Radiation Facility' in Grenoble (France). The monochromator was equipped with a pair of flat Si(311) crystals; collimation and harmonic rejection was achieved by using a Pt-coated cylindrical mirror before the monochromator with an incidence angle of 2 mrad. Further harmonic rejection and focusing was achieved with a Pt toroidal mirror (focusing configuration 2:1) positioned after the monochromator. The beam size on the sample was approximately 0.2 mm. Measurements were carried out at room temperature whereas the XAS signal was collected in fluorescence mode using a 12 elements High Purity Germanium Detector. A Pd foil placed after the sample was used as energy calibration standard compound and its spectrum was always collected together with the samples. XAS data were reduced and analyzed with the ATENA/ARTEMIS codes and the theoretical XAS signals were generated with the FEFF-8.4 code. Structural parameters were obtained by data fits in R space with the transformation ranges in k space varying from case to case (k=[2.5->14] Å-1 for for the best cases, k=[2.5->9] Å-1 for the noisier spectra) and a k2 weight factor. Coordination Numbers (CNs) have been calibrated via the analysis of the Pd metal foil, finding a global amplitude correction factor S02=0.88.

A2.10 EXAFS analysis. EXAFS (extended X-ray absorption fine structure) analysis was carried out modeling the data with two contributions: Pd clusters and Pd–P bond. The model of Pd clusters included 4 coordination shells for Pd foil though in Table 1 in the main text only the first shell is presented. The others were modeled with a single Pd–Pd first shell, other coordination shells being not visible in the FT. An additional Pd–P bond was added to account for the interaction with phosphorus atoms as evidenced by the peak in the FT below 2 Å.

2.7 Chapter II References

[1] T. Wu, J. Fan, Q. Li, P. Shi, Q. Xu, Y. Min, Palladium Nanoparticles Anchored on Anatase Titanium Dioxide-Black Phosphorus Hybrids with Heterointerfaces : Highly Electroactive and Durable Catalysts for Ethanol Electrooxidation, Adv. Energy Mater. 8 (2018) 1701799. https://doi.org/10.1002/aenm.201701799.

[2] T. Wu, Y. Ma, Z. Qu, J. Fan, Q. Li, P. Shi, Q. Xu, Black Phosphorus − Graphene Heterostructure-Supported Pd Nanoparticles with Superior Activity and Stability for Ethanol Electro-Oxidation, ACS Appl. Mater. Interfaces 11 (2019) 5136-5145. https://doi.org/10.1021/acsami.8b20240.

[3] M. Köpf, N. Eckstein, D. Pfister, C. Grotz, I. Krüger, M. Greiwe, T. Hansen, H. Kohlmann, T. Nilges, Access and in situ growth of phosphorene-precursor black phosphorus, J. Cryst. Growth. 405 (2014) 6–10. https://doi.org/10.1016/j.jcrysgro.2014.07.029.

[4] M. Serrano-Ruiz, M. Caporali, A. Ienco, V. Piazza, S. Heun, M. Peruzzini, The Role of Water in the Preparation and Stabilization of High-Quality Phosphorene Flakes, Adv. Mater. Interfaces. 3 (2016) 1500441. https://doi.org/10.1002/admi.201500441.

[5] NIST X-ray Photoelectron Spectroscopy Database, NIST Standard Reference Database Number 20, National Institute of Standards and Technology, Gaithersburg MD, (2000) 20899, doi:10.18434/T4T88K

[6] M. Caporali, A. Guerriero, A. Ienco, S. Caporali, M. Peruzzini, L. Gonsalvi, Water-soluble, 1,3,5-Triaza-7-phosphaadamantane-stabilized palladium nanoparticles and their application in biphasic catalytic hydrogenations at room temperature, ChemCatChem. 5 (2013) 2517–2526. https://doi.org/10.1002/cctc.201300079.

[7] W.H. Zachariasen, The Crystal Structure of Palladium Diphosphide, Acta Crystallogr. 16 (1963) 1253.

[8] S. Rundqvist, Phosphides of the Platinum Metals, Nature 185 (1960) 31–32.

[9] E.A. Owen, E.L. Yates, Precision measurements of crystal parameters, Philos. Mag. 15 (1933) 472.

[10] H.G. Fritsche, R.E. Benfield, Exact Analytical Formulae for Mean Coordination Numbers in Clusters, Z. Phys. D. (1993) S15. https://doi.org/10.1007/BF01425603.

[11] D.J. Darensbourg, T.J. Decuir, N.W. Stafford, J.B. Robertson, J.D. Draper, J.H. Reibenspies, A. Kathó, F. Joó, Water-Soluble Organometallic Compounds. 6.1 Synthesis, Spectral Properties, and Crystal Structures of Complexes of 1,3,5-Triaza-7-phosphaadamantane with Group 10 Metals, Inorg. Chem. 36 (1997) 4218–4226. https://doi.org/10.1021/ic970238x.

[12] A. Boehnecke, J. Kielhorn, G. Konnecker, C. Pohlenz-Michel, I. Mangelsdorf, 4-Chloroaniline, CICADS Report 48, W.H.O., Geneva, 2003.

[13] H.U. Blaser, U. Siegrist, H. Steiner, M. Studer, Fine Chemicals through Heterogeneous Catalysis,Wiley-VCH, Wennheim, 2001, pp. 389 – 406.

[14] J. Song, Z.F. Huang, L. Pan, K. Li, X. Zhang, L. Wang, J.J. Zou, Review on selective hydrogenation of nitroarene by catalytic, photocatalytic and electrocatalytic reactions, Appl. Catal. B Environ. 227 (2018) 386–408. https://doi.org/10.1016/j.apcatb.2018.01.052.

[15] L.B. Belykh, N.I. Skripov, T.P. Sterenchuk, K.L. Gvozdovskaya, S.B. Sanzhieva, F.K. Schmidt, Pd-P nanoparticles as active catalyst for the hydrogenation of acetylenic compounds, J. Nanoparticle Res. 21 (2019) 198. https://doi.org/10.1007/s11051-019-4641-z.

[16] C. Lu, M. Wang, Z. Feng, Y. Qi, F. Feng, L. Ma, Q. Zhang, X. Li, A phosphorus – carbon framework over activated carbon supported palladium nanoparticles for the chemoselective

hydrogenation of para- chloronitrobenzene, Catal. Sci. Technol. 7 (2017) 1581–1589. https://doi.org/10.1039/C7CY00157F.

[17] L. Kou, T. Frauenheim, C. Chen, Phosphorene as a superior gas sensor: Selective adsorption and distinct i - V response, J. Phys. Chem. Lett. 5 (2014) 2675–2681. https://doi.org/10.1021/jz501188k.

[18] A.N. Abbas, B. Liu, L. Chen, Y. Ma, S. Cong, N. Aroonyadet, M. Köpf, T. Nilges, C. Zhou, Black phosphorus gas sensors, ACS Nano. 9 (2015) 5618–5624. https://doi.org/10.1021/acsnano.5b01961.

Interlayer functionalization of black phosphorus with Pd–Pd dimers

3.1 Introduction.

Over the last decade research in heterogeneous catalysis was marked by the growing interest in single- and dual-atom catalysts. This trend was prompted by the simultaneous development of physical techniques, such as EXAFS, XPS, HAADF-STEM, together with highly powerful computational methods, enabling the characterization of low-nuclearity systems with unprecedented accuracy, rivalling the role of single crystal X-ray diffraction in molecular science. Lamentably, this level of accuracy is still lacking within the field of 2D materials, in particular with functionalized BP. Though efforts were made to covalently modify the surface of BP and establish effective functionalization protocols (see Section 1.4.4), the actual nature of the species formed is often uncertain. Furthermore, the few reports concerning the use of metal complexes to decorate BP [1,2] mainly glossed over structural investigations. Thus, merging the separate fields of low-nuclearity catalysis and BP chemistry, the molecular functionalization of BP with a Pd complex was studied, exploiting EXAFS, HAADF-STEM, XPS methods and DFT calculations to unravel the structure of the new functionalized 2D-material. Given the scarce Lewis basicity of BP and the steric concerns arising from the orientation of its lone pairs, a small and substitutionally labile organometallic precursor is necessary to allow for an easy interaction with the layers, hence the allylic dimer complex $[Pd(\eta^3\text{-}C_3H_5)Cl]_2$ (DIM) was chosen. The latter is a common air-stable Pd complex, which easily undergoes opening of the chloride bridge in presence of suitable two-electron donor ligands, L (see Scheme 1) [3].

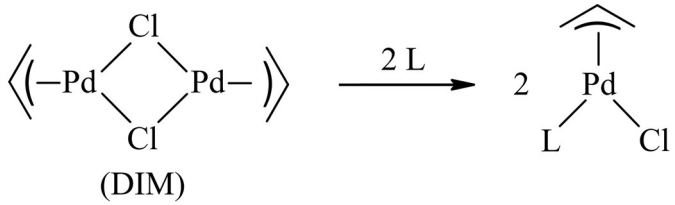

(DIM)

Scheme 1. Schematic representation of the substitutional opening of DIM.

Functionalization of 2D BP with DIM was carried out under mild conditions, working in dry dichloromethane (CH_2Cl_2, DCM) as solvent. DCM was chosen for being innocent and non-nucleophilic and because it easily dissolves the precursor DIM while providing stable dispersions of 2D BP. A complete structural characterization of the functionalized material (named Pd_2/BP) together with *ab*

initio modelling revealed the existence of unprecedented interlayer Pd–Pd dimers, bridging two 'phosphorene' layers. In agreement with this picture, investigations of the catalytic properties of Pd_2/BP showed that metal sites are not exposed on the surface of the flakes, thus remaining inaccessible to larger substrates. Conversely, testing Pd_2/BP for Hydrogen evolution reaction (HER) in acidic medium, a high enhancement in the electrocatalytic activity was observed in comparison to the pristine material.

3.2 Material synthesis

3.2.1 Preparation of 2D BP

The synthesis of bulk BP and its exfoliation in DMSO were carried out as previously described in Section 2.2.1. Washing cycles to remove DMSO were performed as follows: the suspension obtained after LPE (5 mg/5 mL_{DMSO}) was centrifuged at 9500 rpm x 30 minutes to isolate 2D BP as a solid residue. The solid was resuspended in deaerated ethanol with ultrasounds (5 min), then collected by centrifugation. This washing cycle was repeated 4 times in total, using acetone instead of ethanol in the fourth step. The solid was dried under vacuum for 24 h, before an additional final washing with distilled and deaerated DCM was performed.

3.2.2 Functionalization of 2D BP with DIM

In a typical procedure, 5 mg (0.161 mmol) of 2D BP were suspended in 8 mL of CH_2Cl_2 with ultrasonic treatment and the resulting suspension was added under inert atmosphere to a Schlenk flask charged with 6 mg of DIM (0.033 mmol, P/Pd molar ratio = 5) and a magnetic stir bar. The mixture was stirred in the dark for 18 h at RT. After this time, the suspension was transferred under inert atmosphere in a centrifuge tube and the solid material (Pd_2/BP) was collected by centrifugation (9500 rpm x 30 min). Then it was redispersed in fresh DCM (8 mL) using a spatula[1] in order to wash it, and isolated by centrifugation. This washing cycle was repeated 3 times in total. The solid was dried in vacuum and stored under inert atmosphere. ICP-AES analysis revealed a Pd/P molar ratio of 3.3 % (material named Pd_2/BP 3%). Carrying out the reaction under reflux (~ 40 °C) gave a Pd content of 6.2 % (material named Pd_2/BP 6%).

[1] This was meant to avoid the potential decomposition/modification of the newly formed adducts between phosphorus and metal.

3.3 Characterization and discussion

Given the existence of molecular complexes with general formula [Pd(η^3-C_3H_5)(L)Cl] [4-6] and [Pd(η^1-C_3H_5)(LL')Cl] (see Figure 56a,b) [7-9], prepared by the addition of one equivalent of the mono- or bidentate ligand L or LL', respectively, to DIM, a straightforward grafting of the fragment {Pd(C_3H_5)Cl} to the surface of BP might be anticipated. In Figure 56c,d, the optimized structures of two candidate adducts between 1L-BP (phosphorene) and {Pd(C_3H_5)Cl} are shown. As calculated by DFT methods, both these structures are more stable than the isolated reagents, which adds credibility to the working hypothesis to look for the preparation of phosphorene complexes supporting the {Pd(C_3H_5)Cl} moiety. The allyl ligand in such species could indeed bind to the metal either in a trihapto or a monohapto mode, depending on the hapticity of phosphorene itself. In both cases, the Pd(II) center features a square planar coordination geometry with 16 valence electrons.

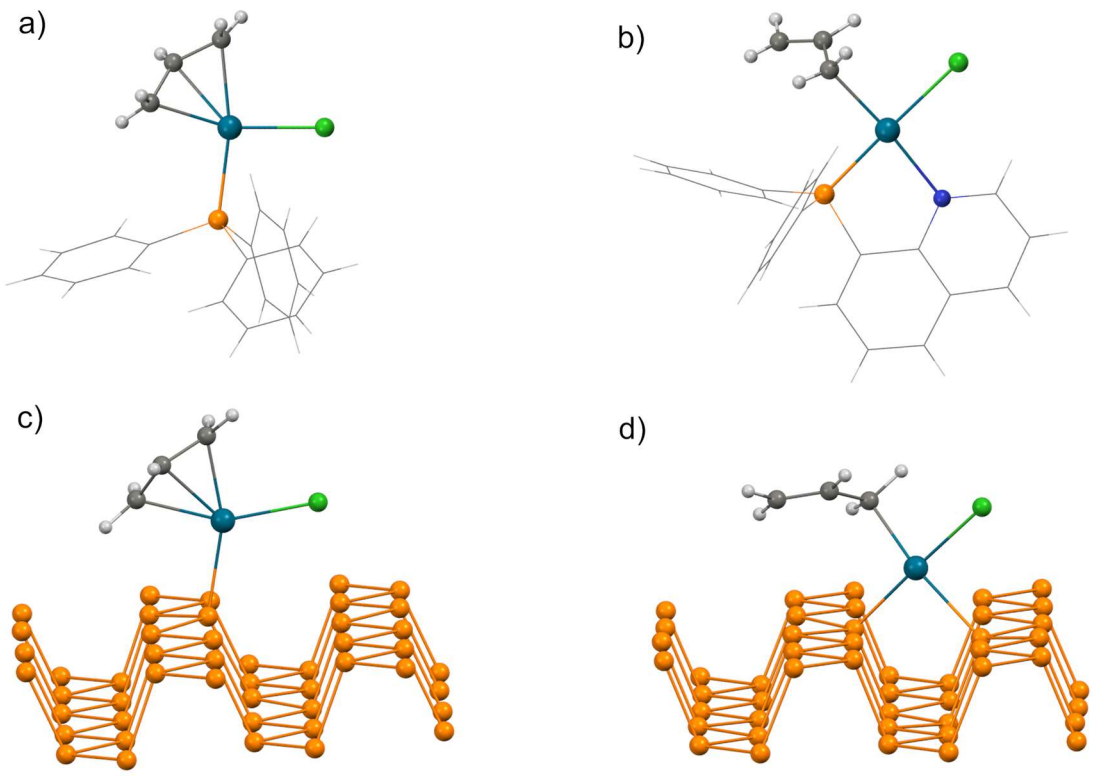

Figure 56. Representative X-ray structures of: (a) a [Pd(η^3-C_3H_5)(L)Cl]-type complex (L=PPh_3, CCDC 1102348) and (b) a [Pd(η^1-C_3H_5)(LL')Cl]-type complex (LL'= 8-diphenylphosphinoquinoline, CCDC 771053). c,d) Optimized structures (B3LYP level of theory) of the adducts between {Pd(C_3H_5)Cl} and 1L-BP.

However, the amount of Pd immobilized on 2D BP upon functionalization (3.3% mol at RT) casted some doubts on this description. Perplexity comes out from considering that exfoliated BP prepared as described in Section 3.2.1 features flake thickness within the range 2-30 nm (corresponding to *ca.* 5-58 layers). Even assuming to deal with an ideal exfoliated material, only consisting of thin BP flakes with

thickness 2 nm (5 layers), the number of exposed surface P atoms (P_{surf}) would be 1/5 of the total. If the Pd/P ratio in the sample is taken as 3.3% (experimental value) and we take into account a *surface* functionalization, it turns out a Pd/P_{surf} ratio of 0.16, corresponding to *ca.* 1 Pd atom every 6 P_{surf}. Considering a flake thickness of 10 nm (19 layers), which is still below the found experimental average, the Pd/P_{surf} ratio would be 0.66 (2 Pd atoms every 3 P on the surface). Both these values look inconsistent with surface grafting, unless some Pd aggregate is also present (*i.e.* Pd NPs or PdP_x phases). As this latter would represent a stimulating working hypothesis, it was decided to carry out an in-depth investigation of this new material getting insights on the morphology of the Pd_2/BP compound by electron microscopy studies. Figure 57a,b shows SEM and TEM images of Pd_2/BP. The BP flakes look perfectly intact after functionalization, keeping their overall morphology unaltered. Notably, no presence of Pd NPs could be detected via TEM.

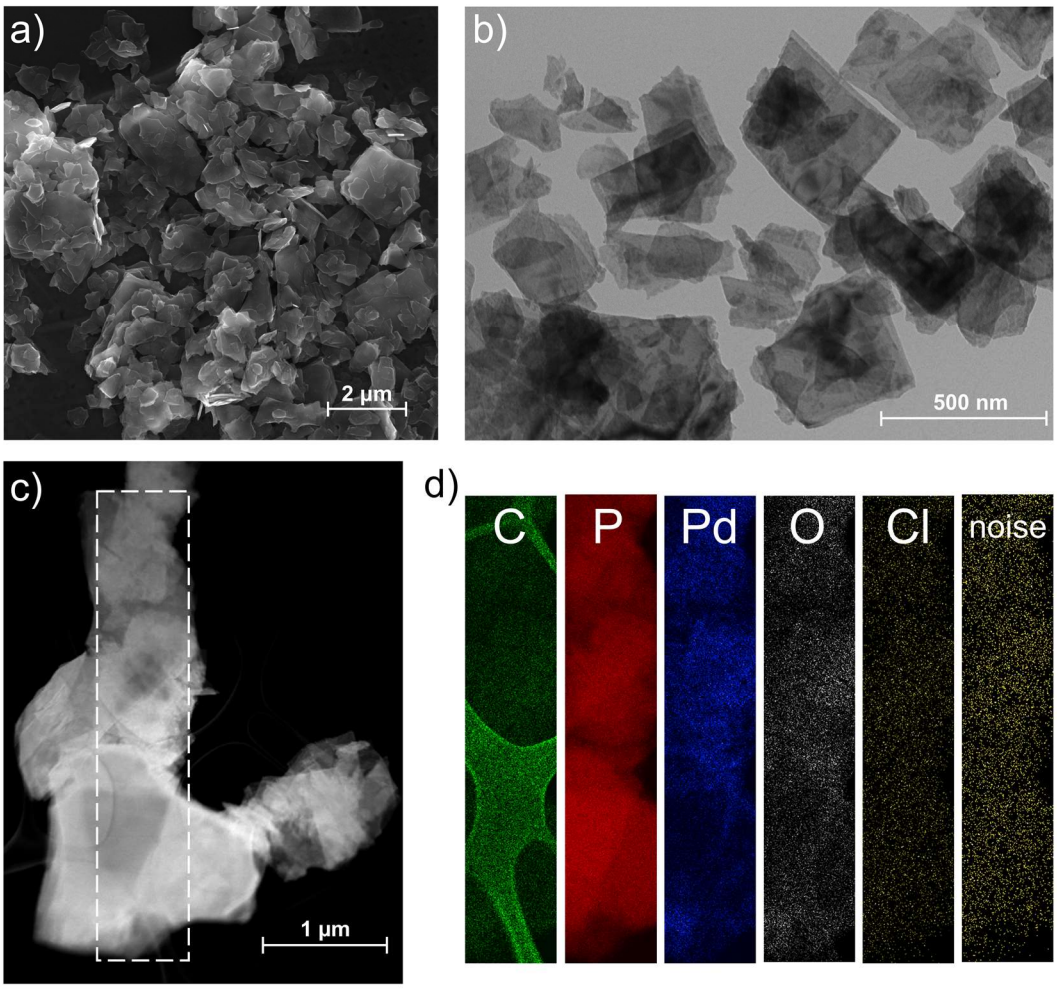

Figure 57. a) SEM and (b) TEM imaging of Pd_2/BP 3%. (c) HAADF-STEM imaging of a flake aggregate dropcasted on carbon grid. d) EDS mapping of the region highlighted in (c). The underlying carbon grid is visible in the C elemental mapping.

EDX spectroscopy was used to study the elemental composition of Pd_2/BP on a nanometric scale. The resulting EDX mappings are shown in Figure 57d. As it turned out, Pd is homogeneously distributed

within a flake, pointing at a very dispersed form of the metal, possibly on the atomic or polyatomic level. Minor presence of oxygen was also observed, due to some unavoidable BP oxidation from sample handling. Excitingly, no presence of chlorine was detected in the material, as its integrated EDS signal was below the noise level, feeding doubts on the working hypothesis about the occurrence of $\{Pd(C_3H_5)Cl\}$ grafting to the 2D BP surface. Since exceedingly small metal NPs and clusters could be missed under survey TEM analysis, high resolution morphological investigations were performed via annular dark field microscopy (HAADF-STEM). Figure 58 shows the high-resolution micrographs taken on Pd_2/BP 3% and 6%. The image in Figure 58d was FFT filtered to enhance resolution, whereas image in Figure 58f is generated from the raw data of Figure 58e upon FFT filtering and false-colour display (warmer colours correspond to higher Z). As can be observed, high-Z domains (brighter colours) look dispersed in the areas under study. Remarkably, the lattice structure of BP is perfectly distinguishable even within high-Z regions (*i.e.* with a higher local concentration of palladium). This can be nicely appreciated from Figure 58d. This finding would be consistent with atomic or molecular functionalization of the flakes, ruling out the presence of both Pd–Pd crystalline domains and Pd-containing amorphous structures such as Pd_xP_y phosphides. The latter would appear otherwise superimposed to the lighter BP lattice in the image, making it look distorted or obscured. At the same time, this evidence proves again the integrity of the BP lattice upon functionalization.

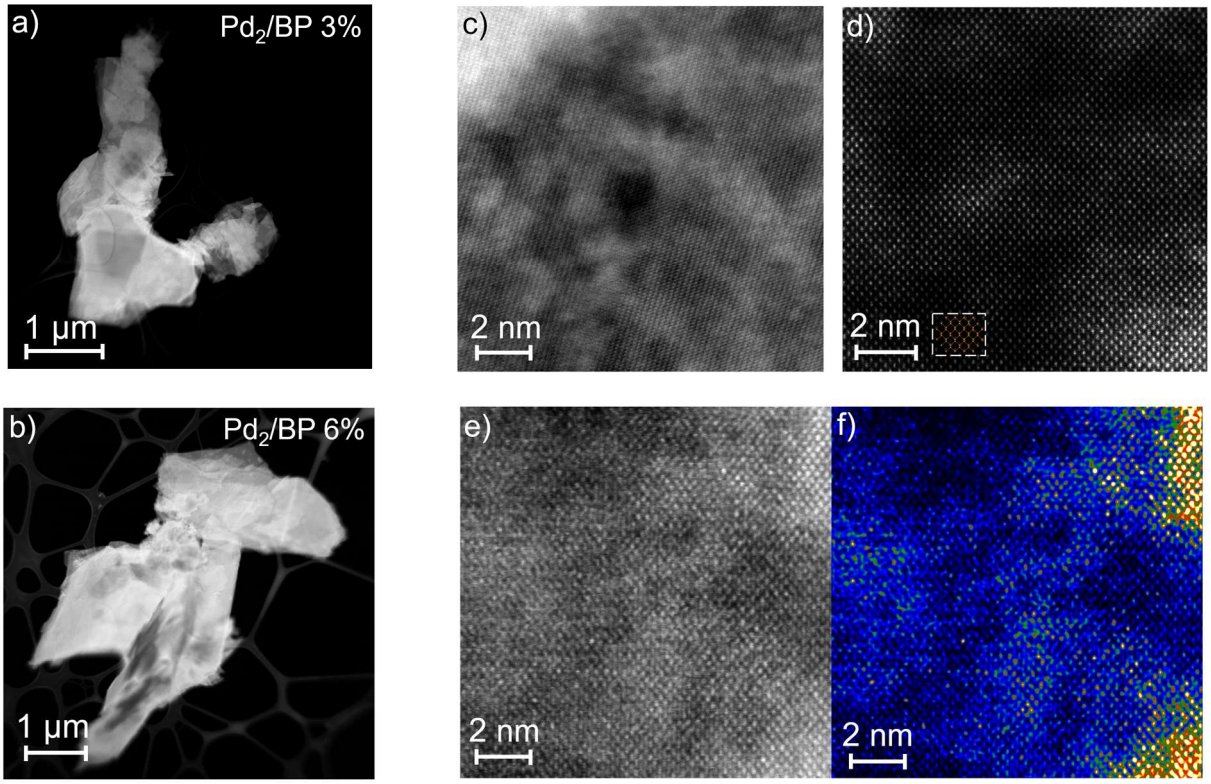

Figure 58. HAADF-STEM characterization of Pd_2/BP at different Pd loadings. Flakes stacking from Pd_2/BP 3% (a) and Pd_2/BP 6% (b) obtained by drop-cast of DCM dispersions on carbon grid. High resolution micrograph of a flake from Pd_2/BP 3% (c) and Pd_2/BP 6% (d, FFT filtered). The inset next to the scale bar in (d) shows the orientation of the BP lattice. Pd-rich areas are distinguished by the higher Z-contrast (brighter areas). e) Micrograph taken from a Pd_2/BP 6% flake (raw data) and (f) corresponding image displayed in false-colours (warmer colour = higher Z).

EELS spectroscopy is a powerful technique for elemental microanalysis, particularly to detect light elements. To further check the absence of chlorine in Pd_2/BP, comparative EELS measurements were carried out on a nanometric scale, confronting Pd-rich areas with Pd-free ones (see Figure B3, Appendix B). The EELS spectra recorded are indistinguishable in the region around 200 eV, corresponding to the expected value of the Cl *L*-edge, with no detectable feature pointing to the presence of chlorine alongside palladium, which unquestionably rules out the presence of chlorine in the palladated adducts on BP.

Since electron microscopy provides information on the local structure of the sample under investigation, to firmly exclude the presence of nanoparticles and further assess the integrity of the BP lattice, bulk techniques were also exploited. Thus, powder X-ray diffraction (XRD) analysis was performed on the material and the recorded spectrum is displayed in Figure 59a, featuring the typical pattern of pristine 2D BP with intense (0*k*0) reflections as an effect of preferential orientation inside the sample (see Section 1.2.3). In detail, the three main peaks located at $2\theta° = 16.9°$, 34.2° and 52.3° correspond to the (020), (040) and (060) reflections of BP, respectively, which suggests the retainment of the BP crystallinity after functionalization. Furthermore, no presence of additional phases could be observed in the XRD spectrum, contrary to Pd NPs/BP previously described (see Figure 49, Section 2.3).

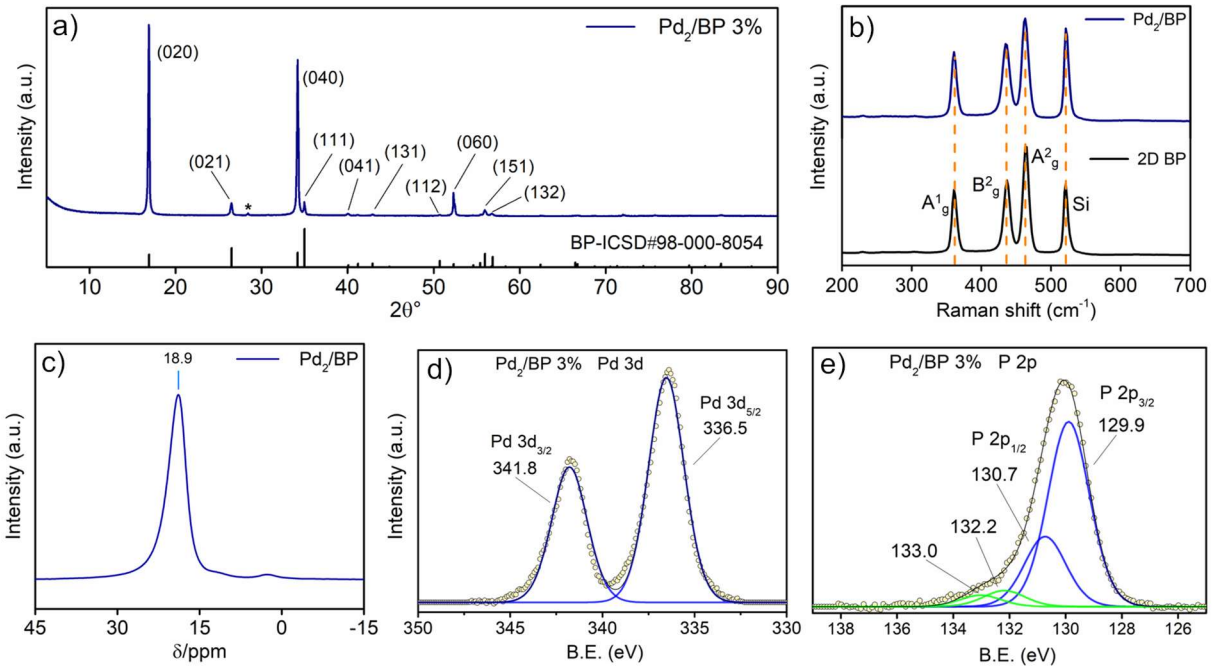

Figure 59. Solid state characterization of Pd_2/BP 3%. a) Powder XRD spectrum. The reference pattern at the bottom corresponds to orthorhombic BP. The peak marked by an asterisk is a sample holder impurity. b) Average Raman spectra of the functionalized material (top) and pristine 2D BP (bottom). c) ^{31}P DE-MAS NMR spectrum. d) Core level Pd 3d and (e) P 2p XPS spectra.

Further studies via lattice-sensitive techniques such as Raman and ^{31}P DE-MAS NMR spectroscopies agreed with the XRD analysis. In particular, the Raman spectrum of Pd_2/BP (Figure 59b), averaged within a set of 15 distinct flakes to account for the polydispersity of the pristine material, features three

characteristic peaks at 360.7, 436.6 and 466.8 cm^{-1}, corresponding to the A^1_g, B_{2g} and A^2_g phonon modes of exfoliated BP, respectively. No relevant frequency shifts were observed compared to pristine BP. ^{31}P DE-MAS NMR measurements (MAS frequency 20 KHz) revealed an intense peak at 18.9 ppm (Figure 59c), typical of exfoliated BP (see Section 1.3), in addition to minor humps at 11.5 and 2.4 ppm (about 1.5 % of the whole area). The latter were attributed to oxidized products, phosphite and phosphate species, respectively, arising from minor surface oxidation during sample manipulation.

To probe the electronic state of phosphorus and palladium in the material, XPS measurements were carried out at the Pd 3d and P 2p core levels. The Pd 3d spectrum of Pd_2/BP 3% shown in Figure 59d could be fitted with a single spin-orbit doublet, with Pd $3d_{5/2}$ component at binding energy (B.E.) = 336.5 eV and the Pd $3d_{3/2}$ component at B.E. = 341.8 eV, suggesting the existence of one single Pd environment. Compared with the precursor complex DIM (see Figure B8, Appendix B), featuring a Pd centre with oxidation state +II, $3d_{5/2}$ and $3d_{3/2}$ components in Pd_2/BP are shifted at lower binding energies by 0.7 eV, pointing to a more reduced state of Pd. Furthermore, these B.E. values are halfway between common Pd(II) compounds and bulk metallic Pd(0) [10], which further stressed the exclusion of Pd NPs [11]. Notably, increasing the Pd content from 3% to 6% had no effect on the Pd 3d spectrum of Pd_2/BP (see Figure B9a, Appendix B), within the experimental error, suggesting an equivalent chemical state of Pd in the two samples. The results of Pd 3d XPS analysis of these materials are summarized in Table 3 below for easier comparison.

Sample	***Pd $3d_{5/2}$ (eV)***	***Pd $3d_{3/2}$ (eV)***
DIM	337.2	342.5
Pd_2/BP 3%	336.5	341.8
Pd_2/BP 6%	336.7	342.0
Pd NPs†	335.8	341.0

Table 3. Experimental Pd 3d binding energies. † The values correspond to metallic Pd(0) core of the NPs (see Section 2.3).

The P 2p core level spectrum in Figure 59e (Pd_2/BP 3%) features two intense peaks at 129.9 and 130.7 eV, assigned to $P2p_{3/2}$ and $P2p_{1/2}$ of pristine BP atoms. In addition, two minor peaks are visible in the spectral deconvolution at 132.2 and 133.0 eV. This region is highly diagnostic of coordinative interactions involving phosphorus atoms [11,12], hence these peaks were assigned to Pd–P bonds. Correspondingly, increasing the extent of functionalization (from 3 to 6 %) led to a growth in its relative contribution (see Figure B9b, Appendix B). PdP_x phases could be firmly ruled out, since no peaks at lower B.E. values than pristine BP were observed in the core level P 2p spectrum, contrary to MP_x – BP heterostructures previously reported [13,14]. Furthermore, the survey XPS spectrum of Pd_2/BP (Figure B7, Appendix B) confirmed the absence of chlorine.

This last issue, established via EDX, EELS and XPS, strongly questioned also the presence of the allylic moiety as well. To clarify this fundamental point, ^{13}C CP-MAS NMR measurements were carried out on 2D BP functionalized with ^{13}C-labelled DIM. The latter was prepared starting from 1-^{13}C-allyl alcohol as described in Appendix B. Interestingly, no signal consistent with the isotopically enriched allyl ligand was detected within the range 30-140 ppm. Notably, the only spectral feature present is a broad signal in the 30-50 ppm region arising from ^{13}C nuclei in natural abundance, likely corresponding to residual solvent molecules remained adsorbed on the flakes. This is in accordance with FTIR-ATR spectra recorded on 2D BP before and after functionalization, showing weak ν_{C-H} stretches between 2840-2950 cm^{-1} (see Figure 60b) as well as with ^{1}H NMR MAS measurements (Figure B10a).

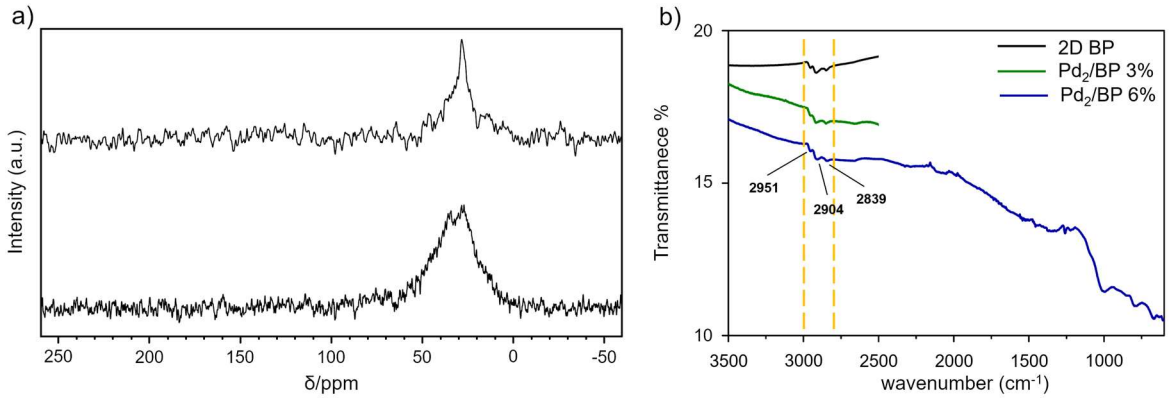

Figure 60. a) ^{13}C CP- (bottom) and DE- (top) MAS spectra of Pd_2/BP 3% prepared from ^{13}C-labelled DIM. b) FTIR-ATR spectra of Pd_2/BP and pristine BP (the plots of 2D BP and Pd_2/BP 3% are reported on different vertical scales).

Since elemental analysis and ^{13}C NMR together ruled out the permanence of both chloride and allyl ligands in the coordination sphere of Pd, it is likely that DIM is involved in a reductive elimination of allyl chloride upon interaction with 2D BP. The problem then arises to infer the actual structure of Pd-sites in the functionalized material in view of the XPS data that pointed to a well-defined Pd environment. Since Pd(0) aggregates were firmly excluded, the occurrence of interlayer structures should be considered to account for the high concentration of the metal, with Pd atoms lying between two phosphorene layers. Indeed, BP intercalation compounds have been reported for alkali metals, namely Li, Na, K, Rb, Cs [15-17], though the latter compounds are better described as formed by a reduced BP^{-} lattice with intercalated M^{+} ions. In 2016 B. Özyilmaz *et al.* [18] reported the doping of a BP flake with Cu atoms via ALD and showed with DFT calculations that single interlayer Cu atoms, alongside surface adatoms, are possible outcome of the ALD process. To gain insights on the Pd coordination shell, X-ray absorption measurements were carried out at the Pd K-edge. Figure 61 shows the k-weighed EXAFS spectra (left) and the corresponding Fourier transforms (right) of Pd_2/BP 3% and 6%. Regardless the metal loading, the FT spectrum of Pd_2/BP shows a first shell coordination just below R = 2 Å, which could be fitted using Pd–P bonds, and a second shell peak below R = 3 Å, safely assigned to Pd–Pd scattering. The accurate bond distances obtained after data fitting and phase correction for

Pd_2/BP and DIM are reported in Table 4. Additional structural parameters of reference materials, according to previous measurements (see Chapter II), are also shown for comparison. Notably, Pd_2/BP 3% and 6% look identical on XAS analysis, suggesting that the coordination sphere of Pd is the same in the two samples, in perfect agreement with XPS evidence.

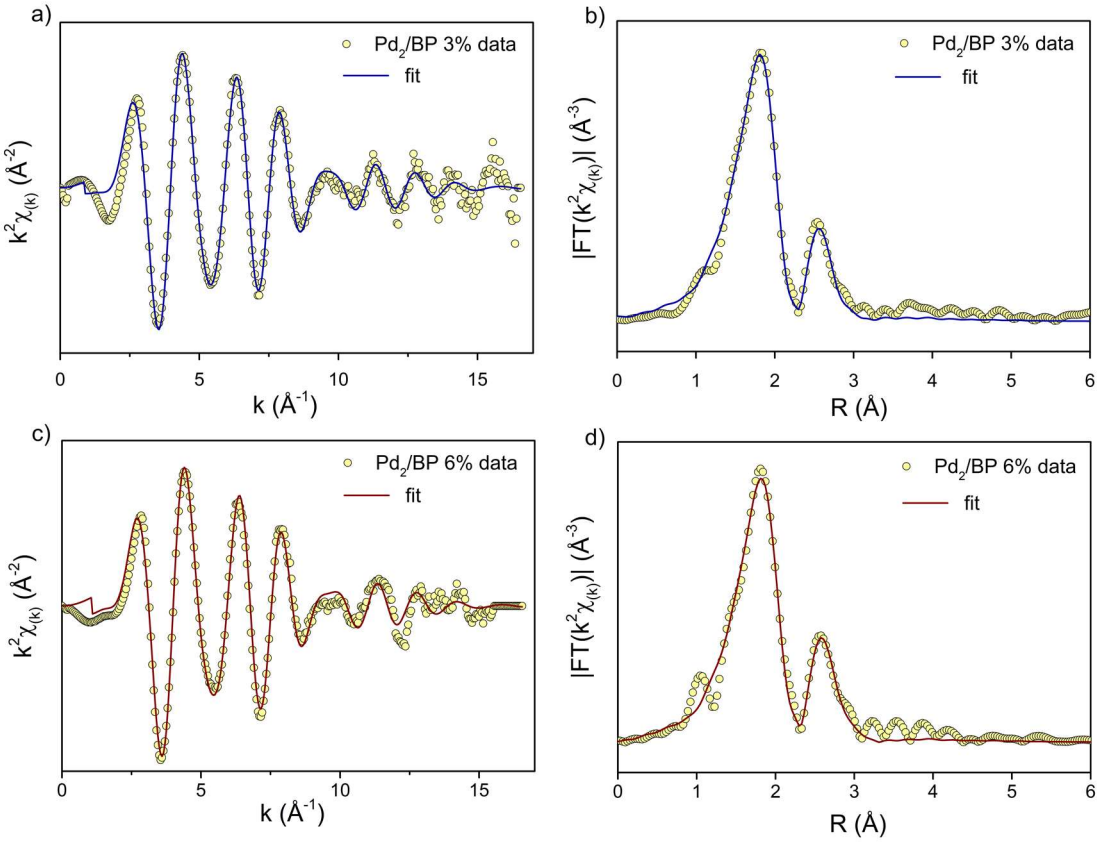

Figure 61. XAS characterization of Pd_2/BP 3% (a, b) and 6% (c, d) at the Pd-K edge. k-weighed EXAFS spectra are shown on the left, the magnitude of their Fourier transforms on the right. Dots are experimental data; continuous lines correspond to the best calculated fit.

The Pd–P distance of 2.34(1) Å in Pd_2/BP points to a quite strong interaction between Pd and BP, consistently with the proven ability of BP to take part in coordinative bonds (see Chapter II). Remarkably, the second shell of Pd features a Pd–Pd distance of 2.82(1) Å, a value which is appreciably larger than the observed separation in metallic Pd(0) (2.751 Å [19]), as also measured in bulk Pd foil (2.74 ± 0.01 Å) and in Pd NPs/BP (2.73 ± 0.02 Å). This discrepancy allows to ultimately rule out the presence of Pd NPs in the system Pd_2/BP, in agreement with all the other techniques, particularly HAADF-STEM and XPS. The Pd–P distance itself, being 2.34(1) Å in Pd_2/BP, is only slightly elongated compared to the value of 2.26(3) Å of Pd(0) NPs/BP. The obtained coordination numbers (CNs) associated to these bonds are extremely valuable to infer a coherent structural model. Remarkably, Pd–P and Pd–Pd CNs have almost integer values, of 3 and 1 respectively, nicely reproduced in the two samples Pd_2/BP 3% and 6%. This points to the existence of well-defined Pd environments, in which

every Pd atom is simultaneously bonded to three P ligands, with average Pd–P distance 2.34(1) Å, and to a second Pd centre at 2.82(1) Å.

Sample	*Path*	*CN*	*r (Å)*	*σ² (Å²)*
Pd_2/BP 3%	Pd–P	2.8(2)	2.34(1)	0.0076(7)
	Pd–Pd	0.8(2)	2.82(1)	0.011(2)
Pd_2/BP 6%	Pd–P	2.7(2)	2.34(1)	0.0078(7)
	Pd–Pd	1.1(3)	2.83(1)	0.012(2)
DIM‡	Pd–C	1.6(3)	2.11(1)	0.0014(2)
	Pd–Cl	2.0(3)	2.41(1)	0.006(2)
	Pd–Pd	3(2)	3.48(3)	0.019(8)
Pd NPs†	Pd–P	1.7(6)	2.26(3)	0.0018(6)
	Pd–Pd	8(2)	2.73(2)	0.0016(4)
Pd foil†	Pd–Pd	12	2.74(1)	0.0059(4)

Table 4. Structural parameters extracted from EXAFS data fitting. Numbers in brackets represent the error on the last digit. ‡ See also Appendix B. † Data from Chapter II.

This finding was very intriguing, since recently discrete dual atom systems are attracting great interest, mainly in view of their potential catalytic applications. Both heteronuclear [20,21] and homonuclear examples have been described, including Fe_2 [22] and Pt_2 [23] examples, but Pd_2-containing materials are almost unexplored. The layered structure of BP with an interlayer distance of 5.2 Å has the possibility of hosting metal atoms or small molecules. Since the overall integrity of the lattice is preserved after functionalization, as pointed out experimentally, the candidate structure should cause only slight distortions. Different models featuring a Pd_2 dimer sandwiched between two phosphorene layers were therefore considered and optimized through a computational analysis. In view of the maintenance of the phosphorene lattice, it is reasonable that the Pd_2 unit must lie parallel to the channel, since otherwise orthogonal arrangement would cause a rather severe elongation of the interlayer distance, which clearly contrasts with the experimental evidence.

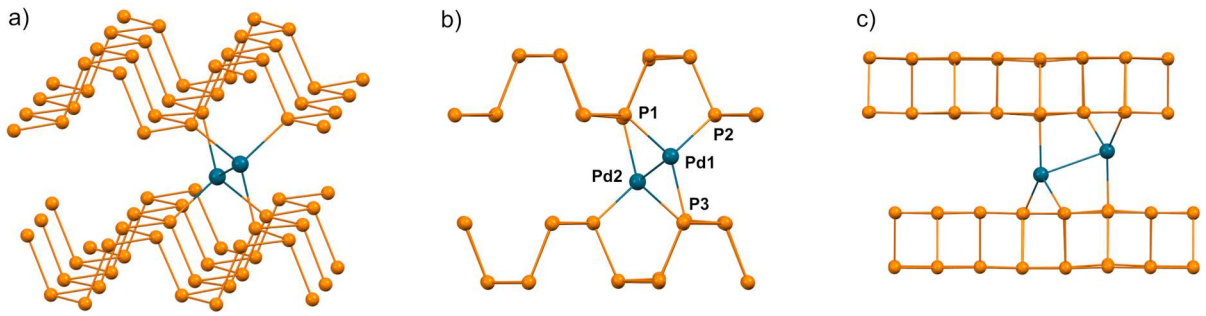

Figure 62. a) DFT optimized model of Pd_2/BP featuring a trigonal-planar ligand geometry around Pd. Different views of the same model along the *zigzag* (b) and armchair (c) directions are shown. Interatomic distances (Å) in (b): Pd1–Pd2 = 3.015; Pd1–P1 = 2.345; Pd1–P2 = 2.367; Pd1–P3 = 2.372.

Different isomers have been modelled with energy variation not higher than 2 kcal mol^{-1} to each other, pointing out a substantial flatness of the potential energy surface (PES) associated to the hosting of Pd_2 between two layers. All the isomers feature a Pd–Pd distance in the range 2.8-3.0 Å, Pd–P distances of 2.3 Å, and Pd–P coordination number between 3 and 4, in fair agreement with EXAFS structural parameters. For the sake of clarity, Figure 62 shows one of the most likely isomer, with a Pd–Pd distance of 3.01 Å and a trigonal planar coordination of phosphorus around each metal center, typically associated to Pd(0), with a staggered conformation of the Pd–P network of bonds. Notably, such an arrangement does not significantly perturb the lattice of phosphorene, the inter-layer distance being elongated by *ca.* 0.55 Å only. A flatness of the PES with respect to metal-metal distance is not completely unknown and earlier experimental and computational investigation [24] highlighted a similar behaviour for some Pt clusters, in which large variation of the Pt–Pt bonds were induced by small variation in chemical conditions, such as the nature of crystallization solvent. An important feature of phosphorene among other 2D-materials is its band gap dependence from the number of the stacked layers (see above, Section 1.2.1), ranging from the upper limit of ~ 2 eV in the monolayer to ~ 0.35 eV in the bulk material. Band gap modulation of phosphorene can also be achieved after covalent functionalization with Lewis acidic species [25]. In the present case, B3LYP-DFT calculations predicted a band gap of *ca*. 2.16 eV for phosphorene, which reduces to 1.86 eV upon interaction with the Pd_2 unit. This can be reasonably accounted for by the newly presence of filled Pd d-levels at the top of the valence band of phosphorene. Since the conduction band is expected to be almost unaltered, the net result is a decreased band gap.

3.4 Catalytic activity

3.4.1 Hydrogenation of alkenes and alkynes

The interlayer location of Pd_2 units in Pd_2/BP was further and indirectly confirmed by *ad-hoc* catalytic studies performed on Pd_2/BP. Although Pd_1-SACs [26-28], Pd(0) NPs [29-31] and PdP_x [32] heterogeneous systems are known to be effective catalyst for the hydrogenation of C≡C and C=C bonds, Pd_2/BP resulted completely inactive in these reactions. In detail, the catalytic activity of Pd_2/BP suspended in DCM was evaluated for the hydrogenation of phenylacetylene and 1-octene (substrate to catalyst ratio = 100) at room temperature. Notably, a null conversion was measured via GC-MS analysis even over a period of 17 h. To evaluate the stability of Pd_2/BP under H_2 atmosphere, a blank suspension of Pd_2/BP in the same solvent was stirred under 5 bar of H_2 for 1 h, then XPS measurements were performed on the recovered material. The core level Pd 3d spectrum (Figure 63a) showed a prominent component with Pd $3d_{5/2}$ = 336.7 eV and Pd $3d_{3/2}$ = 342.0 eV, corresponding to the unaltered Pd_2 in Pd_2/BP, alongside a minor Pd(II) component with Pd $3d_{5/2}$ = 338.1 eV and Pd $3d_{3/2}$ = 343.4 eV, possibly

due to some formed hydridic species [33]. Remarkably, no peaks corresponding to bulk Pd(0) were visible, suggesting that under H_2 atmosphere the system is stable toward the formation of Pd nanoclusters. Indeed, the presence of Pd(0) NPs would likely result in some conversion of the substrate in agreement with the results shown in Chapter II, but this was not observed. Thus, the lack of activity of Pd_2/BP is reasonably due to the morphology of Pd_2/BP, since the Pd_2 active sites remain embedded within the layers of phosphorus atoms and are then inaccessible to most substrates.

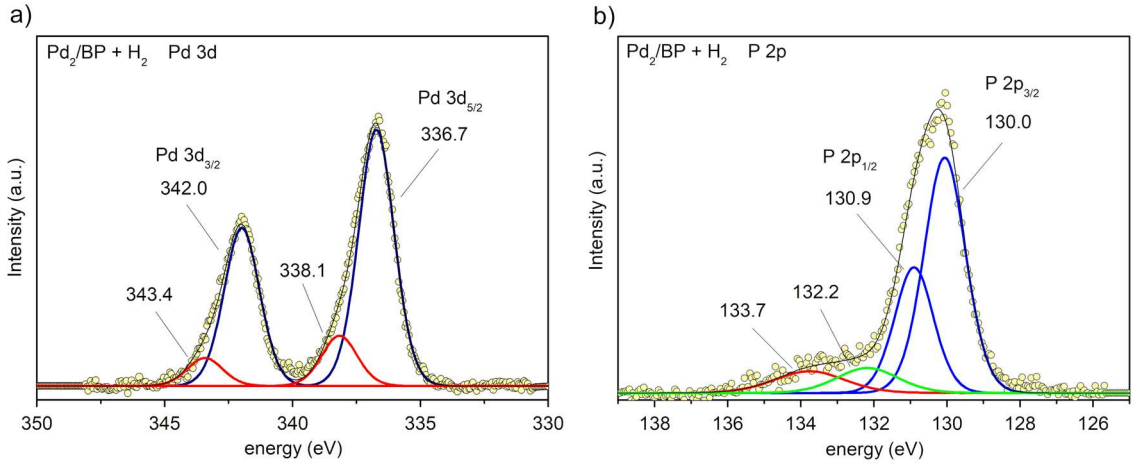

Figure 63. XPS characterization of Pd_2/BP after treatments with H_2 (5 bar for 1 h). a) Core level Pd 3d and (b) P 2p spectrum. The red peak visible in the P 2p deconvolution is likely due to some oxidation from sample manipulation during work-up procedures.

3.4.2 Application in HER

Due to its unique electronic properties (see Section 1.2.1), black phosphorus has received increasing attention for its application in energy conversion [34], including electrochemical energy storage and electrocataysis [35,36]. Notably, 2D BP dropcasted on a GCE electrode was shown to promote the hydrogen evolution reaction (HER) [37,38], though pristine 2D BP is not strongly active itself and performances are highly affected by two issues: a) ambient instability, b) strong tendency of BP flakes to aggregate when deposited on a surface with subsequent reduction of the surface area. To enhance the electrocatalytic activity of BP, surface modifiers such as metal NPs are also usually employed. Since HER in acidic media formally involves the reduction of small H_3O^+ cations, Pd_2/BP was tested in this process and compared with the pristine material. Catalyst evaluation was carried out using a three-electrode cell with a rotating disk working electrode (RDE), a commercial Ag/AgCl reference electrode and an Au gauze as counter electrode (see also Appendix B). The catalyst material was dropcasted above the glassy carbon (GC) surface of the RDE, then a thin Nafion film was applied with a 0.5%$_w$ Nafion solution in 2-propanol to ensure a better adhesion to the GC surface. As shown in Figure 64a, 2D BP prepared according to Section 3.2.1 has a poor activity for HER in 0.5 M H_2SO_4. The observed onset

potential E_{onset} is -0.13 V vs RHE and the maximum current density recorded at -0.6 V vs RHE is about -500 µA cm^{-2}.

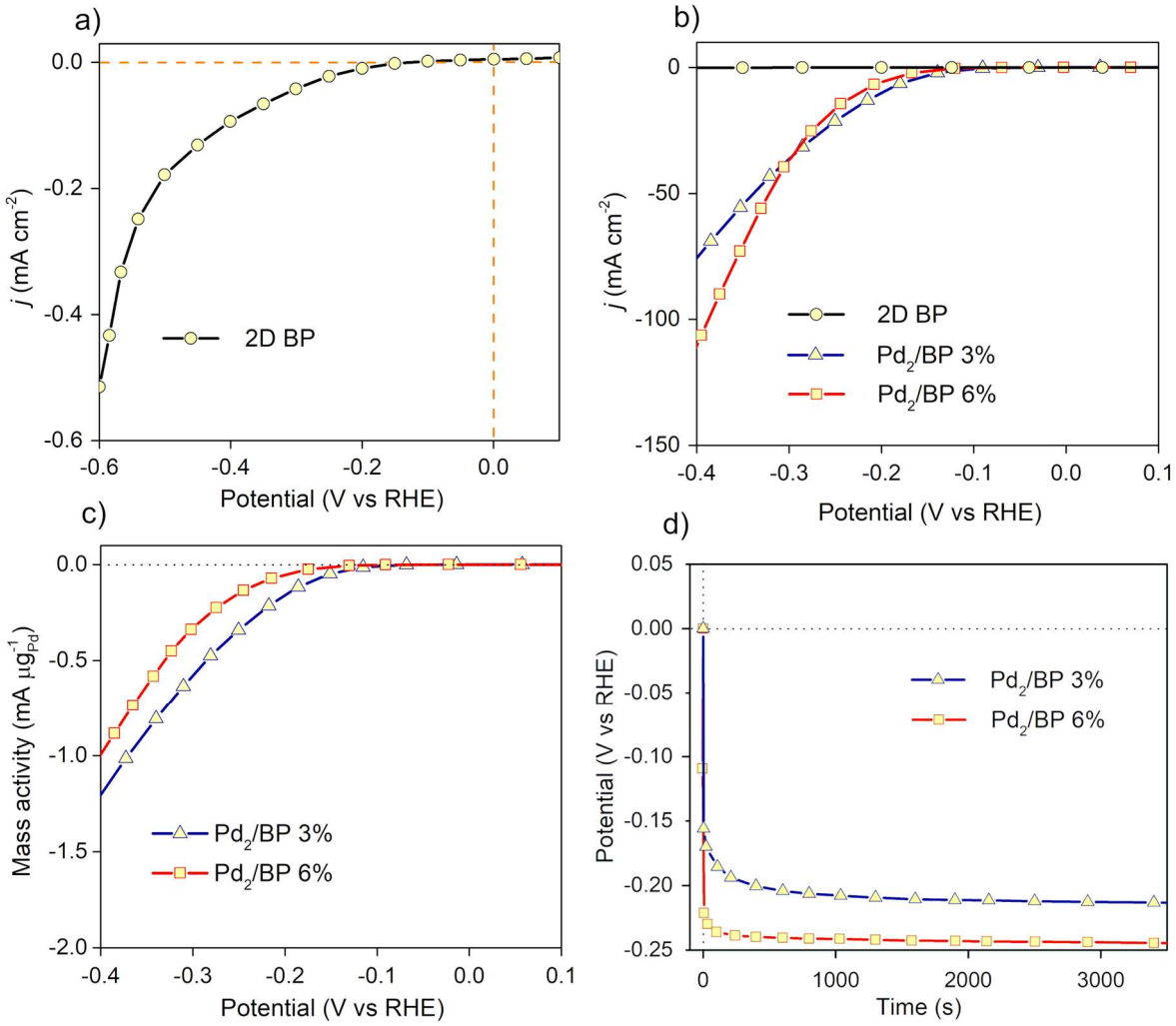

Figure 64. Electrocatalytic activity of 2D BP and Pd_2/BP in HER from 0.5 M H_2SO_4. a) Linear sweep voltammetry (LSV) of 2D BP. Scan rate 1 mV s^{-1}, 1600 rpm RDE rotations. b) Comparison of the LSV activity of 2D BP and Pd_2/BP 3% and 6%. c) LSV normalized to the Pd content. d) Chronopotentiometries at -1 mA (-5 mA cm^{-2}) for 3600 s, 1600 rpm RDE rotations.

On the other hand, Pd_2/BP showed a superior activity for HER compared to pristine 2D BP, as shown in Figure 64b. Both Pd_2/BP 3% and 6% have an onset potential E_{onset} = -0.1 V vs RHE, similar to the one recorded for 2D BP but they reach current densities one order of magnitude higher than the pristine material, namely -110 mA cm^{-2} at -0.4 V vs RHE and -75 mA cm^{-2} at -0.4 V vs RHE for the 6% and 3% catalyst, respectively. Thus, the presence of discrete interlayer Pd_2 units has an active role in promoting the hydrogen evolution reaction. Since the metal loading is related to the current density recorded during the measurements, the LSV voltammograms in Figure 64c were normalized to the palladium content of each catalyst (mass activity). Upon normalization, the two catalysts Pd_2/BP 3% and 6% show a very similar activity, suggesting that the HER is limited solely by the number of Pd active sites on the catalyst. This observation provides an indirect confirmation of their structural analogy, in accordance with

previous structural characterization. Catalyst stability during hydrogen evolution was investigated through galvanostatic experiments, applying to the working electrode a constant current load of -1 mA (5 mA cm^{-2}) for 3600 seconds. As reported in Figure 64d, Pd_2/BP is stable during one hour of electrolysis, with no electrochemical evidence of catalyst alteration under working conditions. To better assess this point, the exhaust 3% catalyst was recovered cleaning the working electrode in 2-propanol with ultrasounds and its morphology was studied via HAADF-STEM. As it turned out, the catalytic process does not affect the overall morphology of the material (see Figure 65), which still features intact flakes with Pd homogeneously dispersed (see EDS map in Figure B4, Appendix B) and absence of metal aggregates, as also revealed by high-resolution imaging, in nice agreement with the electrochemical evidence. Partial oxidation of BP, as well as signs of amorphization observed along the edges of some flakes (see Appendix B), likely arise from the extensive manipulation following catalyst recovery in 2-propanol.

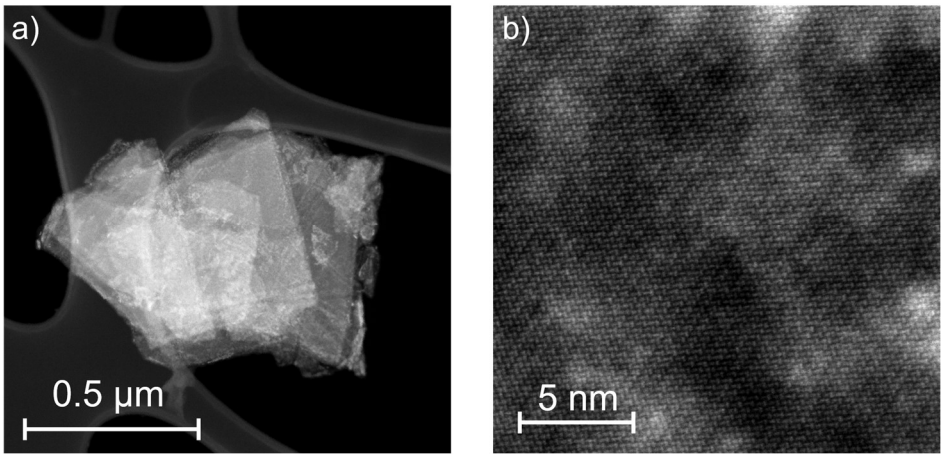

Figure 65. Flakes of Pd_2/BP 3% exhaust catalyst recovered after chronoamperometric experiments, dropcasted above a carbon grid. b) High resolution micrograph taken from the flake in (a).

3.5 Conclusions

In summary, aimed at synthesizing the first examples of discrete organometallic complexes decorating the P-donor surface of a phosphorene flake, an easy and reproducible functionalization protocol was individuated to decorate 2D BP with palladium, based on the use of the organometallic complex $[Pd(C_3H_5)Cl]_2$ as Pd source. While a strict confirmatory evidence was achieved that no covalently coordinated palladium complex has been retained in the final reaction product, this approach resulted in the isolation of a new compound, *i.e.* Pd_2/BP, with palladium uploading up to 6% in weight and, even more intriguing, demonstrates that the integrity of 2D BP flakes has been retained, while avoiding the formation of Pd NPs or other metal aggregates. An in-depth structural investigation was therefore carried out on the Pd_2/BP material to shed light on the structure and bonding of the metallic sites implanted in the phosphorene layers. In particular, EXAFS measurements together with DFT modelling highlighted

the existence of unprecedented interlayer Pd–Pd dimeric units. Consistently with morphological and structural analysis, reactivity studies suggested that metal sites are not exposed on the surface but embedded within the layers of the material. Remarkably, preliminary studies confirmed that Pd_2/BP behaves as an efficient catalyst in the electrochemical hydrogen evolution reaction (HER) from acidic media, strongly enhancing the intrinsic activity already observed for pristine 2D BP. Studies are in progress to better understand the reactivity of this unique dipalladium system and to extend the possible applications of this material in electronics and optics as well as to extend the chemistry leading to Pd_2/BP compound to other transition metals.

3.6 Appendix B:

B1 Synthesis and catalysis

B2 Physical Methods

B.1 Synthesis and Catalysis

B1.1 General Methods and materials. All the synthesis and manipulations involving 2D BP were performed under inert atmosphere using Schlenk line techniques. Dichloromethane (DCM) was distilled from CaH_2, stored above molecular sieves 3Å and degassed prior to use. Phenylacetylene, 1-octene and allyl chloride were purchased from Sigma Aldrich and used as received. $PdCl_2$ was purchased from Strem Chemicals. Black phosphorus (BP) was synthesized and exfoliated as described above in section 3.2.1. Allyl alcohol-1-^{13}C (99% ^{13}C) was purchased from Sigma Aldrich (100 mg batch).

B.1.2 Synthesis of $[Pd(C_3H_5)Cl]_2$ (DIM). $[Pd(C_3H_5)Cl]_2$ was prepared according to a literature method [39] and carefully purified by filtration of the first obtained DIM crop dissolved in anhydrous DCM over neutral Al_2O_3. Upon reduction of the filtered solution to a small volume and addition of dry *n*-pentane, pure DIM was obtained as a yellow crystalline powder (yield 81%). *^1H NMR (400 MHz, CD_2Cl_2, 298K):* δ = 3.05 (d, ^2J = 12.16 Hz, 2H), 4.10 (d, ^3J = 6.74 Hz, 2H), 5.50 ppm (m, 1H).

B.1.3. Synthesis of ^{13}C-labelled $[Pd(1\text{-}^{13}C\text{-}C_3H_5)Cl]_2$ (DIM*). The synthesis was carried out in two steps: First, the labelled allyl alcohol-1-^{13}C (AA*) was converted in the ^{13}C-enriched allyl chloride-1-^{13}C (AC*) and, second, the ^{13}C-labelled dimer $[Pd(C_3H_5)Cl]_2$ was synthesised from AC* (scale-down of B.1.1). Since the overall amount of purchased AA* amounted to 100 mg (~140 µL), a straightforward synthetic protocol to convert AA* in AC* avoiding any intermediate purification step (*i.e.* distillation) was necessary which imposed to revisit and improve a patented procedure [40]. The whole protocol was set up and checked using non-labelled AA before repeating the synthesis with the ^{13}C-labelled organic reagent.

Step 1) 11 mg of $PdCl_2$ (0.062 mmol, used as catalyst) were added to a short NMR tube, used as reactor, followed by 0.56 mL of HCl 37%. Once the solid was dissolved, 100 mg of AA* (1.72 mmol, $[AA^*]^{1/2}/[HCl]$= 0.19) were added, the tube was sealed, a customized refrigerator was mounted on top (see Figure B1) and the solution was heated to 80°C for 1 h. During this time, a colourless organic phase (AC*) formed which separated above the reddish acidic phase (see Figure B1).

Step 2) A glass vial equipped with a magnetic stirring bar was charged with 90 mg of $PdCl_2$ (0.51 mmol, 1 eq) and 68 mg of NaCl (1.16 mmol, 2.3 eq), followed by 410 µL of distilled water. The mixture was stirred until the palladium salt was dissolved forming soluble Na_2PdCl_4. Then, the acidic red phase at the bottom of the NMR tube was removed by syringe and discarded. 1.5 mL of MeOH were added to rinse the tube and collect AC*, which was transferred to the vial containing Na_2PdCl_4. Further 1.0 mL of MeOH was added, then CO was slowly bubbled in the solution under stirring over 1 h (see Figure B1d). A colourless precipitate formed (NaCl) while the solution turned yellow. The suspension was then poured into water (13 mL) and extracted with DCM (3 x 5 mL). The organic phases were collected altogether and washed with water (2 x 6 mL), then left 1 h standing over anhydrous $MgSO_4$. The organic phase was concentrated to *ca.* 10 mL under a nitrogen stream and filtered over Al_2O_3 (via a Pasteur pipette packed with ~ 1 cm of Al_2O_3). The filtrate was reduced to a small volume and *n*-pentane was added to precipitate $[Pd(C_3H_5)Cl]_2$ as a yellow powder (71 mg, 76% yield vs initial $PdCl_2$).

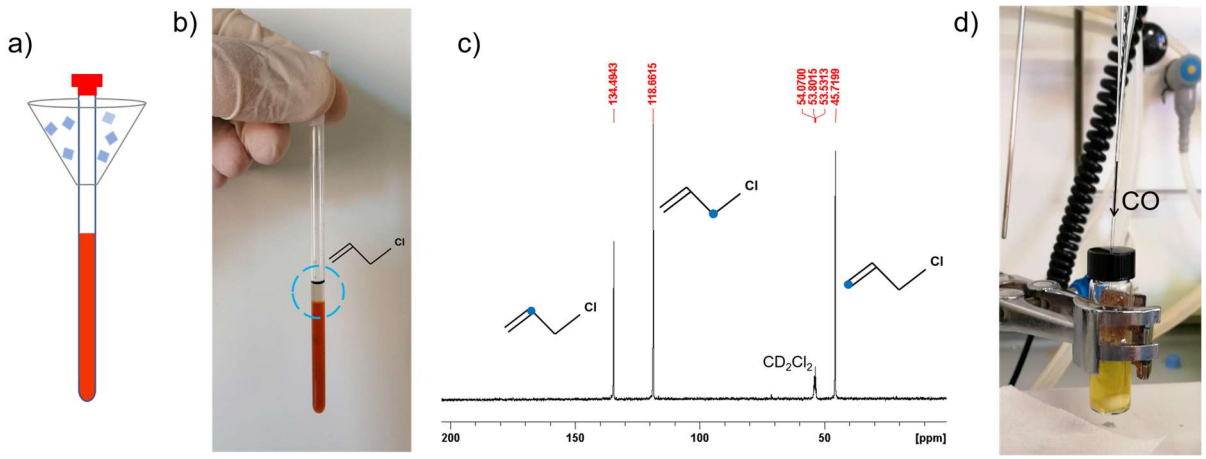

Figure B1. a) Schematic representation of the NMR tube-reactor with an ice-refrigerator (the drilled bottom of a PP centrifuge tube) mounted on top. b) AC* layer formed on top of the acidic aqueous after 1 h at 80 °C. c) ^{13}C NMR spectrum of the organic layer (corresponding to a trial with unlabelled AC) in CD_2Cl_2, showing the presence of AC only. d) Formation of yellow DIM* upon CO bubbling through the solution containing Na_2PdCl_4 and AC*.

^{1}H NMR (CD_2Cl_2, 400 MHz). The ^{1}H NMR spectrum is reported in Figure B2a. ^{13}C labelling of a terminal atom in the allylic moiety turns the A_2E_2M spin system of DIM into a second order AA'EE'MX system (see the labelling scheme in Figure B2a). A simulation of the experimental spectrum (Figure B2) was carried out with SpinWorks 4, with the following *J* (Hz):

J(A,E) = 0.60	J(E,M) = 6.74	J(M,E') = 6.74
J(A,M) = 12.16	J(E,A') = 0.50	J(M,X) = 3.60
J(A,A') = 1.00	J(E,E') = 2.15	J(A',E') = 0.6
J(A,E') = 0.50	J(E,X) = 161.00	J(A',X) = 5.80
J(A,X) = 160.00	J(M,A') = 12.16	J(E',X) = 9.35

$^{13}C\{^{1}H\}$ NMR (CD_2Cl_2, 400 MHz, 298K). The ^{13}C NMR spectrum is shown in Figure B2b. The intense singlet at δ = 62.67 corresponds to the labelled terminal carbon, the small doublet ($^{1}J_{CC}$ = 43.6 Hz) corresponds to the central carbon spin-coupled to the labelled one.

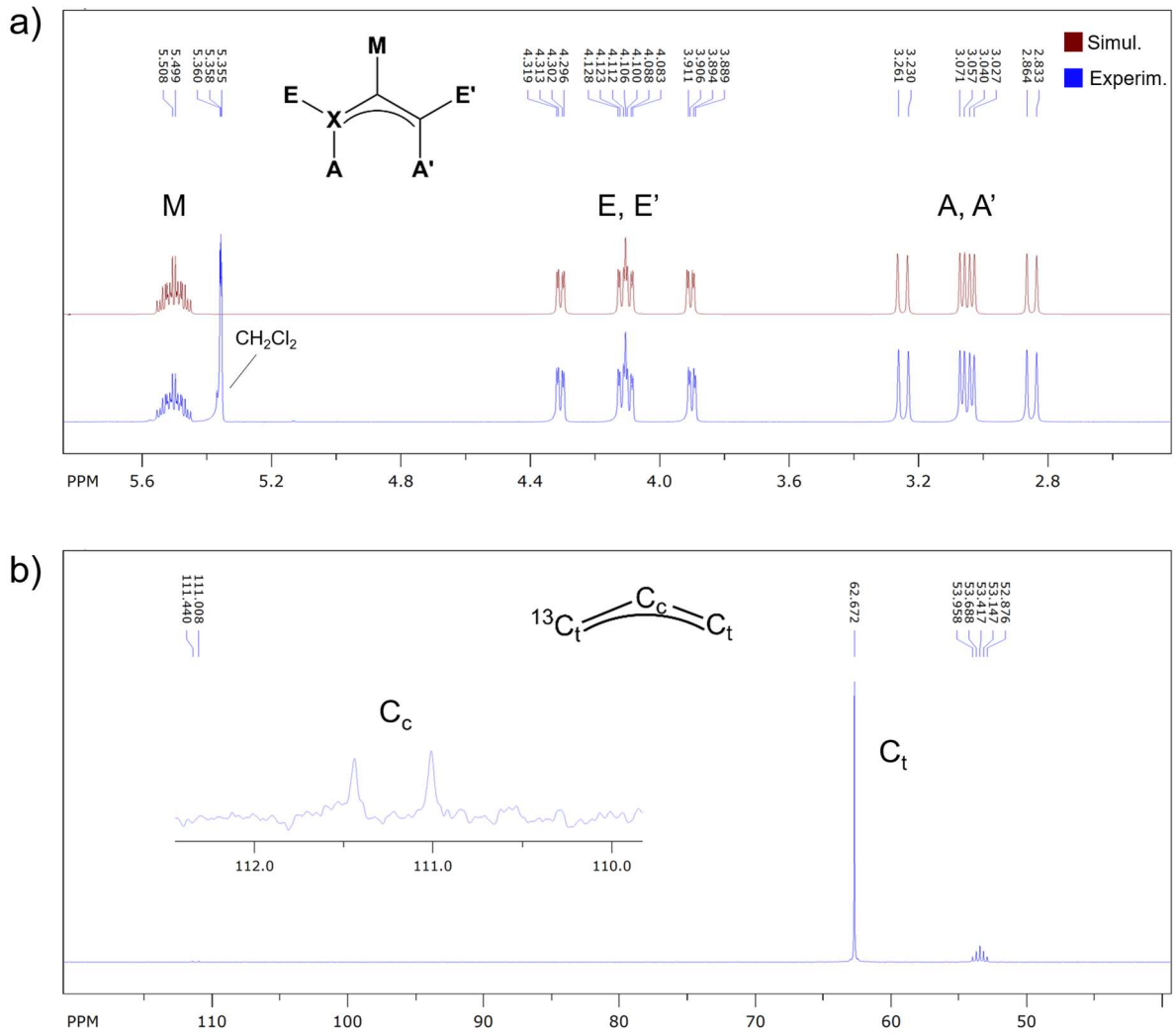

Figure B2. a) ^{1}H and (b) $^{13}C\{^{1}H\}$ NMR spectra of DIM* (CD_2Cl_2, 400 MHz, 298K).

B1.4 Functionalization 2D BP with DIM* (sample for ^{13}C CP-MAS NMR). Functionalization was carried out as described in 3.2.2 working at RT with DIM*, scaling-up the synthesis to 20 mg of 2D BP. Two identical functionalizations were run in parallel and the resulting Pd_2/BP batches were collected for a total of 40 mg of Pd_2/BP (mass referred to the BP content).

B.1.5 H_2 stability test. 5 mg of Pd_2/BP 3% were suspended in 3.5 mL of DCM and transferred in a glass vial equipped with a magnetic stirring bar. The vial was put inside a Parr autoclave, keeping the system under nitrogen stream using a funnel connected to the Schlenk line. The autoclave was sealed, purged four times with H_2, then pressurized to 5 bar with the same gas and kept stirring at room temperature for 1 h. After this time, the autoclave was vented and the suspension was transferred to a centrifuge tube. After centrifugation at 9500 rpm x 30 min, the supernatant was collected and analysed by GC-MS. As expected, no other species were detected in solution beside the solvent DCM. The solid was dried under vacuum at RT and stored under nitrogen for XPS measurements.

B.1.6 Hydrogenation of phenylacetylene. A glass vial equipped with a magnetic stirring bar was charged with a suspension of Pd_2/BP 3% (3 mg in 4 mL). Phenylacetylene was added (32 μL, 0.3 mmol, S/C=100). The vial was transferred inside a Parr autoclave. The autoclave was sealed, purged four times with H_2, pressurized to 10 bar and stirred at RT for 1 h. After this time, the volatiles were vented out and the autoclave was opened. The obtained suspension was centrifuged, and the liquid phase was collected for GC-MS analysis. Conversion = 0%.

B.1.7 Hydrogenation of 1-octene. ***Test 1.*** A catalytic trial was carried out as described above using 2 mg of Pd_2/BP 3% and 30 μL of 1-octene (0.19 mmol, S/C=100). The autoclave was pressurized with 10 bar of H_2 and was kept stirring at room temperature for 2 h. Conversion = 0%.
Test 2. A second test was carried out on 1 mg of Pd_2/BP 6% suspended in 4 mL of DCM and 30 μL of 1-octene (0.19 mmol, S/C=100). The autoclave was pressurized with 5 bar of H_2 and kept stirring at room temperature for 17 h. Conversion = 0%.

B.1.8 Electrocatalytic measurements. All the glassware was cleaned with an H_2O_2/H_2SO_4 solution (1/3 H_2O_2 30% + 2/3 H_2SO_4 98%) overnight and rinsed several times with Milli-Q water prior to use. The working electrode, a RDE glassy carbon disk (0.1963 cm^2) embedded in a PTFE jacket (PINETM) was cleaned by stirring overnight in a 0.05 μm alumina aqueous suspension. After this treatment the electrode was washed in sequence, in acetone, 2-propanol and Milli-Q water. All the aqueous solutions were prepared with Milli-Q water (18.5 mΩ*cm at 25 °C) provided with a Millipore Milli-Q3 apparatus (Nihon Millipore Ltd.). Chemicals were used as purchased from Sigma-Aldrich/Merk. Polarization curves and chronopotentiometries performed in aqueous solutions were acquired in a standard pyrex three-electrode cell (Princeton Applied Research). The reference electrode was a commercial $Ag/AgCl/KCl_{(sat)}$ (Princeton Applied Research) and the counter electrode was a gold gauze enclosed in a glass tube with porous bottom. The RDE working electrode (abbreviated WE) was coated by drop casting 34 μL of the catalyst ink by means of a micropipette. The catalyst layer was then dried under pure nitrogen flow and covered by a thin Nafion film (0.5% wt in 2-propanol) acting as binder to stick the catalyst onto the glassy carbon disk during the RDE rotation at 1600 rpm. All electrochemical studies were carried out at room temperature (20-25°C) using a Parstat 2273 potentiostat–galvanostat (Princeton Applied Research) equipped with a Model 616 Rotating Disk Electrode (PAR/Ametek). All the potentials were reported versus the Reference Hydrogen Electrode RHE.

Polarization experiments. Polarization (aka linear sweep voltammetry, LSV) experiments were performed in a 0.5 M H_2SO_4 aqueous solution (pH 0.3) saturated with hydrogen (30 minutes of pure hydrogen bubbling) with 1 mV s^{-1} scan rate, rotating the WE at 1600 rpm. The hydrogen evolution reaction was evaluated performing the scans between 0.1 and -0.4 V vs RHE without compensating the resistance. The LSV of Pd_2/BP was repeated several times with different depositions batches, showing a strong reproducibility of the measurements, except at high cathodic potentials where the formation of

hydrogen bubbles interrupts the current circulation in the cell. For this reason, it was not possible to push up the LSV at potentials more negative than -0.4 V vs RHE.

Chronopotentiometric experiments. Chronopotentiometric measurements (galvanostatic experiments) were carried out in a 0.5 M H_2SO_4 aqueous solution (pH 0.3) saturated with hydrogen. The experiments were performed at the constant current load of -1 mA (-5 mA cm^{-2}) rotating the working electrode at 1600 rpm for 3600 seconds.

Ink preparation. The ink was prepared in a glass vial suspending the catalyst (2D BP or Pd_2/BP) in CH_2Cl_2 with ultrasounds for 1' in cold water to slow down CH_2Cl_2 evaporation during ink deposition. The suspensions concentration spans between 3.5 to 3.2 mg mL^{-1} and before each deposition the inks were re-suspended with ultrasounds x 1'.

B2 Physical Methods

B2.1 Inductively Coupled Plasma Mass Spectrometry (ICP). ICP-MS measurements were performed with an Agilent 7700 Series spectrometer at the Chemistry Department, University of Florence (Italy). Samples followed a microwave-assisted digestion in nitric acid for trace analysis. Then, different dilutions of each sample with water for trace analysis were prepared, in order to obtain concentrations in the sensitivity range of the instrument for the elements under investigation (namely Pd and P). Standards at different concentrations have also been prepared and measured contextually to sample measurements, in order to obtain a calibration curve for each element under investigation.

B2.2 TEM. TEM (Transmission Electron Microscopy) studies were carried out at Ce.ME CNR (Sesto Fiorentino, Italy) using a Philips electron microscope operating at an accelerating voltage of 80 kV. Few drops of Pd_2/BP suspended in DCM were placed on the TEM copper/carbon grid, air dried, and measured.

B2.3 SEM. SEM (Scanning Electron Microscopy) experiments were carried out at Ce.ME CNR (Sesto Fiorentino, Italy) using a Dual Beam, TESCAN GAIA3 FIB/SEM ultrahigh resolution field emission microscope at 5 KeV voltage. Few drops of Pd_2/BP suspended in DCM were placed on the TEM copper/carbon grid, air dried, and measured.

B2.4 HAADF-STEM and EELS. Atomic-resolution characterization by STEM was performed at CNR- IMM (Catania, Italy) through a probe aberration-corrected JEOL ARM200CF, equipped with a Ceos hexapole-type Cs corrector, named CESCOR, and operated at a primary beam energy of 60 keV. The electron gun is a cold-field emission gun with an energy spread of 0.3 eV. The probe size was 1.0 Å at 60 kV. Micrographs were acquired in Z-contrast mode (High-Angle Annular Dark Field, HAADF).

A Centurio Energy Dispersive Spectrometer (EDS) equipped with a 100 mm^2 Silicon Drift Detector was used for the EDS acquisitions.

A GIF Quantum ER as Electron Energy Loss Spectrometer (EELS) was used for EELS measurements. Both low- and core-loss EELS spectra were acquired with the DualEELS capability through Gatan Digital Micrograph software, which allows the accurate energy calibration of EELS spectra, thanks to the simultaneous alignment of the zero-loss peak position for every single acquisition which removes any artefact coming from energy shifts. The use of Fourier logarithmic deconvolution on a full spectrum obtained by splicing together low- and core-loss EELS allows removing thickness-related plural scattering. All the STEM-EELS and STEM-EDS measurements were performed simultaneously by using the Gatan spectrum imaging (SI) tool.

Further characterization of the samples described in the main text is reported below.

- Pd_2/BP 6%

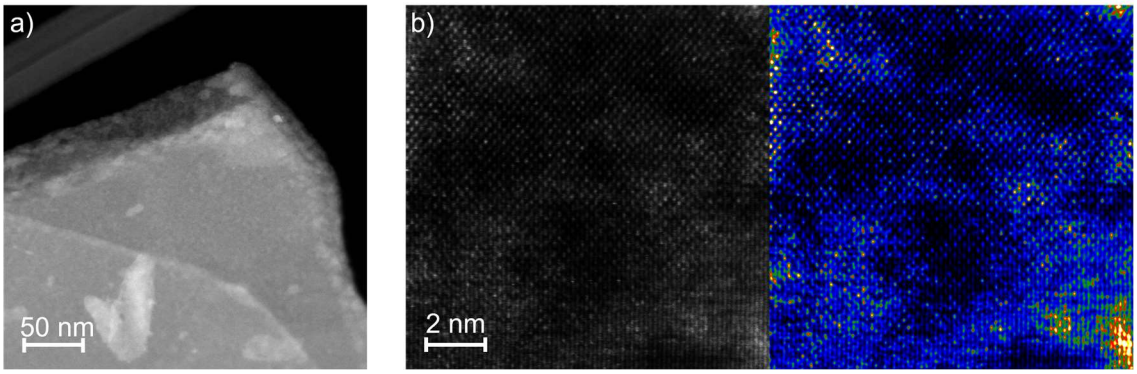

Figure B3. a) Detail of a flake edge. b) Corresponding high-resolution Z-contrast imaging (left). The same micrograph is shown on the right in false-colour (warmer colours correspond to higher Z).

- EELS microanalysis

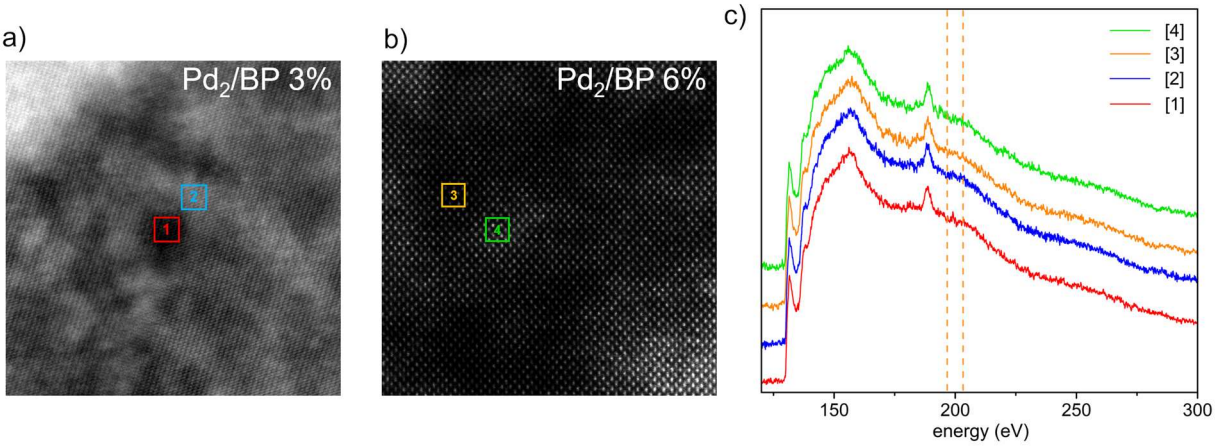

Figure B3. Comparative EELS microanalysis of Pd_2/BP 3% (a) and 6% (b), confronting EELS spectra acquired in Pd-rich regions (highlighted areas labelled 2 and 4) and Pd-poor regions (highlighted areas labelled 1 and 3). EELS spectra in (c) have been shifted on the vertical scale for the sake of comparison. The region around 200 eV highlighted with vertical bars comprises the Cl L-edge (no modifications observed).

- Pd_2/BP 3% post catalysis (HER)

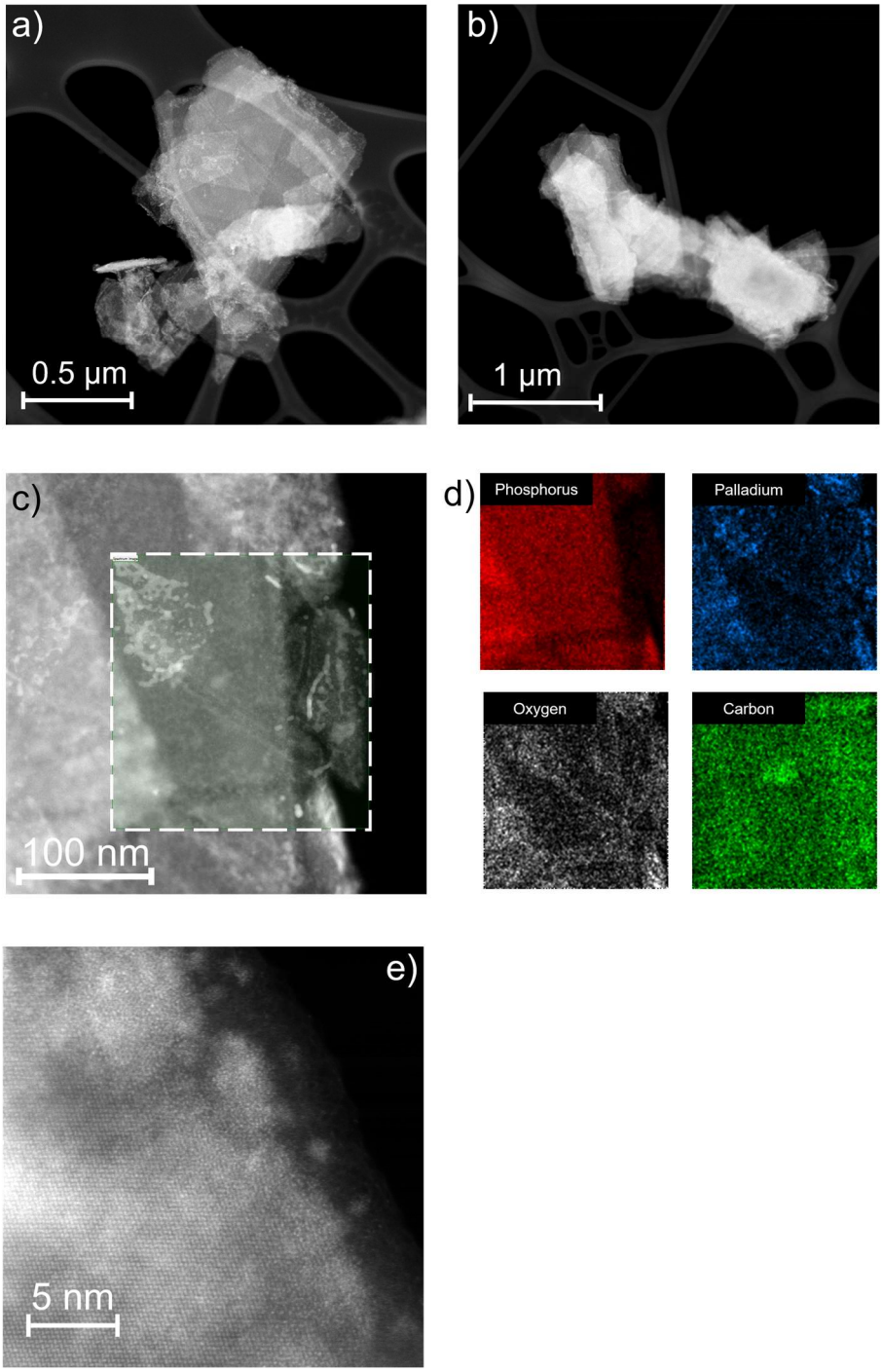

Figure B4. a-c) HAADF-STEM imaging of Pd_2/BP 3% flakes (exhaust catalyst from HER) dropcasted on carbon grid. d) EDS elemental mapping of the flake region highlighted in (c). e) High resolution micrograph of a flake edge featuring amorphization of the BP lattice along the border.

B2.5 Powder X-ray Diffraction (XRD). Data were collected with an X'Pert PRO diffractometer, operating in Bragg-Brentano parafocusing geometry with Cu-Kα radiation (λ = 1.5418 Å) at 40 kV and

30mA. Samples were prepared by slow drop-cast of the material suspended in DCM, directing a nitrogen stream onto the sample holder to speed up solvent evaporation. The process was continued until a uniform film of the material had formed. Data acquisition was carried out under air exposure.

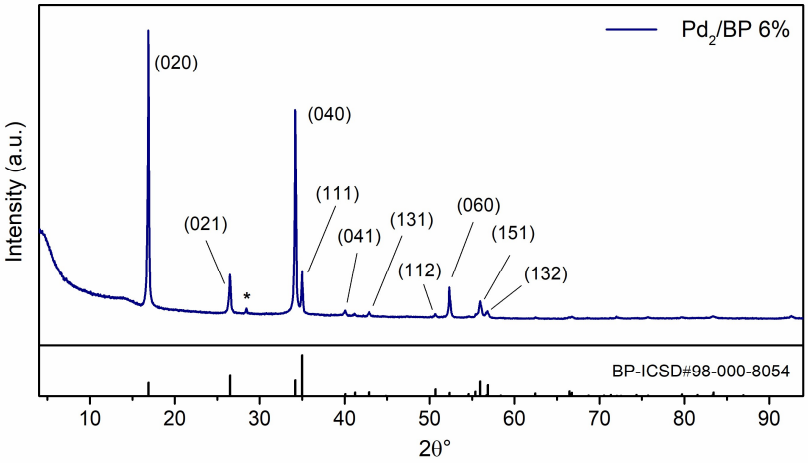

Figure B5. XRD spectrum of Pd_2/BP 6%. The reference pattern of orthorhombic BP is shown at the bottom. The peak marked with an asterisk is due to the sample-holder.

B2.6 Raman scattering. Raman measurements were carried out at CNR-IFAC (Florence, Italy) using a micro-Horiba Xplora system coupled to a 532 nm wavelength laser. The backscattered light was collected by a 100× microscope objective with 0.9 NA, which generates a ~1-μm large laser beam waist. Integration times of 10 s, laser power values in the 1-2 mW range and a grating of 1200 cm^{-1} were employed. The samples were prepared by dropcasting a suspension of 2D BP or Pd_2/BP in CH_2Cl_2 on a Si/SiO_2 wafer. After one minute of exposure, the wafers were rinsed with DCM and dried under a stream of nitrogen for 15'.

B2.7 UV-Vis reflectance. UV/vis spectra of pristine 2D BP and Pd_2/BP were recorded with a Shimadzu UV-2600 spectrometer. Diffuse reflectance spectra were collected with the same instrument in the reflectance mode using an integrating sphere (with $BaSO_4$ as a reference material). The measured samples were prepared by drop-cast of the material suspended in DCM above a $BaSO_4$ pellet. The sample was left to dry under a stream of nitrogen 15' and measured under air. No relevant differences were observed before and after functionalization.

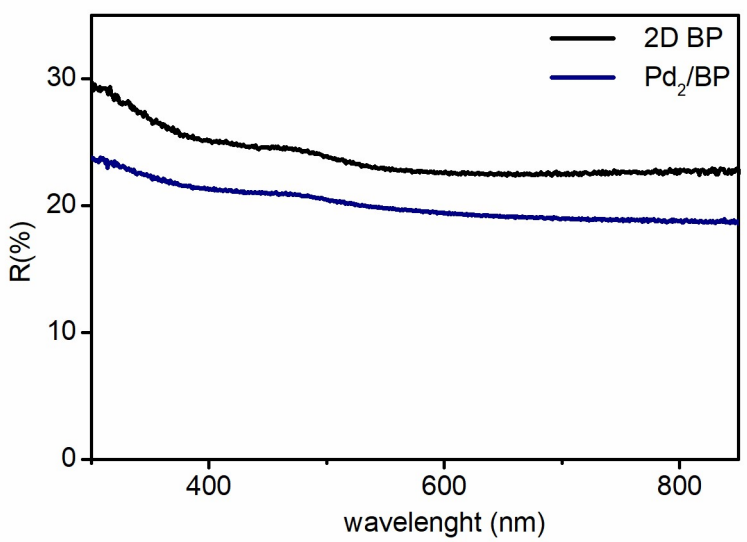

Figure B6. DRS spectra of pristine 2D BP and Pd_2/BP 3%.

B2.8 ATR-FTIR. Attenuated total reflectance spectra were recorded under air with a Perkin-Elmer Two Spectrometer, equipped with an ATR unit with diamond crystal. Spectra acquisition was carried out with a resolution of 4 cm^{-1} using 64 scans.

B2.9 X-ray Photoelectron Spectroscopy (XPS). X-ray Photoelectron Spectroscopy (XPS) measurements were performed at the Chemistry Department, University of Florence (Italy) in an ultra-high vacuum (10^{-9} mbar) system equipped with a VSW HAC 5000 hemispherical electron energy analyser and a non-monochromatized Mg-Kα X-ray source (1253.6 eV). The source power used was 100 W (10 kV×10 mA) and the spectra were acquired in the constant-pass-energy mode at E_{pas} = 44 eV. The overall energy resolution was 1.2 eV as a full-width at half maximum (FWHM) for the Ag $3d_{5/2}$ line of a pure silver reference. The recorded spectra were fitted using XPS Peak 4.1 software employing Gauss-Lorentz curves after subtraction of a Shirley-type background. The samples were dropcasted above the sample holder from a suspension in CH_2Cl_2, dried under a stream of nitrogen and introduced in the UHV system via a loadlock under inert gas (N_2) flux, in order to minimize the exposure to air contaminants and kept in the introduction chamber for at least 12 hours before the measurements.

Additional XPS spectra of samples described in the main text are shown below.

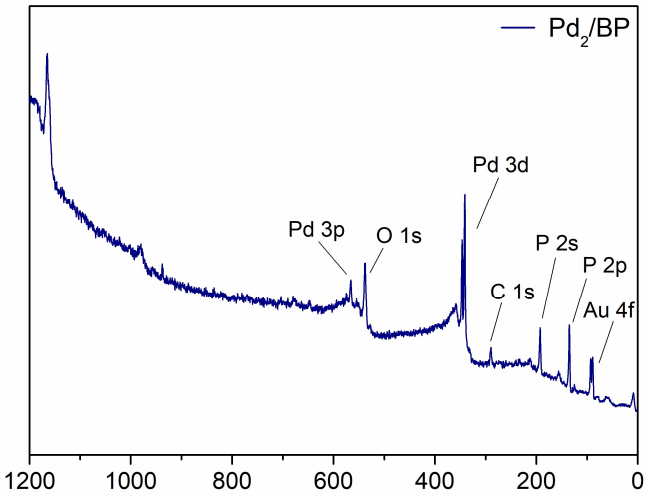

Figure B7. Survey XPS spectrum of Pd_2/BP 3%. The Au signal is due to the substrate where the sample has been dropcasted.

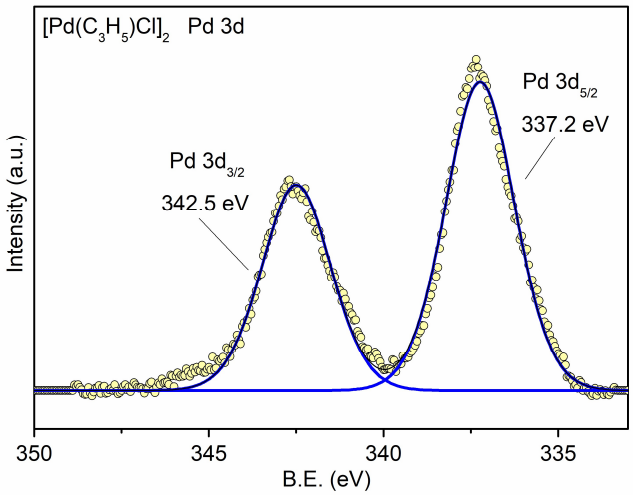

Figure B8. Core level Pd 3d spectrum of DIM.

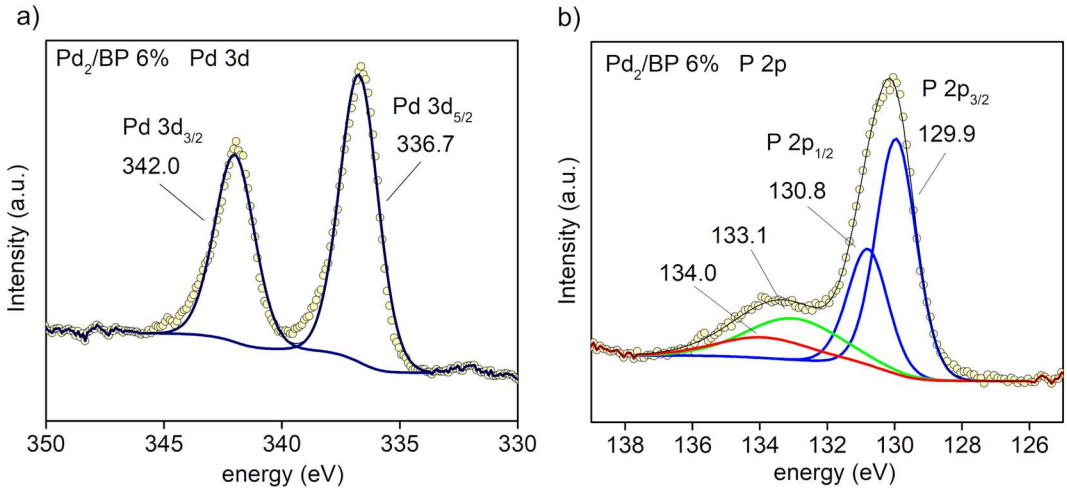

Figure B9. a) Core level Pd 3d and (b) P 2p XPS spectra of Pd_2/BP 6%. The green peak at 133 eV in the P 2p deconvolution is attributed to the P–Pd interaction, the higher energy component in red at 134 eV to surface PO_x species resulting from oxidation.

B2.10 Solid State NMR. NMR MAS measurements were performed in collaboration with CISUP (University of Pisa, Italy). Solid State NMR spectra were recorded on a Bruker Avance Neo spectrometer working at Larmor frequencies of ^{1}H, ^{13}C and ^{31}P nuclei of 500.13, 125.77, 202.46 MHz, respectively, using a triple-resonance Cross Polarization-Magic Angle Spinning (CP-MAS) probehead accommodating rotors with an external diameter of 2.5 mm. ^{31}P MAS spectra were recorded using a Direct Excitation (DE) pulse sequence, under High Power Decoupling from ^{1}H nuclei. A quantitative spectrum was recorded accumulating 16 transients, separated by a recycle delay of 200 s, while a non-quantitative DE-MAS spectrum, highlighting minor peaks, was acquired using a recycle delay of 2 s . ^{13}C MAS spectra, at a MAS frequency of 10 kHz, were recorded using both CP (with a contact time of 1 ms, accumulating 16600 transients with a recycle delay of 3 s) and DE pulse sequences (accumulating 400 scans with a recycle delay of 5 s). The 1H MAS spectrum was recorded at a MAS frequency of 20 kHz, accumulating 16 transients with a recycle delay of 2 s.

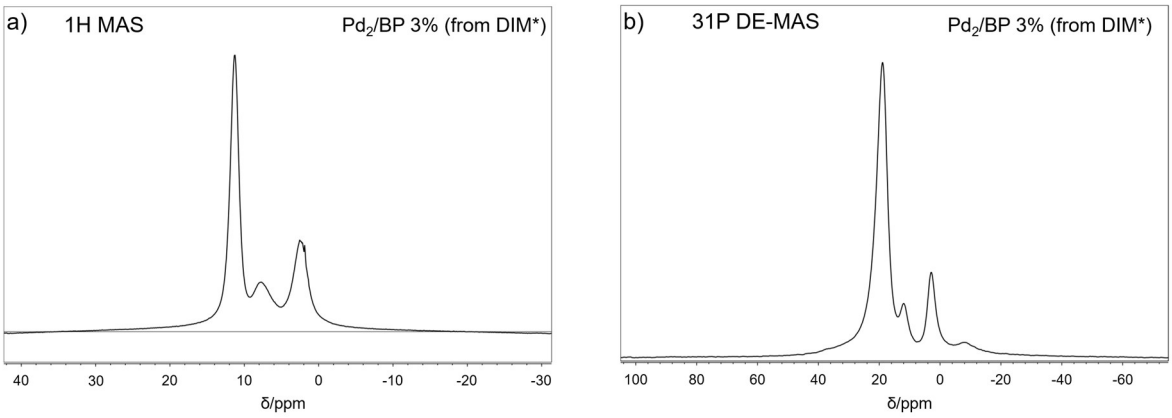

Figure B10. a) 1H MAS spectrum of Pd_2/BP (sample prepared from ^{13}C labelled DIM*). The intense peak at 11.3 ppm can be ascribed to P-OH hydrogen nuclei while those at 7.7 and 2.4 ppm arise from probehead background and organic impurities of the sample (*i.e.* residual solvents), respectively. b) ^{31}P DE-MAS spectrum recorded with a short recycle delay (2 s), in which the main signal of black phosphorus is depressed and minor peaks at -7.4 ppm (pyrophosphates), 2.5 ppm (phosphates), 11.5 ppm (hydrogen phosphites) highlighted.

B2.11 X-ray Absorption Spectroscopy (XAS). Measurements at the Pd-K edge (E = 24350 eV) were performed on the beamline SAMBA at synchrotron SOLEIL (Saint Aubin, France). The beamline is equipped with a sagittal focusing monochromator with a pair of Si(220) crystals and two Pd coated bendable cylindrical mirrors. Mirrors were used to vertically collimate (1st) and focus (2nd) the beam and act as a low energy band pass filter. The beam size at sample position is of about 300x200 μm^2 (HxV). Data were collected in continuous scan mode, each spectrum taking 150 seconds and averaging about 50 spectra. The absorption coefficient was measured in fluorescence mode using a four elements ME4 Vortex silicon drift detector. Ru, Fe and Al filters were used to reduce unwanted fluorescence and scattered radiation, were placed as close as possible to the detector window. A Pd foil placed between

the second and third ionization chamber was used as an energy calibration reference, a first ionization chamber placed before the sample was used to normalize the fluorescence signal. XAS data were reduced and analyzed with the ATENA/ARTEMIS codes whereas the theoretical XAS signals were generated with the FEFF-8.4 code using muffin tin potentials with the electron densities calculated with a Self-Consistent routine and the Hedin-Lundqvist approximation for the potential energy-dependent part. Structural parameters were obtained by data fits in R space with the transformation ranges in k space varying from case to case and a k^2 weighing factor.

Sample preparation: all materials were manipulated under argon inside a glove box. The samples to be analyzed were diluted with *h*-BN, transferred inside a die and made into pellets with a press. Each pellet was fixed to the sample holder using Kapton tape (see Figure B11). During data acquisition, the sample holder was covered with a plastic bag continuously fluxed with argon, in order to keep it under inert atmosphere for the whole measurement.

Figure B11. Sample holder with mounted sample, sticked between Kapton tape (yellow). A plastic glove transparent to X-rays continuously fluxed with argon (not shown in the figure) was put over the sample holder during data acquisition.

- *EXAFS analysis of DIM*

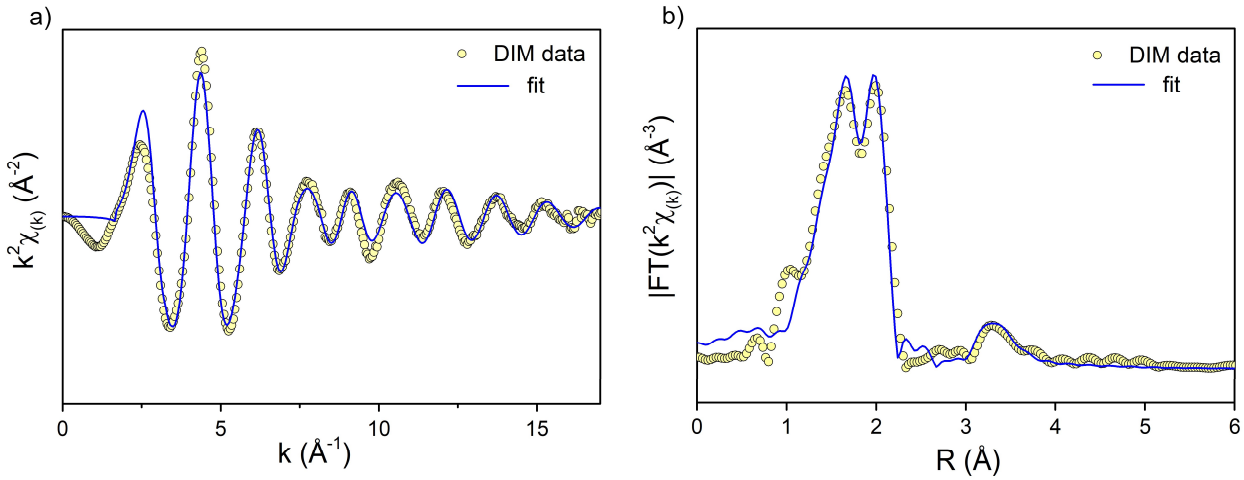

Figure B12. EXAFS spectrum (a) and corresponding Fourier transform (b) of DIM.

Comparison between the structural parameters of DIM obtained from EXAFS fitting (Table B1) and single crystal literature data (values reported in the molecular structure below, CCDC 1102405):

Table B1

Path	CN	r (Å)	σ^2 (Å^2)
Pd–C	1.6(3)	2.11(1)	0.0014(2)
Pd–Cl	2.0(3)	2.41(1)	0.006(2)
Pd–Pd	3(2)	3.48(3)	0.019(8)

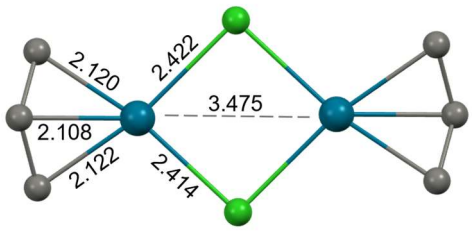

EXAFS data reproduce perfectly the interatomic distances observed by single crystal diffraction, including the non-bonding 3rd shell Pd–Pd distance. The underestimation of the Pd–C coordination number is not a peculiarity of this measurement, as it was observed earlier in molecular allylic complexes of Rh and Ir [41,42].

B2.12 GC-MS analysis. GC analyses were performed on a Shimadzu GC-2010 gas chromatograph equipped with a flame ionization detector and a 30 m (0.25 mm i.d., 0.25 mm film thickness) Varian VF-WAXms apolar capillary column. GC-MS analyses were performed on a Shimadzu QP2010SE spectrometer equipped with an identical capillary column.

B2.13 DFT calculations. *Computational details.* The optimized geometries and energetics of the molecular model of naked and functionalized BP have been studied at B3LYP-DFT27 level of theory by using the CRYSTAL17 package [43]. A *pseudo*-potential has been used for the Pd centers while the TZVP basis set has been employed for all the atomic species. Band and Crystal Overlap Orbital Population (COOP) analyses have been carried out with the available routines of the CRYSTAL17 package. Additional isomers of possible Pd_2/BP interlayer adducts were investigated with VASP 5.4.4

code [44] in the framework of DFT. Calculations were done with projector augmented wave (PAW) pseudopotentials and the exchange-correlation functional used was the Perdew-Burke-Ernzerhof for solids (PBEsol).

Single Pd(0) atom adsorption on the BP surface. The absorption of a single palladium atom on the phosphorene surface has been also investigated via DFT methods. The optimized structure features an η^3-coordination of the metal atom, as shown in Figure B12, with one shorter (2.30 Å) and two longer (2.44 Å) Pd–P distances, due to the non-optimal orientation of the lone pairs at the surface of phosphorene. The η^3 coordination of the metal atom causes a distortion of the structure since while the lone pair of P1 is properly directed, those of P2 and P3 one not, thus a shortening of the relative P2–P3 distance (2.19 *vs* 2.316 Å in pristine phosphorene) may occur to insure a sufficient overlap. A similar arrangement could be excluded both for structural reason, since the Pd(0) coordination is far from the common trigonal planar or tetrahedral geometry around the metal center, and for an unfavourable energy cost.

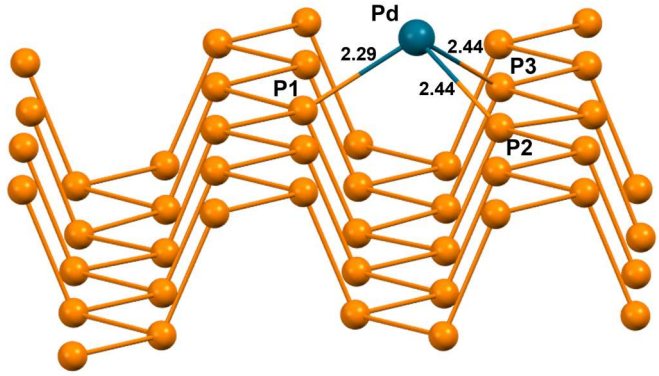

vector	*length (Å)*
Pd−P1	2.29
Pd−P2	2.44
Pd−P3	2.44
P2−P3	3.19

Figure B12. Optimized structure of the η^3 coordinated Pd atom species on phosphorene surface.

3.7 Chapter III References

[1] Y. Zhao, H. Wang, H. Huang, Q. Xiao, Y. Xu, Z. Guo, H. Xie, J. Shao, Z. Sun, W. Han, X.F. Yu, P. Li, P.K. Chu, Surface Coordination of Black Phosphorus for Robust Air and Water Stability, Angew. Chemie - Int. Ed. 55 (2016) 5003–5007. https://doi.org/10.1002/anie.201512038.

[2] L. Wu, J. Wang, J. Lu, D. Liu, N. Yang, H. Huang, P.K. Chu, X.F. Yu, Lanthanide-Coordinated Black Phosphorus, Small. 14 (2018) 1801405. https://doi.org/10.1002/smll.201801405.

[3] J. Lindley, Allyl palladium complexes: A simple experiment illustrating fluxional behavior, J. Chem. Educ. 56 (1980) 671. https://doi.org/10.1021/ed057p671.

[4] A.. Smith, Acta Crystallogr. A. 25 (1969) S161.

[5] J. Wu, J.C. Green, N. Hazari, D.P. Hruszkewycz, C.D. Incarvito, T.J. Schmeier, The reaction of carbon dioxide with palladium-allyl bonds, Organometallics. 29 (2010) 6369–6376. https://doi.org/10.1021/om1007456.

[6] J.W. Faller, N. Sarantopoulos, Retention of configuration and regiochemistry in allylic alkylations via the memory effect, Organometallics. 23 (2004) 2179–2185. https://doi.org/10.1021/om0306224.

[7] P. Braunstein, F. Naud, A. Dedieu, M.M. Rohmer, A. DeCian, S.J. Rettig, Palladium complexes with a new hemilabile bis(oxazoline)phenylphosphonite ligand. Characterization of an unprecedented chloro palladium(II)-(η^1-allyl) complex, Organometallics. 20 (2001) 2966–2981. https://doi.org/10.1021/om010165w.

[8] P. Braunstein, J. Zhang, R. Welter, Monohapto-allyl Pd(II) complexes with bidentate hybrid P,N ligands, J. Chem. Soc. Dalt. Trans. 4 (2003) 507–509. https://doi.org/10.1039/b212393m.

[9] J. Zhang, P. Braunstein, R. Welter, Stable, chloride-induced monohapto-bonding mode for an allyl ligand in a Pd(II) complex bearing a new bidentate phosphonite-oxazoline ligand, Inorg. Chem. 43 (2004) 4172–4177. https://doi.org/10.1021/ic035479l.

[10] NIST X-ray Photoelectron Spectroscopy Database, NIST Standard Reference Database Number 20, National Institute of Standards and Technology, Gaithersburg MD, 20899 (2000), doi:10.18434/T4T88K.

[11] M. Vanni, M. Serrano-ruiz, F. Telesio, S. Heun, M. Banchelli, P. Matteini, A.M. Mio, G. Nicotra, C. Spinella, S. Caporali, A. Giaccherini, F.D. Acapito, M. Caporali, M. Peruzzini, N. Istituto, N. Cnr, S.N. Superiore, P.S. Silvestro, Black Phosphorus/Palladium Nanohybrid: Unraveling the Nature of P − Pd Interaction and Application in Selective Hydrogenation, Chem. Mater. 31 (2019) 5075-5080. https://doi.org/10.1021/acs.chemmater.9b00851.

[12] L. Bai, X. Wang, S. Tang, Y. Kang, J. Wang, Y. Yu, Z. Zhou, C. Ma, X. Zhang, J. Jiang, P.K. Chu, X. Yu, Black Phosphorus / Platinum Heterostructure : A Highly Efficient Photocatalyst for Solar-Driven Chemical Reactions, Adv. Mater. 30 (2018) 18036411. https://doi.org/10.1002/adma.201803641.

[13] J. Wang, D. Liu, H. Huang, N. Yang, B. Yu, M. Wen, X. Wang, P.K. Chu, X. Yu, In-Plane Black Phosphorus / Dicobalt Phosphide Heterostructure for Efficient Electrocatalysis, Angew. Chem. Int. Ed. 57 (2018) 2600 –2604 https://doi.org/10.1002/anie.201710859.

[14] B. Tian, B. Tian, B. Smith, M.C. Scott, R. Hua, Q. Lei, Y. Tian, Supported black phosphorus nanosheets as hydrogen-evolving photocatalyst achieving 5.4% energy conversion efficiency at 353K, Nat. Commun. 9 (2018) 1397. https://doi.org/10.1038/s41467-018-03737-4.

[15] R. Zhang, J. Waters, A.K. Geim, I. V. Grigorieva, Intercalant-independent transition temperature in superconducting black phosphorus, Nat. Commun. 8 (2017) 15036.

https://doi.org/10.1038/ncomms15036.

[16] M. Rajapakse, R. Musa, U.O. Abu, B. Karki, M. Yu, G. Sumanasekera, J.B. Jasinski, Electrochemical Li Intercalation in Black Phosphorus : In Situ and Ex Situ Studies, J. Phys. Chem. C 124 (2020) 10710−10718. https://doi.org/10.1021/acs.jpcc.0c00815.

[17] G. Abell, C. Neiss, V. Lloret, S. Wild, J.C. Chac, K. Werbach, F. Fedi, H. Shiozawa, A. Gçrling, H. Peterlik, T. Pichler, F. Hauke, A. Hirsch, Exploring the Formation of Black Phosphorus Intercalation Compounds with Alkali Metals, Angew. Chem. Int. Ed., 2 (2017) 15267–15273. https://doi.org/10.1002/anie.201707462.

[18] S.P. Koenig, R.A. Doganov, L. Seixas, A. Carvalho, J.Y. Tan, K. Watanabe, T. Taniguchi, N. Yakovlev, A.H.C. Neto, O. Barbaros, Electron Doping of Ultrathin Black Phosphorus with Cu Adatoms, Nano Lett. 4 (2016) 2145-2151, https://doi.org/10.1021/acs.nanolett.5b03278.

[19] R.W.G. Wyckoff, Cubic closest packed, ccp, in: Cryst. Strcutures, Interscience Publisher, New York, 1963: pp. 7–83.

[20] L. Zhang, R. Si, H. Liu, N. Chen, Q. Wang, K. Adair, Z. Wang, J. Chen, Z. Song, J. Li, M.N. Banis, R. Li, T.K. Sham, M. Gu, L.M. Liu, G.A. Botton, X. Sun, Atomic layer deposited Pt-Ru dual-metal dimers and identifying their active sites for hydrogen evolution reaction, Nat. Commun. 10 (2019) 4936. https://doi.org/10.1038/s41467-019-12887-y.

[21] L. Bai, C.S. Hsu, D.T.L. Alexander, H.M. Chen, X. Hu, A Cobalt-Iron Double-Atom Catalyst for the Oxygen Evolution Reaction, J. Am. Chem. Soc. 141 (2019) 14190–14199. https://doi.org/10.1021/jacs.9b05268.

[22] Y. Wei, L. Sun, M. Wang, J. Hong, L. Zou, H. Liu, Y. Wang, M. Zhang, Z. Liu, Y. Li, S. Horike, K. Suenaga, Q. Xu, Fabricating Dual-Atom Iron Catalysts for Efficient Oxygen Evolution Reaction: A Heteroatom Modulator Approach, Angew. Chem. Int. Ed. 132 (2020) 16147–16156. https://doi.org/10.1002/ange.202007221.

[23] H. Yan, Y. Lin, H. Wu, W. Zhang, Z. Sun, H. Cheng, W. Liu, C. Wang, J. Li, X. Huang, T. Yao, J. Yang, S. Wei, J. Lu, Bottom-up precise synthesis of stable platinum dimers on graphene, Nat. Commun. 8 (2017) 1–10. https://doi.org/10.1038/s41467-017-01259-z.

[24] G. Manca, A. Messaoudi, A potential case of the rare Cluster Core Isomerism for phosphido-bridged Pt_3 units suggested by DFT calculations, Inorganica Chim. Acta. 470 (2018) 439–444. https://doi.org/10.1016/j.ica.2017.09.068.

[25] A. Ienco, G. Manca, M. Peruzzini, C. Mealli, Modelling strategies for the covalent functionalization of 2D phosphorene, Dalt. Trans. 47 (2018) 17243–17256. https://doi.org/10.1039/C8DT03628D.

[26] H. Yan, H. Cheng, H. Yi, Y. Lin, T. Yao, C. Wang, J. Li, S. Wei, J. Lu, Single-Atom Pd_1/Graphene Catalyst Achieved by Atomic Layer Deposition: Remarkable Performance in Selective Hydrogenation of 1,3-Butadiene, J. Am. Chem. Soc. 137 (2015) 10484–10487. https://doi.org/10.1021/jacs.5b06485.

[27] S. Zhou, L. Shang, Y. Zhao, R. Shi, G.I.N. Waterhouse, Pd Single-Atom Catalysts on Nitrogen-Doped Graphene for the Highly Selective Photothermal Hydrogenation of Acetylene to Ethylene, Adv. Mater. (2019) 1900509. https://doi.org/10.1002/adma.201900509.

[28] X.P. Yin, S.F. Tang, C. Zhang, H.J. Wang, R. Si, X.L. Lu, T.B. Lu, Graphdiyne-based Pd single-atom catalyst for semihydrogenation of alkynes to alkenes with high selectivity and conversion under mild conditions, J. Mater. Chem. A. 8 (2020) 20925–20930. https://doi.org/10.1039/d0ta07705d.

[29] M. Guo, H. Li, Y. Ren, X. Ren, Q. Yang, C. Li, Improving Catalytic Hydrogenation Performance of Pd Nanoparticles by Electronic Modulation Using Phosphine Ligands, ACS Catal. 8 (2018) 6476-6485. https://doi.org/10.1021/acscatal.8b00872.

[30] J.A. Delgado, O. Benkirane, C. Claver, D. Curulla-Ferré, C. Godard, Advances in the

preparation of highly selective nanocatalysts for the semi-hydrogenation of alkynes using colloidal approaches, Dalton. Trans. 46 (2017) 12381–12403. https://doi.org/10.1039/C7DT01607G.

[31] M.A. Mahdaly, J.S. Zhu, V. Nguyen, Y. Shon, Colloidal Palladium Nanoparticles for Selective Hydrogenation of Styrene Derivatives with Reactive Functional Groups, ACS Omega 4 (2019) 20819-20828. https://doi.org/10.1021/acsomega.9b03335.

[32] M. Zhao, Fabrication of Ultrafine Palladium Phosphide Nanoparticles as Highly Active Catalyst for Chemoselective Hydrogenation of Alkynes, Chem. - An Asian J. 11 (2016) 461–464. https://doi.org/10.1002/asia.201500939.

[33] Z. Zhao, M.M. Flores Espinosa, J. Zhou, W. Xue, X. Duan, J. Miao, Y. Huang, Synthesis of surface controlled nickel/palladium hydride nanodendrites with high performance in benzyl alcohol oxidation, Nano Res. 12 (2019) 1467–1472. https://doi.org/10.1007/s12274-019-2413-9.

[34] J. Pang, A. Bachmatiuk, Y. Yin, B. Trzebicka, L. Zhao, L. Fu, R.G. Mendes, T. Gemming, Z. Liu, M.H. Rummeli, Applications of Phosphorene and Black Phosphorus in Energy Conversion and Storage Devices, Adv. Energy Mater. (2017) 1702093. https://doi.org/10.1002/aenm.201702093.

[35] S. Lin, Y. Li, J. Qian, S.P. Lau, Emerging opportunities for black phosphorus in energy applications, Mater. Today Energy. 12 (2019) 1–25. https://doi.org/10.1016/j.mtener.2018.12.004.

[36] F. Shi, K. Huang, S. Feng, Recent Advances on Black Phosphorus Based Electrocatalysts for Water-Splitting, ChemCatChem. 12 (2020) 1913–1921.

[37] C.C. Mayorga-Martinez, N. Mohamad Latiff, A.Y.S. Eng, Z. Sofer, M. Pumera, Black Phosphorus Nanoparticle Labels for Immunoassays via Hydrogen Evolution Reaction Mediation, Anal. Chem. 88 (2016) 10074–10079. https://doi.org/10.1021/acs.analchem.6b02422.

[38] C.C. Mayorga-Martinez, Z. Sofer, D. Sedmidubský, J. Luxa, B. Kherzi, M. Pumera, Metallic impurities in black phosphorus nanoflakes prepared by different synthetic routes, Nanoscale. 10 (2018) 1540–1546. https://doi.org/10.1039/c7nr05718k.

[39] Y. Tatsuno, T. Yoshida, S. Otsuka, (η^3-allyl)palladium (II) complexes, in: Inorg. Synth., 28, 342-345.

[40] K. Usui, S. Oishi, T. Hiro, T. Arai, Process for producing allyl chloride, US 6,414,204 B1, 2002.

[41] M. Tada, T. Sasaki, Y. Iwasawa, Design of a novel molecular-imprinted Rh-Amine complex on SiO_2 and its shape-selective catalysis for α-methylstyrene hydrogenation, J. Phys. Chem. B. 108 (2004) 2918–2930. https://doi.org/10.1021/jp036421v.

[42] R.J. Trovitch, N. Guo, M.T. Janicke, H. Li, C.L. Marshall, J.T. Miller, A.P. Sattelberger, K.D. John, R. Thomas Baker, Spectroscopic characterization of alumina-supported bis(allyl)iridium complexes: Site-isolation, reactivity, and decomposition studies, Inorg. Chem. 49 (2010) 2247–2258. https://doi.org/10.1021/ic9021036.

[43] R. Dovesi, A. Erba, R. Orlando, C.M. Zicovich-Wilson, B. Civalleri, L. Maschio, M. Rérat, S. Casassa, J. Baima, S. Salustro, B. Kirtman, Quantum-mechanical condensed matter simulations with CRYSTAL, Wiley Interdiscip. Rev. Comput. Mol. Sci. 8 (2018) 1–36. https://doi.org/10.1002/wcms.1360.

[44] G. Kresse, D. Joubert, From ultrasoft pseudopotentials to the projector augmented-wave method, Phys. Rev. B - Condens. Matter Mater. Phys. 59 (1999) 1758–1775. https://doi.org/10.1103/PhysRevB.59.1758.

Acknowledgements

Al termine di un percorso durato tre anni, sono molte le persone con le quali ho condiviso la strada e a cui devo dei ringraziamenti.

Innanzitutto, i miei tutor Maria e Maurizio, per avermi fatto conoscere il mondo affascinante e infinitamente ricco dei materiali 2D e del fosforene in particolare. Per avermi accompagnato lungo tutti i tre anni. A loro va anche una sincera gratitudine per avermi dato l'opportunità di svolgere al CNR il mio dottorato, perché qui ho imparato cosa voglia dire fare ricerca: lavorare sodo, confrontarsi con molti colleghi, collaborare con persone vicine e lontane, pure mettersi in viaggio, per fare misure a volte, per partecipare a un congresso altre. Ho cercato di cogliere tutti questi aspetti, di assaporare i momenti mentre imparavo, di farne tesoro. Alcuni sono stati bellissimi. A volte accusano gli scienziati di essere aridi e affatto inclini al senso poetico. Camminare sul prato immenso del sincrotrone di Grenoble a notte fonda, mentre pioviggina, nel silenzio totale ma circondato da tanta scienza, celata dietro le finestre illuminate, da tanta dedizione... è ispirazione. Forse non poetica, o forse siamo solo un po' più bizzarri degli altri. E alla fine di questa esperienza, la cosa più importante, è che è stata fatta della buona chimica.

Ringrazio tutti gli altri ricercatori e gli amici dell'ICCOM accanto ai quali ho lavorato in questi anni: Gabriele, caro amico, con cui ho avuto il piacere di collaborare e che ho infinitamente stressato portandolo a sognare allili. Andrea Ienco, sempre presente per un aiuto e un consiglio lucido. Werner, eccellente chimico, per i preziosi spunti. Manuel, che ha preparato una tonnellata di fosforene! Compagno di viaggio in tanti congressi. Leo, lab mate e amico, persona di infinita simpatia che ha reso esilaranti anche le giornate più monotone. Lorenzo, vittima dei miei dubbi in chimica organica. Splendide persone come Alessio, Marco, Maria, Giulia e Lapo, che hanno allietato tante giornate, che mi hanno dato una mano, con le quali ho condiviso pranzi, risate e caffè (doveroso menzionare nuovamente Gabri se si dice 'caffè').

Un pensiero particolare lo rivolgo a Lapo, bravissimo chimico, un amico, che oltre alle infinite risate è sempre stato disponibile per un consiglio.

Grazie a Francesca, sempre gentile; ad Andrea Rossin, a cui temo di dovere ancora due o tre caffè (!); al mitico Francesco Barzagli; a Laura e Silvia, vicine di scrivania; a Carlo Mealli, perché per un giovane è un esempio di immutabile amore per la scienza; a Carlo Bartoli, per l'assistenza tecnica e l'aiuto. Agli amici dottorandi con cui ho condiviso tutto o parte del percorso: Iñigo, Giorgio, Rossella, Francesco, Costanza. Un ringraziamento ai colleghi di altri istituti: Silvia e Lucia, con cui ho trafficato fosforene a volontà, sempre disponibili e impeccabili nel loro lavoro; Francesco D'Acapito, che ha messo a disposizione la sua sconfinata conoscenza della spettroscopia XAS; Andrea Giaccherini, che mi ha aiutato negli esperimenti al sincrotrone; Giuseppe Nicotra e Antonio Mio, che hanno scrutato i flake di una miriade di campioni; Stefan Heun e Francesca Telesio per le misure AFM; Stefano Caporali per tutte le misure XPS.

Infine, al di là delle mura del CNR e degli istituti, perché non è facile sopportare le paranoie di un chimico se torna a casa sconsolato per una cattiva giornata, grazie a Benedetta, fidanzata paziente e motivatrice, che ha condiviso i racconti di ogni giorno. Grazie di cuore alla mia famiglia che mi ha supportato e aiutato nel percorso: a mia mamma e a mio papà, a mia nonna e a Mati. Grazie a Fabiola, a Graziano e a Edoardo, per accogliermi sempre da loro a passare serate felici.